Universidade de Aveiro Departamento de Química

Universidad Autónoma de Madrid Departamento de Química Orgánica

Ano 2017

JOANA TELES FERREIRA

FTALOCIANINAS DE RUTÉNIO COMO POTENCIAIS FOTOSSENSIBILIZADORES PARA PRODUÇÃO DE OXIGÉNIO SINGLETO

RUTHENIUM PHTHALOCYANINES AS POTENTIAL PHOTOSENSITIZERS FOR SINGLET OXYGEN GENERATION

FTALOCIANINAS DE RUTENIO COMO FOTOSENSIBILIZADORES POTENCIALES PARA LA GENERACIÓN DE OXÍGENO SINGLETE

Universidade de Aveiro Departamento de Química

Universidad Autónoma de Madrid Departamento de Química Orgánica

Ano 2017

JOANA TELES FERREIRA

FTALOCIANINAS DE RUTÉNIO COMO POTENCIAIS FOTOSSENSIBILIZADORES PARA PRODUÇÃO DE OXIGÉNIO SINGLETO

RUTHENIUM PHTHALOCYANINES AS POTENTIAL PHOTOSENSITIZERS FOR SINGLET OXYGEN GENERATION

FTALOCIANINAS DE RUTENIO COMO FOTOSENSIBILIZADORES POTENCIALES PARA LA GENERACIÓN DE OXÍGENO SINGLETE

Tese apresentada à Universidade de Aveiro para cumprimento dos requisitos necessários à obtenção do grau de Doutor em Química, realizada sob a orientação científica do Doutor Tomás Torres Cebada, Professor Catedrático do Departamento de Química Orgânica da Faculdade de Ciências da Universidade Autónoma de Madrid; do Doutor João Tomé, Professor Associado do Departamento de Engenharia Química do Instituto Superior Técnico de Lisboa; e da Doutora M. Salomé Rodríguez Morgade, Professora Titular do Departamento de Química Orgânica da Faculdade de Ciências da Universidade Autónoma de Madrid.

Financial support came from the Seventh Framework Programme (FP7-People-2012-ITN, SO2S project, grant agreement number: 316975); from FCT to QOPNA (FCT UID/QUI/00062/2013)IBILI (FCT UID/NEU/04539/2013), CQE (FCT UID/QUI/0100/2013) and CQC (PEst-OE/QUI/UI0313/2014) research units, through national funds and where applicable co-financed by the FEDER, within the PT2020 Partnership Agreement; and from Compete (POCI-01-0145-FEDER-007440) to IBILI.

Aos meus pais e ao meu irmão.

o júri

presidente

Prof. Doutor Eduardo Anselmo Ferreira da Silva
Professor Catedrático do Departamento de Geociências da Universidade de Aveiro

Prof. Doutora María Salomé Rodríguez Morgade
Professora titular do Departamento de Química Orgânica da Faculdade de Ciências da Universidade Autónoma de Madrid

Prof. Doutor João Paulo Costa Tomé
Professor associado da Faculdade de Engenharia Química do Instituto Superior Técnico da Universidade de Lisboa

Prof. Doutora Teresa Margarida Vasconcelos Dias de Pinho e Melo
Professor associado com agregação do Departamento de Química da Faculdade de Ciência e Tecnologia da Universidade de Coimbra

Doutor Miguel García Iglesias
Investigador da Faculdade de Ciências da Universidade Autónoma de Madrid

Prof. Doutor Augusto Costa Tomé
Professor associado com agregação do Departamento de Química da Universidade de Aveiro

Doutora Rosa Cristina Simões Fernandes
Investigadora do Instituto Biomédico de Investigação da Luz e da Imagem (IBILI) da Faculdade de Medicina da Universidade de Coimbra

Doutor Pedro Miguel Ribeiro Paulo Neves
Investigador de Pós-doutoramento do Centro de Química Estrutural do Departamento de química do Instituto Superior Técnino da Universidade de Lisboa

agradecimentos

Este trabalho não teria sido possível sem toda a ajuda e apoio que recebi ao longo dos últimos quatro anos.

Em primeiro lugar quero agradecer aos meus orientadores. Ao Dr. João Tomé por me proporcionar esta oportunidade única, ao professor Tomás Torres por me ter recebido no laboratório em Madrid e à Dra. Salomé Rodriguez, por toda a sua ajuda a resolver os mais variados problemas que foram surgindo com o trabalho no laboratório.

Quero agradecer também à Dra. Rosa Fernandes por me proporcionar a oportunidade de realizar estudos *in vitro* no IBILI, e ao Dr. João Pina pela ajuda com as medidas de fosforescência.

Quero agradecer aos meus colegas de laboratório em Aveiro, em especial ao João Rodrigues, por me terem incentivado e encorajado a fazer o doutoramento numa universidade estrangeira.

En Madrid he conocido a mucha gente especial que no olvidaré nunca. Gracias Ettore, Eveline y David no sólo por toda la ayuda en el laboratorio, pero especialmente por todas las veces que hemos salido a conocer Madrid y el resto de España. Javi, gracias por tu paciencia, por todas las veces que me has ayudado con la química y que me has corregido el español. Francesca, gracias por toda tu ayuda con las ftalos de ruténio y con el oxígeno singlete. María y Nico, gracias por todas las veces que me habéis ayudado y alegrado el día. Larita, gracias por todo tu apoyo y amistad. Miguel, has estado presente cuando más he necessitado, gracias por todo. Quiero agradecer a todos los demás, que en algún momento me habéis ayudado, Ana Aljarilla, Giulia, Miguel Ángel, Luís, Julia, German, Sara, Edu, Vero, Marta, Pablo, Bea, Mafalda.

Quero também agradecer ao José Carlos por me ter ensinado a trabalhar com culturas celulares. Obrigado Ana Peixoto, por toda a ajuda e pela companhia que me fizeste em Coimbra.

Fora do trabalho, quero também agradecer à Diana, à Filipa e à Joana, obrigada pela vossa amizade, que resiste ao tempo e à distância.

Por último, quero agradecer ao meu pai, à minha mãe e ao meu irmão. Sem a vossa força, confiança e apoio incondicional nada disto seria possível.

Obrigado!

palavras-chave

Ftalocianinas, ruténio, fotossensibilizadores, terapia fotodinâmica, fotoinactivação de microrganismos, oxigénio singleto, cancro, polietilenoglicol, glucose, galactose, manose, ácido fólico, fosfinas.

resumo

A Terapia Fotodinâmica combina luz, oxigénio molecular e um fotossensibilizador para a produção de espécies reativas de oxigénio, como $^1O_2$ e radicais livres, os quais vão induzir stress oxidativo e, eventualmente, morte celular. Isto permite assim a destruição de células tumorais de uma forma não invasiva, seletiva e localizada, com efeitos secundários reduzidos. As ftalocianinas são compostos promissores para serem aplicados como fotossensibilizadores na produção de oxigénio singleto. No entanto, um inconveniente destes compostos é a sua reduzida solubilidade em meio aquoso. Isto pode ser ultrapassado através da sua funcionalização nas posições periféricas e/ou axiais com grupos hidrofílicos apropriados, como por exemplo hidratos de carbono e cadeias de poliéter. A introdução de ligandos axiais reduz a agregação das ftalocianinas em solução, melhorando a sua eficiência para produzir $^1O_2$.

Este trabalho descreve a síntese de Ftalocianinas de Ruténio (RuPcs) para serem utilizadas como fotossensibilizadores. Estas RuPcs estão funcionalizadas nas posições axiais com ligandos apropriados que proporcionam a solubilidade e/ou seletividade requeridas para a sua aplicação em Terapia Fotodinâmica. Neste sentido, foram sintetizados diferentes derivados de piridina e fosfina funcionalizados com grupos iónicos, cadeias de poliéter, hidratos de carbono ou com unidades de ácido fólico, as quais foram posteriormente coordenadas ao ião central de RuPcs. Adicionalmente, a solubilidade em água foi melhorada através da funcionalização da periferia das RuPcs com cadeias poliéter. Foram estudadas as propriedades físicas e fotofísicas, nomeadamente, a solubilidade em água e a capacidade de produzir oxigénio singleto, de todos os fotossensibilizadores preparados. Além disso, os compostos foram avaliados *in vitro* em células do cancro da bexiga com respeito à sua capacidade para serem internalizados por células cancerígenas a aos seus efeitos tóxicos, tanto no escuro como mediante ativação com luz.

keywords

Phthalocyanines, Ruthenium, photosensitizers, photodynamic therapy, photoinactivation of microorganisms, singlet oxygen, cancer, polyethylene glycol glucose, galactose, manose, folic acid, phosphine.

abstract

The Photodynamic Therapy (PDT) combines light, molecular oxygen and a PS for the production of reactive oxygen species (ROS), such as $^1O_2$ and free radicals, which will induce oxidative stress and, eventually, cell death. This allows for the non-invasive, selective and localized destruction of tumor cells with reduced side effects. Phthalocyanines (Pcs) are promising compounds to be applied as PSs for singlet oxygen generation. However, a major drawback of these compounds is their low solubility in physiological media. This can be overcome through functionalization of the macrocycle at the peripheral and/or axial positions with appropriate hydrophilic functions, such as carbohydrates and polyether chains. The introduction of axial ligands reduces their aggregation in solution, thus improving their $^1O_2$ generation efficiency.

This work describes the synthesis of Ruthenium Phthalocyanines (RuPcs) to be applied as photosensitizers (PSs) for singlet oxygen generation. These RuPcs are endowed with suitable axial ligands, providing the required solubility and/or selectivity. In this respect, several pyridine or phosphine-based structures bearing charged functions, polyether chains, carbohydrate units or folic acid units were synthesized and further coordinated to the central ion of RuPcs. In addition, solubility in water is enhanced through peripheral functionalization with polyether chains. The photophysical properties of the prepared PSs, namely their solubility in water and their ability to generate singlet oxygen were studied. Furthermore, the PSs were also evaluated *in vitro* in bladder cancer cells with respect to their capability to be internalized by cancer cells and their toxic effects, both in the dark and upon activation by light.

palabras clave

Ftalocianinas, rutenio, fotosensibilizadores, terapia fotodinámica, fotoinactivación de microorganismos, oxígeno singlete, cancer, polietileneglicol, glucosa, galactosa, manosa, ácido fólico, fosfina.

resumen

La Terapia Fotodinámica combina luz, oxígeno molecular y un fotosensibilizador para la producción de especies reactivas de oxígeno, como el $^1O_2$ y radicales libres, los cuales inducen estrés oxidativo y, eventualmente, la muerte celular. Esto permite así la destrucción de células tumorales de una forma no invasiva, selectiva y localizada, con efectos secundarios reducidos. Las ftalocianinas muestran un gran potencial para su aplicación como fotosensibilizadores para la producción de oxígeno singlete. Sin embargo, un inconveniente de estos compuestos es su solubilidad reducida en medio acuoso. Esto puede superarse a través de su funcionalización en las posiciones periféricas y/o axiales con grupos hidrofílicos apropiados, como por ejemplo hidratos de carbono y cadenas poliéter. La introducción de ligandos axiales reduce la agregación de las ftalocianinas en disolución, mejorando su eficiencia para producir $^1O_2$.

Este trabajo describe la síntesis de Ftalocianinas de Rutenio (RuPcs) para su utilización como fotosensibilizadores en la producción de oxígeno singlete. Estas RuPcs están funcionalizadas en las posiciones axiales ligandos apropriados que proporcionan la solubilidad y/o selectividad requeridas para una aplicación en Terapia Fotodinámica. En este sentido, se sintetizaron diferentes derivados de piridina y fosfina funcionalizados con grupos cargados, cadenas poliéter, hidratos de carbono o con unidades de ácido fólico, las cuales fueron posteriormente coordinadas al ión central de RuPcs. Además, se mejoró la solubilidad de las RuPcs mediante la introducción de cadenas poliéter en las posiciones periféricas. Se estudiaron las propiedades físicas y fotofísicas, en particular, la solubilidad en agua y la capacidad para producir oxígeno singlete, de los fotosensibilizadores preparados. Además, todos los compuestos se evaluaron *in vitro* en células del cáncer de vejiga urinaria, con respecto a su capacidad para ser internalizados por las células cancerígenas y a sus efectos tóxicos, tanto en la oscuridad como mediante la activación con luz.

Table of Contents

List of Abbreviations

^{13}C NMR	Carbon-13 Nuclear Magnetic Resonance
^{1}H NMR	Proton Nuclear Magnetic Resonance
ADMA	α,α'-(Anthracene-9,10-diyl)bismethylmalonate
AMD	Age-related macular degeneration
BCA	Bicinchoninic acid
COSY	Correlation spectroscopy
DBB	*o*-Dibenzoylbenzene
DCC	N,N'-Dicyclohexylcarbodiimide
DCM	Dichloromethane
DCU	Dicyclohexylurea
DCTB	*Trans*-2-[3-(4-*tert*-buthylphenyl)-2-methyl-2-propenylidene]malononitrile
DMAC	Dimethylacetamide
DMAP	Dimethylaminopyridine
DMF	Dimethylformamide
DMSO	Dimethyl sulfoxide
DPBF	1,3-diphenylisobenzofuran
EDC	*N*-(3-dimethylaminopropyl)-*N*'-ethyl-carbodiimide hydrochloride
EI	Electronic impact
ESI	Electrospray ionization
FA	Folic acid
FAB	Fast atom bombardment
FR	Folate receptor
FT-IR	Fourier Transform Infrared Spectroscopy
HMQC	Heteronuclear Multiple Quantum Coherence
HOMO	Highest occupied molecular orbital
HPD	Hematoporphyrin derivative
LUMO	Lowest unoccupied molecular orbital
m/z	Mass-to-charge ratio
MALDI	Matrix-Assisted Laser Desorption/Ionization
MPc	Metallophthalocyanine
MTT	Methylthiazolyldiphenyl-tetrazolium bromide

MS	Mass Spectrometry
NLO	Nonlinear Optics
nm	Nanometer
NMR	Nuclear Magnetic Resonance
PBS	Phosphate-buffered saline
Pc	Phthalocyanine
PDT	Photodynamic Therapy
PEG	Polyethylene glycol
Por	Porphyrin
ppm	Parts per million
PS	Photosensitizer
RFC	Reduced folate carrier
ROS	Reactive Oxygen Species
SDS	Sodium dodecyl sulfate
S.E.M.	Standard error of mean
TEA	Triethylamine
TEG	Triethylene glycol
THF	Tetrahydrofuran
TLC	Thin Layer Chromatography
TMSOTf	Trimethylsilyl trifluoromethanesulfonate
UV-Vis	Ultraviolet Visible

Introduction

1. General characteristics about Phthalocyanines

Phthalocyanines (Pcs) are a family of aromatic macrocyclic compounds with a similar structure to biologically important molecules, such as hemoglobin and chlorophyll, which consist on synthetic analogues of porphyrins (Por).[1-3] The word phthalocyanine comes from the Greek naphtha (rock oil) and cyanine (dark blue).[4]

The synthesis of the first Pc occurred accidentally in 1907, during the study of the properties of 1,2-cyanobenzamide.[5] Later on, in 1928, a copper phthalocyanine was obtained when attempting to prepare 1,2-dicyanobenzene from dibromobenzene and CuCN.[6] In spite this, it was only in the thirties that Linstead and Robertson determined the crystal structures of metal-free and some metallophthalocyanines (MPcs).[7-13]

1.1. Structure and properties

Pcs are composed of four isoindole units, linked together through their 1,3-positions by *aza*-bridges. This arrangement gives rise to a planar heteroannulene with a 18 π-electron conjugated system, delocalized over 32 carbon and 8 nitrogen atoms (**Figure 1**).[2,3,14]

[1] In *Porphyrin Handbook*; Karl M. Kadish, Kevin M. Smith, R. G., Ed.; San Diego, **2003**.
[2] de la Torre, G.; Claessens, C. G.; Torres, T. *Chem. Commun.* **2007**, No. 20, 2000-2015.
[3] Claessens, C. G.; Hahn, U.; Torres, T. *Chem. Rec.* **2008**, *8* (2), 75–97.
[4] Guillaud, G.; Simon, J.; Germain, J. P. *Coord. Chem. Rev.* **1998**, *178-180*, 1433–1484.
[5] Braun, A.; Tcherniac, J. *Berichte der Dtsch. Chem. Gesellschaft* **1907**, *40* (2), 2709–2714.
[6] de Diesbach, H.; von der Weid, E. *Helv. Chim. Acta* **1927**, *10* (1), 886–888.
[7] Linstead, R. P.; Lowe, A. R. *J. Chem. Soc.* **1934**, No. 0, 1031–1033.
[8] Dent, C. E.; Linstead, R. P.; Lowe, A. R. *J. Chem. Soc.* **1934**, No. 0, 1033–1039.
[9] Robertson, J. M. *J. Chem. Soc.* **1935**, 615–621.
[10] Robertson, J. M.; Linstead, R. P.; C. E. Dent. *Nature* **1935**, 506–507.
[11] Robertson, J. M. *J. Chem. Soc.* **1936**, 1195–1209.
[12] Bradbrook, E. F.; Linstead, R. P. *J. Chem. Soc.* **1936**, 1744–1748.
[13] Robertson, J. M.; Woodward, I. *J. Chem. Soc.* **1937**, 219–230.
[14] de la Torre, G.; Claessens, C. G.; Torres, T. *European J. Org. Chem.* **2000**, *2000* (16), 2821–2830.

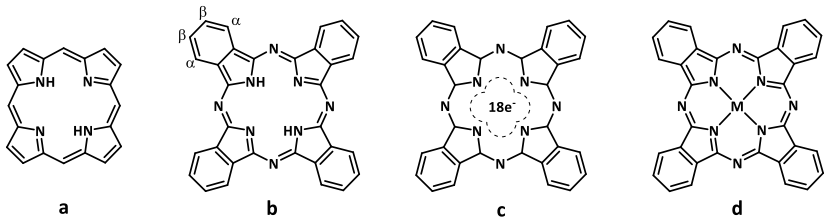

Figure 1 – *(a)* Porphyrin, *(b)* free-base phthalocyanine, *(c)* electronic delocalization over the Pc's anionic ligand, *(d)* Metallophthalocyanine.

As a porphyrin analogue, the systematic name of Pcs according to the IUPAC nomenclature is tetrabenzol[*b,g,l,q*]-5,10,15,20-tetraazaporphyrin. In IUPAC nomenclature, all C and N atoms of Pc are numbered, with the exception of C atoms that correspond to the fusion of pyrrole ring and benzene ring (**Figure 2**).[15]

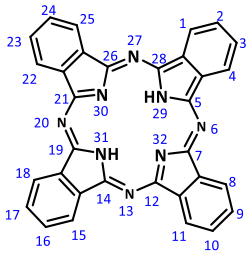

Figure 2 – IUPAC numbering of Phthalocyanines.

Pcs exhibit an enormous versatility, in the way that several substituents can be introduced at the non-peripheral and peripheral positions (α and β positions, respectively, see **Figure 1**) of the macrocycle. Even though the distinction between peripheral and non-peripheral positions is used by several authors, in this thesis the term "peripheral" will be used for both α and β positions, with no distinction between them. Furthermore, free-base Pcs contain two hydrogen atoms in the central cavity of the aromatic ring that can be replaced by more than 70 metal ions giving rise to MPcs. Some of these central ions allow functionalization with axial ligands. This flexibility of Pcs is of great importance, since all these modifications can be used and combined in different ways in order to modulate their physicochemical properties and electronic structure.[2-4,14,16,17]

The aromaticity of Pcs provides them with important electronic and optical properties. Among them, their high stability, both chemically and thermally, as well as their strong absorption

[15] Moss, G. P. *Pure Appl. Chem.* **1987**, *59* (6), 779–832.
[16] de la Torre, G.; Vázquez, P.; Agulló-López, F.; Torres, T. *J. Mater. Chem.* **1998**, *8* (8), 1671–1683.
[17] de laTorre, G.; Vazquez, P.; Agullo-Lopez, F.; Torres, T. *Chem. Rev.* **2004**, *104* (9), 3723–3750.

in the visible region, conferring a dark green-blue color, are responsible for the traditional use of Pcs as dyestuffs for textiles and inks.[2,14,18] Concerning their stability, MPcs are stable at temperatures up to 100 °C and towards strong acids (e.g. conc. H_2SO_4) or strong bases. Besides, these compounds can only be decomposed by strong oxidizing agents, such as dichromate or ceric salts. Another important feature of Pcs is that they can be obtained as high purity materials, since they are easily crystallized and sublimed.[4]

The absorption spectrum of Pcs is characterized by two intense and well-resolved absorption bands: one in the visible region, around 620-700 nm, called Q-band, and another one in the ultraviolet region, around 340 nm, called B-band or Soret band (**Figure 3**). Both Soret and Q bands originate from $\pi \rightarrow \pi^*$ transitions within the macrocycle.[2,16-20] The exact position of these Pc bands is directly linked to the presence and nature of a central atom, the type, number and positions of peripheral substituents, the presence of axial ligands, macrocyclic aggregation and solvent, as well as the symmetry of the Pc π-conjugated system.[17,18,20-22] While MPcs, having a doubly degenerated lowest exited state, exhibit only a single Q band, metal-free Pcs have their Q band split into two main components, due to splitting of the lowest excited state into two components. This is because of the greater symmetry of MPcs (D_{4h}), comparatively to free-base Pcs (D_{2h}), in which only two of their four internal nitrogen atoms are carrying hydrogen atoms (see **Figure 1**).[3,17,20]

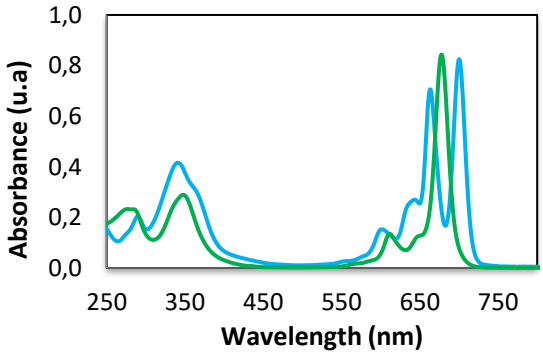

Figure 3 – Typical UV-vis spectrum of free-base (blue) and metallophthalocyanines (green).[17]

Usually, Pcs are characterized by emission of fluorescence from the S_1 state. Nevertheless, this is strongly dependent on the metal ion coordinated in the center of the macrocycle. For

[18] Nyokong, T. In *Functional Phthalocyanine Molecular Materials*; Jiang, J., Ed.; Springer Berlin Heidelberg, 2010; pp 45–88.
[19] Chen, Y.; Hanack, M.; Blau, W.; Dini, D.; Liu, Y.; Lin, Y.; Bai, J. *J. Mater. Sci.* **2006**, *41* (8), 2169–2185.
[20] Rio, Y.; Salome Rodriguez-Morgade, M.; Torres, T. *Org. Biomol. Chem.* **2008**, *6* (11), 1877–1894.
[21] Kobayashi, N.; Ogata, H.; Nonaka, N.; Luk'yanets, E. A. *Chem. Eur. J.* **2003**, *9*, 5123–5134.
[22] Mack, J.; Kobayashi, N. *Chem. Rev.* **2011**, *111* (2), 281–321.

instance, free-base Pcs generally display higher fluorescence quantum yields when compared with the corresponding ZnPcs, due to the heavy-metal effect of Zn.[21] The heavy atom effect results from the enhanced spin-orbit coupling between the metal ion *d*-orbitals and the Pc π-system. Therefore, such MPcs exhibit a greater tendency to undergo intersystem crossing (ISC) from the singlet excited state S_1 to the triplet excited state T_1, which is reflected by high triplet state quantum yields.[23,24]

Moreover, the strong π-π interactions between Pc aromatic rings grant them stacking abilities with the formation of aggregates,[25] which are represented as a coplanar association of rings under formation of trimers and higher order complexes. This aggregation state results from enhanced Van der Waal's attractive forces between Pc rings and depends on the concentration, nature of the solvent, functionalization of the macrocycle and temperature.[2,3,16,17,19,26-28] The formation of such aggregates may be desirable in order to obtain materials with different properties related to those exhibited by the corresponding monomers.[29] Aggregates of Pcs can be classified as H-aggregates and J-aggregates (**Figure 4**). H-aggregates exhibit a blue-shift in their absorption spectra when compared to the corresponding monomers, and are characterized by loss of their fluorescent properties. J-aggregates typically display a red-shift of their Q-band but still maintain emission properties.[29-32] The presence of aggregates may also be undesirable, i.e. for applications as nonlinear optical (NLO) materials[19] and for photodynamic therapy (PDT).[33] The decrease or suppression of the Pc aggregation can be achieved by inserting bulky substituents at the axial positions of the macrocycle and/or at its periphery.[17] Axial substitution effectively prevents the interactions between Pc rings. Among the metals ions that allow axial functionalization are

[23] Solov'ev, K. N.; Borisevich, E. A. *Physics-Uspekhi* **2005**, *48* (3), 231.

[24] Zhang, X.-F.; Shao, X.; Tian, H.; Sun, X.; Han, K. *Dye. Pigment.* **2013**, *99* (2), 480–488.

[25] Hunter, C. A.; Sanders, J. K. M. *J. Am. Chem. Soc.* **1990**, *112* (14), 5525–5534.

[26] Choi, M. T. M.; Li, P. P. S.; Ng, D. K. P. *Tetrahedron* **2000**, *56*, 3881–3887.

[27] Dominguez, D. D.; Snow, A. W.; Shirk, J. S.; Pong, R. G. S. *J. Porphyr. Phthalocyanines* **2001**, *5* (7), 582–592.

[28] Atilla, D.; Durmus, M.; Gurek, A. G.; Ahsen, V.; Nyokong, T. *Dalt. Trans.* **2007**, 1235–1243;

[29] Zhang, X.-F.; Xi, Q.; Zhao, J. *J. Mater. Chem.* **2010**, *20* (32), 6726–6733.

[30] Kameyama, K.; Morisue, M.; Satake, A.; Kobuke, Y. *Angew. Chemie Int. Ed.* **2005**, *44* (30), 4763–4766;

[31] Pescitelli, G.; Di Bari, L.; Berova, N. *Chem. Soc. Rev.* **2014**, *43* (15), 5211–5233.

[32] Bayda, M.; Dumoulin, F.; Hug, G. L.; Koput, J.; Gorniak, R.; Wojcik, A. *Dalt. Trans.* **2017**, *46* (6), 1914–1926.

[33] Dąbrowski, J. M.; Pucelik, B.; Regiel-Futyra, A.; Brindell, M.; Mazuryk, O.; Kyzioł, A.; Stochel, G.; Macyk, W.; Arnaut, L. G. *Coord. Chem. Rev.* **2016**, *325*, 67–101.

indium,[34] gallium,[35] titanium,[36] silicon[37] and ruthenium.[38] This thesis will focus on the synthesis of ruthenium phthalocyanines.

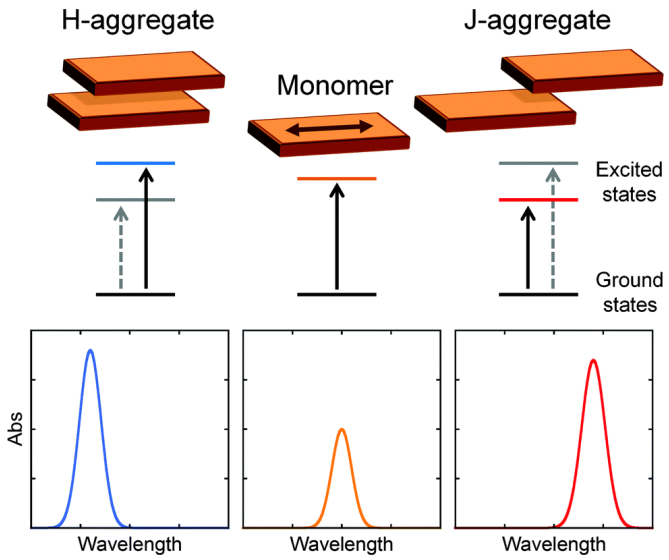

Figure 4 – Typical arrangements of H- and J-aggregates and corresponding effects in the absorption UV-vis spectra. Full arrows depict allowed (strong) transitions, and dashed arrows forbidden (or weak) ones.[31]

Ruthenium is a transition metal and a strong Lewis acid with a coordination number of six, thus allowing the introduction of two axial ligands in Ru(II)Pcs. Since ruthenium shows a high affinity to nitrogen and phosphorous based ligands, the synthesis of a large variety of RuPcs endowed with

[34] Hanack, M.; Heckmann, H. *Eur. J. Inorg. Chem.* **1998**, *1998* (3), 367–373.
[35] Chen, Y.; Subramanian, L. R.; Barthel, M.; Hanack, M. *Eur. J. Inorg. Chem.* **2002**, *2002* (5), 1032–1034.
[36] Barthel, M.; Dini, D.; Vagin, S.; Hanack, M. *European J. Org. Chem.* **2002**, *2002* (22), 3756–3762.
[37] van de Winckel, E.; Schneider, R. J.; de la Escosura, A.; Torres, T. *Chem. – A Eur. J.* **2015**, *21* (51), 18551–18556.
[38] Rawling, T.; McDonagh, A. *Coord. Chem. Rev.* **2007**, *251* (9–10), 1128–1157.

pyridine,[39-44] pyrazine,[45] imidazole,[46] isoquinoline,[47] or phosphine[48-50] based-ligands has been reported, as well as their remarkable photophysical properties and various applications. Ruthenium is a heavy atom. Hence, RuPcs are characterized by high ISC rates and intense phosphorescence emission, as described by Wen-Hsiung and Tzer-Hsiang Huang in 1989.[51] Before this work, G. Ferraudi and D. Prassad had already observed that the properties of the triplet excited state of RuPcs are strongly influenced by the ligands coordinated to the axial positions of Ru(II).[52-54] Later on, in 1996, Michael Hanack and coworkers reported the photophysical properties of a RuPc bearing two pyridines as axial ligands, stating that its phosphorescence emission is originated from a charge-transfer state and not from $\pi \rightarrow \pi^*$ transitions.[55] These initial studies have been further supported by intensive research on the photophysical properties of RuPcs, demonstrating their high triplet state quantum yields, accompanied by strong phosphorescence and low or no fluorescence emission.[56,57]

[39] Rodríguez-Morgade, M. S.; Torres, T.; Castellanos, C. A.; Guldi, D. M. *J. Am. Chem. Soc.* **2006**, *128* (47), 15145–15154.

[40] Rawling, T.; Xiao, H.; Lee, S.-T.; Colbran, S. B.; McDonagh, A. M. *Inorg. Chem.* **2007**, *46* (7), 2805–2813.

[41] O'Regan, B. C.; López-Duarte, I.; Martínez-Díaz, M. V.; Forneli, A.; Albero, J.; Morandeira, A.; Palomares, E.; Torres, T.; Durrant, J. R. *J. Am. Chem. Soc.* **2008**, *130* (10), 2906–2907.

[42] Fischer, M. K. R.; López-Duarte, I.; Wienk, M. M.; Martínez-Díaz, M. V.; Janssen, R. A. J.; Bäuerle, P.; Torres, T. *J. Am. Chem. Soc.* **2009**, *131* (24), 8669–8676.

[43] Jiménez, A. J.; Grimm, B.; Gunderson, V. L.; Vagnini, M. T.; Krick Calderon, S.; Rodríguez-Morgade, M. S.; Wasielewski, M. R.; Guldi, D. M.; Torres, T. *Chem. Eur. J.* **2011**, *17* (18), 5024–5032.

[44] Lourenço, L. M. O.; Hausmann, A.; Schubert, C.; Neves, M. G. P. M. S.; Cavaleiro, J. A. S.; Torres, T.; Guldi, D. M.; Tomé, J. P. C. *Chempluschem* **2015**, *80* (5), 832–838.

[45] Kobel, W.; Hanack, M. *Inorg. Chem.* **1986**, *25* (1), 103–107.

[46] Jacobs, R.; Stranius, K.; Maligaspe, E.; Lemmetyinen, H.; Tkachenko, N. V; Zandler, M. E.; D'Souza, F. *Inorg. Chem.* **2012**, *51* (6), 3656–3665.

[47] Dudnik, A. S.; Ivanov, A. V; Tomilova, L. G.; Zefirov, N. S. *Russ. J. Coord. Chem.* **2004**, *30* (2), 110–114.

[48] Sweigart, D. A. *J. Chem. Soc. Dalt. Trans.* **1976**, No. 15, 1476–1477.

[49] Bulatov, A.; Knecht, S.; Subramanian, L. R.; Hanack, M. *Chem. Ber.* **1993**, *126* (11), 2565–2566

[50] Huang, J.-S.; Yu, G.-A.; Xie, J.; Wong, K.-M.; Zhu, N.; Che, C.-M. *Inorg. Chem.* **2008**, *47* (20), 9166–9181.

[51] Chen, W.-H.; Huang, T.-H.; Rieckhoff, K. E.; Voigt, E. M. *Mol. Phys.* **1989**, *68* (2), 341–357.

[52] Prasad, D. R.; Ferraudi, G. *Inorg. Chem.* **1982**, *21* (12), 4241–4245.

[53] Prasad, D. R.; Ferraudi, G. *J. Phys. Chem.* **1982**, *86* (20), 4037–4040.

[54] Ferraudi, G. J.; Prasad, D. R. *J. Chem. Soc. Dalt. Trans.* **1984**, No. 10, 2137–2140.

[55] Guez, D.; Markovitsi, D.; Sommerauer, M.; Hanack, M. *Chem. Phys. Lett.* **1996**, *249* (5), 309–313.

[56] Charlesworth, P.; Truscott, T. G.; Brooks, R. C.; Wilson, B. C. *J. Photochem. Photobiol. B Biol.* **1994**, *26* (3), 277–282.

[57] Ishii, K.; Shiine, M.; Shimizu, Y.; Hoshino, S.; Abe, H.; Sogawa, K.; Kobayashi, N. *J. Phys. Chem. B* **2008**, *112* (10), 3138–3143.

1.2. Synthetic Methods

Usually, the synthesis of Pcs is accomplished by the cyclotetramerization of phthalic acid derivatives. Among the different precursors available, phthalonitrile and 1,3-diiminoisoindoline derivatives are the most frequently used, although cyclotetramerization of phthalic anhydride, phthalimide, phthalamide and *o*-cyanobenzamide (**Scheme 1**) also provide Pcs. [14,19,22,58-61]

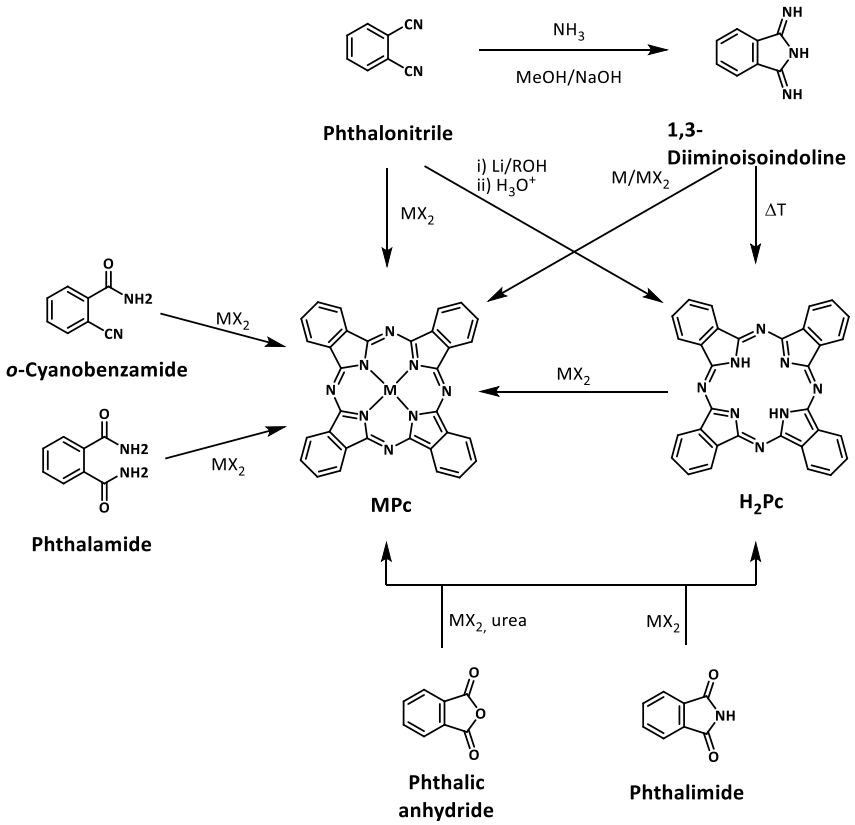

Scheme 1 – Precursors for the synthesis of Pcs.

The reaction mechanism is still unclear, but the most common strategy includes the use of a metal or metal salt as a reactant, which is believed to act as a template and as an electron source, resulting in the synthesis of a MPc.[58-60] An alternative approach consists on the use of lithium or a

[58] Bonnett, R. *Chem. Soc. Rev.* **1995**, *24*, 19–33.
[59] Rager, C.; Schmid, G.; Hanack, M. *Chem. Eur. J.* **1999**, *5* (1), 280–288.
[60] McKeown, N. B.; *Science of Synthesis* **2004**, 17, 1237-1368.
[61] de la Torre, G.; Bottari, G.; Hahn, U.; Torres, T. In *Functional Phthalocyanine Molecular Materials*; Jiang, J., Ed.; Springer Berlin Heidelberg: Berlin, Heidelberg, 2010; pp 1–44.

lithium salt as a template for the cyclotetramerization reaction, resulting a lithium phthalocyanine derivative, which can be easily demetallated to afford the corresponding H_2Pc.[62-64]

The cyclotetramerization reactions are usually performed in high boiling point alcohols, which, according to the mechanism proposed by Stuart W. Oliver and Thomas D. Smith (**Scheme 2**),[65] are responsible for the initiation of the reaction mechanism involving the formation of the corresponding alkoxide. This reacts with phthalonitrile and produces 1-imido-3-alkoxyisoindoline **I**. Intermediate **I** is then thought to react with another molecule of phthalonitrile affording intermediate **II**, composed of two isoindole units. The reaction may proceed either through the condensation of two molecules of **II** or by consecutive reaction with two phthalonitrile moieties, generating intermediate **III**, composed by four isoindole units. The latter, after ring closure, produces the Pc macrocycle. The alkoxide group in intermediate **III** has been shown to be important for the final ring closure reaction, involving the initial nucleophilic attack of the imine group and the loss of the alkoxide group in its oxidized form, the aldehyde. This final step entails the transfer of two electrons that provide the aromatic character of the macrocycle, this being therefore the driving force for the ring closure reaction. Usually, a base is added in the reaction mixture to react with the two protons resulting from the formation of the aldehyde. If a base is not used, the two electrons react with a second molecule of alkoxide.

For the cyclotetramerization of phthalonitriles, a non-nucleophilic base such as 1,8-diazabicyclo-5.4.0]-undec-7-ene (DBU) is often used for the efficient synthesis of both metal-free Pcs and MPcs.[19]

Peripheral substituents can be introduced before or after the cyclotetramerization reaction. The use of symmetrically substituted precursors leads to the synthesis of centrosymmetrically substituted Pcs in moderate yields.[14,16,19]

[62] Foley, S.; Jones, G.; Liuzzi, R.; J. McGarvey, D.; H. Perry, M.; George Truscott, T. *J. Chem. Soc. Perkin Trans. 2* **1997**, No. 9, 1725–1730.

[63] Kobayashi, N.; Higashi, R.; Ishii, K.; Hatsusaka, K.; Ohta, K. *Bull. Chem. Soc. Jpn.* **1999**, *72* (6), 1263–1271.

[64] Seikel, E.; Oelkers, B.; Sundermeyer, J. *Inorg. Chem.* **2012**, *51* (4), 2709–2717.

[65] Oliver, S. W.; Smith, T. D. *J. Chem. Soc. Perkin Trans. 2* **1987**, No. 11, 1579–1582.

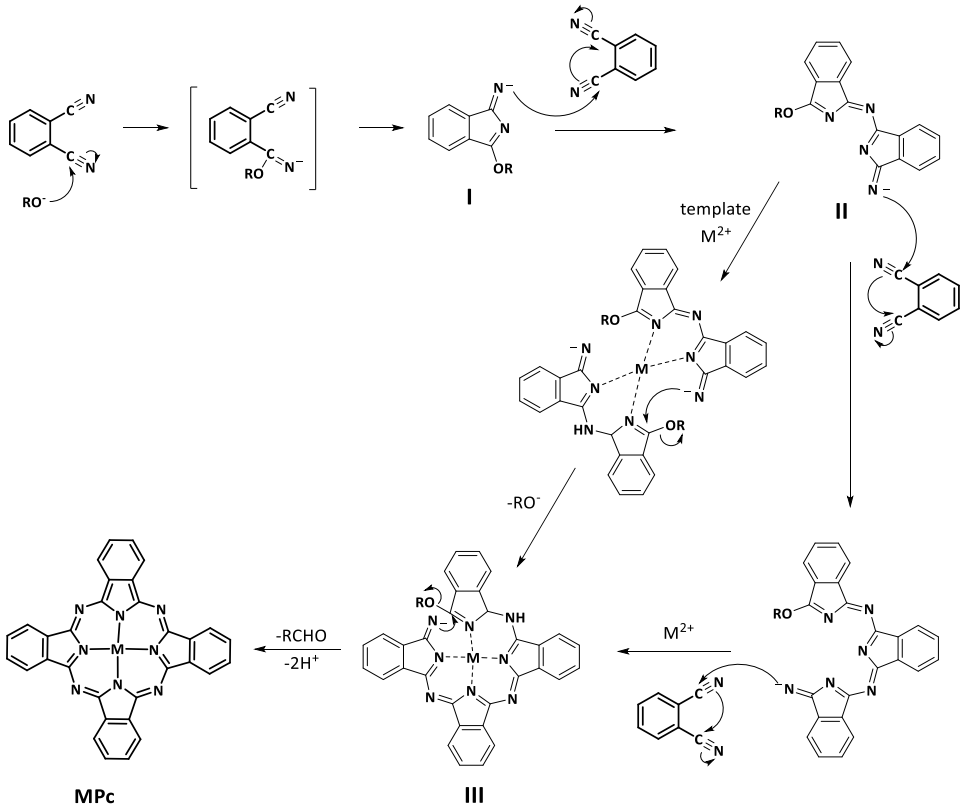

Scheme 2 – Proposed mechanism for the synthesis of MPcs *via* cyclotetramerization of phthalonitriles in the presence of a metal salt and an alkoxide anion.

The use of non-symmetrically substituted precursors results in a mixture of four regioisomers with different D_{2h}, C_{4h}, C_{2v} and C_s symmetries (see for example **Figure 5**).[16,19,59,66,67] The formation of these regioisomers, which are obtained in a 1:1:2:4 ratio, respectively,[14,66] was first acknowledged in 1936 by E. F. Bradbrook and R. P. Linstead[12] during the synthesis of 1,2-naphthalocyanines, but it was only in 1985 that Dieter Wöhrle and coworkers[68] were able to directly observe for the first time the existence of the constitutional isomers of phthalocyanines. In 1996 Michael Hanack and coworkers[66] achieved for the first time the separation of the four regioisomers by HPLC.

[66] Sommerauer, M.; Rager, C.; Hanack, M. *J. Am. Chem. Soc.* **1996**, *118* (42), 10085–10093.
[67] Görlach, B.; Dachtler, M.; Glaser, T.; Albert, K.; Hanack, M. *Chem. Eur. J.* **2001**, *7* (11), 2459–2465.
[68] Wohrle, D.; Gitzel, J.; Okura, I.; Aono, S. *J. Chem. Soc. Perkin Trans. 2* **1985**, No. 8, 1171–1178.

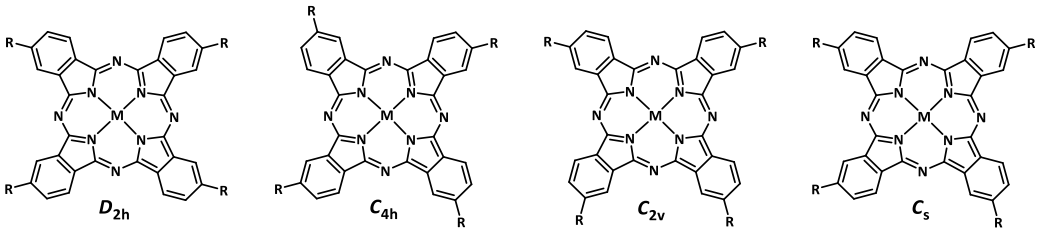

Figure 5 – The four regioisomers of tetrasubstituted phthalocyanines.

1.3. Applications

Besides their common use as dyes and pigments,[21] Pcs exhibit remarkable properties that are useful for other purposes. The high extinction coefficients in the visible and near IR regions exhibited by Pcs have encouraged the use of these macrocycles in organic photovoltaics (OPV),[69] i.e. organic solar cells[70] and dye-sensitized solar cells (DSSC).[71-73] Pcs have also been widely studied as nonlinear optical (NLO) materials by taking advantage of their extended two-dimensional π-electron delocalization.[17,19,74] Besides, the ability of Pcs to produce singlet oxygen[2] is being used for their application in photodynamic therapy (PDT),[75] photocatalytic degradation of pollutants[76] and catalytic oxidation in several processes.[77]

At a supramolecular level, Pcs can form different kinds of condensed phases, such as donor-acceptor nanoaggregates,[78] discotic liquid crystals[79] and thin films.[80] The latter can be employed in

[69] Martinez-Diaz, M. V.; de la Torre, G.; Torres, T. *Chem. Commun.* **2010**, *46* (38), 7090–7108.

[70] Ryan, J. W.; Anaya-Plaza, E.; Escosura, A. de la; Torres, T.; Palomares, E. *Chem. Commun.* **2012**, *48* (49), 6094–6096.

[71] Li, X.; Wang, H.; Wu, H. In *Functional Phthalocyanine Molecular Materials*; Jiang, J., Ed.; Springer Berlin Heidelberg, 2010; pp 229–274.

[72] Listorti, A.; Lopez-Duarte, I.; Martinez-Diaz, M. V.; Torres, T.; DosSantos, T.; Barnes, P. R. F.; Durrant, J. R. *Energy Environ. Sci.* **2010**, *3* (10), 1573–1579.

[73] Ragoussi, M.; Ince, M.; Torres, T. *European J. Org. Chem.* **2013**, 6475–6489.

[74] Fox, J. M.; Katz, T. J.; Van Elshocht, S.; Verbiest, T.; Kauranen, M.; Persoons, A.; Thongpanchang, T.; Krauss, T.; Brus, L. *J. Am. Chem. Soc.* **1999**, *121* (14), 3453–3459.

[75] Setaro, F.; Brasch, M.; Hahn, U.; Koay, M. S. T.; Cornelissen, J. J. L. M.; de la Escosura, A.; Torres, T. *Nano Lett.* **2015**, *15*, 1245.

[76] Colomban, C.; Kudrik, E. V.; Afanasiev, P.; Sorokin, A. B. *Catal. Today* **2014**, *235*, 14–19.

[77] Çakir, V.; Saka, E. T.; Biyiklioglu, Z.; Kantekin, H. *Synth. Met.* **2014**, *197*, 233–239.

[78] Escosura, A. de la; Martínez-Díaz, M. V.; Thordarson, P.; Rowan, A. E.; Nolte, R. J. M.; Torres, T. *J. Am. Chem. Soc.* **2003**, *125*, 12300–12308.

[79] Swarts, J. C.; Langner, E. H. G.; Krokeide-Hove, N.; Cook, M. J. *J. Mater. Chem.* **2001**, *11*, 434–443.

[80] Smolenyak, P.; Peterson, R.; Nebesny, K.; Torker, M.; O'Brien, D. F.; Armstrong, N. R. *J. Am. Chem. Soc.* **1999**, *121*, 8628–8636.

several technological areas, which include gas sensors[81] and other chemical sensors,[82] organic light emitting devices (OLEDs),[83] photovoltaic cells,[84] electrochromic devices,[85] organic field effect transistors (OFETs)[86,87] and organic photoconductors.[88] The use of MPcs has also been exploited for the production of magnetic materials,[89] either by the formation of columnar structures composed by planar Pc rings bearing divalent transition metal ions that display ferromagnetic properties,[90,91] or by the production of single-molecule magnets based on Pc–lanthanide "double-decker" complexes.[92]

This thesis is devoted to the design, synthesis and evaluation of Ruthenium Phthalocyanines (RuPcs) for their application as photosensitizers for PDT. In section 2 we will discuss in detail the main features of PDT, namely the mechanisms involved in the production of singlet oxygen as well as several strategies used to produce suitable photosensitizers for the treatment of cancer. Furthermore, in section 3 we will address specifically the use of Pcs as photosensitizers for PDT.

[81] Kumar, A.; Brunet, J.; Varenne, C.; Ndiaye, A.; Pauly, A.; Penza, M.; Alvisi, M. *Sensors Actuators B Chem.* **2015**, *210*, 398–407.

[82] Arrieta, A.; Rodriguez-mendez, M. L.; de Saja, J. A. *Sensors Actuators B* **2003**, *95*, 357–365.

[83] Mativetsky, J. M.; Wang, H.; S. Lee, S.; Whittaker-Brooks, L.; Loo, Y.-L. *Chem. Commun.* **2014**, *50*, 5319–5321.

[84] Sharma, G. D.; Kumar, R.; Sharma, S. K.; Roy, M. S. *Sol. Energy Mater. Sol. Cells* **2006**, *90*, 933–943.

[85] Rodriguez-Méndez, M. L.; Souto, J.; de Saja, J. A. De; Aroca, R. *J. Mater. Chem.* **1995**, *5* (4), 639–642.

[86] Li, L.; Tang, Q.; Li, H.; Hu, W.; Yang, X.; Shuai, Z.; Liu, Y.; Zhu, D. *Pure Appl. Chem.* **2008**, *80* (11), 2231–2240.

[87] Zhang, Y.; Cai, X.; Bian, Y.; Jiang, J. In *Functional Phthalocyanine Molecular Materials*; Jiang, J., Ed.; Springer Berlin Heidelberg, 2010; pp 275–322.

[88] Hanada, T.; Takiguchi, H.; Okada, Y.; Yoshida, Y.; Tanigaki, N.; Yase, K. *J. Cryst. Growth* **1999**, *204*, 307–310.

[89] Ishikawa, N. In *Functional Phthalocyanine Molecular Materials*; Jiang, J., Ed.; Springer Berlin Heidelberg, 2010; pp 211–228.

[90] Liao, M.-S.; Watts, J. D.; Huang, M. J. *Inorg. Chem.* **2005**, *44*, 1941–1949.

[91] Wu, W. *J. Chem. Phys.* **2014**, *140* (22), 224301.

[92] Ishikawa, N.; Sugita, M.; Ishikawa, T.; Koshihara, S.; Kaizu, Y. *J. Am. Chem. Soc.* **2003**, *125* (29), 8694–8695.

2. Photodynamic Therapy

In the late century, Photodynamic Therapy (PDT) has received an increasing attention for the treatment of cancer and other diseased tissues, since this methodology allows for the non-invasive, selective and localized destruction of tumor cells with reduced side effects. PDT uses light to activate a so-called photosensitizer (PS), which can transfer its energy to surrounding oxygen. The latter results in the formation reactive oxygen species (ROS) that ultimately lead to an effective tumor ablation.[33,93-96] The confined delivery of light to the target area combined with the selective accumulation of the PS in the tumor tissue should reduce damage to healthy cells.[96] PDT was the first example of a drug-device combination approved by Food and Drug Administration (FDA).[97,98]

2.1. Historical development

The use light and a chemical agent for therapeutic proposes can be traced back to 1400 b.c. in ancient Egypt and India. Back then, sunlight was used to activate plants containing psoralens for the repigmentation of vitiligo.[93,97,99] In the 1890's, Niels Finsen made significant advances in phototherapy with the discovery that light exposure could control skin manifestations of tuberculosis, for which he received the Nobel Prize in 1903.[58,100] It was only in 1900 that PDT, as we know it, that is, with the use of an added chemical photosensitizer, was discovered. This was accomplished when Raab[101] exposed Paramecia microorganisms to light in the presence of acridine orange and observed its cytotoxic effects.[93,97,99,100-103] Further experiments, conducted by H. von

[93] Sternberg, E. D.; Dolphin, D.; Brückner, C. *Tetrahedron* **1998**, *54* (17), 4151–4202.

[94] Jiang, Z.; Shao, J.; Yang, T.; Wang, J.; Jia, L. *J. Pharm. Biomed. Anal.* **2014**, *87*, 98–104.

[95] Dolmans, D. E. J. G. J.; Fukumura, D.; Jain, R. K. *Nat Rev Cancer* **2003**, *3* (5), 380–387.

[96] Castano, A. P.; Demidova, T. N.; Hamblin, M. R. *Photodiagnosis Photodyn. Ther.* **2004**, *1* (4), 279–293.

[97] Celli, J. P.; Spring, B. Q.; Rizvi, I.; Evans, C. L.; Samkoe, K. S.; Verma, S.; Pogue, B. W.; Hasan, T. *Chem. Rev.* **2010**, *110* (5), 2795–2838.

[98] Agostinis, P.; Berg, K.; Cengel, K. A.; Foster, T. H.; Girotti, A. W.; Gollnick, S. O.; Hahn, S. M.; Hamblin, M. R.; Juzeniene, A.; Kessel, D.; Korbelik, M.; Moan, J.; Mroz, P.; Nowis, D.; Piette, J.; Wilson, B. C.; Golab, J. *CA. Cancer J. Clin.* **2011**, *61* (4), 250–281.

[99] Hamblin, M. R. *Curr. Opin. Microbiol.* **2016**, *33*, 67–73.

[100] Allison, R. R.; Downie, G. H.; Cuenca, R.; Hu, X.-H.; Childs, C. J.; Sibata, C. H. *Photodiagnosis Photodyn. Ther.* **2004**, *1* (1), 27–42.

[101] Raab, O. *Z Biol* **1900**, *39*, 524–546.

[102] Maisch, T. *Lasers Med. Sci.* **2007**, *22* (2), 83–91.

[103] Jori, G.; Camerin, M.; Soncin, M.; Guidolin, L.; Coppellotti, O. In *Photodynamic Inactivation of Microbial Pathogens: Madicinal and Environmental Applications*; Hamblin, M. R., Jori, G., Eds.; Royal Society of Chemistry, 2011; pp 1–18.

Tappainer[104] (Raab's teacher), led to the conclusion that the observed toxic effects were caused not by heat but by oxygen, which was a key ingredient for the effective killing of bacteria, introducing for the first time the term "photodynamic reaction" in 1904.[102,103]

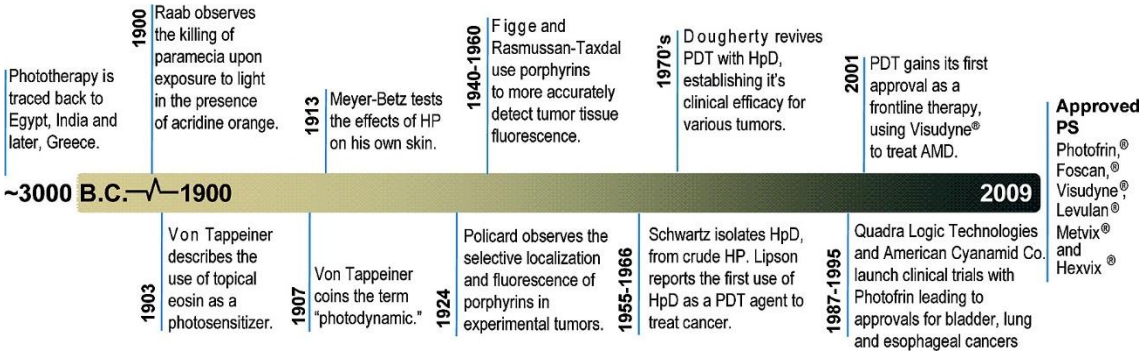

Figure 6 – Timeline of selected milestones in the historical development of PDT.[97]

The modern era of PDT began in 1960 at the Mayo Clinic, where Schwartz and Lipson observed that injections of crude preparations of hematoporphyrin resulted in fluorescence of neoplastic lesions visualized during surgery. Treatment of hematoporphyrin with acetic acid and sulfuric acid led to the development of the so called "hematoporphyrin derivative" (HPD). This consisted of a mixture of several porphyrin monomers, dimers and oligomers that localized in tumors and could be activated by red light leading to a PDT mediated tumor destruction.[58,93-95,97,105,106] The clinical efficiency of HPD against various tumors was proved by Dougherty in the 1970s, transforming PDT in a viable clinical technique against cancer. Partial purification of HPD, with removal of most inactive porphyrin' monomers, ultimately lead to the production of Photofrin®, which constitutes the most used PS in PDT (**Figure 7**).[58,97,105]

Photofrin®, consists of a mixture of mono-, di- and oligomers that contain the porphyrin moiety. The major advantage of Photofrin® is its high singlet oxygen quantum yield, Φ_{Δ} = 0.89, and it was with this compound as PS that PDT was first approved in 1993 by a regulatory authority in Canada, for the prophylactic treatment of bladder cancer.[94,95,97,105,107] Later on, Photofrin® was also approved in The Netherlands and France for treatment of esophageal and lung cancers; in Germany for treatment of early stage lung cancer; in Japan for treatment of cervical dysplasia and early stage

[104] Tappeiner, H. *Dtsch med Wochenschr* **1904**, *30* (16), 579–580.

[105] Dougherty, T. J.; Gomer, C. J.; Henderson, B. W.; Jori, G.; Kessel, D.; Korbelik, M.; Moan, J.; Peng, Q. *J. Natl. Cancer Inst.* **1998**, *90* (12), 889.

[106] Nyman, E. S.; Hynninen, P. H. *J. Photochem. Photobiol. B Biol.* **2004**, *73* (1–2), 1–28.

[107] Ormond, A. B.; Freeman, H. S. *Materials.* **2013**, *6* (3), 817–840.

lung cancer, as well as esophageal, gastric and cervical cancers.[105,108] US FDA also approved Photofrin® in 1995 for palliation of obstructive esophageal cancer, as well as for treatment of early stage lung cancer and Barrett's esophagus, in 1998 and in 2003, respectively.[97,105,107]

Besides Photofrin®, other types of hematoporphyrin derivatives have been approved for clinical use, namely Photocarcinorin, Photogem®, approved in Russia and Brazil, and Photosan-3®, approved in the EU.[58,107]

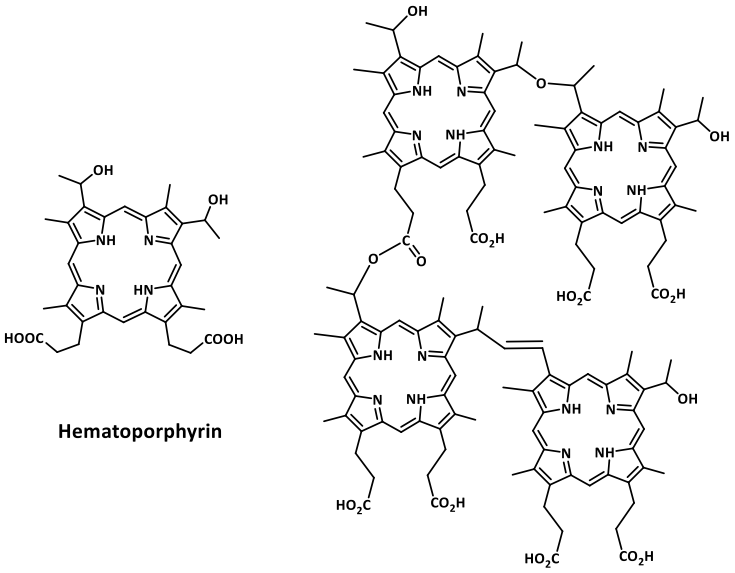

Figure 7 – Chemical structure of Hematoporphyrin and Photofrin®.

2.2. Mechanism of action: photophysics and photochemistry

As outlined above, PDT combines light, molecular oxygen and a photosensitizer (PS) for the production of reactive oxygen species (ROS), such as singlet oxygen ($^1O_2$) and free radicals that will induce oxidative stress and, eventually, cell death.[95,96,109]

Usually, the ground state of a PS (S_0) has a singlet state configuration, with paired electrons with a total spin of S=0 and a spin multiplicity of 1.[33,96,98,110]

[108] Detty, M. R.; Gibson, S. L.; Wagner, S. J. *J. Med. Chem.* **2004**, *47* (16), 3897–3915.

[109] Ding, H.; Yu, H.; Dong, Y.; Tian, R.; Huang, G.; Boothman, D. A.; Sumer, B. D.; Gao, J. *J. Control. Release* **2011**, *156* (3), 276–280.

[110] Plaetzer, K.; Krammer, B.; Berlanda, J.; Berr, F.; Kiesslich, T. *Lasers Med. Sci.* **2009**, *24* (2), 259–268.

The PS is administrated topically or intravenously and, after its selective accumulation in the tumor tissues, it is irradiated with laser light of specific wavelength. This boosts one of the paired electrons to a previously unoccupied higher energy orbital, while keeping its spin, giving rise to a singlet excited state (S_x, x = 1, 2, 3, …).[95,96,110] Within an excited state, an electron can decay *via* vibrational relaxation (VR) to the lowest vibrational level of that state, with dissipation of energy as heat. This relaxation pathway also allows for the decay from a higher energy state (S_x) to the first excited singlet state S_1 (**Figure 8**).[33,95,110]

The short-lived singlet excited state S_1 may decay through molecular relaxation to S_0. This can occur by heat dissipation or by emission of a secondary photon (fluorescence emission), a process that always occurs from the lowest vibrational level of S_1.[33,96,98,110]

Alternatively, S_1 may experience a non-radiative process called intersystem crossing (ISC), which involves the spin inversion of one electron, thus decaying to the triplet excited state T_1, characterized by two unpaired electrons with the same spin. ISC is a spin-forbidden process because it violates the rule of spin conservation. Nevertheless, spin-orbit coupling (SOC)[111-113] makes ISC competitive against other decay routes of the S_1 state.[33,93,95,96,98,110]

After vibrational relaxation to the lowest vibrational level, T_1 may decay to S_0 *via* emission of a photon (phosphorescence emission), involving another spin inversion. This route is again a "spin-forbidden" process which involves the direct conversion from a triplet state to a singlet state. For this reason, T_1 is characterized by a relatively long lifetime.[33,93,96,110]

[111] Spin-orbit coupling (SOC) is the energetic contribution arising from the interaction between the spin magnetic moment of the electron and the magnetic field that it feels as a result of orbiting around a positively charged nucleus. This interaction leads to a mixing of the singlet and triplet wave functions, making it possible for ISC to take place.

[112] Beljonne, D.; Shuai, Z.; Pourtois, G.; Bredas, J. L. *J. Phys. Chem. A* **2001**, *105* (15), 3899–3907.

[113] Marian, C. M. *Wiley Interdiscip. Rev. Comput. Mol. Sci.* **2012**, *2* (2), 187–203.

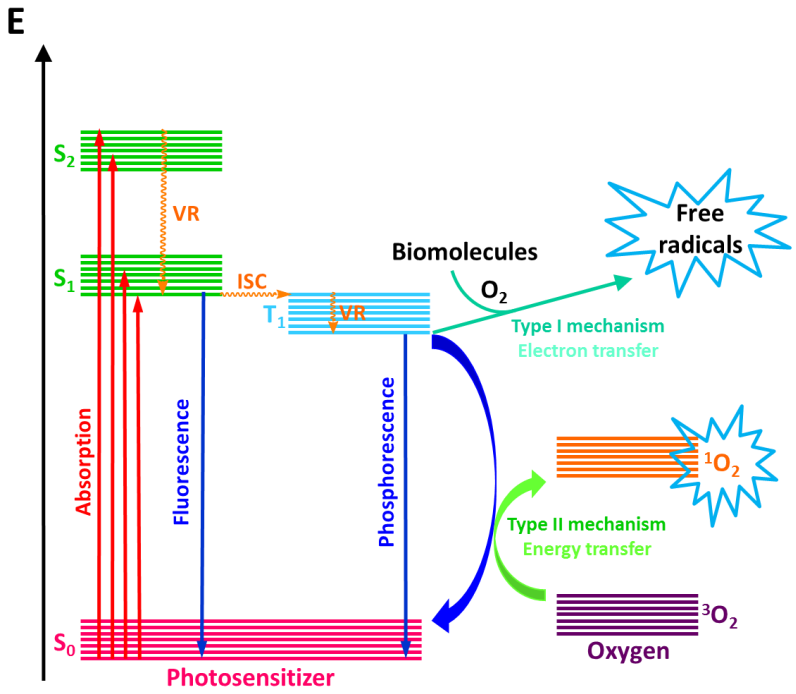

Figure 8 – Jablonski diagram depicting the electronic transition states and energy or electon transfer phenomena between the PS molecule and O_2 in PDT that ultimately leads to oxidative cell damage.

Since T_1 is longed lived, it can participate in reactions with other molecules. In particular, T_1 can undergo two different reactions in PDT. On one hand, it can transfer its energy to molecular oxygen ($^3O_2$) to produce $^1O_2$ that will be responsible for the oxidation of cellular substrates and eventually lead to cell death. This is called the Type-II (energy transfer) mechanism. On the other hand, the PS triplet excited state can react directly with a cellular substrate, through hydrogen or electron transfer, forming radicals such as the superoxide anion ($O_2^{\bullet-}$), the hydroxyl radical ($OH^{\bullet}$) and hydrogen peroxide (H_2O_2). The latter react with molecular oxygen producing oxygenated species. This is the so-called Type-I (electron transfer) mechanism (**Scheme 3**).[33,95,96,98,109,110,114-116] The use of PSs with increased ISC and high triplet-state quantum yields is therefore of extreme importance since this allows for an efficient production of singlet oxygen and other ROS.[33,115]

Both type I and type II reactions occur simultaneously, but it is believed that type-II mechanism is the principal responsible for cell death in PDT. For this reason, singlet oxygen quantum yield is an important parameter to take into account in the development of new PSs.[114,115]

[114] Maree, M. D.; Kuznetsova, N.; Nyokong, T. *J. Photochem. Photobiol. A Chem.* **2001**, *140* (2), 117–125.

[115] Lang, K.; Mosinger, J.; Wagnerová, D. M. *Coord. Chem. Rev.* **2004**, *248* (3–4), 321–350.

[116] Nyokong, T. *Pure Appl. Chem.* **2011**, *83* (9), 1763–1779.

Type-II Mechanism

$PS \xrightarrow{h\nu} {}^1PS^* \xrightarrow{ISC} {}^3PS^*$

${}^3PS^* + {}^3O_2 \rightarrow PS + {}^1O_2$

${}^1O_2 + S \rightarrow$ oxidized S

Type-I Mechanism

$PS \xrightarrow{h\nu} {}^1PS^* \xrightarrow{ISC} {}^3PS^*$

${}^3PS^* + O_2 \rightarrow PS^{\bullet+} + O_2^{\bullet-}$

${}^3PS^* + S \rightarrow PS^{\bullet-} + S^{\bullet+}$

$PS^{\bullet-} + O_2 \rightarrow PS + O_2^{\bullet-}$

$O_2^{\bullet-} \xrightarrow{H^+} HO_2^{\bullet}$

$HO_2^{\bullet} + S\text{-}H \rightarrow H_2O_2 + S^{\bullet}$

$S^{\bullet+}$, $S^{\bullet}$, $H_2O_2 \rightarrow$ oxidized S

Scheme 3 – Overview of Type I and Type II photoreactions during PDT (S stands for substrate).[114,116]

2.3. Applications

As mentioned before, PDT is a methodology that finds application on the oncological field, for the palliative and curative treatment of some forms of cancers. After its approval for the treatment of bladder cancer in 1993, several other cancer diseases have been treated with this technique. For example, the topical application of 5-amino-levulineic acid (ALA) and its methyl ester (MAL) has been approved for the PDT based treatment of actinic keratosis.[93,107,117]

In addition, PDT is a versatile technique that can be used for the treatment of a large variety of illnesses that go beyond the cancer malignancies. Examples are *(i)* prevention of arterial restenosis after ballon angioplasty, *(ii)* treatment of benign prostatic hyperplasia, *(iii)* therapy of autoimmune disorders, *(iv)* treatment of epidermal or dermal pathologies, such as psoriasis and acne and *(v)* treatment of choroidal neovascularization secondary to age-related macular degeneration (AMD).[93,118]

[117] Szeimies, R. M.; Karrer, S.; Radakovic-Fijan, S.; Tanew, A.; Calzavara-Pinton, P. G.; Zane, C.; Sidoroff, A.; Hempel, M.; Ulrich, J.; Proebstle, T.; Meffert, H.; Mulder, M.; Salomon, D.; Dittmar, H. C.; Bauer, J. W.; Kernland, K.; Braathen, L. *J. Am. Acad. Dermatol.* **2002**, *47* (2), 258-262.

[118] Jori, G.; Fabris, C.; Soncin, M.; Ferro, S.; Coppellotti, O.; Dei, D.; Fantetti, L.; Chiti, G.; Roncucci, G. *Lasers Surg. Med.* **2006**, *38* (5), 468–481.

2.4. Active components in PDT

2.4.1. Singlet oxygen

Since its discovery in 1924, singlet oxygen and its physical and chemical properties have been the object of intense study among the scientific community. Molecular oxygen, having two singlet states lying close above its triplet ground state, has a very unique configuration that is responsible for a number of important photophysical interactions, among them the photosensitized production of singlet oxygen ($^1O_2$).[119,120] This phenomenon can be applied in a large range of areas, i.e. in organic synthesis,[121] in photodegradation of pollutants,[122] photodamage of viruses,[123] DNA damage,[124,125] photocarcinogenesis[126] and, as mentioned before, in photodynamic therapy (PDT).[95,127]

The unusual ground state of molecular oxygen has the following electronic configuration: $(1\sigma_g)^2(1\sigma_u)^2(2\sigma_g)^2(2\sigma_u)^2(3\sigma_g)^2(3\sigma_u)^2(3\pi_g)^4(3\pi_u)^2$. This corresponds to an open-shell electronic configuration with two unpaired electrons occupying separate antibonding (π*) orbitals with parallel electronic spins (**Figure 9**). This is commonly designated as a spin triplet: $^3O_2$ or O_2 ($^3\Sigma_g^-$), where the superscript "3" represents the triplet state, the "Σ" denotes that the orbital angular momentum (M_L) equals 0, and the subscript "g" signifies that the symmetry of the molecule is pair (g from the German *gerade*). Hence, unlike most organic molecules, which usually consist on nonradical diamagnetic species, molecular oxygen is a paramagnetic biradical with pairs of electrons with the same spin orientation.[110,128-130]

[119] DeRosa, M. C.; Crutchley, R. J. *Coord. Chem. Rev.* **2002**, *233–234*, 351–371.
[120] Schweitzer, C.; Schmidt, R. *Chem. Rev.* **2003**, *103* (5), 1685–1758.
[121] Aubry, J.-M.; Pierlot, C.; Rigaudy, J.; Schmidt, R. *Acc. Chem. Res.* **2003**, *36* (9), 668–675.
[122] Ozoemena, K.; Kuznetsova, N.; Nyokong, T. *J. Mol. Catal. A Chem.* **2001**, *176* (1), 29–40.
[123] Wagner, S. J.; Skripchenko, A.; Robinette, D.; Foley, J. W.; Cincotta, L. *Photochem. Photobiol.* **1998**, *67* (3), 343–349.
[124] Lu, W.; Liu, J. *Chem. Eur. J.* **2016**, *22* (9), 3127–3138.
[125] Zamadar, M.; Greer, A. In *Handbook of Synthetic Photochemistry*; Albini, A., Fagnoni, M., Eds.; Wiley-VCH Verlag GmbH & Co. KGaA, 2010; pp 353–386.
[126] Black, H. S.; Mathews-Roth, M. M. *Photochem. Photobiol.* **1991**, *53* (5), 707–716.
[127] Macdonals, I. J.; Dougherty, T. J. *J. Porphyr. Phthalocyanines* **2001**, *5*, 105–129.
[128] Tørring, T.; Helmig, S.; Ogilby, P. R.; Gothelf, K. V. *Acc. Chem. Res.* **2014**, *47* (6), 1799–1806.
[129] Krumova, K.; Cosa, G. In *Singlet Oxygen: Applications in Biosciences and Nanosciences*; The Royal Society of Chemistry, **2016**; Vol. 1, pp 1–21.
[130] Boix-Garriga, E.; Rodríguez-Amigo, B.; Planas, O.; Nonell, S. In *Singlet Oxygen: Applications in Biosciences and Nanosciences*; Nonell, S., Flors, C., Eds.; Royal Society of Chemistry, 2016; pp 25–44.

A spin restriction applies to $^3O_2$, which must accept a pair of electrons with the same spin (*i.e.* nondiamagnetic) in order to participate in redox reactions. This restriction is responsible for the inefficiency of molecular oxygen to oxidize molecules *via* a 2-electron process. Instead, molecular oxygen can easily accept one electron at a time, as in redox reactions with other radicals or other species bearing unpaired electrons, such as transition metals. This one-electron reduction of oxygen generates superoxide radical anion, $O_2^{\bullet-}$ (**Figure 9**), which can undergo further successive one-electron reductions to form other reactive oxygen species (ROS).[129]

On the other hand, it is possible to transfer energy to molecular oxygen, *via* irradiation of a photosensitizer, forming singlet oxygen, designated as $^1O_2$ or O_2 ($^1\Delta_g$), where Δ means that the orbital angular momentum (M_L) equals 2. This electronic state has two paired electrons with opposite spins, thus removing the spin restriction that applies to $^3O_2$. The removal of such spin restriction is responsible for the increased reactivity of singlet oxygen, when compared with ground state oxygen (**Figure 9**).[110,129-131]

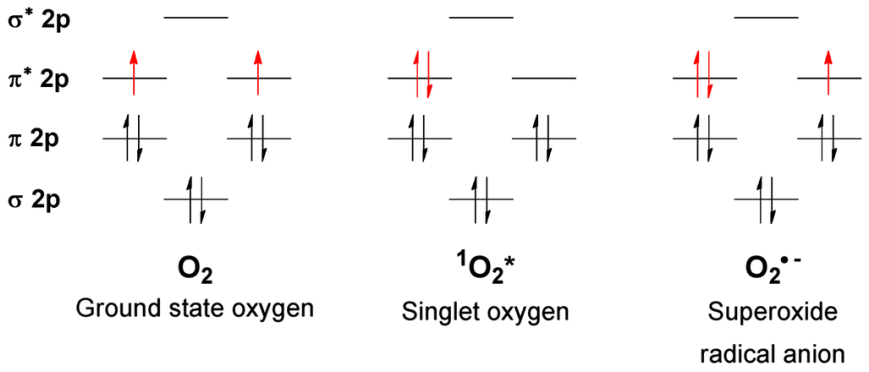

Figure 9 – Electronic configuration of ground state oxygen, singlet oxygen and superoxide radical anion.[129]

Singlet oxygen has an estimated lifetime (τ) of 3 x 10^{-6} s in water. Due to the presence of reacting molecules in the cytoplasm, this lifetime is significantly reduced in the intracellular environment to a maximum of 10^{-7}s. Therefore, the radius of diffusion of singlet oxygen is inferior than 50 nm. The short half-life of singlet oxygen conjugated with its high reactivity leads to the localized production of ROS, resulting in an oxidative damaged that is limited to the irradiated areas, shrinking the probability of harming healthy cells. Consequently, PDT should produce reduced side-effects, in opposition to chemotherapy.[96,98,110,132,133]

[131] Hoffmann, N. *Chem. Rev.* **2008**, *108* (3), 1052–1103.
[132] Mitton, D.; Ackroyd, R. *Photodiagnosis Photodyn. Ther.* **2008**, *5* (2), 103–111.
[133] Mari, C.; Pierroz, V.; Ferrari, S.; Gasser, G. *Chem. Sci.* **2015**, *6* (5), 2660–2686.

The fact the molecular oxygen is a key ingredient for an effective photodynamic effect poses a drawback in PDT, since tumor tissues are known to develop hypoxia in some regions, hindering the production of singlet oxygen. Besides, by using the intracellular molecular oxygen reserves and by damaging the tissue vasculature, PDT creates acute hypoxia. To overcome this complication, several strategies have been studied.[105,134,135] One possibility consists on the downward adjustment of fluence rate of the light used to irradiate the tumor, thus slowing down the O_2 consumption and facilitating the maintenance of the tissue O_2 levels. Using a PS that suffers some level of photobleaching upon irradiation and production of singlet oxygen also reduces the rate of O_2 consumption, being thus and important factor in the maintenance of O_2 levels.[105,135] Fractional PDT is another alternative, which consists on the use of intermittent irradiation (20-50 seconds), thus allowing cells to restore the intracellular oxygen levels during the dark periods.[105,134,135]

2.4.2. Light

The success of PDT relies as well in the **light source** that is applied to activate the PS. The choice of light wavelength is given by the maximum absorption of the PS. In this respect, the use of wavelengths that range from 700 to 850 nm (the so called "phototherapeutic window", **Figure 10**) is important since this maximizes the light penetrating depth. The limited penetration of light into tissues arises from scattering, absorption, reflection and refraction phenomena. In particular, scattering, which is responsible for loss of intensity and directionality of the light beam, manly accounts for the low penetration depth of lower (than therapeutic window) wavelength light. Radiation with longer wavelengths suffers less scattering. Absorption by endogenous chromophores is the second major factor preventing deep tissue penetration. PSs absorbing light of wavelength below 700 nm are not ideal due to the presence of endogenous light absorbers, such as oxyhemoglobin (HbO_2), deoxyhemoglobin (Hb), bilirubin and melanin, resulting in poor tissue penetration. Absorption by water accounts for the low penetration of light with wavelengths above 850 nm.[33,96,110,136] Summarizing, a penetration depth of about 3 mm is achieved with light of wavelength around 630 nm (wavelength used with Photofrin®), whereas radiation of wavelengths between 700 and 800 nm is able to increase twofold the penetration depth.[96,110] The penetration

[134] Turan, I. S.; Yildiz, D.; Turksoy, A.; Gunaydin, G.; Akkaya, E. U. *Angew. Chemie Int. Ed.* **2016**, *55* (8), 2875–2878.

[135] Castano, A. P.; Demidova, T. N.; Hamblin, M. R. *Photodiagnosis Photodyn. Ther.* **2005**, *2* (2), 91–106.

[136] Puri, A. *Pharmaceutics* **2014**, *6* (1), 1–25.

depth of light may also be hindered by the PS absorption itself, a phenomenon called "self-shielding".[96]

PSs should not have absorption maxima at wavelengths longer than 850 nm either, since such absorptions generate triplet excited states without sufficient energy to excite molecular oxygen to its singlet excited state.[96,98,110]

Due to the obstacles posed by light penetration issues, light-guided treatments have been mostly applied in skin and oral cavity diseases, for example esophagus and bladder. Therefore, it is of extreme importance the development of photosensitizers able to absorb light in the "phototherapeutic window" in order to be effective for treatment of deeper localized tumors.[33,136]

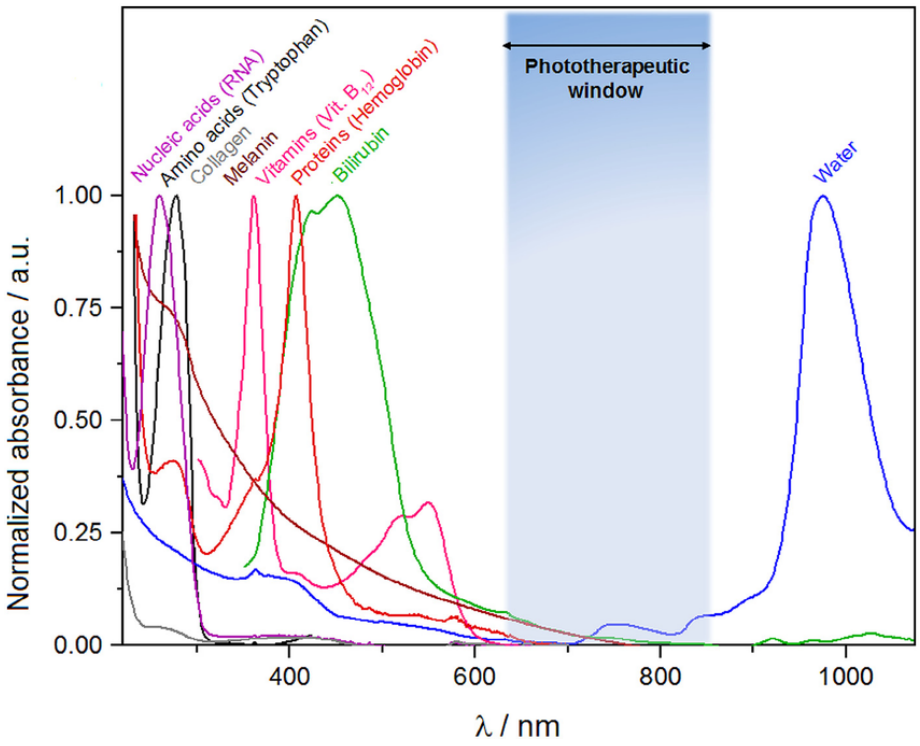

Figure 10 – Ideal Phototherapeutic window.[33]

The mode of **light delivery** is also an important factor in PDT. At the beginning, conventional lamps and filters were used to define the wavelength of irradiation. However, these lamps produce non-coherent light with intense heat release. Several efforts have been made for developing new light sources, with lasers being the primary choice, since they produce coherent light of a specific wavelength and allow to use optical fibers to deliver the light directly to the site of treatment. These include pumped dye lasers, which are expensive and inefficient, and semi-conductor diode lasers,

which are relatively cheap and more efficient. Light-emitting diodes (LEDs) are another fairly inexpensive alternative, which also allow a narrow wavelength range and high fluence rates.[96,98,132]

Finally, it also necessary to take into account the different optical properties of each tissue type in order to optimize the clinical outcome of the PDT treatment.[96]

2.4.3. Photosensitizers

The PS plays a crucial role in PDT, a fact that has led to an extensive research on PS design and synthesis over the years. Suitable PSs for PDT can be divided in two main groups, namely porphyrinoid or non-porphyrinoid derivatives.[107,108,137-139]

Non-porphyrinoid PSs include *(i)* phenothiazines, such as Methylene Blue and Toluidine Blue, *(ii)* xanthenes, for instance Rose Bengal, *(iii)* squarines, *(i*v) BODIPY (boron-dipyrromethane) dyes, *(v)* phenalenones, *(vi)* anthraquinones, like Hypericin, *(vii)* cyanines, *(viii)* curcuminoids, *(ix)* chalcogenopyrylium dyes and *(x)* transition metal compounds, from which ruthenium(II) polypyridyl complexes are the most studied.[107,137-139]

Porphyrinoid based derivatives are the most used in PDT applications, since their extended π-systems provide them with singular photochemical characteristics most valuable for their use as photosensitizers.[33,93, 138,139]

Within the porphyrinoid PSs, they are usually separated in first, second and third generation photosensitizers.[100,137]

2.4.3.1. First generation photosensitizers

HPD, Photofrin® and other porphyrins made in the 1970s and 1980s are known as first generation photosensitizers.[100,107,137,138] As mentioned before, Photofrin® is the most used PS in PDT, being a reliable, activatable, pain-free and non-toxic drug. However, Photofrin®, presents some important disadvantages, such as its composition. Therefore, although it has a useful maximum of absorption at 630 nm, large concentrations of compound and light are required since it is composed by an uncertain mixture of compounds and, thus, it exhibits a low absorption

[137] O'Connor, A. E.; Gallagher, W. M.; Byrne, A. T. *Photochem. Photobiol.* **2009**, *85* (5), 1053–1074.

[138] Yano, S.; Hirohara, S.; Obata, M.; Hagiya, Y.; Ogura, S.; Ikeda, A.; Kataoka, H.; Tanaka, M.; Joh, T. *J. Photochem. Photobiol. C Photochem. Rev.* **2011**, *12* (1), 46–67.

[139] Abrahamse, H.; Hamblin, M. R. *Biochem. J.* **2016**, *473* (4), 347–364.

coefficient at this wavelength. Furthermore, Photofrin® shows poor selectivity for tumor tissues and causes long-lasting skin photosensitization for several weeks.[58,94,95,100,107,137,138]

2.4.3.2. Second generation photosensitizers

A great effort has been devoted to develop a second generation of photosensitizers. There are several factors that should be taken into account in their design: *(i)* the PS should be a single and chemically pure compound; *(ii)* it should be stable and present a good solubility in pharmaceutically acceptable formulations and in biological media; *(iii)* it should exhibit high triplet state quantum yield and lifetime for the efficient production of ROS upon light activation; *(iv)* it must show no dark toxicity; *(v)* it should show specificity for cancer tissues; *(vi)* it should have a strong absorbance in the therapeutic window (700-850 nm), allowing for a deeper tissue penetration as well as for a triplet state with sufficient energy for the production of $^1O_2$; *(vii)* it should exhibit high absorption coefficients to minimize the amount of PS necessary for effective treatment; *(viii)* it should be easily eliminated from the organism, either by metabolization or photodegradation, without the formation of toxic products; and *(ix)* it must not result in mutagenicity or carcinogenicity.[58,94,96,100,110,115,116]

Taking all these factors into account, a large variety of photosensitizers has been developed over the years, with several being already approved for the treatment of different diseases (**Figure 11**, **Table 1**).[33,95,100,105,140-143]

An example is **ALA**, which is a prodrug. It consists on a naturally occurring aminoacid that is enzymatically converted in protoporphyrin, the actual photosensitizer. In 1999, US FDA approved ALA for non-oncological PDT treatment of actinic keratosis. Several ALA derivatives have been prepared to enhance its absorption or activity, namely Metvix® (methylated ALA), Hexvix® and Benzix®.[96,100,107,127,138,144]

[140] Allison, R. R.; Bagnato, V. S.; Cuenca, R.; Downie, G. H.; Sibata, C. H. *Futur. Oncol.* **2006**, *2* (1), 53–71.

[141] Ethirajan, M.; Chen, Y.; Joshi, P.; Pandey, R. K. *Chem. Soc. Rev.* **2011**, *40* (1), 340–362.

[142] Sekkat, N.; Van Den Bergh, H.; Nyokong, T.; Lange, N. *Molecules* **2012**, *17* (1), 98–144.

[143] Wagner, A.; Kiesslich, T.; Neureiter, D.; Friesenbichler, P.; Puespoek, A.; Denzer, U. W.; Wolkersdorfer, G. W.; Emmanuel, K.; Lohse, A. W.; Berr, F. *Photochem. Photobiol. Sci.* **2013**, *12* (6), 1065–1073.

[144] Juarranz, Á.; Jaén, P.; Sanz-Rodríguez, F.; Cuevas, J.; González, S. *Clin. Transl. Oncol.* **2008**, *10* (3), 148–154.

Porphyrins are widely used as PSs in PDT. This family of compounds exhibit the longest wavelength absorption band around 630 nm, however with low absorption coefficients.[96] Examples include *m*-tetra(hydrophenyl)porphyrin (*m*-THPP) and 5,10,15,20-tetrakis(4-sulfatophenyl)-21H,23H-porphyrin (TPPS4).[107]

Texaphyrins are expanded porphyrins and are commercially available through Pharmacyclics. Examples are Xcytrin®, a putative radiation sensitizer, and luthenium texaphyrin, which has several commercial names depending on the application, including Lutex, Lutrin®, Optrin™ and Antrin®.[100,107,127,137,138]

Chlorins are also commonly used as photosensitizers. These are porphyrin analogues that lack a double bond in one of the pyrrole units. Chlorins display a bathochromic shift of their longest wavelength absorption band, with an increase in its absorption coefficient.[33,96,139] Examples are Foscan®, a temoporfin, Purlytin, a tin-ethyl-etiopurpurin, NPe6 or Talaporfin, and Photochlor®.[100,107,127,137,138] Benzoporphyrin derivatives (BPD) are also included in the chlorin family and, likewise, exhibit a red-shift in their absorption maxima when compared with porphyrins. An example is Visudyne™, which consists on a liposome formulation that contains benzoporphyrin derivative monoacid ring A, called verteporfin, as active agent.[100,107,127,136]

Another family of porphyrin analogues that has been studied for application in PDT are the **bacteriochlorins**, which have two pyrrole units with reduced double bonds. Bacteriochlorins display a further red-shift and intensity increase of their longest wavelength absorption band.[33,96,139] An example is Tookad® or padofrin, which is a lipophilic photosensitizer that rapidly clears from circulation without skin photocytotoxicity, in comparison with Visudyne™ and Lutrin®.[107,137,138]

Porphycenes constitute isomers of porphyrins with strong absorptions above 600 nm and efficient production of singlet oxygen. Hence, much attention has been paid to this class of second generation photosensitizers. Their structural versatility is one of their strong points with a view of improving their therapeutic properties.[137]

Phthalocyanines (Pcs) are another family of second generation photosensitizers, which have a higher degree of conjugation when compared with porphyrins. Pcs exhibit bathochromically shifted Q-bands related to those of porphyrins, with absorption maxima around 670 nm.[107,137] The use of these macrocycles as PS will be described in more detail in section 3.

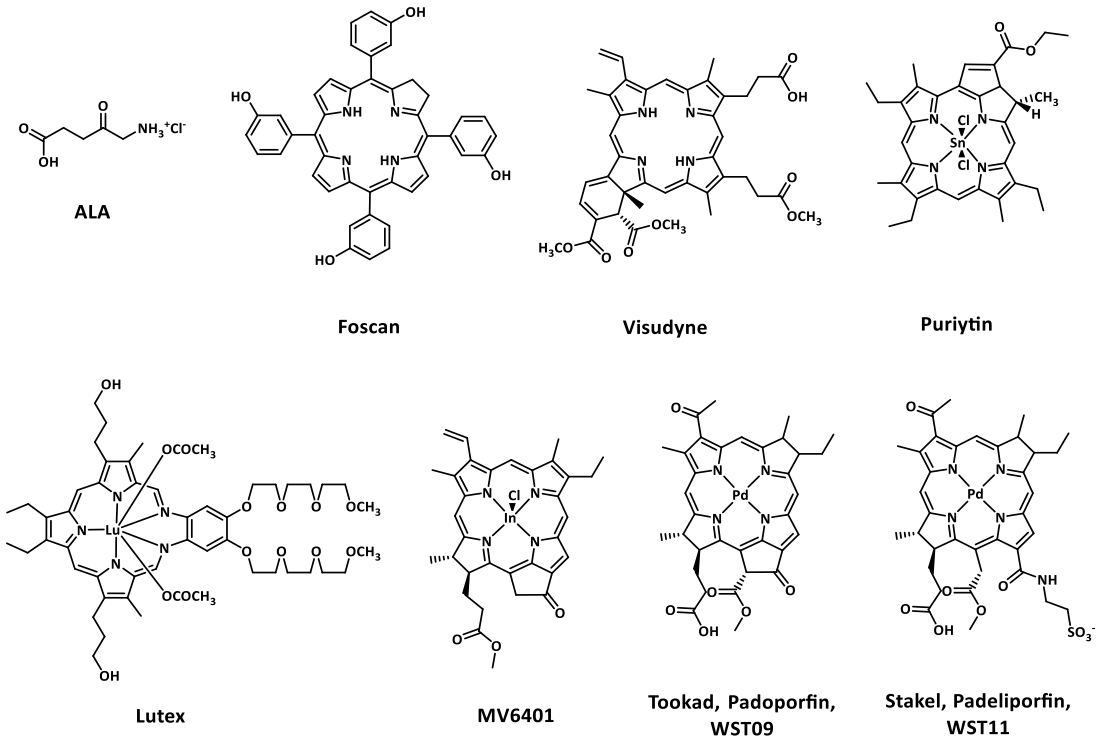

Figure 11 – Examples of Second Generation Photosensitizers that are currently under clinical trials or already in clinical use.

Table 1 – Characteristics of Second Generation Photosensitizers that are currently under clinical trials or already in clinical use.

Name	Drug	Clinical stage or Approval	Application
ALA, Levulan Kerasticks®	5-Aminolevulinic acid	Approved worldwide	Basal cell and squamous cell cancers of the skin, head and neck tumors, bladder cancer, actinic keratosis
Tookad® Padoporfin, WST09	Palladium Bacteriochlorin	Clinical trials revealed systemic toxicity due to high lipophilicity	Prostate cancer
Tookad® Soluble Stakel, Padeliporfin, WST11,	Palladium Bacteriochlorin	Phase III clinical trials in US	Prostate cancer
Purlytin, Rostaporfin, SnEt2	Tin Etiopurpurin / chlorin	Phase II/III clinical trials	Breast cancer, Kaposi's sarcoma, prostate cancer,
MV6401	Indium Pyropheophorbide	Phase II clinical trial	Mammary cancer, psoriasis
Lutex, Motexafin lutetium	Lutetium Texaphyrin	Clinically used	Cervical, prostate and brain tumors, age-related macular degeneration (AMD)
Photofrin®, Porfirmer sodium	Free-base porphyrin, Hematoporphyrin derivative	Approved worlwide: Canada, 1993; Japan, 1994; USA, 1995	Bladder cancer, lung cancer, esophageal cancer, Barrett's esophagus
Visudyne®	Verteporfin / benzoporphyrin derivative monoacid	Approved worldwide (AMD): USA, 2000; Canada, 2000; EU, 2000; Japan, 2003 Trials in UK	AMD, serous chorioretinopathy, pathologic myopia, histoplasmosis
LUZ11, Redaporfin	Free base bacteriochlorin	Phase II clinical trial	Head and neck
Metvixia®	Methyl aminolevulinate	Approved: USA,2004; EU, 2001; New Zealand, 2002; Australia, 2003	Actinic keratosis, basal cell carcinoma, non-melanoma skin cancer
Levulan®	Aminolevulinic acid	Approved in USA, 1999	Actinic keratosis, esophageal dysplasia
Foscan®	Temeporfin /Tetra(*m*-hydroxyphenyl)chlorin/*m*THPC	Approved in EU, 2001 Trials in US	Head and neck cancer
Laserphyrin®	Talaporfin / mono-L-aspartyl chlorin e6 / NPe6	Approved in Japan, 2004 Trials in US	Lung cancer, skin cancers, ophthalmic lesions
BPD-MA	Benzoporphyrin derivative-monoacid ring A	Clinically used	AMD

2.4.3.3. Third generation photosensitizers

Third generation photosensitizers consist on drugs that are actively targeted towards tumor cells through the conjugation with moieties with specificity for antigens or receptors that are overexpressed or only expressed in tumor cells.[100,145] The use of Pcs as third generation photosensitizers is will be discussed in section 3.2.

2.5. Tumor tissue targeting, intracellular localization and mechanisms of tumor destruction

There are several characteristics of cancerous tissues that may contribute to a selective localization of PSs. These include *i)* high expression of low-density lipoprotein (LDL) receptors, *ii)* high number of macrophages, responsible for phagocytosis and monomerization of aggregated PSs, *iii)* low pH value; *iv)* elevated amount of collagen, which is known to bind porphyrins; *v)* increased amount of lipids, which have a high affinity for lipophilic drugs; and *vi)* the abnormal structure of tumor stroma, known as the enhanced permeability and retention (EPR) effect.[98,105,110,146,147] The EPR effect arises from the imbalance of angiogenic regulators of fast-growing tumor cells, resulting in a highly permeable vasculature with enlarge gap junctions between endothelial cells and in a compromised lymphatic drainage, which allows for the selective accumulation of macromolecules in tumor tissues.[146,147]

Cellular PDT targets include lysosomes, the plasma membrane, nuclei, the mitochondria, the Golgi apparatus and the endoplasmic reticulum.[96,105,144] PSs that are unable to be taken by cells show a very inefficient PDT effect, since the short half-life of $^1O_2$ only allows for photodamage of nearby targets.[105,144] Furthermore, the intracellular localization of the PS strongly determines the cellular pathways triggered by the PDT treatment.[96,144]

Aggregated, anionic and hydrophilic drugs are likely to enter the cell through pinocytosis or endocytosis, so that the drug is localized in lysosomes and endosomes. This greater tendency of aggregated PSs to accumulate in lysosomes may be in the basis of the lower efficacy shown by lysosomal localization of PSs.[96,105]

Mitochondria is considered the optimal target for an effective photodynamic effect.[96,105] Cationic PSs, even those having cationic charges but still hydrophobic, localize preferentially in the

[145] Sharman, W. M.; van Lier, J. E.; Allen, C. M. *Adv. Drug Deliv. Rev.* **2004**, *56* (1), 53–76.
[146] Sobolev, A. S.; Jans, D. A.; Rosenkranz, A. A. *Prog. Biophys. Mol. Biol.* **2000**, *73* (1), 51–90.
[147] Cho, K.; Wang, X.; Nie, S.; Chen, Z. (Georgia); Shin, D. M. *Clin. Cancer Res.* **2008**, *14* (5), 1310–1316.

mitochondria. This may be related with both the mitochondrial membrane potential and the lipid bilayer of the membrane. Moreover, this preferential accumulation of cationic drugs is more pronounced in cancer cells than in normal tissues.[96]

The plasma membrane is a less common target in PDT.[96] There are also scarce examples of PSs that target the cell nuclei. Therefore, PDT is not likely to cause DNA damage, mutations or carcinogenesis.[105]

There are three different mechanisms of cell death, apoptosis, necrosis, and autophagy. Several factors determine which type of cell death is triggered upon PDT treatment, including cell type, subcellular localization of the PS and light dose. Apoptosis is favored by the use of lower light doses, whereas the use of higher doses enhances a necrotic response.[98,144,148] While localization of PSs in the mitochondria and endoplasmatic reticulum are most likely to trigger cell death by apoptosis, localization in the cellular membrane and inside lysosomes is more likely to cause cell death by necrosis.[96,100,105,144,148]

Necrosis is an unprogrammed process that affects numerous cell populations. It triggers a response by the cytokine familly, resulting in cytoplasm sweling, desintegration of organelles and desruption of the plasma membrane. These phenomena culminate in cellular fragmentation with release of the intracellular contents into the extracellular enviroment, causing inflammation.[100,148] Apoptosis is iniciated by a process that involves the transcriptional activation of specific genes and results in cell shrinkage and blebbing of the plasma membrane, with the frangmentation of the cell into membrane-enclosed particles, which are engulfed by phagocytes, thus reducing the release of inflammatory products.[105,148]

Radiation and chemotherapy trigger apoptosis *via* cell-cicle checkpoints and intermediate signal transduction pathways that usually are lacking in malignat cells, resulting in the increased ability of cancer cells to survive such kind of therapies. On the other hand, by allowing the direct development of an apoptotic cell death without the need for such transduction pathways, through an acute stress response that involves mitochondrial damage, PDT provides means to destroy otherwise drug-resistant cell types.[105,148]

The direct cell death, *via* apoptosis or necrosis, by itself, is not enough for tumor cure. Causes for this inefectiveness include the heterogeneus distribution of the PS within the tumor and the hypoxia enviroment experienced by tumor tissues, as discussed above. Furthermore, it has also

[148] Castano, A. P.; Demidova, T. N.; Hamblin, M. R. *Photodiagnosis Photodyn. Ther.* **2005**, *2* (1), 1–23.

been shown that tumor cells that localize farther apart from vascular supply exhibith a reduced PS accumulation and a consequent reduced cell death.[95,105,135]

Therefore, the efficiency of PDT arises from secondary tumoricidal activities that are caused by the oxidative stress induced by the PDT treatment. These include damage to the tumor-associated vasculature and tumor-sensitized immune reaction. Targeting the tumor vasculature is a promising strategy for cancer treatment since it is responsible for both supply of oxygen and nutrients and for the dissemination of cancer cells to other organs. Vascular damage occurs after PDT treatment and leads to severe deprivation of oxygen and nutrients, being thus an important factor in long-term tumor control. The impartment of the tumor vasculature combined with the alterations caused in the plasma membrane ultimately lead to the release of inflammatory mediators responsible for the development of an inflammatory response. An efficient PDT-mediated tumor ablation is strongly dependent on a powerful inflammatory response, which induces a tumor-specific immune reaction. This generation of immune memory cells plays an important role in achieving long-term tumor control. Such inflammatory/immune responses of PDT prompted its combination with immunotherapy treatment to attain long-term tumor control.[95,98,105,135,144]

A necrotic response with its associated inflammatory reaction are preferred in order to stimulate a strong tumor-specific immune reaction important for long-term tumor control. Nevertheless, there are also reports supporting the idea that cell death by apoptosis with less inflammation is preferred for malignancies such as brain tumor, where swelling is undesirable.[98]

2.6. Photodynamic Inactivation of Microorganisms (PDI)

Although PDT was discovered as an antimicrobial therapy, the discovery of antibiotics diverted the attention from this strategy. PDT was studied as a cancer therapy for many years, and it was only in the 1990's that its antimicrobial potential was again explored, arising from the need for new antimicrobial approaches due to the rise in antibiotic resistence.[99,102,103,149,150] PDI allows to target a large variety of microorganisms, such as bacteria, fungi, yeasts and parasitic protozoa, this being useful in the treatment of herpes lesions, papillomatosis, wound infections, psoriasis, acne vulgaris, superficial fungal infections of the skin and infections by *Helicobacter pylori*, which are known to be related with gastric ulcers, chronic gastritis and gastric cancer.[102,103,118,150]

[149] Malik, Z.; Ladan, H.; Nitzan, Y. *J. Photochem. Photobiol. B Biol.* **1992**, *14* (3), 262–266.
[150] Hamblin, M. R.; Hasan, T. *Photochem. Photobiol. Sci.* **2004**, *3* (5), 436–450.

While PDT treatment against cancer usually involves the intravenous injection of the PS followed by its preferential accumulation in the tumor tissue, PDI for localized infections can be achieved through direct delivery of the PS by topical application, instillation, interstitial injection or aerosol delivery, hence reducing the risk for damage to healthy tissues.[150]

Moreover, the great potential of PDI also comes from the possibility of making a PS that selectively binds to microbial cells, preventing the damage of host mammalian cells.[99,103] This can be achieved, for example, through the introduction of cationic functions on the PS, since some microbial cells have a more pronounced negative charge than mammalian cells.[99] Bacteria, yeasts, fungi, mycoplasmas and pathogenic protozoa have been efficiently photoinactivated by different cationic PSs, such as phenothiazines, porphyrins and phthalocyanines, making these PSs the best suited for clinical PDI.[118]

Whereas inactivation of Gram-positive bacteria has been successfully accomplished with anionic and neutral PSs, these PSs were ineffective in killing Gram-negative bacteria.[102,103,150] It has been demonstrated that the presence of positive charges on the PS are required for effective PDI treatment against Gram-negative bacteria.[99,102,103,118,151] Gram-positive bacteria display a highly porous outer wall manly constituted by peptidoglycan layers, that allows the diffusion of macromolecules of about 60000 Da. Contrasting, Gram-negative bacteria are characterized by an outer wall with a rigid structural element located outside the peptidoglycan compartment, which is composed by lipoproteins, lipopolysaccharides, teichoic and lipoteichoic acid. This surface, which is densely packed with negative charges, inhibits the penetration of macromolecules and allows triggering resistance mechanisms against antibiotics. Consequently, only relatively hydrophilic compounds with less than 600-700 Da are able to diffuse through the porin channels present at the outer wall of Gram-negative bacteria.[99,103,118,150,151] It is believed that cationic PSs are able to penetrate the Gram-negative outer wall through the self-promoted uptake pathway, which consists on the displacement of divalent cations from their binding sites present on the cell surface. This mechanism can be combined with the disruption of the normal barrier features of the outer wall by the bulkiness and amphiphilicity of the polycyclic photosensitizers.[118]

Another important advantage of PDI is the reduced probability of bacteria developing resistance, since PDI has multiple cellular targets, in contrast with conventional antibiotics that target single enzymes.[99,102,103,152] Furthermore, since the PSs preferentially bind the cytoplasmic

[151] Mantareva, V.; Kussovski, V.; Angelov, I.; Borisova, E.; Avramov, L.; Schnurpfeil, G.; Wöhrle, D. *Bioorg. Med. Chem.* **2007**, *15* (14), 4829–4835.

[152] Zheng, X.; Sallum, U. W.; Verma, S.; Athar, H.; Evans, C. L.; Hasan, T. *Angew. Chemie - Int. Ed.* **2009**, *48*, 2148–2151.

membrane, cell death will mainly occur *via* membrane damage, without involving the genetic material, reducing the risk of inducing mutagenic effects.[102,103]

The great potential of PDI has led to intensive research on the design of photosensitizers that can be used as antimicrobial agents.[153] These include fullerenes,[154,155] benzo[α]phenoxazinium dyes and derivatives,[152] chlorins,[156,157] bacteriochlorins,[158] porphyrins[159-163] and phthalocyanines.[159,164-167]

[153] Hamblin, M. R.; Sharma, S. K.; Kharkwal, G. B. In *Photodynamic Inactivation of Microbial Pathogens: Madicinal and Environmental Applications*; Hamblin, M. R., Jori, G., Eds.; Royal Society of Chemistry, 2011; pp 69–82.

[154] Milanesio, M. E.; Durantini, E. N. In *Photodynamic Inactivation of Microbial Pathogens: Madicinal and Environmental Applications*; Hamblin, M. R., Jori, G., Eds.; Royal Society of Chemistry, 2011; pp 161–184.

[155] Spesia, M. B.; Milanesio, M. E.; Durantini, E. N. *Eur. J. Med. Chem.* **2008**, *43* (4), 853–861.

[156] Mesquita, M. Q.; Menezes, J. C. J. M. D. S.; Pires, S. M. G.; Neves, M. G. P. M. S.; Simões, M. M. Q.; Tomé, A. C.; Cavaleiro, J. A. S.; Cunha, Â.; Daniel-da-Silva, A. L.; Almeida, A.; Faustino, M. A. F. *Dye. Pigment.* **2014**, *110*, 123–133.

[157] Ferreyra, D. D.; Reynoso, E.; Cordero, P.; Spesia, M. B.; Alvarez, M. G.; Milanesio, M. E.; Durantini, E. N. *J. Photochem. Photobiol. B Biol.* **2016**, *158*, 243–251.

[158] Huang, L.; Krayer, M.; Roubil, J. G. S.; Huang, Y.-Y.; Holten, D.; Lindsey, J. S.; Hamblin, M. R. *J. Photochem. Photobiol. B Biol.* **2014**, *141*, 119–127.

[159] Almeida, A.; Cunha, A.; Faustino, M. A. F.; Tomé, A. C.; Neves, M. G. P. S. In *Photodynamic Inactivation of Microbial Pathogens: Madicinal and Environmental Applications*; Hamblin, M. R., Jori, G., Eds.; Royal Society of Chemistry, 2011; pp 83–160.

[160] Mondal, D.; Bera, S. *Adv. Nat. Sci. Nanosci. Nanotechnol.* **2014**, *5* (3), 1–14.

[161] Caminos, D. A.; Durantini, E. N. *J. Porphyr. Phthalocyanines* **2005**, *9* (5), 334–342.

[162] Xing, C.; Xu, Q.; Tang, H.; Liu, L.; Wang, S. *J. Am. Chem. Soc.* **2009**, *131* (36), 13117–13124.

[163] Gomes, M. C.; Woranovicz-Barreira, S. M.; Faustino, M. A. F.; Fernandes, R.; Neves, M. G. P. M. S.; Tome, A. C.; Gomes, N. C. M.; Almeida, A.; Cavaleiro, J. A. S.; Cunha, A.; Tome, J. P. C. *Photochem. Photobiol. Sci.* **2011**, *10* (11), 1735–1743.

[164] Mantareva, V. N.; Angelov, I.; Wöhrle, D.; Borisova, E.; Kussovski, V. *J. Porphyr. Phthalocyanines* **2013**, *17* (06n07), 399–416.

[165] Ke, M.-R.; Eastel, J. M.; Ngai, K. L. K.; Cheung, Y.-Y.; Chan, P. K. S.; Hui, M.; Ng, D. K. P.; Lo, P.-C. *Eur. J. Med. Chem.* **2014**, *84*, 278–283.

[166] Lourenco, L. M. O.; Sousa, A.; Gomes, M. C.; Faustino, M. A. F.; Almeida, A.; Silva, A. M. S.; Neves, M. G. P. M. S.; Cavaleiro, J. A. S.; Cunha, A.; Tome, J. P. C. *Photochem. Photobiol. Sci.* **2015**, *14* (10), 1853–1863.

[167] Rocha, D. M. G. C.; Venkatramaiah, N.; Gomes, M. C.; Almeida, A.; Faustino, M. A. F.; Almeida Paz, F. A.; Cunha, A.; Tome, J. P. C. *Photochem. Photobiol. Sci.* **2015**, *14* (10), 1872–1879.

3. Phthalocyanines as photosensitizers for Photodynamic Therapy

Phthalocyanines exhibit singular properties that have encouraged their intense study for PDT. Among such properties, their strong absorption in the red/NIR region of the electromagnetic spectrum is of extreme relevance. As discussed above, strong red absorption increases the tissue penetration depth. This is very advantageous when compared with other tetrapyrrolic based photosensitizers, such as the commonly used porphyrins. Moreover, the Pc Q-band absorption can be shifted further into the NIR region through the extension of the π-conjugation, or by introducing electron-donor substituents. Additionally, Pcs show low absorption at 400 to 600 nm, which may possibly result in a lower photosensitization of skin when exposed to visible light.[33,116,142,168] Other interesting characteristics of Pcs include their efficiency in generating singlet oxygen, lack of dark toxicity and flexibility for their structural modifications.[142,168]

Up to date, there are only four Pc derivatives available for clinical trials or clinical uses, namely, CGP55847, Pc 4, Photocyanine, and Photosens® (**Figure 12**, **Table 2**).[33,100,142,169]

CGP55847 consists on an unsubstituted ZnPc which is formulated in liposomes of palmitoyl-oleoyl-phosphatidylcholine and di-oleoyl phosphatidylserine. It constitutes on the first Pc tested in clinical trials. However, due to non-medical reasons, its clinical trials were discontinued.[33,142,170]

Pc4 is a SiPc bearing two different axial substitutions, i.e. one hydroxyl group and a -$OSi(CH_3)_3$-$(CH_2)_3N(CH_3)_2$ chain at the other side. It is one of the most efficient Pc based photosensitizers. Pc4 underwent two FDA approved Phase I clinical trials, which demonstrated that Pc4 is well tolerated by subjects and has promising potential for topical delivery.[142,171,172]

Photosens® consists of a mixture of sulfonated aluminum phthalocyanine derivatives that has shown to be effective in the treatment of a large variety of cancers, including skin, breast and lung cancers. In 2001, it was approved in Russia, where it is commercialized by NIOPIK.[33,100,138,142,169]

Photocyanine is the trade name of Suftalan Zinc, an amphiphilic photosensitizer consisting on a mixture of four isomers of di-(potassium sulfonate)-di-phthalimidomethyl zinc phthalocyanine.

[168] Makhseed, S.; Tuhl, A.; Samuel, J.; Zimcik, P.; Al-awadi, N.; Novakova, V. *Dye. Pigment.* **2012**, *95*, 351–357.

[169] Master, A.; Livingston, M.; Sen Gupta, A. *J. Control. Release* **2013**, *168* (1), 88–102.

[170] Ben-hur, E.; Chan, W.-S. In *The Porphyrin Handbook*; Kadish, K. M., Smith, K. M., Guilard, R., Eds.; Academic Press: Amsterdam, 2003; pp 1–35.

[171] He, J.; Larkin, H. E.; Liz, Y.; Rihter, B. D.; Zaidi, S. I. A.; Rodgers, M. A. J.; Mukhtar, H.; Kenney, M. E.; Oleinick, N. L. *Photochem. Photobiol.* **1997**, *65* (3), 581–586.

[172] Lee, T. K.; Baron, E. D.; Foster, T. H. *J. Biomed. Opt.* **2008**, *13* (3), 30503–30507.

The FDA of China approved Phase I clinical trials of Photocyanine, which started in 2008, and phase II clinical trials are currently undergoing.[142,173,174]

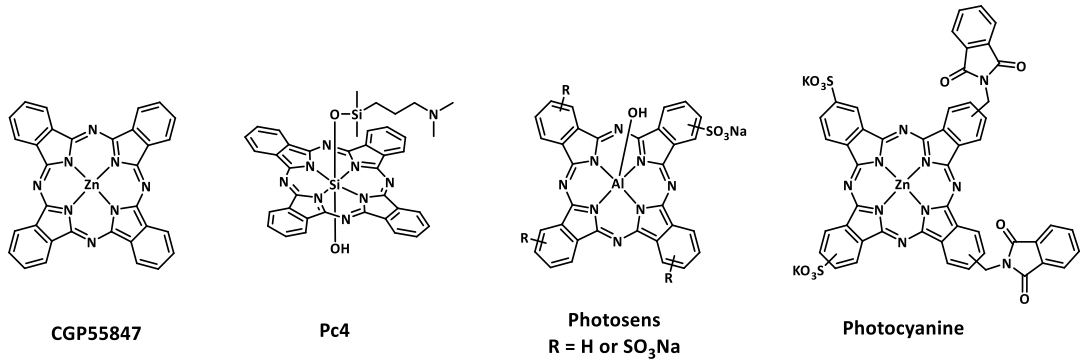

Figure 12 – Examples of phthalocyanines as second generation photosensitizers that are currently under clinical trials or already in clinical use.

Table 2 – Characteristics of clinically used phthalocyanines as Second Generation Photosensitizers.

Name	Drug	Approval information	Application
CGP55847	Zinc Phthalocyanine	Phase I/II clinical trials in Switzerland	Squamous cell carcinoma of upper aerodigestive tract
Pc4	Silicon Phthalocyanine	Phase I clinical trials	Cutaneous neoplasms
Photosens®	Aluminum phthalocyanine	Approved in Russia, 2001	Skin, breast, lung, cervical cancer, larynx, head and neck cancers
Photocyanine	Zinc Phthalocyanine	Phase II clinical trials	

3.1. Phthalocyanines soluble in water for PDT

As mentioned before, solubility in water is a crucial requirement of photosensitizers when applied in PDT. The administration of drugs with poor solubility in water leads to low bioavailability, particularly upon oral administration. Moreover, hydrophobic drugs may aggregate upon intravenous administration, causing serious problems such as embolism, with concomitant side effects including failure of the respiratory system. The aggregation of hydrophobic drugs may also

[173] Huang, J.; Naisheng, C.; Jiandong, H.; Ersheng, L.; Jinping, X.; Suling, Y.; Ziqiang, H.; Jiancheng, S. *Sci. China. Ser. B, Chem.* **2001**, *44* (2), 113–122.

[174] Bi, B.-T.; Zou, B.-Y.; Deng, L.-T.; Zhan, J.; Liao, H.; Feng, K.-Y.; Li, S. *J. Anal. Methods Chem.* **2014**, *2014*, 1–8.

lead to toxic effects that arise from their local accumulation.[175,176] Contrasting, a hydrophilic drug shows improved circulation in the bloodstream, a feature that greatly facilitates the delivery of the drug to the target site.[100] However, the hydrophilic drugs are unable to cross the hydrophobic cellular membrane, this resulting in poor cellular uptake. Furthermore, these drugs display a short life-time in the circulation system and a low bioavailability, due to their reduced stability against proteolytic and hydrolytic degradation.[176]

For these reasons, amphiphilic drugs are thought to be the most promising compounds to be used as photosensitizers, facilitating both circulation in the blood stream and traversing of the cellular membrane.[110,116,177] Thus, amphiphilic molecules are easily localized both at hydrophobic-hydrophilic interfaces of the cellular membranes and on the surface of proteins eventually leading to enhanced PDT effect.[127,178]

The aromatic nature of Pcs poses an important drawback when using these macrocycles in biological media, since it is responsible for their low solubility in water and their strong tendency to form aggregates.[94,179] Hence, several strategies have been adopted to increase the Pc hydrophilicity and make them more bio-compatible.[179] The synthesis of Pcs soluble in water is addressed through two different strategies: their functionalization with ionic functions[180,181] or the introduction of strongly hydrophilic groups, such as peptides,[182] polyethylene glycol (PEG)[183,184] and carbohydrates.[185,186]

[175] Torchilin, V. P. *Pharm. Res.* **2006**, *24* (1), 1–16.

[176] Sun, T.; Zhang, Y. S.; Pang, B.; Hyun, D. C.; Yang, M.; Xia, Y. *Angew. Chemie Int. Ed.* **2014**, *53* (46), 12320–12364.

[177] Çakır, V.; Çakır, D.; Pişkin, M.; Durmuş, M.; Bıyıklıoğlu, Z. *J. Lumin.* **2014**, *154*, 274–284.

[178] Lo, P.-C.; Huang, J.-D.; Cheng, D. Y. Y.; Chan, E. Y. M.; Fong, W.-P.; Ko, W.-H.; Ng, D. K. P. *Chem. Eur. J.* **2004**, *10* (19), 4831–4838.

[179] Dumoulin, F.; Durmuş, M.; Ahsen, V.; Nyokong, T. *Coord. Chem. Rev.* **2010**, *254* (23–24), 2792–2847.

[180] Sharman, W. M.; van Lier, J. E. *J. Porphyr. Phthalocyanines* **2005**, *9* (9), 651–658.

[181] Li, H.; Jensen, T. J.; Fronczek, F. R.; Vicente, M. G. H. *J. Med. Chem.* **2008**, *51* (3), 502–511.

[182] Ranyuk, E.; Cauchon, N.; Klarskov, K.; Guérin, B.; Van Lier, J. E. *J. Med. Chem.* **2013**, *56* (4), 1520–1534.

[183] Mineo, P.; Alicata, R.; Micali, N.; Villari, V.; Scamporrino, E. *J. Appl. Polym. Sci.* **2012**, *126* (4), 1359–1368.

[184] Dinçer, H.; Mert, H.; Çalışkan, E.; Atmaca, G. Y.; Erdoğmuş, A. *J. Mol. Struct.* **2015**, *1102*, 190–196.

[185] Iqbal, Z.; Hanack, M.; Ziegler, T. *Tetrahedron Lett.* **2009**, *50* (8), 873–875.

[186] Crucius, G.; Hanack, M.; Ziegler, T. *J. Porphyr. Phthalocyanines* **2013**, *17*, 807–813.

3.1.1. Charged functions

A common strategy to increase the solubility of phthalocyanines in aqueous media is the covalent attachment of charged functions to the macrocycle. The presence of charged units also prevents the aggregation of the aromatic rings through electrostatic repulsion forces.[187,188]

The introduction of cationic moieties can be achieved *via* quaternization of nitrogen atoms,[179] to give salts such as ammonium groups,[177,178,188,189] pyridinium units,[166,190,191] imidazium moieties,[187] quinolinium functions,[192] or morpholinium substituents.[193] For example, ZnPc derivatives bearing ammonium groups at β- (**Figure 13**a) and α-positions were prepared by Petr Zimcik and coworkers and showed strong far-red absorption as well as efficient phototoxic effect towards tumor cells.[188] A ZnPc substituted at the peripheral positions with methylpyridinium units (**Figure 13**b) proved to be a promising PS for PDT against tumors.[191] Ammonium functions were introduced at the axial positions of SiPcs, affording an amphiphilic Pc (**Figure 13**c) with high *in vitro* phototoxicity.[178] The ZnPc functionalized with imidazolium units (**Figure 13**d) also exhibited promising results in the *in vitro* studies against cancer cells.[187] Furthermore, cationic Pc derivatives have been applied in PDI against Gram negative bacteria. For instance, Tomé and coworkers synthesized two inverted methoxypyridinium ZnPcs (**Figure 13**e), which could efficiently photoinactivate pathogenic Gram negative bacteria.[166]

[187] Makhseed, S.; Machacek, M.; Alfadly, W.; Tuhl, A.; Vinodh, M.; Simunek, T.; Novakova, V.; Kubat, P.; Rudolf, E.; Zimcik, P. *Chem. Commun.* **2013**, *49* (95), 11149–11151.

[188] Machacek, M.; Cidlina, A.; Novakova, V.; Svec, J.; Rudolf, E.; Miletin, M.; Kučera, R.; Simunek, T.; Zimcik, P. *J. Med. Chem.* **2015**, *58* (4), 1736–1749.

[189] Sesalan, B. Ş.; Koca, A.; Gül, A. *Dye. Pigment.* **2008**, *79* (3), 259–264.

[190] Mantareva, V.; Angelov, I.; Kussovski, V.; Dimitrov, R.; Lapok, L.; Wöhrle, D. *Eur. J. Med. Chem.* **2011**, *46* (9), 4430–4440.

[191] Moeno, S.; Krause, R. W. M.; Ermilov, E. A.; Kuzyniak, W.; Hopfner, M. *Photochem. Photobiol. Sci.* **2014**, *13* (6), 963–970.

[192] Bıyıklıoğlu, Z.; Kantekin, H. *Synth. Met.* **2011**, *161* (11), 943–948.

[193] Zheng, B. Y.; Ke, M. R.; Lan, W. L.; Hou, L.; Guo, J.; Wan, D. H.; Cheong, L. Z.; Huang, J. D. *Eur. J. Med. Chem.* **2016**, *114*, 380–389.

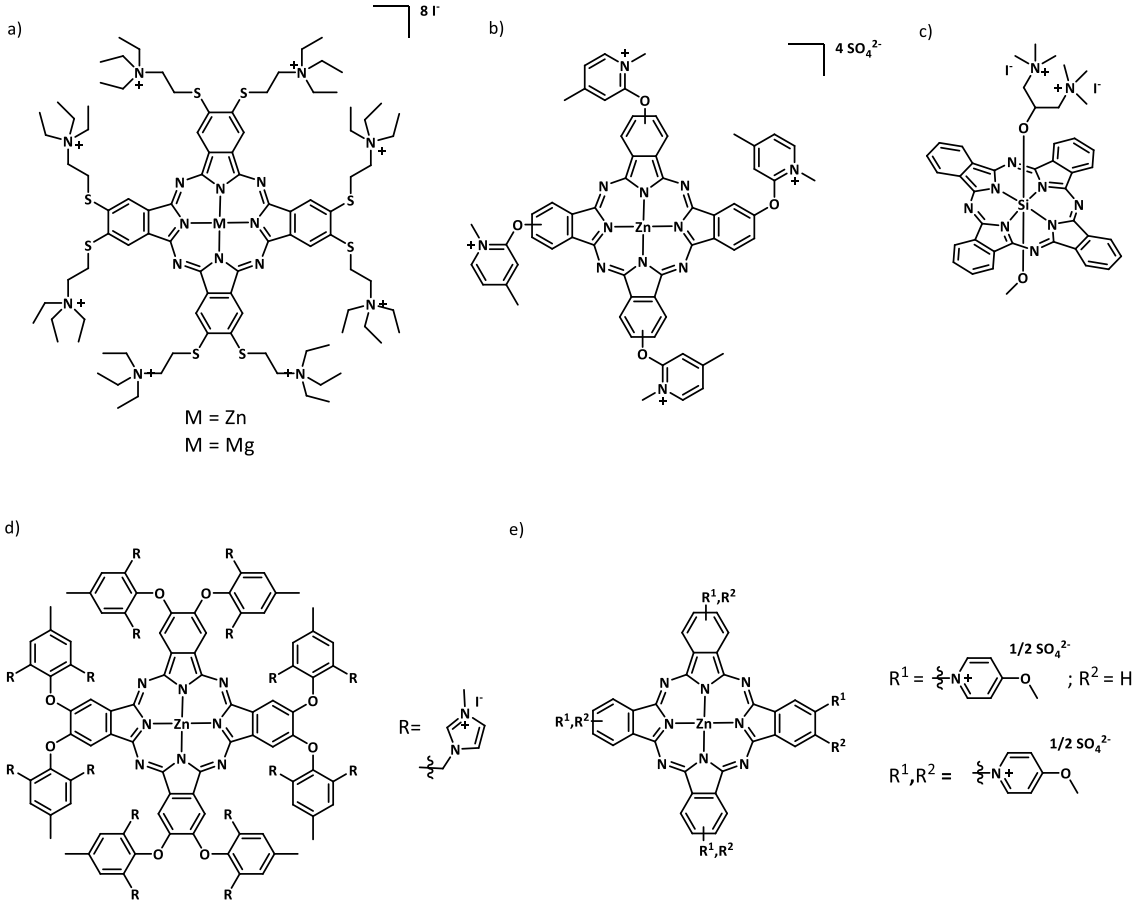

Figure 13 – Examples of cationic Pcs used as photosensitizers for PDT.

Anionic moieties have also been applied to increase the solubility in water of Pcs. Such functionalities include carboxylic acids,[194,195] sulfonic acids[151,196,197] and phosphonic acids.[198,199] The solubility in water of anionic Pcs is strongly dependent of the pH, since the acidic forms of these compounds may not exhibit the same water solubility as their corresponding carboxylates.[179] In particular, Torres and coworkers introduced dendrimers bearing carboxylate functions at the periphery of ZnPcs (**Figure 14**a) and demonstrated the great potential of such water-soluble compounds for the generation of singlet oxygen.[195] Shen and coworkers prepared an amphiphilic ZnPc bearing 5-sulfo-1-naphthoxy substituents (**Figure 14**b), which exhibited a high efficiency of

[194] Liu, W.; Jensen, T. J.; Fronczek, F. R.; Hammer, R. P.; Smith, K. M.; Vicente, M. G. H. *J. Med. Chem.* **2005**, *48* (4), 1033–1041.

[195] Setaro, F.; Ruiz-González, R.; Nonell, S.; Hahn, U.; Torres, T. *J. Inorg. Biochem.* **2014**, *136*, 170–176.

[196] Wei, S.; Zhou, J.; Huang, D.; Wang, X.; Zhang, B.; Shen, J. *Dye. Pigment.* **2006**, *71*, 61–67.

[197] Arslan, S.; Yilmaz, I. *Polyhedron* **2007**, *26* (12), 2387–2394.

[198] Sharman, W. M.; Kudrevich, S. V.; van Lier, J. E. *Tetrahedron Lett.* **1996**, *37* (33), 5831–5834.

[199] Venkatramaiah, N.; Pereira, P. M. R.; Almeida Paz, F. A.; Ribeiro, C. A. F.; Fernandes, R.; Tome, J. P. C. *Chem. Commun.* **2015**, *51* (85), 15550–15553.

singlet oxygen generation.[196] Tomé and coworkers prepared Zn and free-base Pcs functionalized with phosphonic acids at the periphery (**Figure 14**c),[199] designed to increase the selectivity towards tumor tissues, given the acidic pH characteristic of cancer cells. *In vitro* studies revealed high cellular uptake and efficient phototoxic effects for these derivatives.

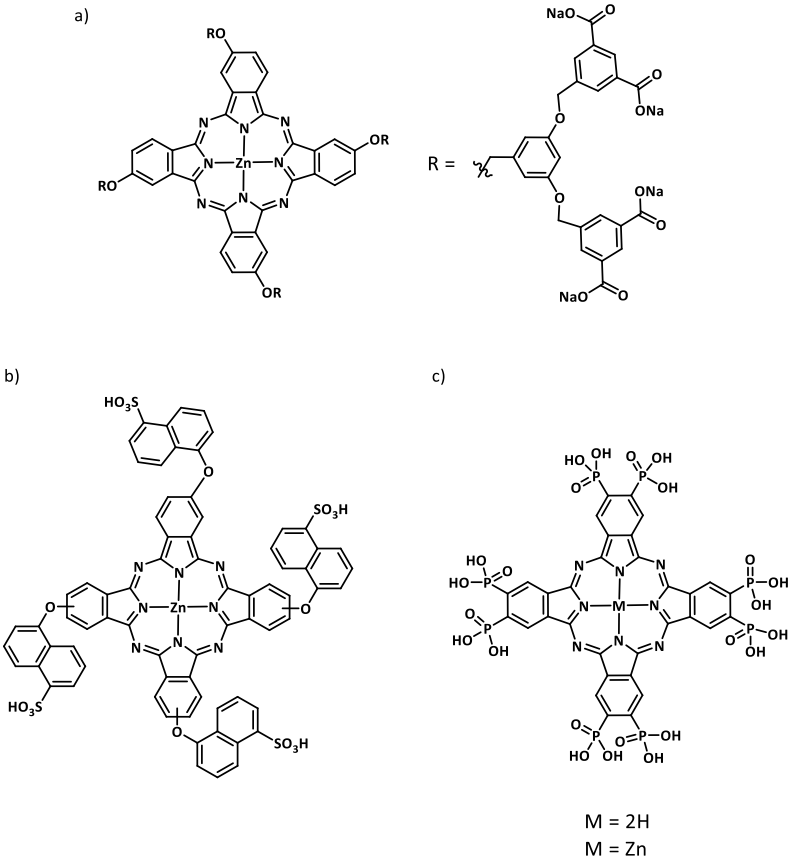

Figure 14 – Examples of anionic Pcs used as photosensitizers for PDT.

3.1.2. Polyethylene glycol (PEG) chains

The use of PEG chains is a popular approach to enhance the biocompatibility of otherwise hydrophobic drugs. PEG comprises a chemically inert structure with the general formula HO-$(CH_2CH_2O)_n$-CH_2CH_2-OH.[200] The incorporation of PEG moieties in nanoparticles for the delivery of hydrophobic drugs has been described,[201] as well as their use as blocks for the formation of polymeric micelles, used as carriers for such drugs.[175]

[200] van Vlerken, L. E.; Vyas, T. K.; Amiji, M. M. *Pharm. Res.* **2007**, *24* (8), 1405–1414.

[201] Tudisco, C.; Bertani, F.; Cambria, M. T.; Sinatra, F.; Fantechi, E.; Innocenti, C.; Sangregorio, C.; Dalcanale, E.; Condorelli, G. G. *Nanoscale* **2013**, *5* (23), 11438–11446.

Besides improving the hydrophilicity of the drug or nanoformulation, the introduction of PEG chains has other advantages, as it leads to a prolonged blood circulating lifetime, allows for the minimization of non-specific uptake and favors the EPR effect. These features combined result in an elevated concentration of the drug at the tumor site.[200,202]

A commonly used strategy to improve the hydrophilicity of Pcs is the introduction of polyether chains at their peripheral positions. This approach has proven to enhance the solubility in a variety of solvents, including non-polar solvents like benzene, aprotic polar solvents like DCM, acetone, dioxane and DMSO, and protic polar solvents such as water and methanol.[62,63,203,204]

Despite this improved solubility, some degree of aggregation in most solvents is always observed. In particular, the formation of columnar aggregates in protic solvents, like methanol and water, is a common phenomenon of polyether functionalized Pcs, and it is characterized by absorption spectra with broadened, weaker and blue-shifted Q-bands.[62,203,204] When both monomeric and aggregated species coexist, the absorption spectrum shows a lower energy Q-band, corresponding to the monomeric species, and an additional, higher energy Q-band that arises from the aggregated macrocycles.[63,203,204]

Several Pcs functionalized with different PEG chains have been studied as PSs for the generation of singlet oxygen. For instance, Zn and Pb complexes of peripherally PEG-octafunctionalized Pcs (**Figure 15**a) have been prepared by Truscott.[62] PEG-tetrafunctionalized ZnPcs, attached through oxygen atoms to the α-positions (**Figure 15**b),[204] and through sulfur atoms to the β-positions (**Figure 15**c),[205] were reported by Ahsen. Polyether chains with an average molecular weight of 550 or 750 have been introduced at the axial positions of SiPcs (**Figure 15**d), by Ng and coworkers, affording compounds with enhanced hydrophilicity, reduced aggregation and high *in vitro* phototoxic effect.[206]

[202] Liu, J.-Y.; Jiang, X.-J.; Fong, W.-P.; Ng, D. K. P. *Org. Biomol. Chem.* **2008**, *6* (24), 4560–4566.

[203] Kroon, J. M.; B. M. Koehorst, R.; van Dijk, M.; Sanders, G. M.; J. R. Sudholter, E. *J. Mater. Chem.* **1997**, *7* (4), 615–624.

[204] Tuncel, S.; Dumoulin, F.; Gailer, J.; Sooriyaarachchi, M.; Atilla, D.; Durmus, M.; Bouchu, D.; Savoie, H.; Boyle, R. W.; Ahsen, V. *Dalt. Trans.* **2011**, *40* (16), 4067–4079.

[205] Atilla, D.; Saydan, N.; Durmuş, M.; Gürek, A. G.; Khan, T.; Rück, A.; Walt, H.; Nyokong, T.; Ahsen, V. *J. Photochem. Photobiol. A Chem.* **2007**, *186* (2–3), 298–307.

[206] Huang, J.-D.; Wang, S.; Lo, P.-C.; Fong, W.-P.; Ko, W.-H.; Ng, D. K. P. *New J. Chem.* **2004**, *28* (3), 348–354.

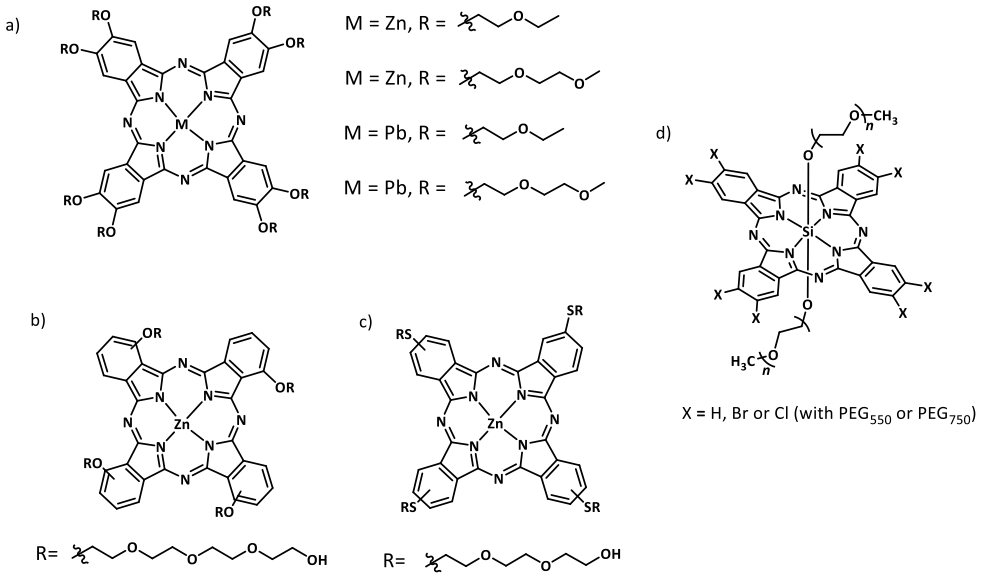

Figure 15 – Examples of PEG functionalized Pcs used as PSs for PDT.

3.2. Phthalocyanines as third generation photosensitizers: improved selectivity

Traditional cancer treatment like radiotherapy and chemotherapy lead to toxic effects to normal cells with pronounced side effects that arise from the nonspecific distribution of anticancer drugs in the body.[145,147,207] Even though PDT allows for some level of selectivity through the confined irradiation of the tumor site, most of second-generation PSs shown only a small selectivity for cancer cells, resulting in high uptake by healthy cells with concomitant phototoxic and photoallergic reactions, as well as pronounced skin sensitivity.[145,208] It is, therefore, of great importance to develop selective PSs in order to reduce side effects.

One way to selectively promote the entry of the drug into tumor cells consists on taking advantage of pathophysiological characteristics of cancer tissues (discussed in section 2.5) to promote the entry of the drug into tumor cells. This strategy is often referred as "passive targeting".[146,147,208]

Third-generation PSs are designed including targeting moieties capable of guiding the drug to antigens or receptors overexpressed, or even only expressed, in tumor cells. This strategy is known as "active targeting" and often allows for the receptor-mediated endocytosis of the drug resulting in its increased accumulation in the intracellular medium.[145-147,176,207,208]

[207] David, A. *Isr. J. Chem.* **2010**, *50* (2), 204–219.
[208] Bugaj, A. M. *Photochem. Photobiol. Sci.* **2011**, *10* (7), 1097–1109.

The design of Pcs as tumor-selective PSs include coupling to antibodies,[209] peptides,[182] carbohydrates,[210] cyclodextrins,[211] folic acid,[212] estrogens (e.g. estrone[213]) and steroids (e.g. colestrol[213]). In this thesis, the functionalization with carbohydrates and with folic acid were selected.

3.2.1. Carbohydrates

In order to understand the role of carbohydrates as targeting agents in cancer therapy, it is first necessary to comprehend the mechanisms that underline the formation of tumor cells.

The first biochemical characteristic of tumor cells was discovered by a German biochemist and physiologist named Otto Heinrich Warburg (1883-1970).[214] He observed that tumor cells were characterized by a shift in glucose metabolism from respiration (oxidative phosphorylation) to glycolysis (fermentation), even in oxygenated conditions.[214-216] His work granted him the Nobel Prize in Physiology and Medicine in 1931.[216] Warburg defended that a defect in bioenergetics and cellular energy metabolism was the basis for the development of cancer cells, which occurred in two different phases.[214,216] The first step consists on the irreversible damage to respiration of normal cells, which causes an energy deficiency. This forces cells to struggle for survival, as the second stage of cancer development. Here, a selective process takes place, with some cells dying from lack of energy, and others being able to remain alive replacing the loss of respiration by an increase in fermentation.[214] Such increase in fermentation leads to the production of large amounts of lactic acid as a by-product, the latter being responsible for the acidic pH characteristic of cancer cells.[216] The morphological inferiority of fermentation energy, with respect to respiration energy, is responsible for the transformation of highly differentiated cells into cancer cells, that is, wildly-growing undifferentiated cells.[214]

[209] Sato, K.; Nakajima, T.; Choyke, P. L.; Kobayashi, H. *RSC Adv.* **2015**, *5* (32), 25105–25114.

[210] Lourenço, L. M. O.; Neves, M. G. P. M. S.; Cavaleiro, J. A. S.; Tomé, J. P. C. *Tetrahedron* **2014**, *70* (17), 2681–2698.

[211] Lourenço, L. M. O.; Pereira, P. M. R.; Maciel, E.; Valega, M.; Domingues, F. M. J.; Domingues, M. R. M.; Neves, M. G. P. M. S.; Cavaleiro, J. A. S.; Fernandes, R.; Tome, J. P. C. *Chem. Commun.* **2014**, *50* (61), 8363–8366.

[212] Li, Y.; Wang, J.; Zhang, X.; Guo, W.; Li, F.; Yu, M.; Kong, X.; Wu, W.; Hong, Z. *Org. Biomol. Chem.* **2015**, *13* (28), 7681–7694.

[213] Maree, S. E.; Nyokong, T. *J. Porphyr. Phthalocyanines* **2001**, *5* (11), 782–792.

[214] Warburg, O. *Science* **1956**, *123* (3191), 309–314.

[215] Shaw, R. J. *Curr. Opin. Cell Biol.* **2006**, *18* (6), 598–608.

[216] Airley, R. E.; Mobasheri, A. *Chemotherapy* **2007**, *53* (4), 233–256.

Hence, cancer cells exhibit an elevated glycolytic rate and are highly dependent on glucose as energy source. The entry of glucose and other monosaccharides is mediated by a family of integral membrane transport proteins, the GLUT family. This family includes the GLUT 1 and GLUT 3 transporters, which are known to be overexpressed in a large variety of cancers, and thus can be used as targets for the selective delivery of cancer drugs.[216]

There is now evidence that this altered metabolism of tumor cells is originated from genetic mutations, which are also responsible for the loss of growth control and cellular differentiation characteristic of cancer cells.[215,216]

For instance, carbohydrate-binding proteins, called lectins, are known to be involved in the development of cancer.[207,217-219] Lectins participate in the selective endocytosis of glycoproteins, in cell-cell interactions, in the recognition of pathogens, in the immune defense and in cell differentiation and formation of organs.[207,217,218,220,221] They are therefore implicated in several stages of tumorigenic processes, including the initiation of the transformed phenotype of tumors, regulation of apoptosis and cell growth, formation of tumor metastasis and the development by the host of inflammatory and immune responses against tumors.[207,218,220-222] A class of lectins that is particularly involved in these processes are the galectins, which have affinity for β-galactosides and that are often overexpressed in many tumor types, such as astrocytoma, melanoma, prostate, thyroid, colon, bladder and ovary cancers, and thus are a common target for carbohydrate-mediated delivery systems.[207,218,221-223]

The use of carbohydrate moieties for selective delivery of drugs to cancer cells is a widely-used strategy[207,224] and many examples can be found in the literature, involving the conjugation of carbohydrates to porphyrins[225] and phthalocyanines.[210]

Momenteau and coworkers reported the first synthesis of carbohydrate-Por and carbohydrate-Pc conjugates. They incorporated four glucofuranose units, *via* C-3, at the *meso*

[217] Dwek, R. A. *Chem. Rev.* **1996**, *96* (2), 683–720.
[218] Liu, F.-T.; Rabinovich, G. A. *Nat. Rev. Cancer* **2005**, *5* (1), 29–41.
[219] Kang, B.; Opatz, T.; Landfester, K.; Wurm, F. R. *Chem. Soc. Rev.* **2015**, *44* (22), 8301–8325.
[220] Sharon, N.; Lis, H. *Science* **1989**, *246* (4927), 227–234.
[221] Ingrassia, L.; Camby, I.; Lefranc, F.; Mathieu, V.; Nshimyumukiza, P.; Kiss, F. D. and R. *Current Medicinal Chemistry*. 2006, pp 3513–3527.
[222] Rabinovich, G. A. *Br. J. Cancer* **2005**, *92* (7), 1188–1192.
[223] Huflejt, M. E.; Leffler, H. *Glycoconj. J.* **2004**, *20* (4), 247–255.
[224] Singh, S.; Aggarwal, A.; Bhupathiraju, N. V. S. D. K.; Arianna, G.; Tiwari, K.; Drain, C. M. *Chem. Rev.* **2015**, *115* (18), 10261–10306.
[225] Cavaleiro, J. A. S.; Tomé, J. P. C.; Faustino, M. A. F. In *Heterocycles from Carbohydrate Precursors*; El Ashry, E. S. H., Ed.; Springer Berlin Heidelberg: Berlin, Heidelberg, 2007; pp 179–248.

positions of a porphyrin and at the peripheral positions of a zinc phthalocyanine (**Figure 16**a).[226] The bulky glucose units improved the solubility of macrocycles in water and also reduced aggregation. Ziegler and coworkers prepared a ZnPc peripherally tetrasubstituted with glucopyranose moieties through the anomeric carbon (**Figure 16**b).[227] In addition, several ZnPcs tetra (**Figure 16**c and e)[228] and octafunctionalized (**Figure 16**d)[229] with galactopyranose units linked *via* carbon C-6 have been reported. The *in vitro* studies of these water-soluble compounds revealed that the presence of the monosaccharide units improved their cellular uptake.[230] Galactodendritic ZnPc bearing sixteen galactopyranose monosaccharides (**Figure 16**g)[231] also showed strong PDT efficiency in *vitro*.[232] The effect of number and position of glucose units in the *in vitro* efficacy of Pcs, as well as the difference between deprotected and isopropylidene protected carbohydrates has been established by Ng, showing that the di-α-substituted ZnPc bearing protected monosaccharides (**Figure 16**f) exhibited the highest phototoxic effect.[233] Protected galactopyranose moieties have also been incorporated at the axial positions of SiPcs (**Figure 16**h), affording compounds with low aggregation tendency that revealed an high photodynamic efficiency in the *in vitro* studies.[234]

[226] Maillard, P.; Gaspard, S.; Guerquin-Kern, J. L.; Momenteau, M. *J. Am. Chem. Soc.* **1989**, *111* (25), 9125–9127.

[227] Alvarez-Mico, X.; Calvete, M. J. F.; Hanack, M.; Ziegler, T. *Tetrahedron Lett.* **2006**, *47* (19), 3283–3286.

[228] Ribeiro, A. O.; Tomé, J. P. C.; Neves, M. G. P. M. S.; Tomé, A. C.; Cavaleiro, J. A. S.; Iamamoto, Y.; Torres, T. *Tetrahedron Lett.* **2006**, *47* (52), 9177–9180.

[229] Soares, A. R. M.; Tomé, J. P. C.; Neves, M. G. P. M. S.; Tomé, A. C.; Cavaleiro, J. A. S.; Torres, T. *Carbohydr. Res.* **2009**, *344* (4), 507–510.

[230] Soares, A. R. M.; Neves, M. G. P. M. S.; Tomé, A. C.; Iglesias-de la Cruz, M. C.; Zamarrón, A.; Carrasco, E.; González, S.; Cavaleiro, J. A. S.; Torres, T.; Guldi, D. M.; Juarranz, A. *Chem. Res. Toxicol.* **2012**, *25* (4), 940–951.

[231] Silva, S.; Pereira, P. M. R.; Silva, P.; Almeida Paz, F. A.; Faustino, M. A. F.; Cavaleiro, J. A. S.; Tome, J. P. C. *Chem. Commun.* **2012**, *48* (30), 3608–3610.

[232] Pereira, P. M. R.; Silva, S.; Cavaleiro, J. A. S.; Ribeiro, C. A. F.; Tomé, J. P. C.; Fernandes, R. *PLoS One* **2014**, *9* (4), 1–13.

[233] Liu, J.-Y.; Lo, P.-C.; Fong, W.-P.; Ng, D. K. P. *Org. Biomol. Chem.* **2009**, *7* (8), 1583–1591.

[234] Lee, P. P. S.; Lo, P.; Chan, E. Y. M.; Fong, W.; Ko, W.; Ng, D. K. P. *Tetrahedron Lett.* **2005**, *46*, 1551–1554.

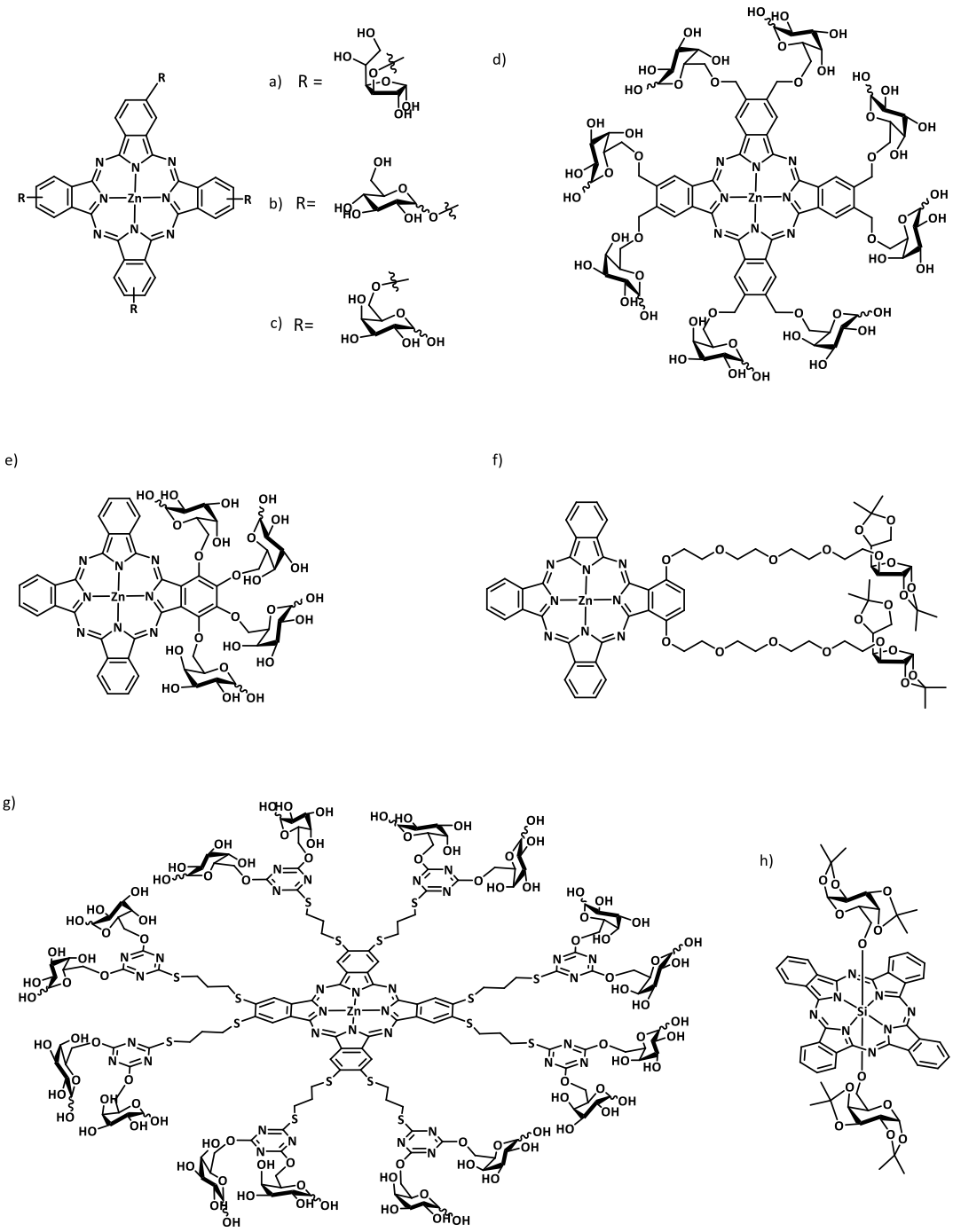

Figure 16 - Examples of carbohydrate functionalized Pcs used as photosensitizers for PDT.

3.2.2. Folic acid

Folic acid (FA) is a small water-soluble molecule that belongs to the vitamin B family. Its chemical structure is composed by three different parts: a pterin residue, a *p*-aminobenzoate and a glutamic acid residue (**Figure 17**).[235] Folates may exist in an oxidized form as folic acid, or in a reduced tetrahydrofolate form.[236] These vitamins play key roles in metabolic reactions that are crucial for cell division and, most importantly, are essential for rapidly growing cells, namely tumor cells.[237,238]

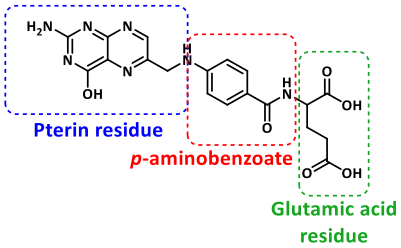

Figure 17 – Chemical structure of folic acid.

There are several characteristics of FA that makes it suitable for tumor targeting strategies. These include *(i)* its stability in storage and circulation; *(ii)* its cheapness and easy access; *(iii)* it is non-toxic and non-immunogenic; *(iv)* its small size; *(v)* its compatibility with both organic and aqueous solvents; and *(vi)* is high affinity for folate receptors.[208,235]

FA penetration into cells is mediated by three different transporters, namely the reduced folate carrier (RFC), a proton-coupled folate transporter and the folate receptor (FR), also known as high affinity folate receptor.[235,236,239]

The RFC is a low-affinity, high-capacity and ubiquitously expressed folate transporter that mediates the transport of reduced folates (water-soluble B vitamins) *via* a bidirectional anion-exchange mechanism. This allows the maintenance of adequate FA levels in normal cells, under physiological pH.[236,238,239]

[235] Stallivieri, A.; Baros, F.; Jetpisbayeva, G.; Frochot, B. M. and C. *Curr. Med. Chem.* **2015**, *22* (27), 3185–3207.

[236] Assaraf, Y. G.; Leamon, C. P.; Reddy, J. A. *Drug Resist. Updat.* **2014**, *17* (4–6), 89–95.

[237] Russell-Jones, G.; McTavish, K.; McEwan, J.; Rice, J.; Nowotnik, D. *J. Inorg. Biochem.* **2004**, *98* (10), 1625–1633.

[238] Ledermann, J. A.; Canevari, S.; Thigpen, T. *Ann. Oncol.* **2015**, *26* (10), 2034-2043.

[239] Salazar, M. D.; Ratnam, M. *Cancer Metastasis Rev.* **2007**, *26* (1), 141–152.

The proton-coupled folate transporter is the major folate transporter at the acidic pH of the upper small intestine.[236,239]

The FR is a cell surface glycosyl phosphatidylinositol-anchored glycopolypeptide which has high affinity for FA and 5-methyltetrahydrofolate, mediating their cellular uptake by endocytosis.[147,235,236,238,239,240] There are four isoforms of FR, FRα, FRβ, FRγ and FRδ, but tumor-targeting studies have laid their attention mainly on the α isoform.[236,238,239] In healthy tissues, FRα expression is limited to a small number of polarized epithelia, including the uterus, placenta, choroid plexus, lung and kidney. It is mainly localized at the luminal surface of these polarized cells and therefore is inaccessible to circulating folates or intravenously administrated FA conjugates.[235,236,238,239] On the other hand, FRα is known to be overexpressed in various cancer tissues, such as cancers of the ovary, uterus, lung, kidney, breast, colon, bladder, head and neck as well as in ependymal brain tumors, adenocarcinomas and testicular choriocarcinomas. It is distributed throughout the entire surface of the cell, being thus accessible to the folates in the circulation.[147,236-239,241,242] Moreover, high expression of FRα is associated with poorly differentiated and more aggressive tumors.[237,239] This specific overexpression of FRα in the surface of tumor cells conjugated for its high affinity for FA provide a promising strategy for the selective delivery of FA-drug conjugates.[238,239,241] FA-drug conjugates bind the FR on the cell surface and become internalized in an endosome, formed by invagination of the plasma membrane. Activation of lysozymes and FR conformational changes triggered by the drop of the pH within the endosome lumen result in the release of the conjugate into the cytoplasm.[147,238,240]

FA has been conjugated to different tetrapyrrolic photosensitizers,[235] namely porphyrins and chlorins.[243,244,245] FA has been also covalently attached to a zinc tetraaminophthalocyanine phthalocyanine, affording a water-soluble compound (**Figure 18**a),[246] with specific affinity to FR-positive cells.[247] A similar conjugate lacking amino functionalization (**Figure 18**b),[248] that was

[240] Leamon, C. P.; Reddy, J. A. *Adv. Drug Deliv. Rev.* **2004**, *56* (8), 1127–1141.

[241] Shia, J.; Klimstra, D. S.; Nitzkorski, J. R.; Low, P. S.; Gonen, M.; Landmann, R.; Weiser, M. R.; Franklin, W. A.; Prendergast, F. G.; Murphy, L.; Tang, L. H.; Temple, L.; Guillem, J. G.; Wong, W. D.; Paty, P. B. *Hum. Pathol.* **2008**, *39* (4), 498–505.

[242] Wang, S.; Low, P. S. *J. Control. Release* **1998**, *53* (1–3), 39–48.

[243] Schneider, R.; Schmitt, F.; Frochot, C.; Fort, Y.; Lourette, N.; Guillemin, F.; Müller, J.-F.; Barberi-Heyob, M. *Bioorg. Med. Chem.* **2005**, *13* (8), 2799–2808.

[244] Li, D.; Li, P.; Lin, H.; Jiang, Z.; Guo, L.; Li, B. *J. Photochem. Photobiol. B Biol.* **2013**, *127*, 28–37.

[245] Stallivieri, A.; Colombeau, L.; Jetpisbayeva, G.; Moussaron, A.; Myrzakhmetov, B.; Arnoux, P.; Acherar, S.; Vanderesse, R.; Frochot, C. *Bioorg. Med. Chem.* **2017**, *25* (1), 1–10.

[246] Khoza, P.; Antunes, E.; Chen, J.-Y.; Nyokong, T. *J. Lumin.* **2013**, *134*, 784–790.

[247] Wang, B. S.; Wang, J.; Chen, J.-Y. *J. Mater. Chem. B* **2014**, *2* (11), 1594–1602.

[248] Ogbodu, R. O.; Antunes, E.; Nyokong, T. *Polyhedron* **2013**, *60*, 59–67.

immobilized onto single walled carbon nanotubes showed significant PDT efficiency.[249] The peripheral amines have also been replaced by three PEG (**Figure 18**c) or three glycerol groups (**Figure 18**d) giving rise to PSs with high selectivity for tumor cells.[212] On the other hand, FA units attached to the axial positions of a SiPc (**Figure 18**e) afforded a non-aggregated compound with high phototoxicity.[250]

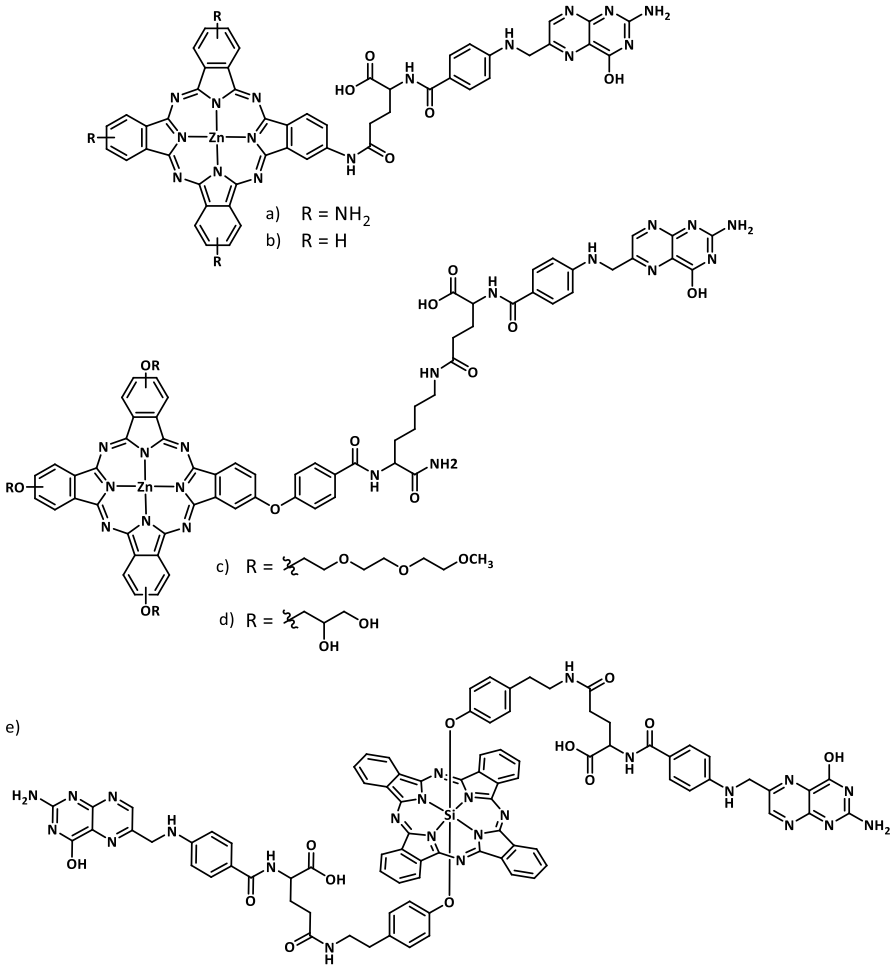

Figure 18 - Examples of FA functionalized Pcs used as photosensitizers for PDT.

[249] Ogbodu, R. O.; Ndhundhuma, I.; Karsten, A.; Nyokong, T. *Spectrochim. Acta Part A Mol. Biomol. Spectrosc.* **2015**, *137*, 1120–1125.

[250] Zheng, Y.-W.; Chen, S.-F.; Zheng, B.-Y.; Ke, M.-R.; Huang, J.-D. *Chem. Lett*. **2014**, 43 (11), 1701–1703.

3.3. Ruthenium Phthalocyanines for PDT

In general, MPcs with non-transition metals, such as Zn^{2+}, Al^{3+} and Ga^{3+}, are preferred when preparing PSs, since these closed-shell diamagnetic ions provide the resulting MPcs with high-yield and long-lived triplet states.[62,96,251,252] In opposition, metals with a paramagnetic nature like Fe, Cu or Gd, are not ideal for applications as PSs.[96,116]

In addition, transition metals, i.e. Platinum[253,254] and Ruthenium,[255-257] which give rise to MPcs with short triplet lifetimes,[252] have been successfully used in other medical applications, namely as anti-cancer agents. The cytotoxic effect of Ru(III) complexes arises from their reduction to the more labile Ru(II) species, and it is characterized by inhibition of DNA replication, causing mutagenic activity, induction of the SOS repair mechanism, binding to nuclear DNA and reduction of RNA synthesis.[258]

Ru(II) polypyridyl complexes have been widely used as photosensitizers for PDT due to their outstanding photophysical characteristics, such as efficient production of singlet oxygen and excellent chemical and photostability.[133,259] Besides Ru(II) polypyridyl complexes, Ruthenium Phthalocyanines (RuPcs) have also been reported for their application in PDT, on the basis of the ability of ruthenium to provide high yields of the triplet excited state, ultimately leading to high yields of singlet oxygen generation.[55]

[251] Ogunsipe, A.; Chen, J.; Nyokong, T. *New J. Chem.* **2004**, *28*, 822–827.

[252] Ali, H.; van Lier, J. E. *Chem. Rev.* **1999**, *99* (9), 2379–2450.

[253] Lebwohl, D.; Canetta, R. *Eur. J. Cancer* **1998**, *34* (10), 1522–1534.

[254] Aztopal, N.; Karakas, D.; Cevatemre, B.; Ari, F.; Icsel, C.; Daidone, M. G.; Ulukaya, E. *Bioorg. Med. Chem.* **2017**, *25* (1), 269–276.

[255] Joshi, T.; Pierroz, V.; Mari, C.; Gemperle, L.; Ferrari, S.; Gasser, G. *Angew. Chemie Int. Ed.* **2014**, *53* (11), 2960–2963.

[256] Giovagnini, L.; Sitran, S.; Castagliuolo, I.; Brun, P.; Corsini, M.; Zanello, P.; Zoleo, A.; Maniero, A.; Biondi, B.; Fregona, D. *Dalt. Trans.* **2008**, No. 47, 6699–6708.

[257] Pierroz, V.; Joshi, T.; Leonidova, A.; Mari, C.; Schur, J.; Ott, I.; Spiccia, L.; Ferrari, S.; Gasser, G. *J. Am. Chem. Soc.* **2012**, *134* (50), 20376–20387.

[258] Messori, L.; Vilchez, F. G.; Vilaplana, R.; Piccioli, F.; Alessio, E.; Keppler, B. *Met. Based. Drugs* **2000**, *7* (6), 335–342.

[259] Huang, H.; Yu, B.; Zhang, P.; Huang, J.; Chen, Y.; Gasser, G.; Ji, L.; Chao, H. *Angew. Chemie Int. Ed.* **2015**, *54* (47), 14049–14052.

As discussed in section 1.1, Pcs are characterized by strong aggregation in solution. This is responsible for reduction of the triplet state lifetime and consequently for low yields of singlet oxygen, due to quenching of the Pc excited state through nonreactive energy relaxation pathway.[33,168,181,234] Different strategies have been used for the inhibition of such aggregation, namely the functionalization of the macrocycle with long chains,[205] bulky groups[168] charged functions,[181] or even the functionalization of the peripheral positions that block one of the faces of the Pc ring.[27] Another strategy is the introduction of axial substituents,[234] which, as mentioned before, can be achieved through the synthesis of RuPcs.

Owing to the ability of RuPcs to strongly coordinate axial ligands that reduce Pc aggregation, some examples of these complexes, although scarce, have been reported to be applied as PSs for PDT. Among them, a RuPc coordinated to phosphines ligands functionalized with sulphonates (**Figure 19**a) revealed promising *in vitro* PDT activity.[56,260,261] An asymmetric RuPc with a carbonyl unit as axial ligand (**Figure 19**b) also showed activity as PDT agent.[57] The synergetic production of singlet oxygen and nitric oxide by two nitrosyl RuPc complexes (**Figure 19**c-d) has been reported.[262,263] Several RuPcs bearing polyether-based dendrimers (**Figure 19**e)[264] or anionic functions (**Figure 19**f)[75,265] at the axial positions, showed good solubility in water and high singlet oxygen quantum yields. Finally, a cholesteryl oleate-appended RuPc (**Figure 19**g) was studied as photosensitizer for the treatment of cutaneous leishmaniasis.[266]

[260] Bossard, G. E.; Abrams, M. J.; Darkes, M. C.; Vollano, J. F.; Brooks, R. C. *Inorg. Chem.* **1995**, *34* (6), 1524–1527.

[261] Abrams, M. J. *Platin. Met. Rev.* **1995**, *39* (1), 14–18.

[262] Carneiro, Z. A.; de Moraes, J. C. B.; Rodrigues, F. P.; de Lima, R. G.; Curti, C.; da Rocha, Z. N.; Paulo, M.; Bendhack, L. M.; Tedesco, A. C.; Formiga, A. L. B.; da Silva, R. S. *J. Inorg. Biochem.* **2011**, *105* (8), 1035–1043.

[263] Heinrich, T. A.; Tedesco, A. C.; Fukuto, J. M.; da Silva, R. S. *Dalt. Trans.* **2014**, *43* (10), 4021–4025;

[264] Hahn, U.; Setaro, F.; Ragas, X.; Gray-Weale, A.; Nonell, S.; Torres, T. *Phys. Chem. Chem. Phys.* **2011**, *13* (8), 3385–3393.

[265] Setaro, F.; Ruiz-González, R.; Nonell, S.; Hahn, U.; Torres, T. *J. Porphyr. Phthalocyanines* **2016**, *20*, 378–387.

[266] Contreras, L. E. S.; Zirzlmeier, J.; Kirner, S. V; Setaro, F.; Martínez, F.; Lozada, S.; Escobar, P.; Hahn, U.; Guldi, D. M.; Torres, T. *J. Porphyr. Phthalocyanines* **2015**, *19* (01–03), 320–328.

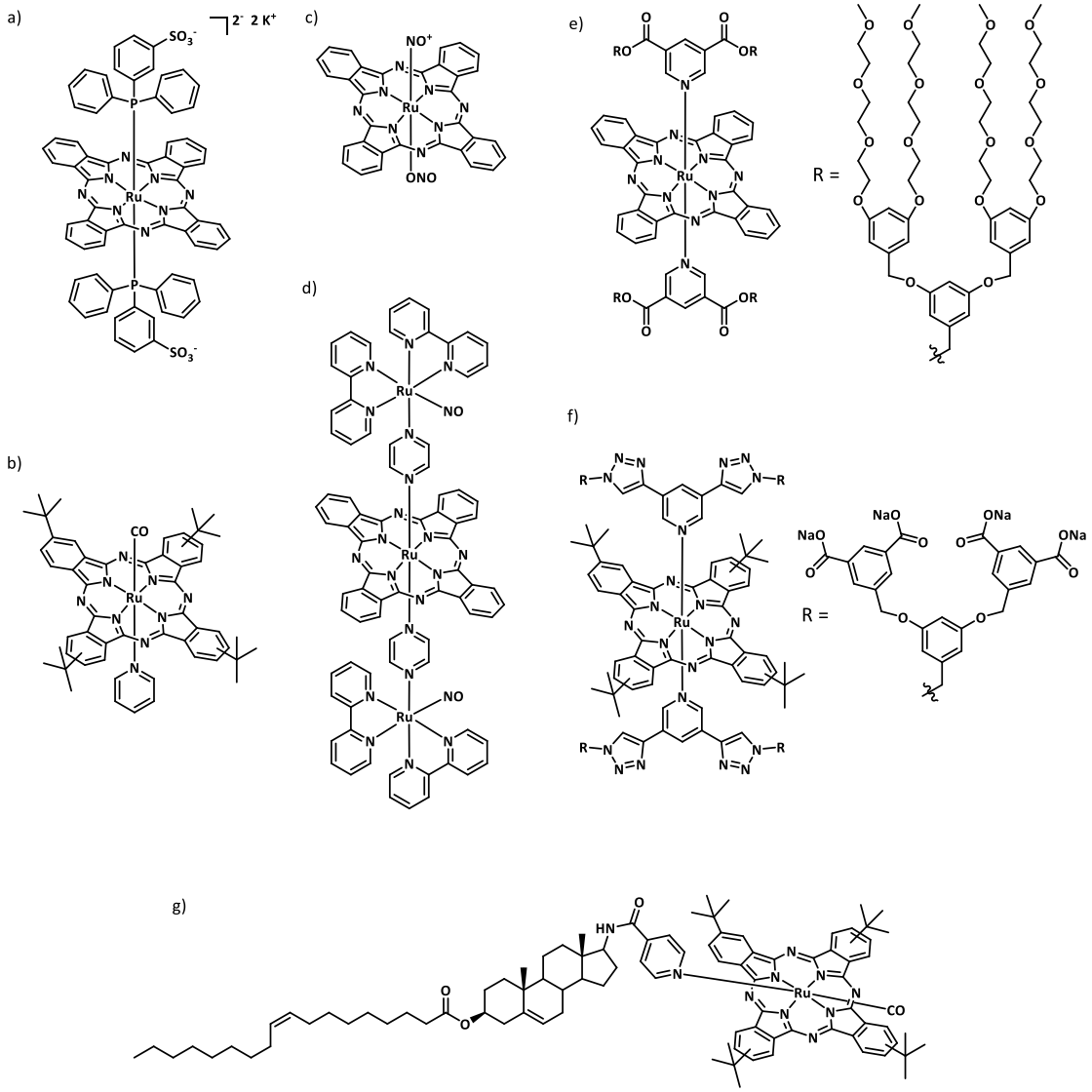

Figure 19 – Examples of RuPcs used as photosensitizers for PDT.

General Objectives

The main aim of this thesis is the synthesis of Pcs derivatives containing ruthenium (II) as the central ion, with the general formula presented in **Figure 20**, to be applied as PSs for PDT. These Pcs will be donated with axial substituents L^1 and L^2 able to efficiently reduce Pc self-aggregation in solution and confer other properties that should enhance the potential of Pcs as photosensitizers for PDT and/or PDI.

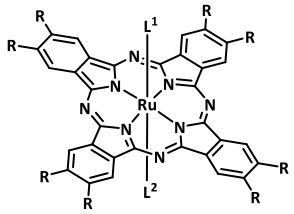

Figure 20 – General formula of RuPc derivatives.

As mentioned before, the low solubility of Pcs in water is a drawback of these compounds when applied in PDT. We intend to enhance the hydrophilicity of Pcs through introduction of PEG chains at the axial positions of the macrocycles, *via* PEG-functionalized pyridine ligands, which is the main focus of **Chapter 1**. In order to further improve the hydrophilicity of the compounds, some PEG chains containing charged functions will also be incorporated. Besides the axial functionalization of RuPcs, derivatives containing PEG chains at the peripheral β-positions will also be prepared. This will enhance the hydrophilic character of those derivatives and, in addition, will shift the absorption Q-band towards longer wavelengths, thus increasing the penetration depth of the light used in the PDT treatment. Another strategy to red-shift the Q-band is the introduction of a carbonyl group as axial ligand. Therefore, the synthesis of RuPcs bearing one pyridyl unit and a carbonyl group ($L^1 \neq L^2$) as axial ligands will also the assessed.[38,57]

Chapter 2 deals with design and synthesis of RuPcs as third generation PSs, through the conjugation of RuPcs with tumor targeting agents. Therefore, to increase the tumor selectivity of Pcs, RuPcs bearing carbohydrates will be prepared. The carbohydrates will be incorporated at the axial positions of RuPcs through coordination to appropriate pyridine-based ligands. Folic acid (FA), another tumor targeting moiety, will also be introduced as axial ligand of RuPcs, through the synthesis of pyridyl-FA conjugates.

Besides pyridyl ligands, Ru(II) also has affinity to phosphorous based ligands. In **Chapter 3** we intend to use this property of Ru(II) to prepare RuPcs axially functionalized with triphenylphosphine derivatives. These ligands will be endowed with charged functions to confer solubility in water in order to use the final RuPcs as PSs for PDT applications.

In **Chapter 4** the *in vitro* studies of some of the RuPcs prepared in the previous chapters will be described. These studies aim to assess the potential of RuPcs to be used as PSs for cancer PDT. Hence, RuPcs will be evaluated regarding their ability to accumulate inside cancer cells, their dark toxicity and their phototoxic effects.

The specific targets of this thesis are:

1. Preparation of RuPcs without peripheral substituents or substituted at the periphery with polyether chains, bearing PEG-functionalized pyridine units at the axial positions ($L^1 = L^2$).
2. Preparation of RuPcs without peripheral substituents or substituted at the periphery with polyether chains, bearing carbohydrate-functionalized pyridine units at the axial positions ($L^1 = L^2$).
3. Preparation of RuPcs without peripheral substituents or substituted at the periphery with polyether chains, bearing both PEG- and carbohydrate-functionalized pyridine units at the axial positions ($L^1 \neq L^2$).
4. Preparation of RuPcs substituted at the periphery with polyether chains, bearing folic acid-functionalized pyridine units at the axial positions ($L^1 = L^2$).
5. Preparation of RuPcs substituted at the periphery with polyether chains, bearing at the axial positions one functionalized pyridine unit as L^1 and a carbonyl group as L^2.
6. Preparation of RuPcs without substituents at the periphery bearing charged triphenylphosphine units as axial ligands ($L^1 = L^2$).
7. Study of the photophysical properties, aggregation and singlet oxygen generation abilities of the prepared complexes.
8. *In vitro* evaluation of the prepared complexes regarding their uptake by cancer cells, their dark toxicity and their phototoxicity.

Chapter 1 – Design, Synthesis and Characterization of Ruthenium Phthalocyanines Containing Axial PEG Chains to be Applied as Photosensitizers for the Generation of Singlet Oxygen

1.1. Overview

The objectives of this chapter are the preparation of ruthenium phthalocyanines with enhanced solubility in water by introduction of PEG chains at the axial positions through pyridyl ligands. In addition, the hydrophilicity, as well as the position of the Q-band will be further modulated by attaching eight PEG chains at the periphery of the Pc macrocycle.

1.2. Synthesis of Ruthenium Phthalocyanines

The main strategy for the preparation of RuPcs bearing pyridyl substituents at the axial positions consists on the synthesis of RuPcs axially functionalized with nitrile ligands to be used as starting materials for the coordination of pyridine-based ligands. Ru(II) bears a weak association constant with nitrile ligands and, therefore, they can easily be replaced by ligands with a stronger affinity for the Ru(II) atom, such as pyridyl-based ligands (**Scheme 4**). Hence, preparing pyridines substituted with different functional groups allows for a large variety of substituents to be introduced at the axial positions of RuPcs, by direct displacement of the labile nitrile ligands.

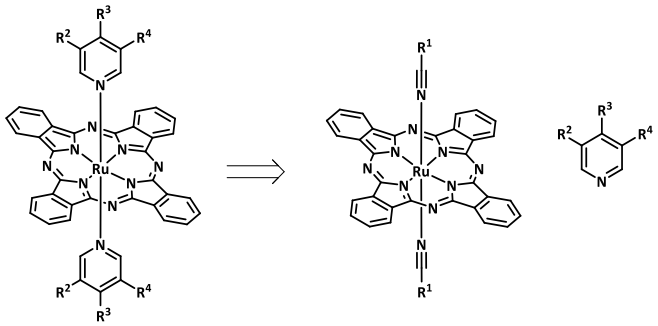

Scheme 4 – Retrosynthesis of RuPcs endowed with pyridyl axial ligands from RuPcs coordinating labile nitrile ligands.

1.2.1. Synthesis of RuPcs coordinating axial nitrile ligands

Two different RuPcs bearing nitrile ligands were prepared for their posterior use for coordination to different pyridine ligands.

An efficient and versatile method for the preparation of RuPcs consists in the metalation reaction of preformed free-base phthalocyanines using $Ru_3(CO)_{12}$. The reaction conditions depend

on the structure of the desired axial ligands, which can be the same (L^1=L^2) or different ones ($L^1 \neq L^2$), one of them being a carbonyl ligand. The introduction of the labile nitrile ligands can either take place during the metalation reaction, using a high boiling point nitrile as solvent, or after the metalation reaction, by replacement of the carbonyl ligand with nitrile substituents.

The preparation of the free base Pc was performed through cyclotetramerization reactions of the corresponding phthalonitrile derivatives, in the presence of lithium alcoholate, which acts both as the metal template and nucleophile, followed by demetallation.

RuPc A was prepared in moderate yield following the procedure described in the literature (**Scheme 5**).[267,268] First, free-base Pc **1** was prepared through the cyclotetramerization of 1,2-dicyanobenzene in pentanol using Li as the template. Subsequently, Pc **1** was refluxed in benzonitrile, in the presence of $Ru_3(CO)_{12}$, to give **RuPc A.** Due to the high insolubility of Pc **1** both in organic and inorganic solvents, no characterization was made for this compound. The structure of **1** was confirmed by the following reaction, with the formation of **RuPc A**, whose structure was confirmed by UV-Vis and ^{1}H NMR spectroscopy**.**

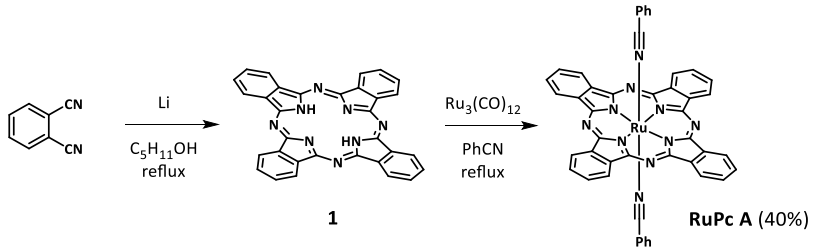

Scheme 5 – Synthesis of **RuPc A**.

In order to increase the solubility in water of the final compounds and also modulate their electronic properties, a RuPc functionalized with triethyleneglycol (TEG) chains at the eight peripheral positions was also prepared. For this purpose, phthalonitrile **5** was prepared according to a reported synthetic procedure (**Scheme 6**),[62,63] which consists in alkylation of dibromocatecol (**3**) with TEG chains using the corresponding tosylate **2**. The resulting PEGylated dibromobenzene **4** was converted into the corresponding phthalonitrile derivative **5** through a cyanation reaction with zinc cyanide in the presence of tetrakis(triphenylphosphine)palladium(0) as a catalyst. All of these compounds were characterized by ^{1}H NMR spectroscopy.

[267] Cammidge, A. N.; Berber, G.; Chambrier, I.; Hough, P. W.; Cook, M. J. *Tetrahedron* **2005**, *61* (16), 4067–4074.

[268] Rodriguez-Morgade, M. S.; Planells, M.; Torres, T.; Ballester, P.; Palomares, E. *J. Mater. Chem.* **2008**, *18*, 176–181.

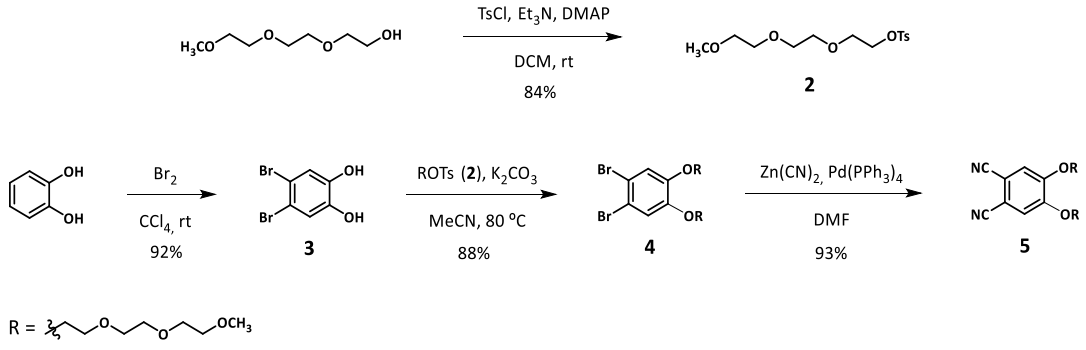

Scheme 6 - Synthesis of phthalonitrile **5**.

The preparation of a Pc bearing eight TEG chains at the peripheral positions was carried out following a reported procedure,[62] consisting in the cyclotetramerization of the phthalonitrile **5** in 1-pentanol, in the presence of lithium carbonate. This leads to the formation of Pc **6** (**Scheme 7**), as a free-base Pc. For the metalation reaction and introduction of nitrile ligands, a different strategy was selected than that used for **RuPc A**. Thus, Pc **6** was metallated with Ru(II) by treatment with $Ru_3(CO)_{12}$ in refluxing phenol affording **RuPc C**.[39] The strongly coordinated carbonyl ligand of **RuPc C** was cleaved upon irradiation in acetonitrile solution, affording **RuPc B**, axially substituted with two acetonitrile ligands, in good yields.[269] The characterization of all of these Pcs was performed by ^{1}H NMR spectroscopy, MS and FT-IR. The latter displays the characteristic strong band of the carbonyl group at 1926 cm^{-1} for **RuPc C**, while the nitrile bands for **RuPc A** and **B** are observed at 2241 and 2921 cm^{-1}, respectively.[38]

[269] Rodriguez-Morgade, M. S.; Athans, A. J.; Carbonell, E.; Miguel, G. De; Guldi, D. M.; Echegoyen, L. *J. Am. Chem. Soc.* **2009**, *131* (30), 10484–10496.

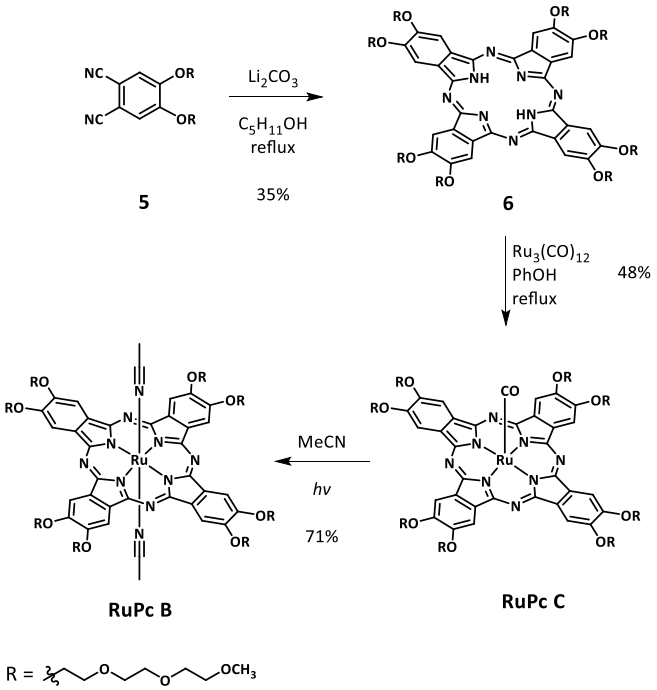

Scheme 7 – Synthesis of **RuPc B**.

1.2.2. Preparation of a reference PS

An unsubstituted RuPc endowed with pyridyl ligands at its axial positions (**RuPc D**) was prepared to be used as a reference compound in photophysical studies. The synthesis of **RuPc D** was performed according to a commonly used methodology,[267,268] i.e., the replacement of the benzonitrile ligands in **RuPc A** by the pyridine units, which bear a higher affinity to ruthenium. For this, **RuPc A** and pyridine were stirred in chloroform at room temperature, in the dark, affording **RuPc D** in 78% yield. The structure of **RuPc D** was confirmed by ^{1}H NMR (see experimental part).

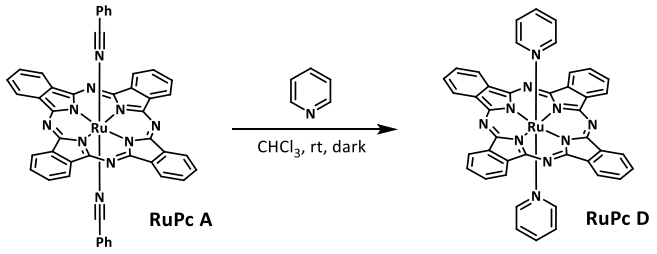

Scheme 8 – Synthesis of **RuPc D**.

1.2.3. Characterization of RuPc precursors by UV-Vis spectroscopy

As mentioned before, a typical UV-Vis absorption spectrum of a Pc displays two bands that arise from $\pi \rightarrow \pi^*$ transitions, one around 620-700 nm (Q-band) and another one around 340 nm (B-band or Soret band). In the particular case of RuPcs, the Q-bands appear as broad features around 620-640 nm, due to the presence of additional bands that lie under the singlet. An additional weak band at 340-385 has been attributed to a charge transfer (CT) from the axial ligand to the Pc ring through the metal.[38,270,271]

The UV-Vis spectra of **RuPcs A**, **B**, **C** and **D** were measured in DMSO (**Figure 21** and **Table 3**), where the characteristic absorption bands of RuPcs can be observed. It is possible to observe the strong influence of axial ligands on the UV-Vis absorption of RuPcs. Upon the replacement of the benzonitrile ligands of **RuPc A** by the pyridine units in **RuPc D**, the Q-band decreases its molar absorptivity to a third, and is shifted to the blue by 17 nm. This is in good agreement with previous reports,[267,268,270,271] where the coordination of axial ligands with increased π-acceptor and reduced σ-donor properties results in a hypsochromic shift of the Q-band. As expected, the PEG-substituted **RuPc B** shows a slight red shift of the Q-band (7 nm) and a considerable decrease (by half) of the molar extinction coefficient. As it is characteristic of RuPcs coordinating carbonyl ligands, **RuPc C** exhibits a blue-shifted Soret band (9 nm) and a red-shifted (4 nm) and more intense Q-band, when compared to **RuPc B**.[38,57]

[270] Stuzhin, P. A.; Vagin, S. I.; Hanack, M. *Inorg. Chem.* **1998**, *37* (11), 2655–2662.

[271] Gorbunova, Y. G.; Enakieva, Y. Y.; Sakharov, S. G.; Tsivadze, A. Y. *Russ. Chem. Bull.* **2004**, *53* (1), 74–79.

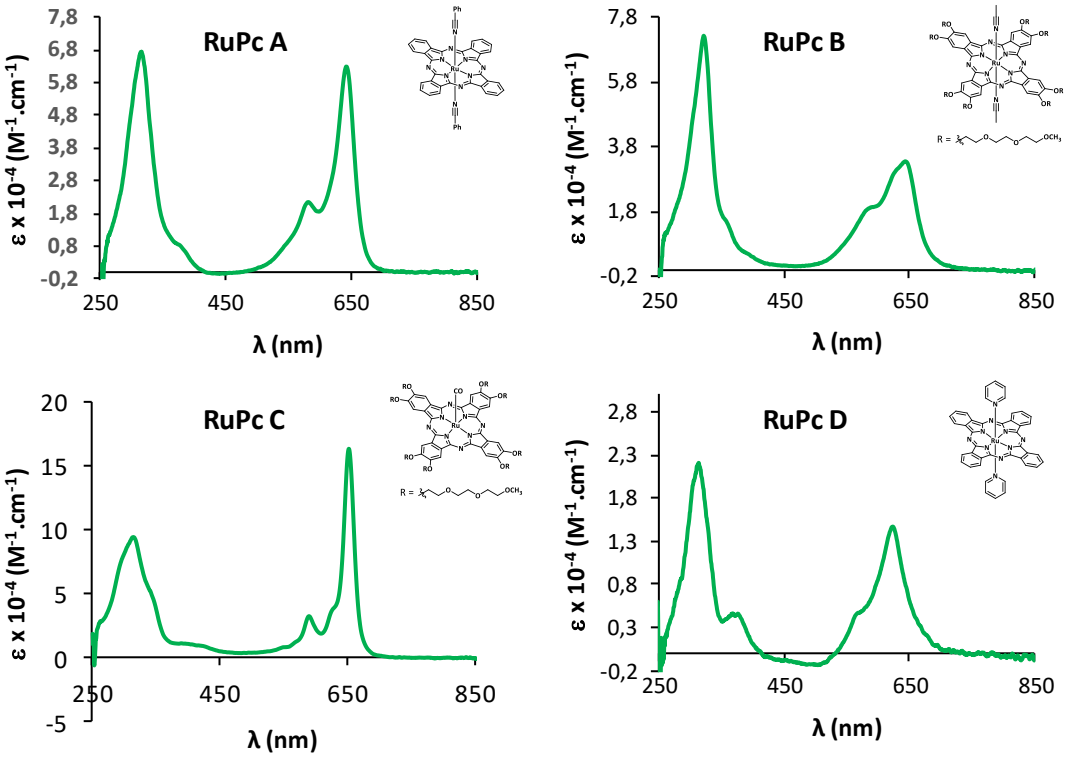

Figure 21 – UV-Vis Spectra in DMSO of RuPcs A, B, C and D.

Table 3 – UV-Vis absorption data in DMSO for **RuPcs A**, **B** and **D**.

RuPc	Absorption maximum, nm (ε x 10^{-4}, $M^{-1}.cm^{-1}$)	
	Soret band	**Q-band**
A	315 (6.77)	642 (6.31)
B	323 (7.20)	649 (3.34)
C	314 (9.45)	653 (16.4)
D	315 (2.22)	625 (1.48)

1.3. RuPcs donated with axial pyridyl ligands functionalized with PEG chains

1.3.1. Synthesis of the pyridyl-based ligands functionalized with PEG chains

The synthesis of pyridine-based ligands functionalized with two polyether chains is depicted in **Scheme 9**. The preparation of ligand **L1**, containing two hydroxyl-terminated PEG chains, was based on a methodology already described.[272] Hence, esterification reaction of pyridine-3,5-carboxilic acid with [2-(2-chloroethoxy)ethoxy]ethanol in DMF in the presence of $CsCO_3$ afforded **L1** in good yields. The structure of **L1** was confirmed by ^{1}H NMR (see experimental part).

Ligand **L2**, bearing terminal amino groups, was also prepared through the esterification of pyridine-3,5-carboxilic acid, this time using 2-[2-(dimethylamino)ethoxy]ethanol in the presence of N-(3-dimehtylaminopropyl)-N'-ethyl-carbodiimide hydrochloride (EDC) as carboxyl activating agent, and dimethylaminopyridine (DMAP) as a catalyst. The characterization of this new ligand was performed by ^{1}H and ^{13}C NMR and FT-IR spectroscopies, as well as MS. **Figure 22** represents the ^{1}H NMR spectrum of **L2**. The pyridyl signals appear as a doublet at 9.37, corresponding to protons H^2 and H^6, and as a triplet at 8.87 ppm, corresponding to protons H^4. The PEG signals appear as a set of four triples, at 4.54, 3.81, 3.62 and 2.52 ppm. Among these peaks, the most deshielded one can be assigned to the $COOCH_2$ unit, while the most shielded one corresponds to the NCH_2 protons, since these are influenced by the different electronegative character of oxygen and nitrogen. Finally, the singlet at 2.26 ppm is attributed to the NCH_3 unit.

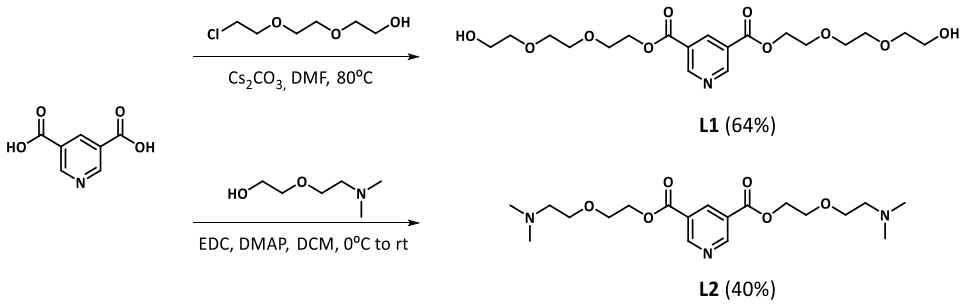

Scheme 9 - Synthesis of ligands **L1** and **L2**.

[272] Gunter, M. J.; Mullen, K. M. *Inorg. Chem.* **2007**, *46* (12), 4876–4886.

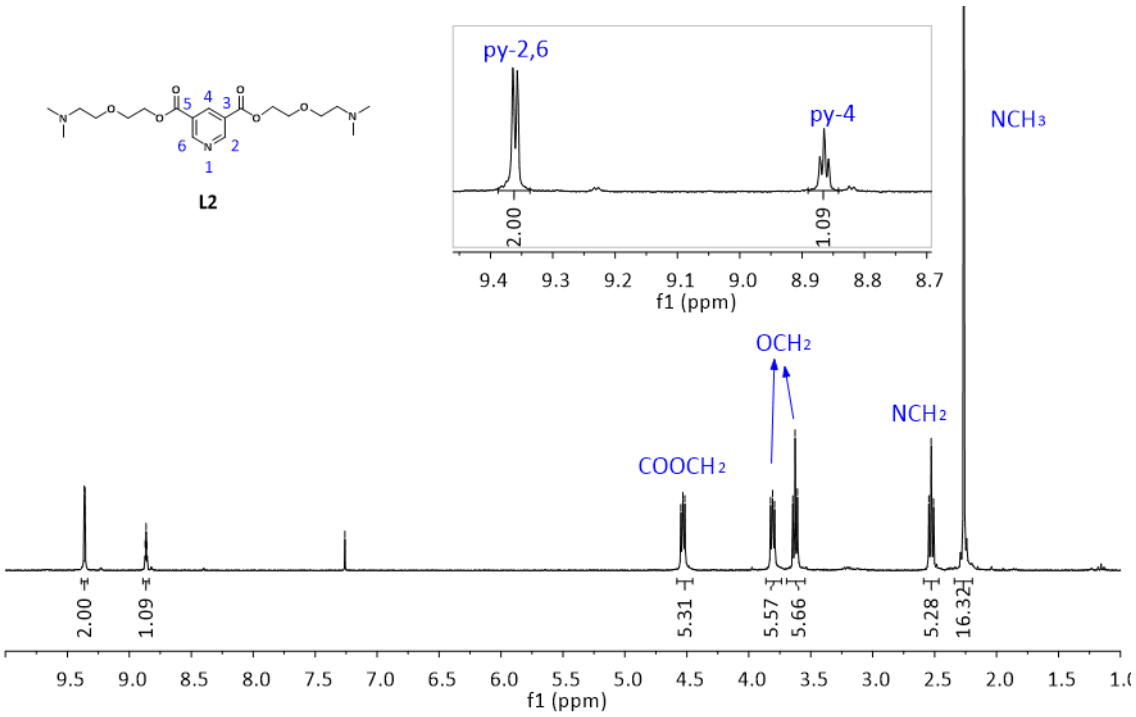

Figure 22 – ^{1}H NMR spectrum in $CDCl_3$ of **L2**.

In order to increase the solubility in water of the final photosensitizers, we designed other pyridyl ligand functionalized with a higher number of PEG chains. Our first target was compound **7** (**Scheme 10**), the synthesis of which was tackled by nucleophilic aromatic substitution of 3,4,5-trichloropyridine with 2-[2-(2-methoxyethoxy)ethoxy]ethanol. Under the conditions depicted in **Scheme 10**, and even using a large excess of nucleophile, the *p*-substituted derivative was the only observed product. In an attempt to force the substitution at the *meta* positions, we tried to activate them by treatment with DMAP and TMSOTf with the purpose of obtaining compound **8.** The latter should show an enhanced reactivity related to that of trichloropyridine.[273] Also in this case, the reaction only afforded the *para* substituted compound (see **Scheme 10**).

[273] Schmidt, A.; Mordhorst, T.; Habeck, T. *Org. Lett.* **2002**, *4* (8), 1375–1377.

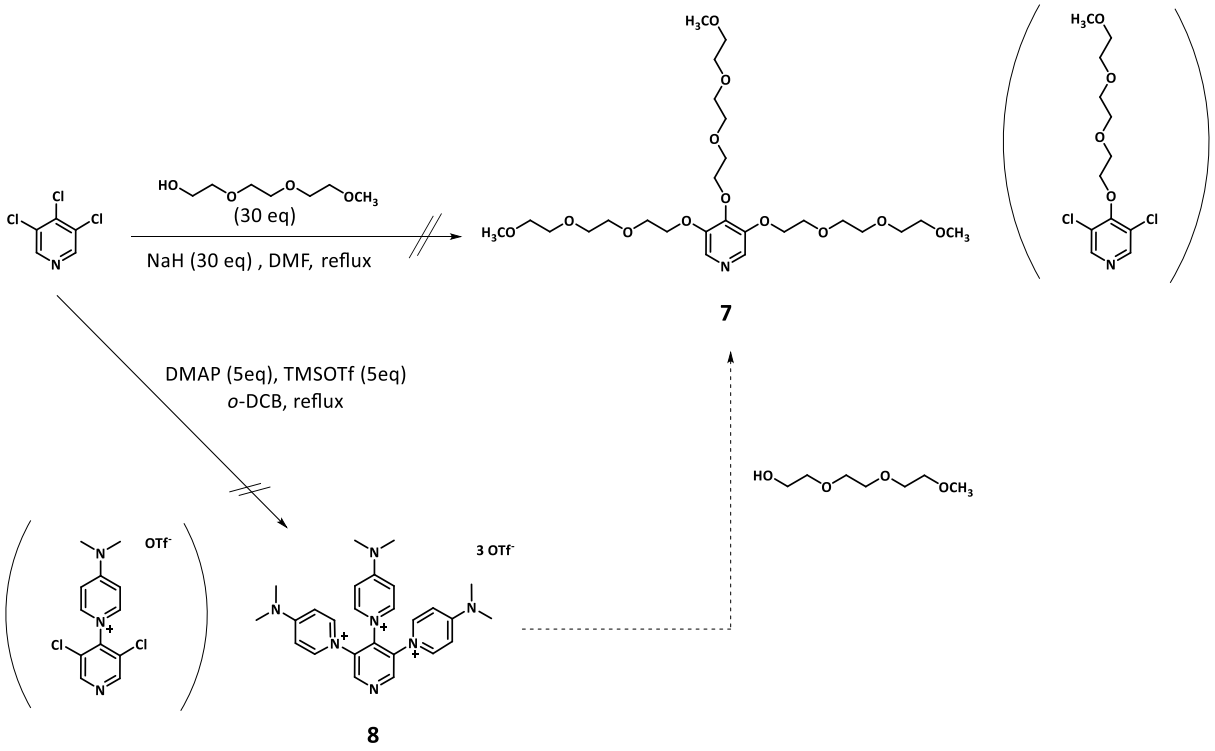

Scheme 10 – Synthetic routes tested for the preparation of ligand **7**. The structures of the obtained *p*-substituted products are depicted in parenthesis.

The synthesis of ligand **L3**, bearing six PEG chains, was accomplished following **Scheme 11**. Starting from galic acid methyl ester, an alkylation reaction with 2-[2-(2-methoxyethoxy)ethoxy]ethanol, followed by a reduction of the ester group using lithium aluminum hydride afforded the alcohol **10**.[274,275] The esterification reaction of alcohol **10** with pyridine-3,5-carboxilic acid in the presence of DCC as carboxyl activating agent and DMAP as catalyst yielded ligand **L3**, functionalized with six PEG chains. The characterization of this new ligand was performed by ^{1}H and ^{13}C NMR spectroscopy, as well as MS. The ^{1}H NMR spectrum of **L3** is represented in **Figure 23**, where the pyridyl signals can be observed at 9.33 and 8.85 ppm. The singlets at 6.65 and 5.26 ppm correspond to aromatic protons, $H^{2'}$ and $H^{6'}$, and to the benzylic protons, respectively. The PEG chains appear as a series of multiplets, with the one at higher field corresponding to the OCH_2 closest to the aromatic ring, $H^{2''}$, since it is placed in the deshielding plane of the benzene unit. Finally, the singlet corresponding to the methyl protons appears at 3.32 ppm. In **Figure 24** the ^{13}C NMR spectrum of **L3** can be observed. The most deshielded signal, at 164.35 ppm, can be assigned

[274] Baars, M. W. P. L.; Kleppinger, R.; Koch, M. H. J.; Yeu, S. L.; Meijer, E. W. *Angew. Chemie - Int. Ed.* **2000**, *39* (7), 1285–1288.

[275] Jonkheijm, P.; Fransen, M.; Schenning, A. P. H. J.; Meijer, E. W. *J. Chem. Soc., Perkin Trans. 2* **2001**, No. 8, 1280–1286.

to the carbonyl function. The seven aromatic signals, corresponding both to the pyridine unit and to the benzene rings, are present between 154.38 and 108.66 ppm. The peak at 106.79 is attributed to the resonance of the benzylic carbon. The methylene carbons of the PEG chains appear as twelve peaks between 72.46 and 65.32 ppm, and the peak at 59.09 ppm corresponds to the methyl carbons.

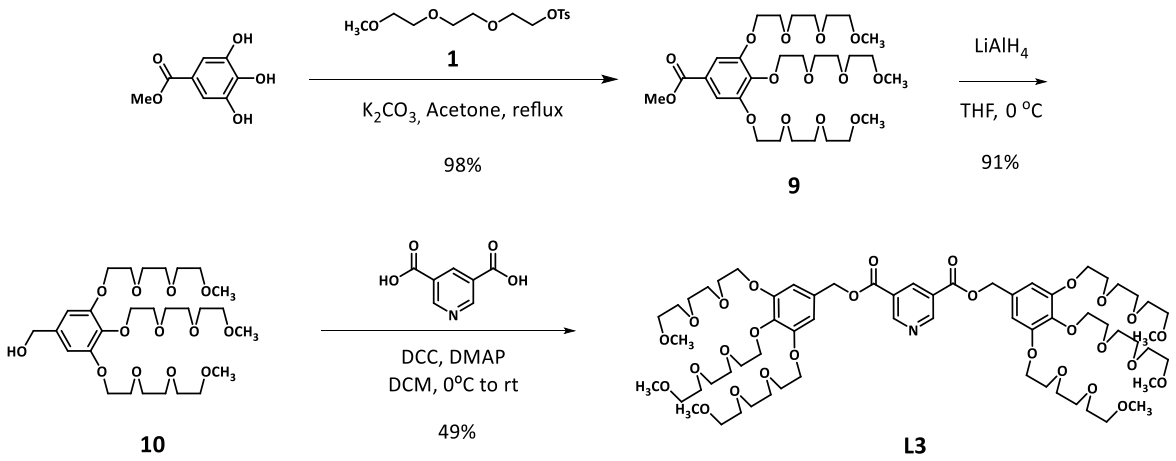

Scheme 11 – Synthesis of **L 32**.

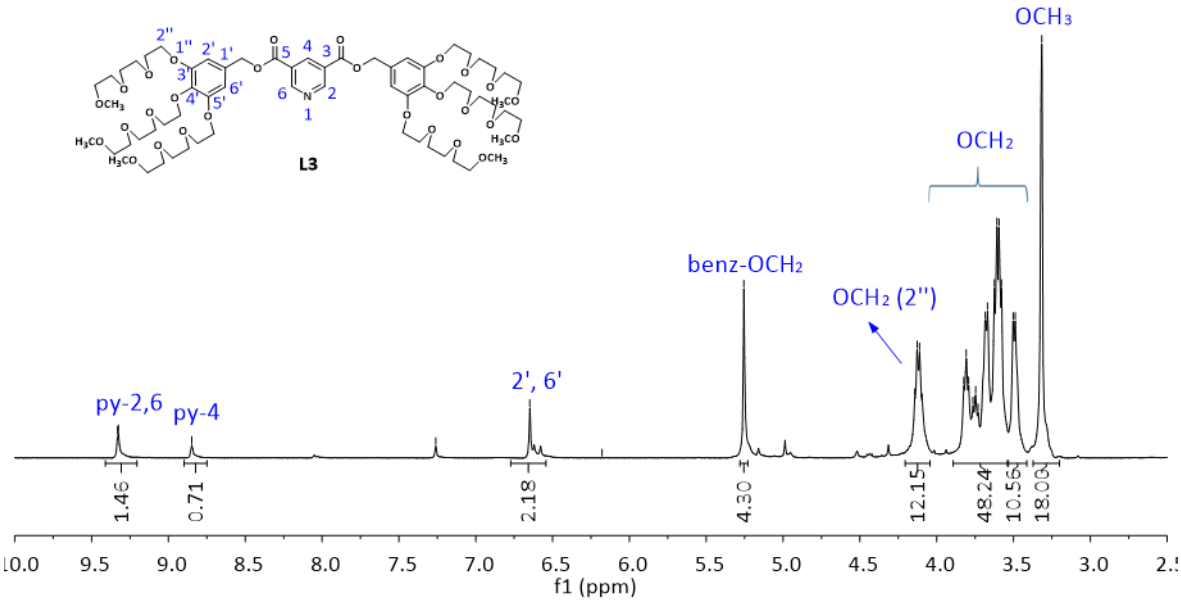

Figure 23 – ^{1}H NMR spectrum in $CDCl_3$ of **L3**.

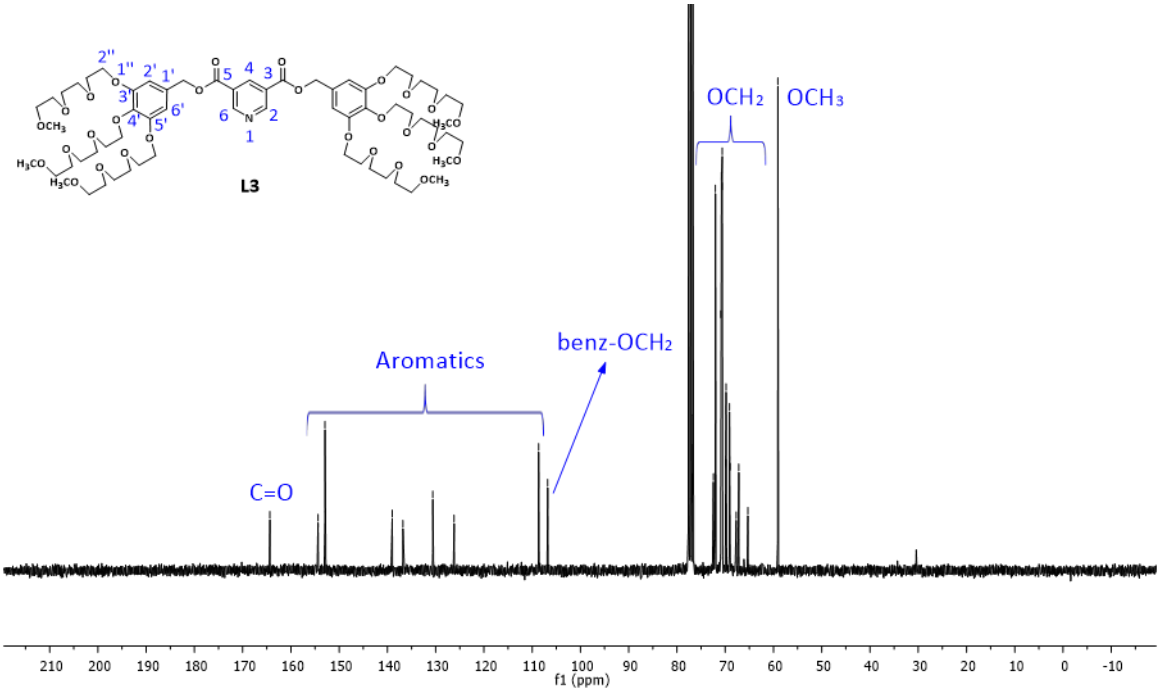

Figure 24 – ^{13}C NMR spectrum in $CDCl_3$ of **L3**.

1.3.2. Coordination reactions to RuPc A and RuPc B

RuPcs endowed with four to twelve PEG chains attached to axial pyridyl ligands were prepared by replacement of the two benzonitrile or acetonitrile ligands of **RuPcs A** or **B**, respectively, with the stronger-ligating **L1**, **L2** and **L3** pyridyl ligands (**Scheme 12**). All these coordination reactions were carried out in $CHCl_3$, at 50 °C and protected from light, using 2.5 equivalents of pyridine ligand per Pc. **PS1** was purified by size exclusion chromatography in BioBeads using THF as the eluent, to remove the excess of ligand, affording the final RuPc in 28% yield. The purification of **PS3** and **PS4** was also carried out by gel permeation chromatography in BioBeads, this time using DCM as eluent. **PS2** was obtained in good yield after precipitation in hexane, since **L2** is soluble in this solvent.

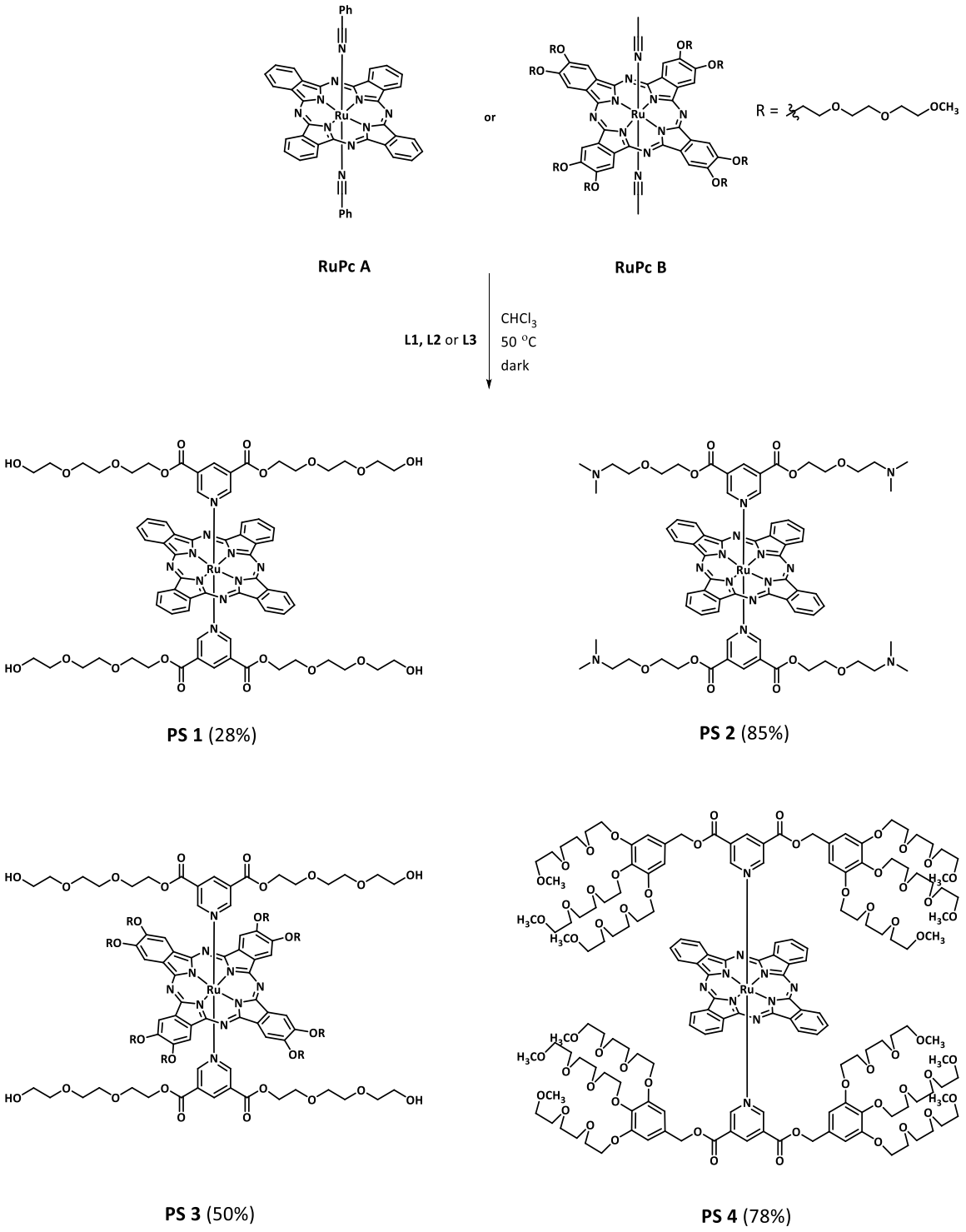

Scheme 12 – Preparation of **PS1-4**.

Once isolated, all complexes **PS1-4** where characterized by ^{1}H and ^{13}C NMR, MS, UV-Vis and FT-IR.

Figure 25 shows the comparative ^{1}H NMR spectra of the starting **RuPc A** and **L1** precursors together with **PS1**. In **PS1-4** the axial ligands are influenced by the diatropic ring current of the Pc, falling on the shielding cone. As a consequence, all the signals corresponding to axial ligands in PS are shifted to high field with respect to the same signals in the spectrum of the non-coordinated ligand. This anisotropic effect is stronger the closer the proton is to the Pc ring. Therefore, the strongest upfield shift should be observed for the H^2 and H^6 pyridyl protons. In particular, **PS1** shows the H^2 and H^6 pyridyl protons at 3.13 ppm, that is, 6.28 ppm upfield shifted with respect to the corresponding proton in ligand **L1**. Moreover, H^4 appears at 7.22 ppm (1.69 upfield shifted), and the signals corresponding to the PEG chain are also shielded, with the closest $COOCH_2$ signal showing an upfield shift of 0.65 ppm.

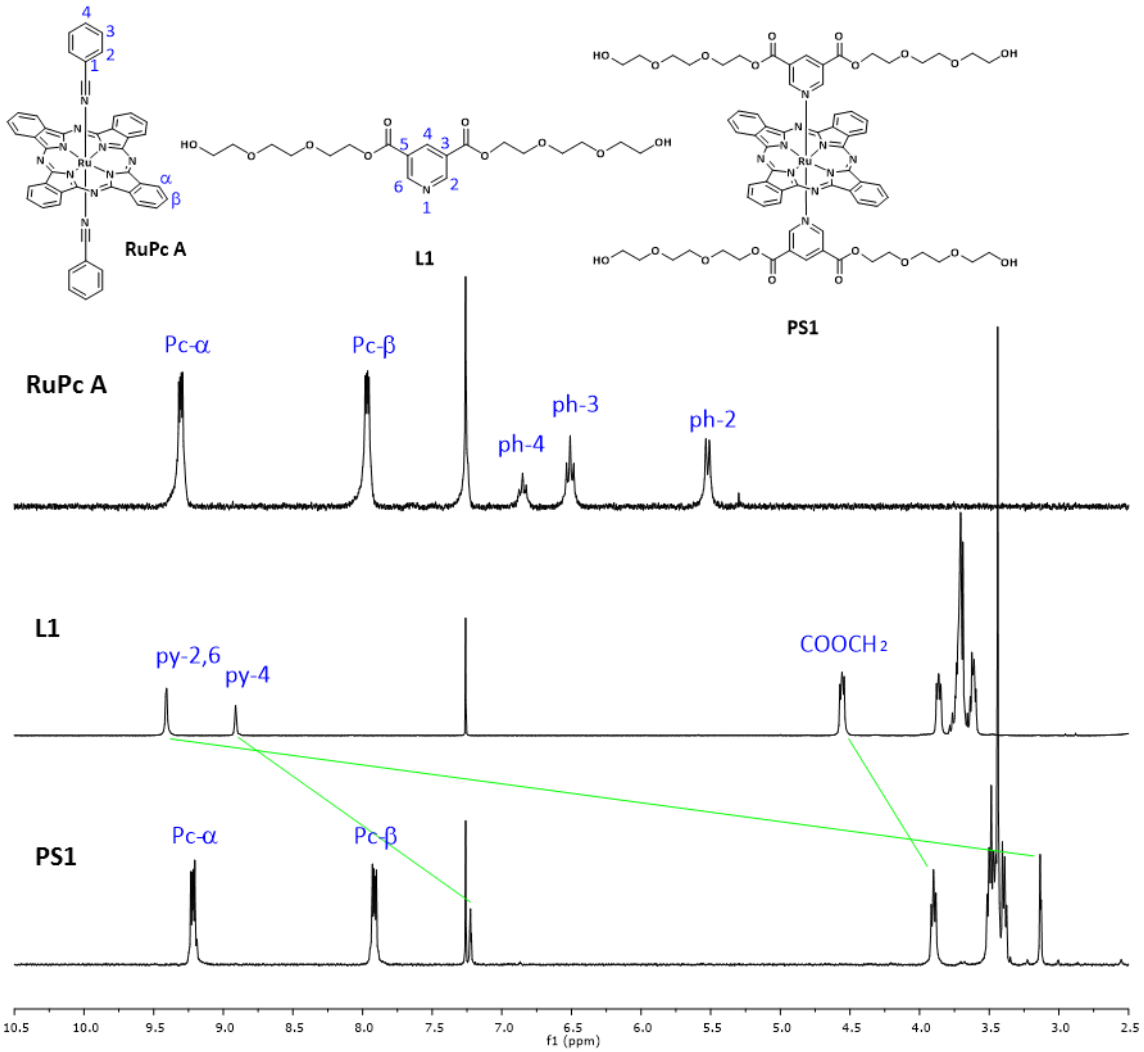

Figure 25 – Comparative ^{1}H NMR spectra in $CDCl_3$ of **RuPc A**, non-coordinated **L1** and **PS1**.

The ^{1}H NMR characterization of **PS2** and **PS4** was carried out following the same considerations as those outlined for **PS1**. In the case of **PS2** (**Figure 26**), the largest chemical shift was shown by the H^{2} and H^{6} pyridyl protons, with an upfield displacement of 6.26 ppm, followed by H^{4} pyridyl protons which were shielded by 1.67 ppm. All the PEG protons also suffered shielding upon coordination to the RuPc, with $COOCH_2$ signal exhibiting an upfield shift of 0.66 ppm and resonances of NCH_2 and NCH_3, which are further apart, being shifted by 0.13 and 0.08 ppm, respectively.

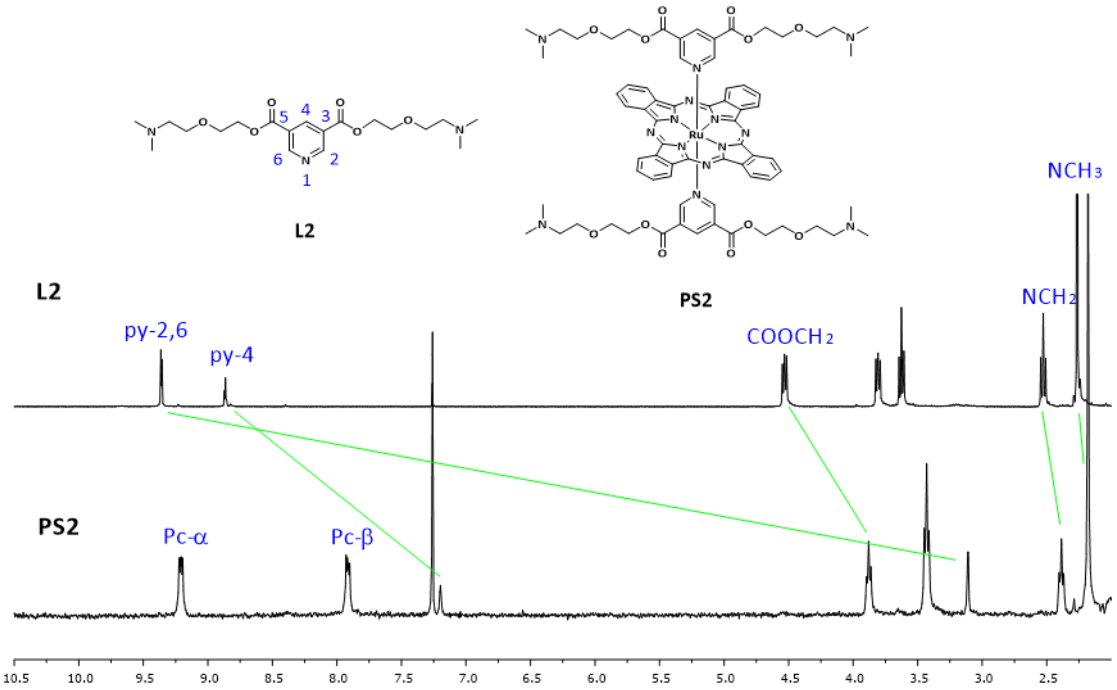

Figure 26 – Comparative ^{1}H NMR spectra in $CDCl_3$ of non-coordinated **L2** and **PS2**.

With respect to **PS4** (**Figure 27**), similar upfield shifts were observed, with a 6.27 ppm shift for H^{2} and H^{6} pyridyl protons and a 1.72 ppm shift for H^{4} pyridyl protons. The resonances of the benzylic protons and of the aromatic $H^{2'}$ and $H^{6'}$ protons experienced shifts of 0.67 and 0.43 ppm, respectively, to higher fields. No shielding was observed for the PEG signals owing to their larger distance to the macrocycle.

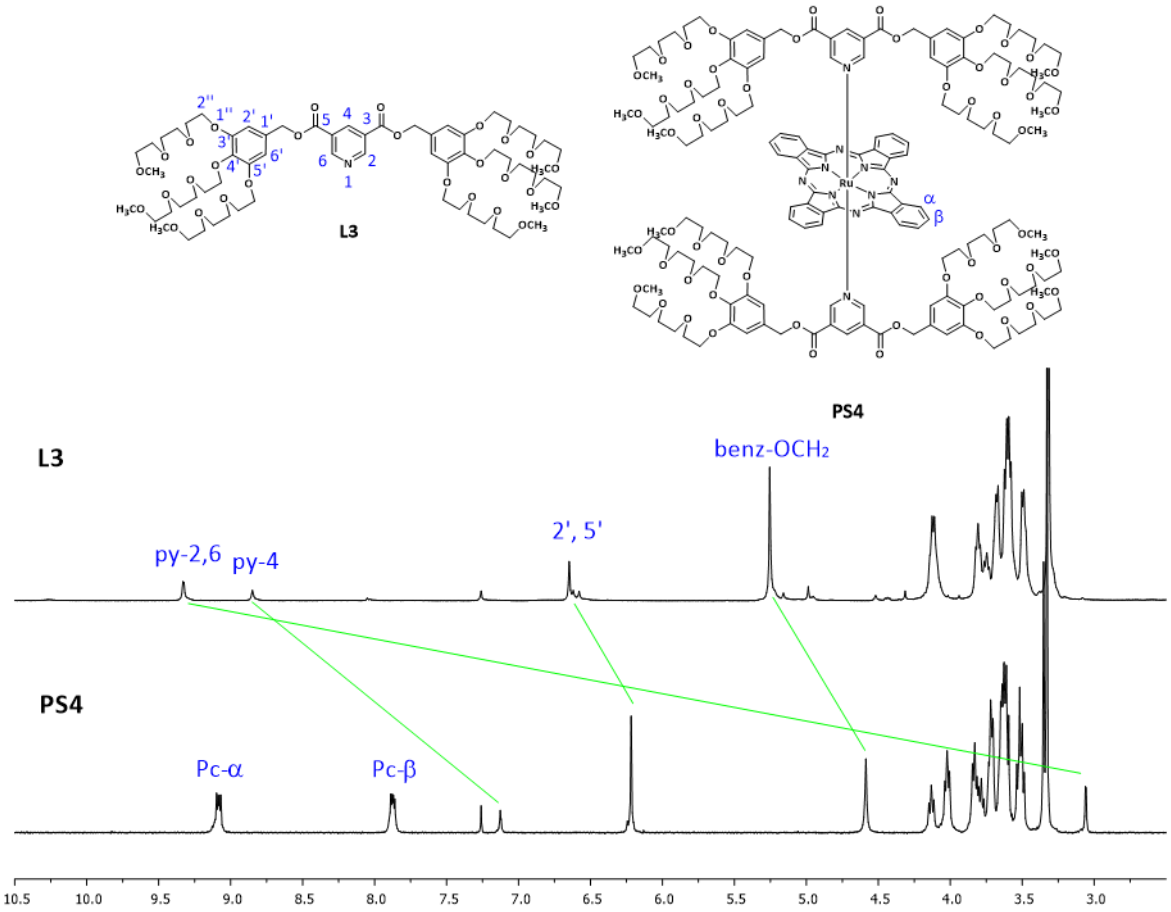

Figure 27 – Comparative ^{1}H NMR spectra in $CDCl_3$ of non-coordinated **L3** and **PS4**.

The ^{1}H NMR spectrum of **PS3** exhibited similar upfield shifted signals as observed before for **PS1, PS2** and **PS4** (**Figure 28**). The pyridyl protons closest to the macrocycle (H^2 and H^6) are shielded by 6.29 ppm, while the H^4 protons only move by 1.71 ppm. As for **PS1**, the TEG chain of the ligand also shows shielded signals, with the $COOCH_2$ protons appearing at δ = 4.69 ppm, that is, 0.61 ppm upfield shifted with respect to the non-coordinated **L1**.

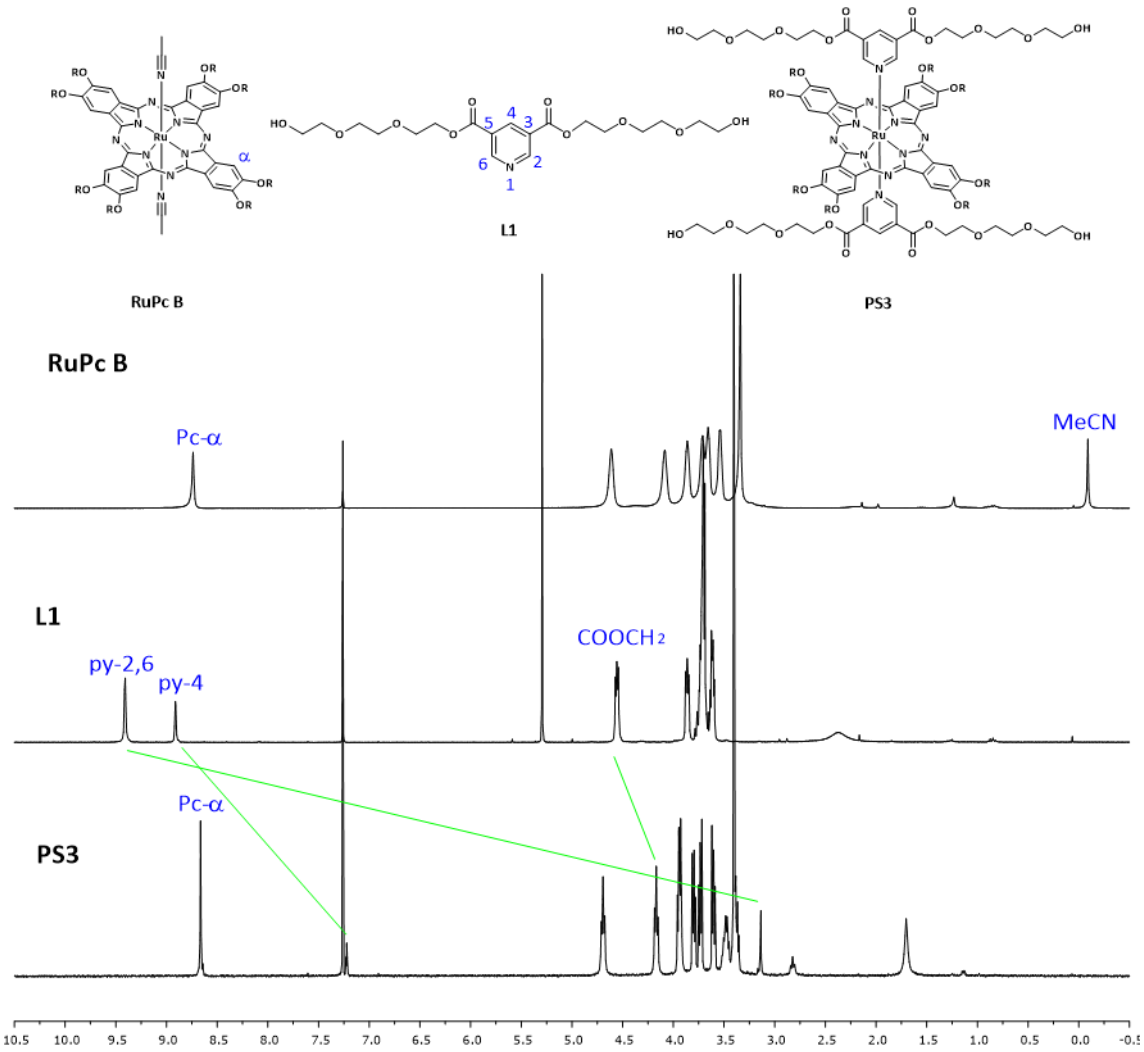

Figure 28 – Comparative ^{1}H NMR spectra in $CDCl_3$ of non-coordinated **L1** and **PS3**.

1.3.3. Synthesis of a tetracationic RuPc bearing PEG chains with terminal ammonium salts

In order to obtain PSs with enhanced solubility in water, ammonium salts were prepared from the corresponding PS containing axial amino functions. The quaternization of the four amino groups of **PS2** was performed by treatment with MeI in DMF (**Scheme 13**). The complete methylation was confirmed by ^{1}H NMR in DMSO-d_6 (**Figure 29**). Hence, the $(CH_3)_3N^+$ protons of **PS2a** appear by 0.86 ppm deshielded with respect to the corresponding amino substituents in **PS2**, as a consequence of the more electron-deficient nitrogen in the ammonium salt. Furthermore, the methylene protons of the ammonium group show a down-field shift of 1.34 ppm.

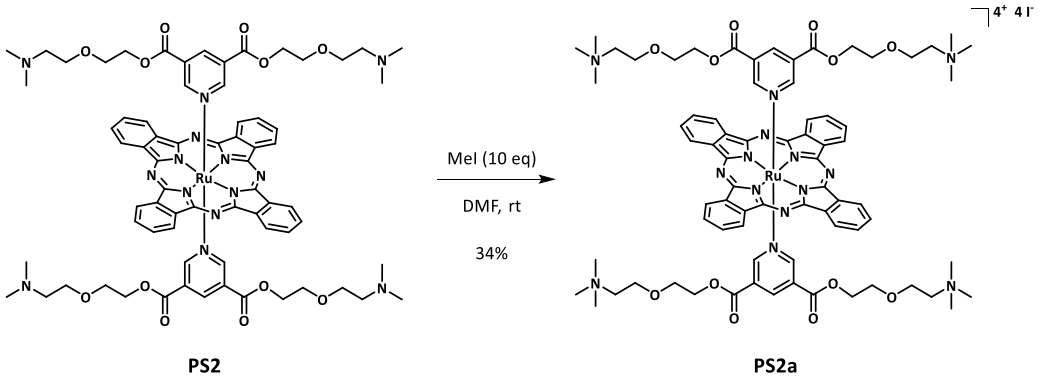

Scheme 13 – Synthesis of **PS2a**.

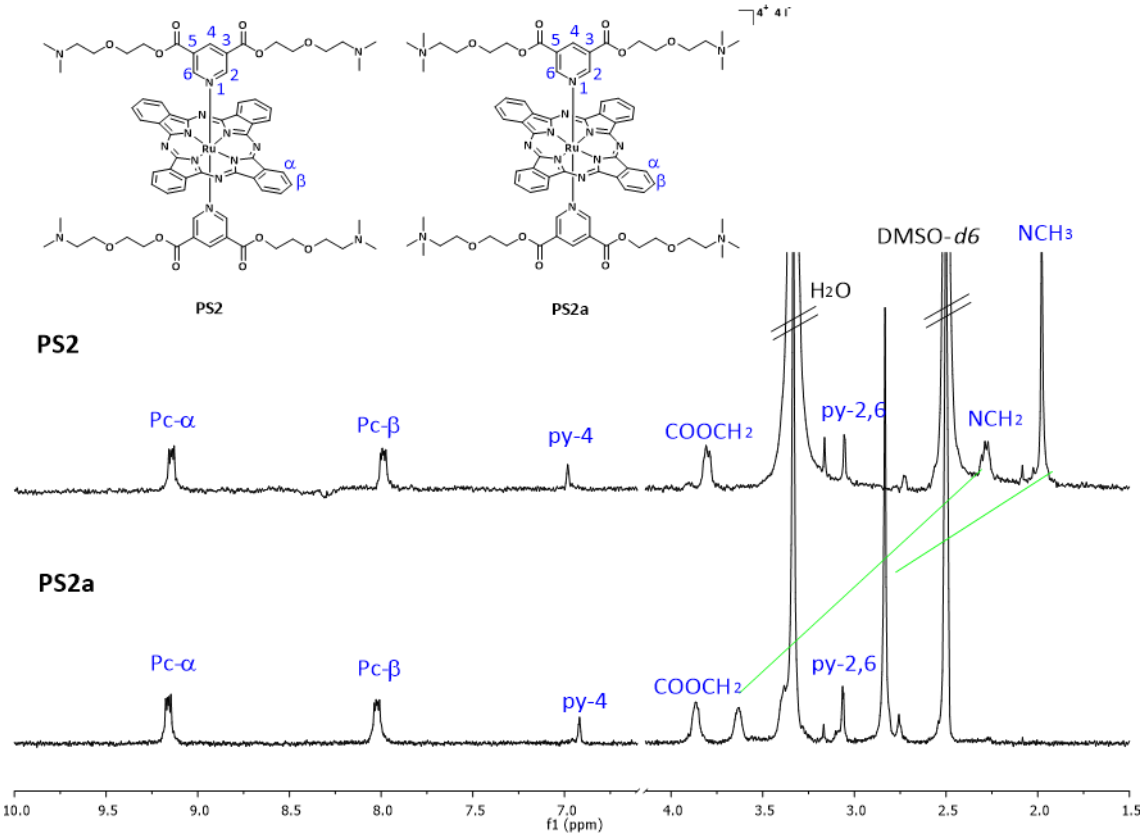

Figure 29 – Comparative ^{1}H NMR spectra in DMSO-d_6 of **PS2** and **PS2a**.

1.3.4. UV-Visible spectra of PSs and aggregation studies

The UV-Vis absorption spectra of **PS1-4** are represented in **Figure 30**. **Table 4** includes the values of Q-band absorption maxima and absorption coefficients (ε).

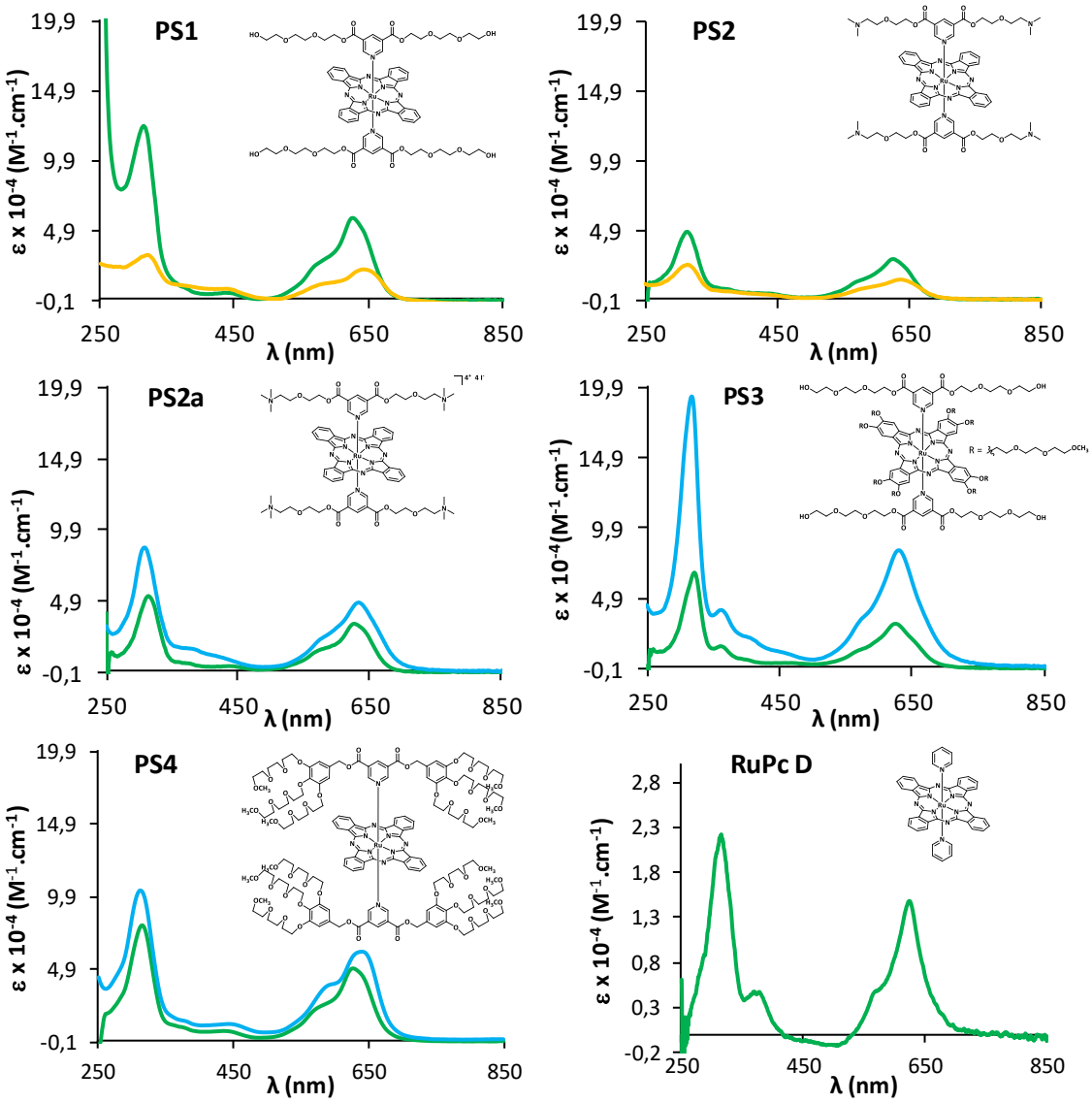

Figure 30 – Absorption spectra of **PS1-4** and **RuPc D** in DMSO (green line), in a 99:1 mixture of H_2O/DMSO (orange line) and H_2O (blue line).

The spectra of **PS2a**, **PS3** and **PS4** were recorded both in DMSO and water. Owing to the lack of solubility of **PS1** and **PS2** in neat water, their spectra were recorded in DMSO and in a 99:1 mixture of H_2O/DMSO. No changes in the position of the Q-band are observed compared to **RuPc D**, suggesting little effect on the electronic properties of the RuPcs upon functionalization of the axial pyridyl ligands. Peripherally unsubstituted **PS1** and **PS2** showed a drastic decrease in their

absorption intensities when the spectra were recorded in the mixture of H_2O and DMSO, related to the spectra recorded in neat DMSO. Since both Soret and Q bands decrease in the same order of magnitude, we believe that this effect arises from partial precipitation of the PS in the solvent mixture. Aggregation species in solution should show a larger decrease of the Q-band in relation to the intensity of the Soret band, a phenomenon that is not observed for any of the prepared PSs.

In order to further evaluate the solubility and aggregation features of these compounds in the 99:1 mixture of H_2O/DMSO, the UV-vis spectra of **PS1** was recorded in concentrations ranging from 0.5 μM to 100 μM (**Figure 31A**). For the verification of the Lamber-Beer law, an analysis of linear regression between the intensity of the Q-band and the concentration of **PS1** was performed. The results show that the Lamber-Beer was fulfilled (**Figure 31B**), with a R^2 value of 0.98 at a concentration up to 50 μM. This assesses the solubility, as well as the lack of aggregation, of **PS1** in this range of concentrations. For more detailed studies on the solubility of **PS1-4**, see Chapter 4, where UV-Vis dilution studies are carried out in a physiologically relevant medium (PBS).

Upon quaternization of the four amino groups (**PS2a**) it was possible to confer solubility in water to the RuPc. Likewise, increasing the number of PEG chains at the axial positions up to twelve (**PS4**), or introducing eight TEG chains at the periphery of the macrocycle (**PS3**) resulted in PSs with enhanced solubility in water. The UV-Vis spectra of **PS2a**, **PS3** and **PS4**, in DMSO and in neat H_2O, are shown in **Figure 30**. All three compounds exhibit higher absorption coefficients in water than in DMSO. We believe that this increase in the absorption coefficient could be produced by partial precipitation of the PSs in DMSO, as a result of the high number of hydrophilic functions of the PSs.

Table 4 – UV-Vis absorption data for **PS1-4** and **RuPc D**.

PS	Q-band maximum, nm (ε x 10^{-4}, $M^{-1}.cm^{-1}$)		
	DMSO	**H_2O/DMSO (99:1)**	**H_2O**
1	625 (5.81)	641 (2.73)	
2	625 (2.86)	637 (1.44)	
2a	626 (3.35)		633 (4.79)
3	626 (3.14)		631 (8.31)
4	627 (5.03)		640 (6.09)
RuPc D	625 (1.48)		

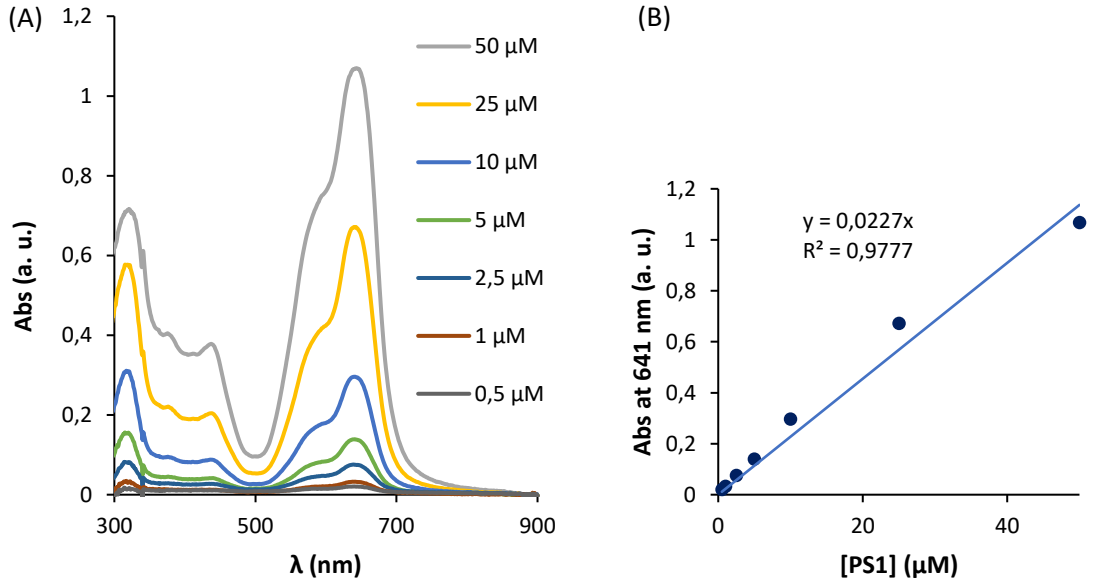

Figure 31 – UV-Vis dilution studies of **PS1** a 99:1 mixture of H_2O/DMSO.

1.3.5. Photostability studies

It is known that, when irradiated with visible light, chromophores are chemically modified or even degraded. This phenomenon is commonly referred as photobleaching, which consists in the loss of absorption or emission intensity caused by light. There are two different types of photobleaching processes arising from a chemical change in the dye: *(i)* photomodification, characterized by modification of the molecular skeleton or side groups of the chromophore with concomitant loss of absorption or emission at some wavelengths and appearance of new absorption bands; and *(ii)* true photobleaching or photodegradation, which results in splitting of the PS into small fragments that no longer absorb visible light (loss of intensity or disappearance of absorption bands), and thus lose their PDT effect.[110,276-278]

Several photochemical reactions may be involved in the photobleaching of dyes. These include photoadditions, photocyclizations, electron transfer processes, photoreductions and photooxidations. In PDT, where oxygen is present, the photobleaching process usually comprises photooxidation reactions. In fact, the presence of oxygen accelerates the photobleaching process,

[276] Bonnett, R.; Djelal, B. D.; Hamilton, P. A.; Martinez, G.; Wierrani, F. *J. Photochem. Photobiol. B Biol.* **1999**, *53* (1), 136–143.
[277] Bonnett, R.; Martínez, G. *Tetrahedron* **2001**, *57* (47), 9513–9547.
[278] Kuznetsova, N. A.; Kaliya, O. L. *J. Porphyr. Phthalocyanines* **2012**, *16* (07n08), 705–712.

since the singlet oxygen and other ROS produced upon excitation of the PS may oxidize the PS itself, a process called self-sensitized oxidative photobleaching.[110,276-279]

Photobleaching in PDT presents both advantages and disadvantages. If the PS is present in low levels in tumor tissues, its complete degradation may occur before achieving total tumor ablation. On the other hand, photobleaching may also have benefic effects, in the sense that it allows for destruction of PS localized in normal tissues. In this way, if the amount of PS in healthy tissues is significantly inferior than that present in cancer tissues, it is possible to keep the concentration of PS in normal cells below the threshold levels for photosensitization, while still producing phototoxic effects in tumor cells. Therefore, with an adequate dose of PS, damage to healthy cells can be avoided, even when using high doses of light.[276,280,281] Additionally, photobleaching of PS in normal tissues may allow for a deeper tissue penetration.[281]

Being an important parameter in PDT, the photobleaching of our PSs was evaluated. The experiments were carried out in 5 μM solutions in DMSO. The photostability of the more hydrophilic compounds (**PS2a**, **PS3** and **PS4**) was also measured in DMSO-PBS solutions, where the percentage of DMSO was kept under 0.45%. Compounds were irradiated with red light at a fluence rate of 20 mW/cm^2 at intervals of 10 min for a total of 60 min.

Figure 32 and **Table 5** describe the photostability studies of **PS1-4**. None of the compounds showed new absorption bands, nor changes in the shape of their Q-bands. This means that no photomodification took place.

PS1 and **PS2** do not show photobleaching in DMSO after 60 min of irradiation. With respect to the **PS2a**, **PS3** and **PS4**, all of them showed high photostability in DMSO. However, their photostability was reduced to 12, 63 and 53%, respectively, from the initial absorption in PBS, after 60 min of irradiation. The effect of different solvents on the photobleaching rates of PSs has been reported, with the overall conclusion that photostability is higher in organic solvents than in aqueous solutions.[177,251,276,281,282] This has been attributed to the dielectric constants of solvents, which are lower for most organic compounds than for water, suggesting that higher dielectric constants result in increased photobleaching rates.[281] Another possible explanation may be related to the increased capability of more polar solvents to stabilize polar or dipolar transition states formed during the reaction of singlet oxygen with the chromophore.[276] Cationic **PS2a** showed the

[279] Sinclair, R. S. *Photochem. Photobiol.* **1980**, *31* (6), 627–629.

[280] Mang, T. S.; Dougherty, T. J.; Potter, W. R.; Boyle, D. G.; Somer, S.; Moan, J. *Photochem. Photobiol.* **1987**, *45* (4), 501–506.

[281] Spikes, J. D. *Photochem. Photobiol.* **1992**, *55* (6), 797–808.

[282] Çakir, D.; Çakir, V.; Biyiklioğlu, Z.; Durmuş, M.; Kantekin, H. *J. Organomet. Chem.* **2013**, *745–746*, 423–431.

lowest photostability in PBS. The reduced photostability of PSs upon quaternization of amino groups has been observed before.[177,282]

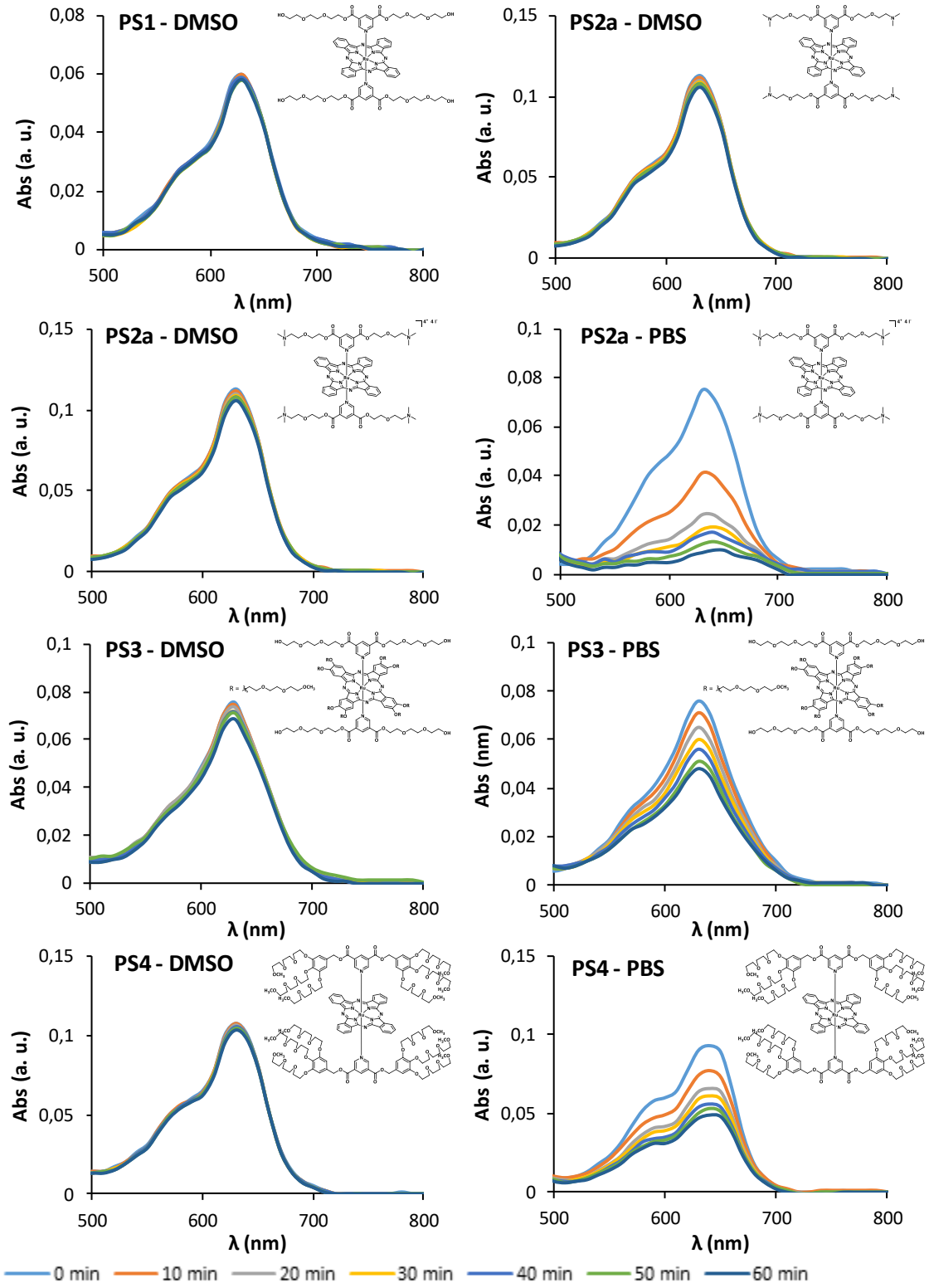

Figure 32 – Photostability of **PS1-4** in 5µM solutions in DMSO (for all PSs) and in PBS (for **PS2a**, **PS3** and **PS4**), after irradiation with red light, at a fluence rate of 20 mW/cm^2, at intervals of 10 min, for a total of 60 min.

Table 5 – Photostability of **PS1-4** in 5μM solutions in DMSO (for all PSs) and in PBS (for **PS2a**, **PS3** and **PS4**), after irradiation with red light, at a fluence rate of 20 mW/cm^2, at intervals of 10 min, for a total of 60 min. Results are given as % related to Abs at t = 0 min.

PS	Solvent	Time (min)						
		0	**10**	**20**	**30**	**40**	**50**	**60**
1	DMSO	100	100	98	98	98	97	97
2	DMSO	100	100	100	100	100	100	100
2a	DMSO	100	99	97	96	96	96	94
	PBS	100	55	32	24	21	16	12
3	DMSO	100	99	97	95	95	93	91
	PBS	100	93	86	79	74	67	63
4	DMSO	100	100	99	98	98	97	96
	PBS	100	83	71	66	60	57	53

1.3.6. Generation of singlet oxygen

The singlet oxygen quantum yields (Φ_Δ) were measured in DMSO following a reported methodology.[114,116] The photoinduced decomposition of 1,3-diphenylisobenzofuran (DPBF), which is an efficient $^1O_2$ quencher in organic media, was followed by UV-Vis spectroscopy after irradiation with a halogen lamp of oxygen saturated solutions of each PS and DPBF. Non-substituted ZnPc was used as the reference compound (Φ_Δ = 0.67 in DMSO).

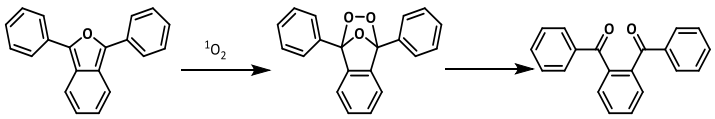

Scheme 14 – Oxidation process of DBPF by singlet oxygen, into *o*-dibenzoylbenzene (DBB).[116,283]

Additionally, singlet oxygen quantum yields (Φ_Δ) were also measured in water for the compounds soluble in water (**PS2a, PS3** and **PS4**). In this case, Eosin Y was used as the reference (Φ_Δ =0.60) and α,α'-(anthracene-9,10-diyl)bimethylmalonate (ADMA) as the scavenger.[116] The experiments were performed in D_2O, in order to increase the extremely short lifetime of $^1O_2$ in H_2O.[284] This is explained by the stronger absorption of H_2O around 1267 nm, which is the wavelength where singlet oxygen emits when decaying to its triplet ground state. Therefore, deactivation of singlet oxygen takes place by energy transfer from this species to water. The

[283] Mayeda, E. A.; Bard, A. J. *J. Am. Chem. Soc.* **1973**, *95* (19), 6223–6226.
[284] Ma, J.; Chen, J. Y.; Idowu, M.; Nyokong, T. *J. Phys. Chem. B* **2008**, *112* (15), 4465–4469.

absorption of D_2O at this wavelength is smaller; thus singlet oxygen shows some stabilization in D_2O compared to H_2O.[251]

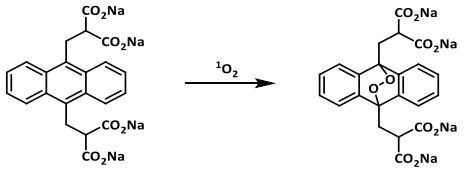

Scheme 15 – Oxidation of ADMA by singlet oxygen.[285]

Singlet oxygen quantum yields (Φ_Δ) were calculated according to the following equation:

$$\phi_\Delta^S = \phi_\Delta^R \frac{k^S I_{aT}^R}{k^R I_{aT}^S}$$

Where k is the slope of a plot of $\ln(A_0/A_t)$ *versus* irradiation time t, with A_0 and A_t being the absorbance of the scavenger at the monitored wavelength (417 nm for DPBF and 379 nm for ADMA) before and after irradiation time t, respectively. *R* and *S* superscripts indicate reference and sample, respectively. I_{aT} is the total amount of light absorbed by the dye and it is given by the sum of intensities of the absorbed light I_a at wavelengths from 530 nm (DMSO) or 455 nm (D_2O) to 800 nm (step 0.5 nm). Light under 530 nm or 455 nm is completely filtered off using a filter, while light above 800 nm is not absorbed by the dye. I_a at a given wavelength is calculated using Beer's law:

$$I_a = I_0(1 - e^{-2.3A})$$

Where I_0 corresponds to the transmittance of the filter at a given wavelength and *A* refers to the absorbance of the dye at that wavelength.

The Φ_Δ values in DMSO for **PS1-4** are described on **Table 6**. **PS1, PS2, PS2a** and **PS4**, unsubstituted at their periphery, exhibited high quantum yields for singlet oxygen generation, between 0.76 and 0.79. However, the introduction of PEG chains at the periphery (**PS3**) resulted in a significant decrease of the efficiency in the production of singlet oxygen (Φ_Δ = 0.20). These results suggest that the presence of π-donor groups at the periphery of the macrocycle reduces the ability of the dye for generation of singlet oxygen. This is in agreement with previous reports, where Pcs

[285] Kuznetsova, N. A.; Gretsova, N. S.; Yuzhakova, O. A.; Negrimovskii, V. M.; Kaliya, O. L.; Luk'yanets, E. A. *Russ. J. Gen. Chem.* **2001**, *71* (1), 36–41.

with peripheral substituents showed lower singlet oxygen quantum yields than the non-substituted derivatives.[28,188,251]

To study the influence of the axial ligands in the ability of RuPcs to generate singlet oxygen, the singlet oxygen quantum yields were also measured for **RuPc D** (**Table 6**). The latter showed a lower Φ_Δ value than **PS1**, **PS2** and **PS4**. We have rationalized these results on the basis of the electron-withdrawing ability of the carboxylic groups connected to the axial pyridyl ligands. This type of functionalization seems to result in an enhanced aptitude to produce singlet oxygen.

Regarding **PS2** and **PS2a**, no significant changes were observed in singlet oxygen quantum yields for these compounds. This is in good agreement with a previous report by Dennis Ng and coworkers, where a SiPc with four tertiary amino groups at axial positions shows similar singlet oxygen efficiency when compared with the cationic counterpart.[178] In contrast to amino groups, ammonium salts are electron acceptors. But in **PS2** and **PS2a** they are situated far away from the Pc core, so no electronic influence on the macrocycle is expected.

With respect to the Φ_Δ values in D_2O, the same trend was observed. Compounds unsubstituted at the periphery (**PS2a** and **PS4**) showed a higher Φ_Δ value when compared to **PS3**. All PSs showed a marked decrease in the Φ_Δ values in D_2O, compared to the Φ_Δ values in DMSO. This is a result of the absorption of D_2O at 1267 nm, as mentioned above. DMSO does not absorb at this wavelength, hence the higher Φ_Δ values in this solvent.[251]

Table 6 - Singlet oxygen quantum yields (Φ_Δ) for **PS1-4** and **RuPc D**.

PS	Φ_Δ	
	DMSO	**D_2O**
1	0.76	
2	0.76	
2a	0.79	0.20
3	0.20	0.06
4	0.77	0.48
RuPc D	0.56	

1.4. Summary and conclusions

In this chapter, pyridine-based ligands designed to confer good solubility in water have been prepared. Their coordination to the axial positions of RuPcs has been accomplished with good yields.

- Studies on the solubility of the compounds showed that Pcs bearing four ammonium salt functions (**PS2a**), twelve axial PEG chains (**PS4**) or eight peripheral PEG chains (**PS3**) are soluble in water. Peripherally unsubstituted RuPcs, (**PS1** and **PS2**) show solubility in 99:1 mixtures of water and DMSO, although they are insoluble in neat water.
- All the RuPcs show good photostability upon irradiation with red light of 20 mw/cm^2 during 60 min.
- All compounds are able to produce singlet oxygen upon light activation. Peripherally unsubstituted **PS1**, **PS2**, **PS2a** and **PS4**, show higher singlet oxygen quantum yields (Φ_Δ values between 0.76 and 0.79 in DMSO) than **PS3**, bearing PEG chains at the periphery (Φ_Δ = 0.20 in DMSO).

1.5. Experimental

1.5.1. General remarks

UV-Vis spectra were recorded with a Jasco V-660 spectrometer. IR spectra were recorded with a Bruker Vector 22 spectrophotometer. EI-MS, MALDI-MS, ESI-MS and FAB-MS spectra were determined on GCT Agilent Technologies 6890N from Waters, Bruker Ultrareflex III, Applied Biosystems QSTAR and VG AutoSpec instruments, respectively. NMR spectra were recorded with a Bruker AV-300 instrument. Column chromatography was performed with Merck 60 (230-400mesh, 60 Å) silica gel and with Biobeads SX-3. Reagents were purchased from Sigma-Aldrich, AlfaAesar and Acros and used without further purification. Solvents were purchased from Carlo Erba Reagents. Anhydrous solvents were dried with molecular sieves of 0.4 nm purchased from Merk.

1.5.2. Synthesis of Ruthenium Phthalocyanines

1.5.2.1. Synthesis of RuPcs coordinating axial nitrile ligands

Ruthenium(bisbenzonitrile)phthalocyanine (RuPc A)[264]

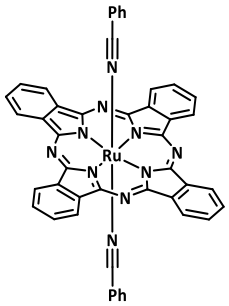

To dry 1-pentanol (10 mL), lithium (140 mg, 20.3 mmol) was added and the mixture was stirred under argon at reflux. When all the lithium was dissolved, 1,2-dicyanobenzene (1g, 7.8 mmol) was added and the reaction mixture was stirred at reflux overnight. The reaction mixture was allowed to reach room temperature and it was poured into 200 mL of a 1:1 mixture of H_2O/MeOH. The resulting suspension was centrifuged and the filtrate was removed. The remaining solid was suspended into a 2:1 mixture of H_2O/MeOH, filtrated and washed with methanol,

acetone, DCM and hexane, to afford the free-base Pc as a dark blue solid. The free-base Pc (100 mg, 0.19 mmol) was dissolved in benzonitrile (5mL) and dodecacarbonyltrisruthenium (270 mg, 0.42 mmol) was added. The reaction mixture was stirred in a sealed tube at reflux for 24 hours. The solvent was evaporated under reduced pressure and the residue was chromatographed on silica gel using a 4:1 mixture of DCM/heptane as the eluent. The blue fraction containing **RuPc A** was evaporated and washed with hexane, affording a blue powder with an overall yield of 40%.

^{1}H NMR (300 MHz, $CDCl_3$) δ_H 9.31 (dd, *J* = 5.6, 3.0 Hz, 8H, Pc-H^{α}), 7.97 (dd, *J* = 5.6, 3.0 Hz, 8H, Pc-H^{β}), 6.85 (t, *J* = 7.6 Hz, 2H, Ar-H^4), 6.51 (t, *J* = 7.3 Hz, 4H, Ar-H^3), 5.52 (d, *J* = 7.3 Hz, 4H, Ar-H^2);
UV-Vis (DMSO) λ_{max} nm (ε x 10^{-4}): 315 (6.77), 642 (6.31).
FT-IR (KBr) ν cm^{-1}: 3057, 2241 (C≡N), 1641, 1489, 1414, 1326, 1288, 1168, 1122, 1065, 980, 754, 736, 628.

2-(2-(2-methoxyethoxy)ethoxy)ethyl-4-methylbenzenosulfonate (2) [286]

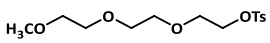

A mixture of 2-(2-(2-methoxyethoxy)ethoxy)ethanol (10g, 60.9 mmol), 4-toluene sulfonyl chloride (14.3g, 74.7 mmol), 7.6g of TEA (74.7 mmol) and a catalytic amount of DMAP in DCM (140 mL) was stirred at room temperature overnight. The resulting solution was transferred to a separatory funnel, washed with diluted HCl (aq) and with $NaHCO_3$ (aq) 0,5M and dried over anhydrous Na_2SO_4. After filtration and evaporation of the solvent, the crude was chromatographed on silica gel using a 4:1 mixture of DCM/heptane as the eluent. The pure product was obtained in 84% yield as a yellow oil.

^{1}H NMR (300 MHz, $CDCl_3$) δ_H 7.79 (d, *J* = 8.3, 2H, Ar-H), 7.33 (d, *J* = 8.0 Hz, 2H, Ar-H), 4.18-4.15 (m, 2H, OCH_2), 3.70-3.67 (m, 2H, OCH_2), 3.63-3.59 (m, 8H, OCH_2), 3.37 (3H, s, OCH_3), 2.45 (3H, s, CH_3).

[286] Li, R.; Ma, P.; Dong, S.; Zhang, X.; Chen, Y.; Li, X.; Jiang, J. *Inorg. Chem.* **2007**, *46* (26), 11397–11404.

4,5-dibromobenzene-1,2-diol (3) [287]

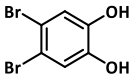

A solution of Br_2 (10g, 0.0625 mol) in CCl_4 (5 mL) was added dropwise to a suspension of benzene-1,2-diol (3.44 g, 0.0313 mol) in CCl_4 (250 mL) at 0 °C. The reaction mixture was stirred overnight at room temperature. The resulting precipitate was filtered and washed with CCl_4 to afford **3** in 92% yield as a white solid.

^{1}H NMR (300Hz, $CDCl_3$) δ_H 7.14 (2H, s).

1,2-dibromo-4,5-bis(2-(2-(2-methoxyethoxy)ethoxy)ethoxy)benzene (4)[286]

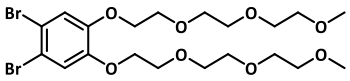

A mixture of **3** (1 g, 3.7 mmol), **2** (4,79 g, 15.0 mmol) and K_2CO_3 (5 g, 36.2 mmol) in acetonitrile (30 mL) was stirred at reflux, under argon, overnight. The resulting precipitate was filtered off and washed with DCM. The solvent of the filtrate was removed under reduced pressure and the residue was chromatographed on silica gel using EtOAc and then a 9:1 mixture of EtOAc/MeOH as the eluent. The pure compound was obtained as a yellow oil in 88% yield.

^{1}H NMR (300 MHz, $CDCl_3$) δ_H 7.13 (2H, s, Ar-H), 4.13 (t, *J* = 5.0 Hz, 4H, OCH_2), 3.84 (t, *J* = 5.0 Hz, 4H, OCH_2), 3.72-3.70 (m, 4H, OCH_2), 3.66-3.62 (m, 8H, OCH_2) 3.55-3.52 (m, 4H, OCH_2), 3.36 (6H, s, OCH_3).

4,5-bis(2-(2-(2-methoxyethoxy)ethoxy)ethoxy)phthalonitrile (5)[288]

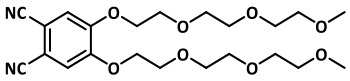

[287] van Nostrum, C. F.; Picken, S. J.; Schouten, A.-J.; Nolte, R. J. M. *J. Am. Chem. Soc.* **1995**, *117* (40), 9957–9965.

[288] Zango, G.; Zirzlmeier, J.; Claessens, C. G.; Clark, T.; Martinez-Diaz, M. V.; Guldi, D. M.; Torres, T. *Chem. Sci.* **2015**, *6* (10), 5571–5577.

A mixture of **4** (500 mg, 0.892 mmol), $Zn(CN)_2$ (230.5 mg, 2.0 mmol) and $Pd(PPh_3)_4$ (206.2 mg, 0.178 mmol) in anhydrous DMF (10 mL) was stirred at reflux, under argon, for 3 hours. The resulting solution was diluted with DCM, transferred to a separatory funnel, washed with water, and dried over anhydrous Na_2SO_4. After filtration and evaporation of the solvent, the crude was chromatographed on silica gel using a 2:1 mixture of EtOAc/Heptane as the eluent. The pure product was obtained as yellow oil in 93% yield.

^{1}H NMR (300 MHz, acetone-d_6) δ_H 7.61 (2H, s, Ar-H), 4.38 (t, J = 4.6 Hz, 4H, OCH_2), 3.89 (t, J = 4.5 Hz, 4H, OCH_2), 3.70-3.66 (m, 4H, OCH_2), 3.61-3.55 (8H, m, OCH_2), 3.47-3.44 (4H, m, OCH_2), 3.28 (6H, s, OCH_3).

2,3,9,10,16,17,23,24-Octakis-(2-(2-(2-mehtoxyethoxy)ethoxy)ethoxy)phthalocyanine (6)[63]

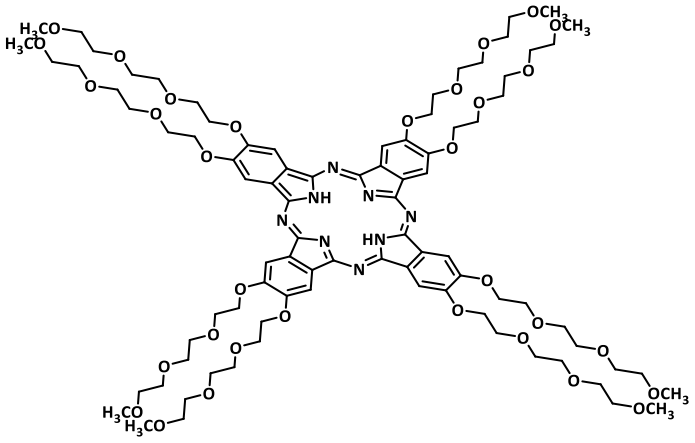

A mixture of **5** (2.16 g, 4.78 mmol) and Li_2CO_3 (1.76 g, 23.9 mmol) in dry 1-pentanol (17 mL) was stirred at reflux, under argon, for 3 days. After removing the solvent under reduced pressure, the residue was dissolved in DCM and filtrated to remove the excess of Li_2CO_3. The filtrate was evaporated under reduced pressure and the residue was chromatographed on silica gel using first a 9:1 mixture of EtOAc/MeOH as the eluent, to remove side products. The green fraction containing **6** was then eluted with a 95:5 mixture of $CHCl_3$/MeOH. After evaporation under reduced pressure, the residue was dissolved in the minimum amount of DCM, hexane was added and the resulting precipitate was filtrated and washed with hexane. The final product was obtained in 35% yield as a green, waxy solid.

^{1}H NMR (300 MHz, $CDCl_3$) δ_H 8.38 (s, 8H, Pc-H$^\alpha$), 4.76-4.72 (m, 16H, OCH_2), 4.29-4.26 (m, 16H, OCH_2), 4.04-4.01 (m, 16H, OCH_2), 3.87-3.83 (m, 16H, OCH_2), 3.77-3.74 (m, 16H, OCH_2), 3.61-3.58 (m, 16H, OCH_2), 3.38 (s, 24H, OCH_3), -2.49 (broad s, 2H, Pc-NH);

MS (MALDI, DCTB) *m/z* 1811.8 (M^+);

UV-Vis (DMSO) λ_{max} nm (ε x 10^{-4}): 349 (11.4), 667 (17.1), 701 (17.5).

2,3,9,10,16,17,23,24-Octakis-(2-(2-(2-mehtoxyethoxy)ethoxy)ethoxy)phthalocyaninato Ruthenium(carbonyl) (RuPc C)

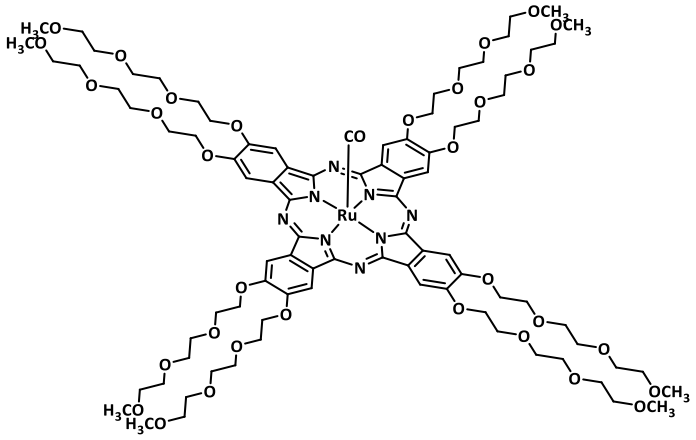

A mixture of **6** (136 mg, 0.075 mmol) and dodecacarbonyltrisruthenium (96 mg, 0.15 mmol) in phenol (8.3 g) was stirred in a sealed tube at reflux, under argon, for 8 hours. The resulting solution was diluted with DCM and transferred to a separatory funnel, washed with an aqueous solution of NaOH and then with water. After evaporation under reduced pressure, the residue was chromatographed on silica gel using a 96:4 mixture of $CHCl_3$/MeOH as the eluent. The fraction containing RuPc C was evaporated under reduced pressure to afford the pure product as a blue, waxy solid in 48% yield.

^{1}H NMR (300 MHz, DMSO-*d_6*) δ_H 8.86 (s, 8H, Pc-H$^\alpha$), 4.72-4.70 (m, 16H, OCH_2), 4.09-4.06 (m, 16H, OCH_2), 3.84-3.80 (m, 16H, OCH_2), 3.70-3.66 (m, 16H, OCH_2), 3.62-3.59 (m, 16H, OCH_2), 3.48-3.45 (m, 16H, OCH_2), 3.24 (s, 24H, OCH_3);

MS (ESI^+, MeOH + 0.1% formic ac.) *m/z* 970.4 $[M + 2H]^{2+}$, 1939.8 $[M + H]^+$;

UV-Vis (DMSO) λ_{max} nm (ε x 10^{-4}): 314 (9.45), 653 (16.4);

FT-IR (KBr) ν *cm^{-1}*: 2917, 1926 (C≡O), 1721, 1607, 1497, 1451, 1405, 1349, 1279, 1199, 1112, 1059, 943, 752, 734.

2,3,9,10,16,17,23,24-Octakis-(2-(2-(2-mehtoxyethoxy)ethoxy)ethoxy)phthalocyaninato Ruthenium(bisacetonitrile) (RuPc B)

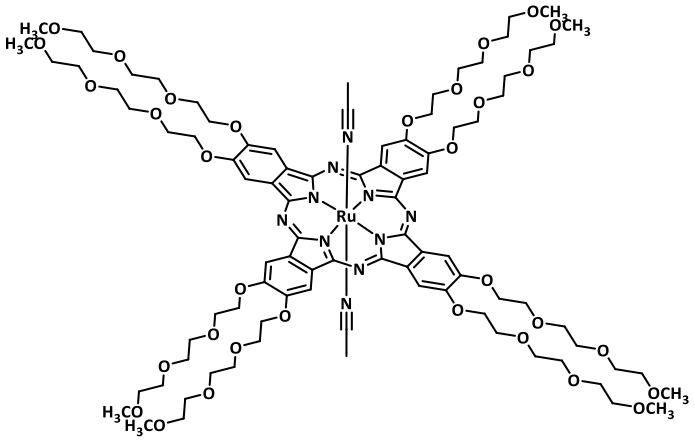

The photochemical cleavage of the carbonyl ligand was carried out in an immersion well apparatus with a Pyrex filter and a 120 W medium-pressure Hg arc lamp. A solution of **RuPc C** (135 mg, 0.070 mmol) in acetonitrile (300 mL) was purged for 1 h with argon and irradiated under a positive pressure of argon for 1 h. The reaction course was monitored by TLC. After completion, the solvent was evaporated under reduced pressure and the residue was washed with MeOH and filtrated to afford **RuPc B** in 71% yield as a dark blue, waxy solid.

^{1}H NMR (300 MHz, $CDCl_3$) δ_H 8.74 (8H, s, Pc-H$^{\alpha}$), 4.61 (m broad signal, 16H, OCH_2), 4.08 (m broad signal, 16H, OCH_2), 3.86 (m broad signal, 16H, OCH_2), 3.71 (m broad signal, 16H, OCH_2), 3.66 (m broad signal, 16H, OCH_2), 3.55 (m broad signal, 16H, OCH_2), 3.34 (s, 24H, OCH_3), -0.09 (6H, s, CH_3CN);
MS (ESI^+, MeOH + 0.1% formic ac.) 956.4 $[(M - 2L) + 2H]^{2+}$, 997.4 $[M + 2H]^{2+}$, 1993.8 $[M + H]^+$;
UV-Vis (DMSO) λ_{max} nm (ε x 10^{-4}): 323 (7.20), 649 (3.34);
FT-IR (KBr) ν *cm^{-1}*: 3384, 2921(C≡N), 1606, 1496, 1451, 1406, 1350, 1276, 1199, 1111, 1066, 945, 853, 755.

1.5.2.2. Preparation of a reference PS

Ruthenium(bispyridine)phthalocyanine (RuPc D)

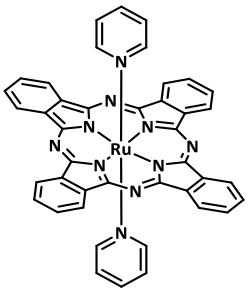

The synthesis was accomplished following a reported methodology.[267,268] To a solution of **RuPc A** (10 mg, 0.012 mmol) in $CHCl_3$ (3 mL) 2 µL of pyridine (0.025 mmol) were added and the reaction mixture was stirred at room temperature, under argon, in the dark, overnight. The resulting solution was evaporated under reduced pressure and the residue was washed with hexane to afford **RuPc D** in 78% yield as a blue solid.

^{1}H NMR (300 MHz, $CDCl_3$) δ_H 9.15 (dd, *J* = 5.6, 3.0 Hz, 8H, Pc-H$^{\alpha}$), 7.89 (dd, *J* = 5.6, 3.0 Hz, 8H, Pc-H$^{\beta}$), 6.04 (t, *J* = 7.4 Hz, 2H, py-Ar-H^4), 5.23 (t, *J* = 7.1 Hz, 4H, py-Ar-H^{3,5}), 2.45 (d, *J* = 5.2 Hz, 4H, py-Ar-H^{2,6}); **UV-Vis** (DMSO) λ_{max} nm (ε x 10^{-4}): 315 (2.22), 625 (1.48).

1.5.3. RuPcs donated with axial pyridyl ligands functionalized with PEG chains

1.5.3.4. Synthesis of the pyridyl-based ligands functionalized with PEG chains

Pyridine-3,5-dicarboxylic acid bis-(2-(2-(hydroxyethoxy)ethoxy)ethyl) ester (L1)[272]

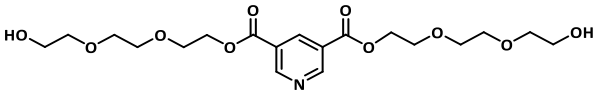

3,5-Pyridinedicarboxylic acid (1 g, 6mmol) and Cs_2CO_3 (1.9 g, 6mmol) were dissolved in the minimum amount of water and the solvent was evaporated under reduced pressure. After drying the residue at 50 °C at 1 mmHg, 2-[2-(2-chloro-ethoxy)-ethoxy]-ethanol (2.02g, 12 mmol) and dry

DMF (50 ml) were added and the reaction mixture was stirred at 80 °C, under argon, for 5 days. The resulting solution was evaporated under reduced pressure and the residue was dissolved in DCM, transferred to a separatory funnel, washed with water and dried over anhydrous Na_2SO_4. After filtration and evaporation of the solvent, the crude was chromatographed on silica gel using a 9:1 mixture of DCM/MeOH as the eluent. The fraction containing **L1** was evaporated under reduced pressure to afford the pure compound in 64% yield as a yellow oil.

^{1}H NMR (300 MHz, $CDCl_3$) δ_H 9.42 (d, *J* = 2.0 Hz, 2H, py Ar-$H^{2,6}$), 8.93 (t, *J* = 2.0 Hz, 1H, py Ar-H^4), 4.56 (t, *J* = 4.5 Hz, 4H, OCH_2), 3.86 (t, *J* = 4.5 Hz, 4H, OCH_2), 3.74-3.69 (m, 12H, OCH_2), 3.64-3.60 (m, 4H, OCH_2).

Pyridine-3,5-dicarboxylic acid bis-(2-(2-(dimethylamine)ethoxy)ethyl) ester (L2).

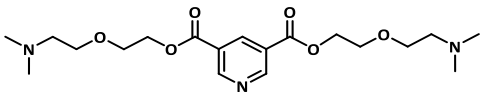

To a mixture of pyridine-3,5-dicarboxylic acid (1 g, 6 mmol), 2-[2-(dimethylamino)ethoxy]ethanol (1.75 g, 13.2 mmol) and DMAP (146.6 mg, 1.2 mmol) in DCM (40 mL) at 0˚C, EDC (2.53g, 13.2 mmol) was added and the reaction mixture was stirred at 0˚C under argon for one hour. The mixture was allowed to reach room temperature and then, was stirred for two days at this temperature. The resulting solution was transferred to a separatory funnel, washed with water, and dried over anhydrous Na_2SO_4. After filtration and evaporation of the solvent, the crude was chromatographed on silica gel using a 89:10:1 mixture of THF/MeOH/TEA (triethylamine) as the eluent. The fraction containing **L2** was redissolved in DCM and washed with water to remove the remaining TEA, affording **L2** in 40% yield as a yellow oil.

^{1}H NMR (300 MHz, $CDCl_3$) δ_H 9.37 (d, *J* = 2.1, 2H, py Ar-$H^{2,6}$), 8.87 (t, *J* = 2.1, 1H, py Ar-H^4), 4.54 (t, *J* = 4.9 Hz, 4H, $COOCH_2$), 3.81 (t, *J* = 4.8 Hz, 4H, OCH_2), 3.62 (t, *J* = 5.7 Hz, 4H, OCH_2), 2.52 (t, *J* = 5.7 Hz, 4H, NCH_2), 2.26 (s, 12H, NCH_3);
^{13}C NMR (75.5 MHz, $CDCl_3$) δ_C 164.35, 154.27, 138.09, 125.97, 69.39, 68.71, 64.72, 58.72, 45.80;
MS (FAB^+, m-NBA) *m/z* 398.4 $[M + H]^+$;
FT-IR (KBr) ν cm^{-1}: 2946, 2866, 2820, 2770, 1731 (C=O), 1602, 1575, 1455, 1358, 1310, 1238, 1103, 1029, 955, 858, 783, 746, 692, 647, 558.

Methyl 3,4,5-tris(2-(2-(2-methoxyethoxy)ethoxy)ethoxy)benzoate (9)[274]

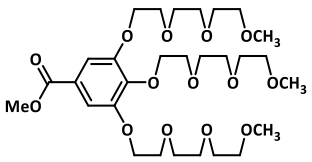

A mixture of trihydroxybenzoate methylester (1.56 g, 8.5 mmol), **2** (9.47 g, 29.7 mmol) and K_2CO_3 (11.75 g, 85.0 mmol in acetone (42 mL) was stirred at reflux, under argon, for 24 hours. The resulting precipitate was filtered off. The filtrate was evaporated under reduced pressure. The residue was dissolved in $CHCl_3$, transferred to a separatory funnel, washed with water, HCl aq. (1M) and water again. The organic phase was dried over anhydrous Na_2SO_4, filtrated and evaporated. The residue was chromatographed on silica gel using a 95:5 mixture of EtOAc/MeOH as the eluent. The fraction containing **9** was evaporated under reduced pressure to afford the pure product in 98% yield as a yellow oil.

^{1}H NMR (300 MHz, $CDCl_3$) δ_H 7.29 (2H, s, Ar-H), 4.23-4.17 (6H, m, OCH_2), 3.88 (3H, s, CO_2CH_3) 3.88-3.84 (4H, m, OCH_2) 3.81-3.77 (2H, t, OCH_2), 3.75-3.69 (6H, m, OCH_2), 3.68-3.61 (12H, m, OCH_2), 3.55-3.51 (6H, m, OCH_2), 3.37 (9H, s, OCH_3).

3,4,5-Tris(2-(2-(2-methoxyethoxy)ethoxy)ethoxy)benzyl alcohol (10)[275]

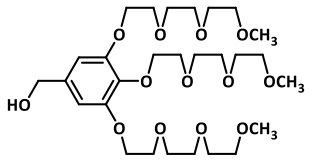

To a suspension of $LiAlH_4$ (2.43 g, 64.0 mmol) in dry THF (7 mL), under argon, at 0 °C, a solution of **9** (4.97 g, 8.0 mmol) in dry THF (29 mL) was added. The reaction mixture was stirred at reflux overnight. The resulting solution was poured into crushed ice and 10 mL of H_2SO_4 aq. (10%) were added. The solution was then transferred to a separatory funnel and extracted with DCM. The organic phase, containing **10**, was dried over anhydrous $MgSO_4$, filtrated and evaporated to afford the pure compound in 91% yield as a yellow oil.

^{1}H NMR (300 MHz, $CDCl_3$) δ_H 6.61 (2H, s, Ar-H), 4.55 (2H, s, CH_2OH), 4.10-4.17 (6H, m, OCH_2), 3.84-3.81 (4H, m, OCH_2), 3.79-3.75 (2H, m, OCH_2), 3.73-3.69 (6H, m, OCH_2), 3.66-3.61 (12H, m, OCH_2), 3.54-3.51 (6H, m, OCH_2), 3.36 (9H, s, OCH_3).

Pyridine-3,5-dicarboxylic acid bis(3,4,5-tris(2-(2-(2-methoxyethoxy)ethoxy)ethoxy)benzyl)ester (11)

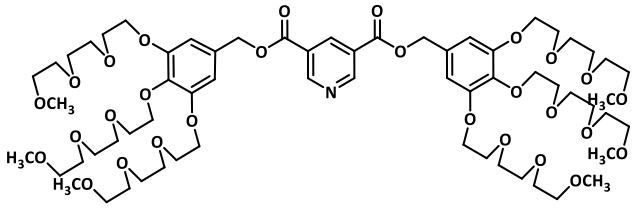

A mixture of 3,5-pyridinedicarboxylic acid (648.7 mg, 3.9 mmol), **10** (4.34 g, 7.3 mmol), DCC (1.51 g, 7.3 mmol) and DMAP (89.2 mg, 0.73 mmol) in dry DCM (50 mL) was stirred at room temperature overnight. The resulting dicyclohexylurea (DCU) was filtered off. The filtrate was transferred to a separatory funnel, washed with water and dried over anhydrous $MgSO_4$. After filtration end evaporation of the solvent, the residue was chromatographed on silica gel using a (2:1) mixture of dioxane/heptane as the eluent. **L3** was obtained as a yellow oil in 49% yield.

^{1}H NMR (300 MHz, $CDCl_3$) δ_H 9.33 (2H, d, *J* = 2.1 Hz, py Ar-$H^{2,6}$), 8.85 (1H, t, *J* = 2.1 Hz, py Ar-H^4), 6.65 (4H, s, Ar-$H^{2',6'}$), 5.26 (4H, s, benz-OCH_2), 4.14-4.09 (12H, m, OCH_2) 3.82-3.79 (8H, m, OCH_2), 3.76-3.73 (4H, m, OCH_2), 3.68-3.67 (12H, m, OCH_2), 3.62-3.58 (24H, m, OCH_2), 3.50-3.49 (12H, m, OCH_2), 3.32 (18H, s, OCH_3);
^{13}C NMR (75.5 MHz, $CDCl_3$) δ_C 164.35, 154.38, 152.93, 139.01, 136.80, 130.59, 126.19, 108.66, 106.79, 72.46, 72.03, 70.91, 70.78, 70.64, 69.93, 69.83, 69.13, 68.99, 67.73, 67.18, 65.32, 59.09;
MS (FAB^+, m-NBA) *m/z* 1320.8 $[M + H]^+$, 1342.8 $[M + Na]^+$.

1.5.3.2. Coordination reactions to RuPc A and RuPc B

*General procedure for the synthesis of **PS1-4**:* **RuPc A** or **RuPc B** (0.08 mmol) and the ligand (**L1-3**) (0.20 mmol) were stirred in $CHCl_3$ at 50 °C, under argon, and protected from light. The reaction was followed by ^{1}H NMR in $CDCl_3$. When the reaction was complete, the solvent was removed under reduced pressure and the residue was treated as indicated below.

PS1

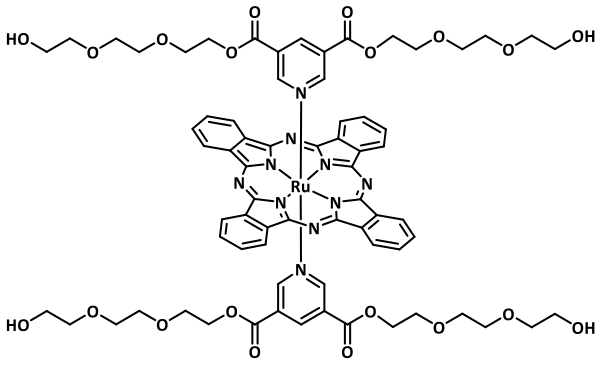

Prepared from **RuPc A** and **L1**. The crude was subjected to size exclusion chromatography on Biobeads using THF as the eluent. The fraction containing **PS1** was precipitated with hexane, affording the pure product in 28% yield as a blue solid.

^{1}H NMR (300 MHz, $CDCl_3$) δ_H 9.22 (dd, *J* = 5.6, 3.0 Hz, 8H, Pc-H^{α}), 7.92 (dd, *J* = 5.6, 3.0 Hz, 8H, Pc-H^{β}), 7.23 (t, *J* = 1.8 Hz, 2H, py Ar-H^4), 3.92-3.88 (m, 8H, OCH_2), 3.52-3.38 (m, 40H, OCH_2), 3.13 (d, *J* = 1.8 Hz, 4H, py Ar-$H^{2,6}$);

^{13}C NMR (75.5 MHz, $CDCl_3$) δ_C 160.95 (C=O), 154.39, 143.95, 140.77, 135.11, 128.37, 125.29, 121.75, 72.50, 70.69, 70.33, 68.40, 64.45, 61.70;

MS (ESI^+) *m/z* 1477.5 $[M + H]^+$;

UV-Vis (DMSO) λ_{max} nm (ε x 10^{-4}): 314 (5.09), 370 (3.97), 625 (5.81);

FT-IR (KBr) ν cm^{-1}: 3421 (OH), 2917, 1741 (C=O), 1601, 1489, 1413, 1324, 1288, 1249, 1169, 1123, 1065, 913, 779, 754, 573.

PS2

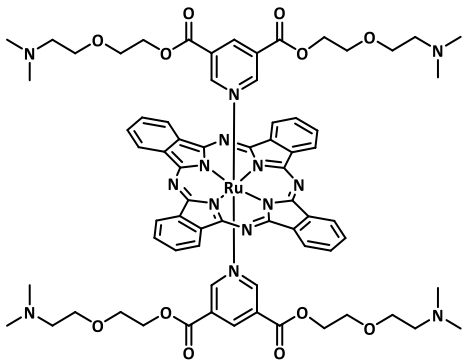

Prepared from **RuPc A** and **L2**. The crude was suspended in hexane and filtrated, affording **PS2** in 85% yield, as a blue solid.

^{1}H NMR (300 MHz, $CDCl_3$) δ_H 9.21 (dd, *J* = 5.6, 3.0 Hz, 8H, Pc-H$^{\alpha}$), 7.92 (dd, *J* = 5.6, 3.0 Hz, 8H, Pc-H$^{\beta}$), 7.20 (t, *J* = 1.8 Hz, 2H, py Ar-H^4), 3.88 (t, *J* = 5.4 Hz, 8H, $COOCH_2$), 3.43 (t, *J* = 5.5 Hz, 16H, OCH_2), 3.11 (d, *J* = 1.8 Hz, 4H, py Ar-H^{2,6}), 2.39 (t, *J* = 5.4 Hz, 8H, NCH_2), 2.18 (s, 24H, NCH_3);
^{13}C NMR (75.5 MHz, $CDCl_3$) δ_C 160.98 (C=O), 154.54, 144.01, 140.93, 135.07, 128.45, 125.36, 121.78, 69.25, 68.25, 64.41, 58.78, 45.86;
MS (ESI$^+$) *m/z* 614.1 [(M – 2L) + H]$^+$, 1011.3 [(M – L) + H]$^+$, 1408.5 [M + H]$^+$;
UV-Vis (DMSO) λ_{max} nm (ε x 10^{-4}): 314 (4.68), 374 (3.87), 625 (2.86);
FT-IR (KBr) ν *cm^{-1}*: 2920, 2851, 1740 (C=O), 1610, 1488, 1414, 1241, 1168, 1122, 1066, 778, 754.

PS3

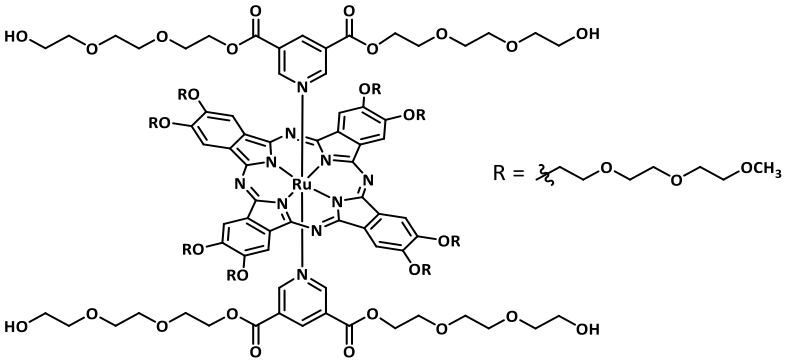

Prepared from **RuPc B** and **L1**. The crude was subjected to size exclusion chromatography on Biobeads using DCM as the eluent. The fraction containing **PS3** was precipitated with hexane, affording the pure product in 50% yield as a blue, waxy solid.

^{1}H NMR (300 MHz, $CDCl_3$) δ_H 8.67 (s, 8H, Pc-H$^{\alpha}$), 7.22 (t, *J* = 1.8 Hz, 2H, py Ar-H^4), 4.69 (t, *J* = 5.1 Hz, 16H, Pc-OCH_2), 4.17 (t, *J* = 5.1 Hz, 16H, Pc-OCH_2), 3.96-3.93 (m, 16H + 8H, Pc-OCH_2 + Py-OCH_2), 3.81-3.78 (16H, m, 16H, Pc-OCH_2), 3.75-3.72 (m, 16H, Pc-OCH_2), 3.62-3.57 (m, 16H, Pc-OCH_2), 3.50-3.45 (m, 8H, Py-OCH_2), 3.40-3.35 (m, 24H + 32H, Pc-OCH_3 + Py-OCH_2), 3.14 (d, *J* = 1.8 Hz, 4H, py Ar-H^{2,6});
^{13}C NMR (75.5 MHz, $CDCl_3$) δ_C 161.13 (C=O), 154.79, 150.42, 143.61, 143.61, 134.56, 106.10, 782.58, 72.12, 71.17, 70.93, 70.74, 70.64, 70.28, 69.99, 69.40, 68.48, 64.49, 61.64, 59.21;

MS (ESI$^+$, MeOH + 0.1% fomic acid) *m/z* 956.4 $[(M - 2L) + 2H]^{2+}$, 1171.9793 $[(M - L) + 2H]^{2+}$, 1387.6 $[M + 2H]^{2+}$, 1911.8 $[(M - 2L)+H]^+$, 2342.3 $[(M - L)+H]^+$, 2774.2 $[M + H]^+$;

UV-Vis (DMSO) λ_{max} nm (ε x 10^{-4}): 322 (6.77), 626 (3.14);

FT-IR (KBr) ν *cm^{-1}*: 3421 (OH), 2874, 1735 (C=O), 1607, 1495, 1451, 1407, 1276, 1199, 1114, 1061, 943, 874, 748.

PS4

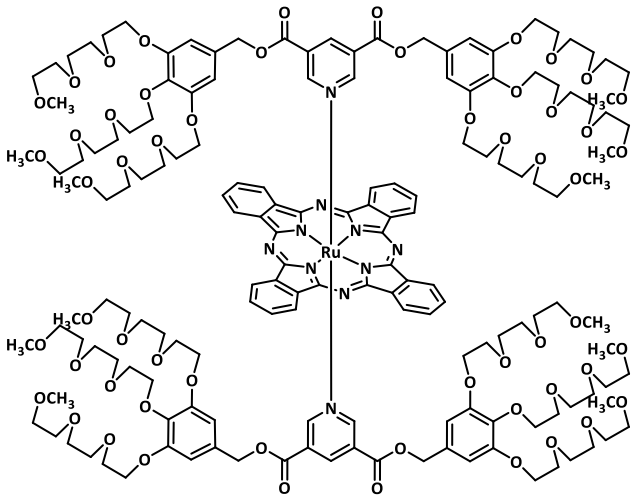

Prepared from **RuPc A** and **L3**. The crude was subjected to size exclusion chromatography on Biobeads using DCM as the eluent. The fraction containing **PS4** was precipitated with hexane, affording the pure compound in 78% yield.

^{1}H NMR (300 MHz, $CDCl_3$) δ_H 9.08 (dd, *J* = 5.6, 3.2 Hz, 8H, Pc-H$^{\alpha}$), 7.87 (dd, *J* = 5.6, 3.2 Hz, 8H, Pc-H$^{\beta}$), 7.13 (t, *J* = 1.7 Hz, 2H, py Ar-H^4), 6.22 (s, 8H, Ar-H$^{2',6'}$), 4.59 (s, 8H, benz-OCH_2), 4.13 (t, *J* = 5.1, 8H, OCH_2), 4.02 (t, *J* = 4.8, 16H, OCH_2), 3.49-3.85 (m, 120H, OCH_2), 3.52 (s, 12H, OCH_3), 3.33 (s, 24H, OCH_3), 3.06 (d, *J* = 1.7, 4H, py Ar-H^{2,6});

^{13}C NMR (75.5 MHZ, $CDCl_3$) δ_C 161.03, 152.75, 143.85, 140.70, 138.98, 129.71, 128.31, 125.21, 121.57, 108.68, 72.47, 72.09, 72.07, 70.97, 70.94, 70.96, 70.67, 69.88, 69.04, 59.15;

MS (ESI$^+$, MeOH + 1%TFA) *m/z* 3255.4 $[M + H]^+$;

UV-Vis (DMSO) λ_{max} nm (ε x 10^{-4}): 314 (7.98), 627 (5.03);

FT-IR (KBr) *v* cm^{-1}: 2872, 1731 (C=O), 1589, 1489, 1438, 1307, 1235, 1120, 948, 849, 781, 740.

1.5.3.3. Synthesis and characterization of a cationic RuPc endowed with axial pyridine ligands functionalized with PEG chains with terminal ammonium salts

PS2a

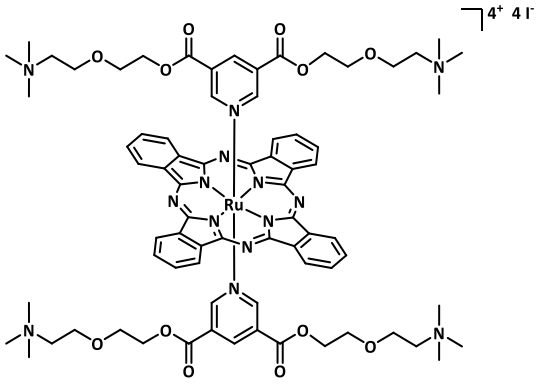

In a sealed tube, a solution of **PS2** (12.7 mg, 0.00902 mmol) in dry DMF (1 mL) was purged with an argon stream. Then, MeI (12.8 mg, 0.0902 mmol) was added and the reaction mixture was stirred at room temperature, in the dark, for 2 hours. The resulting solution was added to MeOH (50 mL) and it was allowed to stand for one hour. All the volatiles were evaporated under reducer pressure and the residue was precipitated with DCM and filtrated to give **PS2a** in 34% yield as a blue powder.

^{1}H NMR (300 MHz, DMSO-d_6) δ_H 9.16 (dd, J = 5.2, 3.4 Hz, 8H, Pc-H$^\alpha$), 8.02 (dd, J = 5.4, 3.2 Hz, 8H, Pc-H$^\beta$), 6.92 (t, J = 1.5 Hz, 2H, py Ar-H), 3.88-3.85 (m, 8H, OCH_2), 3.64-3.62 (m, 8H, NCH_2), 3.41-3.37 (m, 16H, OCH_2), 3.06 (d, J = 1.5 Hz, 4H, py Ar-H), 2.83 (s, 36H, NCH_3);
MS (ESI$^+$, MeOH + 0.1% formic acid) m/z 521.2 $[M - L]^{2+}$, 615.1 $[(M - 2L) + H]^+$;
UV-Vis (DMSO) λ_{max} nm (ε x 10^{-4}): 314 (5.28), 626 (3.35);
FT-IR (KBr) ν cm^{-1}: 2923, 1737 (C=O), 1633, 1488, 1263, 1123, 741

Chapter 2 – Design, Synthesis and Characterization of Ruthenium Phthalocyanines Containing Axial Carbohydrate or Folic Acid Units to be Applied as Photosensitizers for the Generation of Singlet Oxygen

2.1. Overview

In this chapter, we aim at the synthesis of pyridyl-based ligands endowed with carbohydrate moieties or folic acid units, which will be attached to the axial coordination sites of RuPcs. This will allow the synthesis of RuPcs as third generation PSs, with enhanced selectivity towards tumor cells, a crucial feature to reduce side effects in cancer PDT treatment.

2.2. RuPcs donated with axial pyridyl ligands functionalized with carbohydrate units

2.2.1. Synthesis of the pyridyl-based ligands functionalized with carbohydrate units

To study the influence of specific carbohydrate moieties on the selectivity towards tumor cells, three different ligands were prepared from three different protected carbohydrate units: 1,2:5,6-di-*O*-isopropylidene-α-D-glucofuranose, 1,2:3,4-di-*O*-isopropylidene-α-D-galactopyranose and 2,3:5,6-di-*O*-isopropylidene-α-D-mannofuranose. Furthermore, the distinct monosaccharides were connected to the pyridine ring through different positions, C-3, C-6 and C-1, respectively, in order to attest its effect on the specificity of the resulting PSs.

The preparation of pyridine-based ligands bearing carbohydrate moieties is illustrated in **Scheme 16**. Both **L4** and **L5** ligands were prepared *via* nucleophilic aromatic substitution of the chlorine atom on 4-chloropyridine, with the alkoxide of the corresponding protected carbohydrate unit. In the case of **L4** 1,2:5,6-Di-*O*-isopropylidene-alpha-D-glucofuranose, in which the C-3 is the only carbon with an unprotected hydroxyl group, was used to couple to 4-chloropyridine. 1,2:3,4-Di-*O*-isopropylidene-D-galactopyranose, with and unprotected hydroxyl group at C-6, was used to obtain **L5**. When this methodology was used for the nucleophilic aromatic substitution using 2,3:5,6-Di-*O*-isopropylidene-α-D-mannofuranose, the desired product was not obtained. In order to increase the reactivity of the pyridine derivative, 4-fluoropyridine hydrochloride was used instead of 4-chloropyridine hydrochloride. This reaction was performed in DMF and dimethylacetamide (DMAC), with better yields obtained for the latter solvent. Thus, **L6** was prepared in 11% yield from 4-fluoropyridine hydrochloride, in DMAC and in the presence of NaH. These ligands were characterized by NMR spectroscopy and MS.

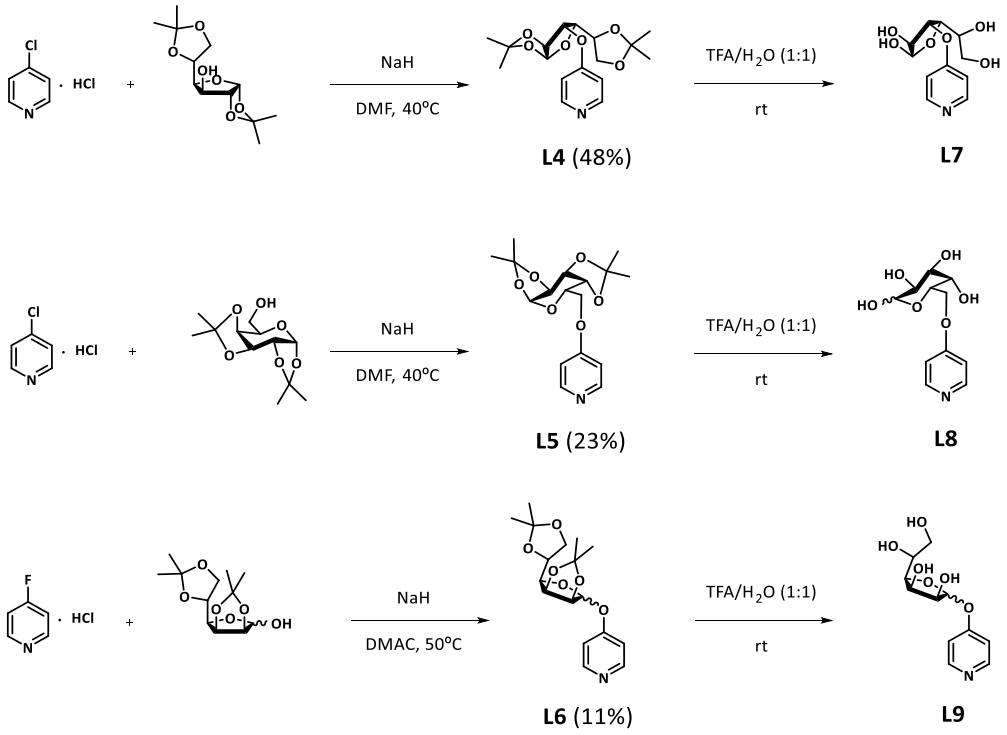

Scheme 16 – Synthesis of ligands **L4-9**.

The ^{1}H NMR spectrum of **L4** is represented in **Figure 33**. The two magnetically different pyridine protons appear as double doublets at 8.48 and 6.91 ppm, respectively. From those, the protons closest to the nitrogen atom display their signal at lower field. The glucose anomeric carbon shows its proton resonance as a doublet at 5.93 ppm. Since this proton is connected to a carbon bearing two oxygen atoms, the corresponding resonance appears as the most deshielded among the signals assigned to glucose protons. The coupling constant of Glu-H^{1} ($^{3}J_{1,2}$ = 3.8 Hz) allowed the identification of the signal corresponding to Glu-H^{2}, at 4.56 ppm. The latter was confirmed by COSY NMR (**Figure 34**). The dihedral angle between Glu-H^{2} and Glu-H^{3} is 90°. Therefore, according to the Karplus equation, their vicinal H–H coupling constant ($^{3}J_{HH}$) is zero. The doublet of doublet of doublets (ddd) at 4.40 ppm could be assigned to Glu-H^{5} because this is the only proton that couples to three different protons: Glu-H^{4} and the diastereotopic Glu-H^{6} protons (Glu-H^{6} are non-equivalent protons, since they are bound to a carbon that is next to a chiral carbon, namely Glu-C^{5}). COSY NMR allowed the identification of Glu-H^{6} signals, through their coupling to Glu-H^{5}. These are two doublet of doublets, each one corresponding to the coupling to Glu-H^{5} ($^{3}J_{5,6}$ = 5.9 and $^{3}J_{5,6}$ = 5.2 Hz) and to the coupling with Glu-H^{6} ($^{2}J_{6,6}$ = 8.7 Hz). The remaining Glu-H^{5} coupling constant ($^{3}J_{4,5}$ = 8.1 Hz), allowed to assign to the Glu-H^{4} proton the doublet of doublets appearing at 4.28 ppm. Taking all this into consideration, the remaining doublet at 4.79 ppm should correspond to Glu-H^{3} (this proton

only couples to Glu-H[4]), as confirmed by its coupling constant ($^3J_{3,4}$ = 3.0 Hz) and the COSY NMR spectrum. Finally, four singlets at 1.56, 1.42, 1.32 and 1.30 ppm correspond to the methyl groups.

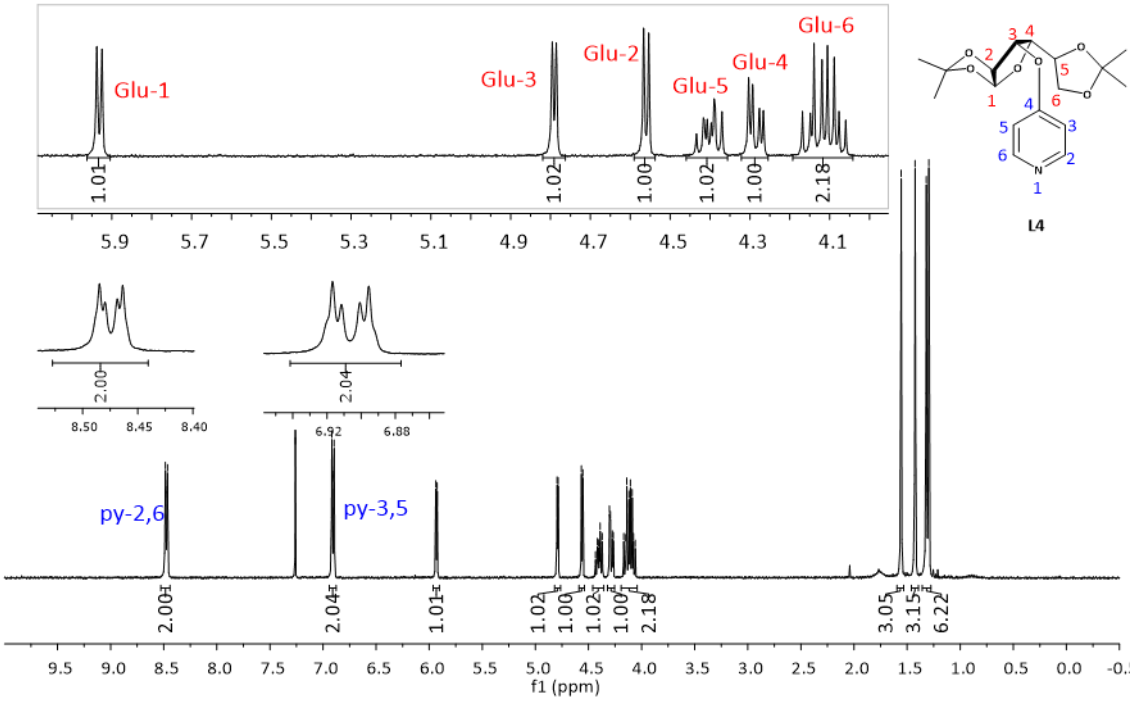

Figure 33 - ^{1}H NMR spectrum of **L4** in $CDCl_3$.

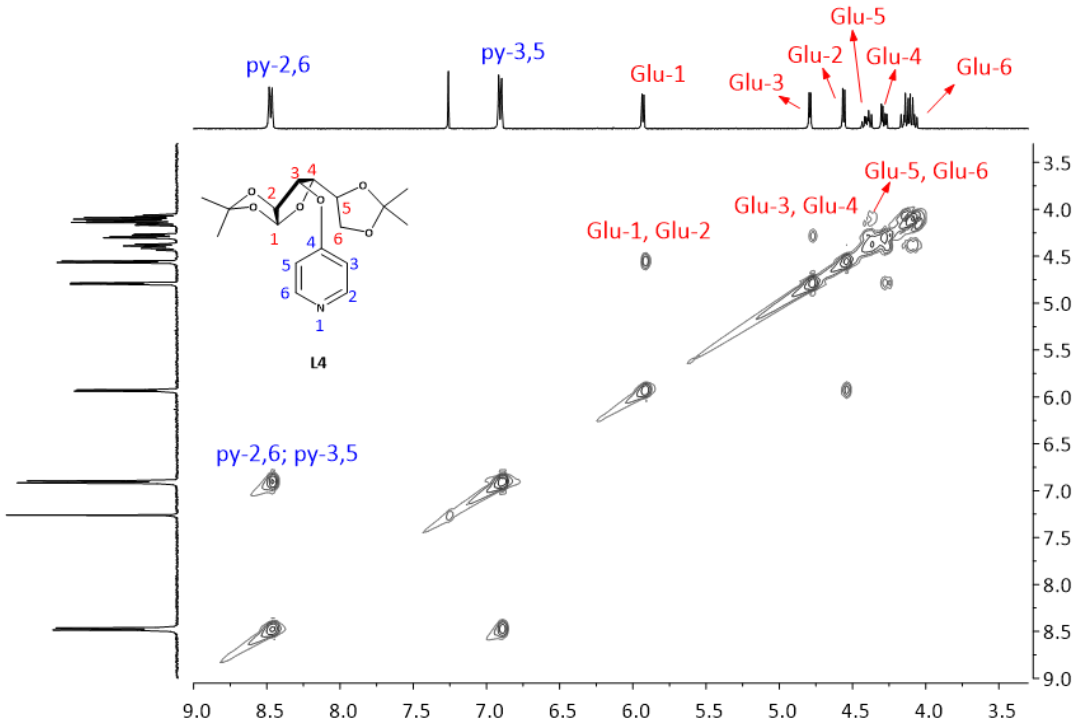

Figure 34 – COSY NMR spectrum of **L4** in $CDCl_3$.

Once identified all the signals of the ^{1}H NMR spectrum of **L4**, it was possible to assign the signals of the ^{13}C NMR spectrum by HMQC NMR spectroscopy (**Figure 35**). The peaks that show no correlation in the HMQC NMR spectrum correspond to the H^{4} pyridyl proton, at 163.22 ppm (not seen in the HMQC NMR spectrum) and to the two ketal carbons, at 112.50 and 109.53 ppm, respectively.

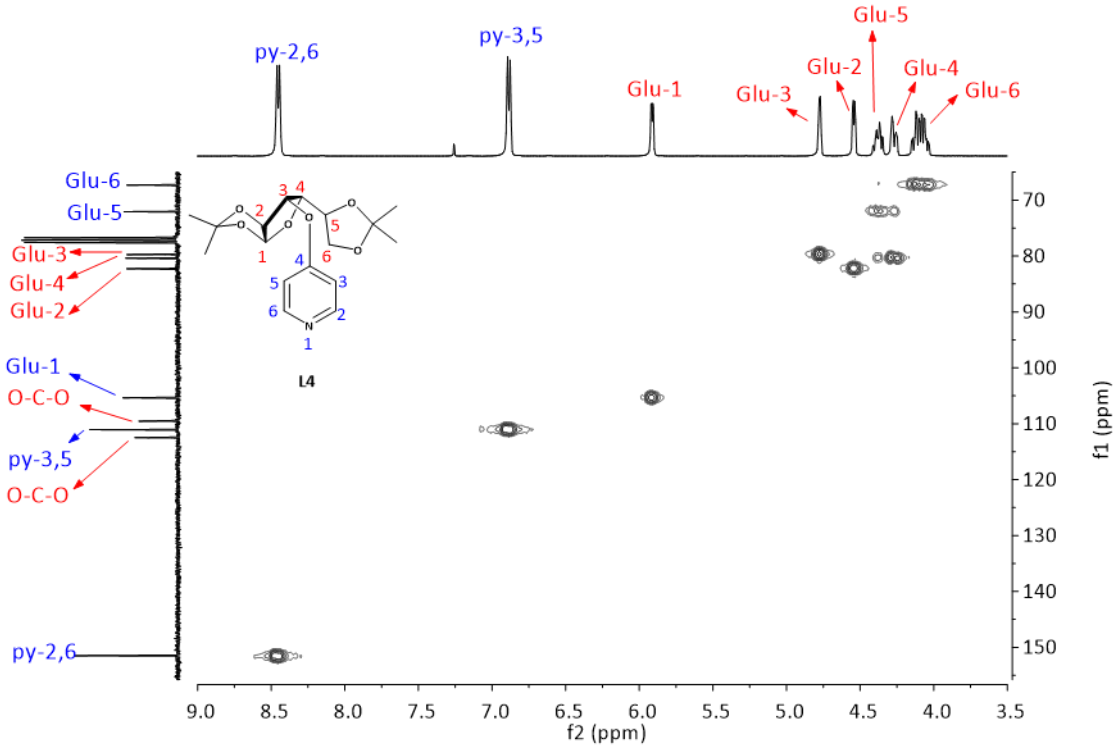

Figure 35 – Detail of the HMQC NMR spectrum of **L4** in $CDCL_3$.

With respect to **L5**, once more, the $H^{2,6}$ and $H^{3,5}$ pyridyl protons appear as double doublets at 8.41 and 6.84, respectively (**Figure 36**). Among the signals of the galactose unit, the proton of the anomeric carbon appears as a doublet at lower field (5.56 ppm) due to the proximity of two oxygen atoms. This signal is a doublet due to the coupling to Gal-H^{2}, which appears as a multiplet at 4.34 ppm, overlapped with the resonance of Gal-H^{4}, as deduced by COSY NMR (**Figure 37**). Gal-H^{3}, on the other hand, displays a double doublet at 4.65 ppm. Thus, the COSY spectrum shows two distinct coupling constants for this multiplet. One of them corresponds to the Gal-H^{2}/Gal-H^{4}–Gal-H^{3} coupling. The other coupling constant, which is very small as it is expected for the coupling of a proton at equatorial position (Gal-H^{4}) with one at axial position (Gal-H^{5}), is attributed to the Gal-H^{4}–Gal-H^{5} coupling. Finally, signals attributed to Gal-H^{5} and Gal-H^{6} overlap, appearing as a multiplet

at 4.18 ppm, integrating for three protons.[185,186] **Figure 38** represents the HMQC NMR spectrum of **L5** in $CDCl_3$.

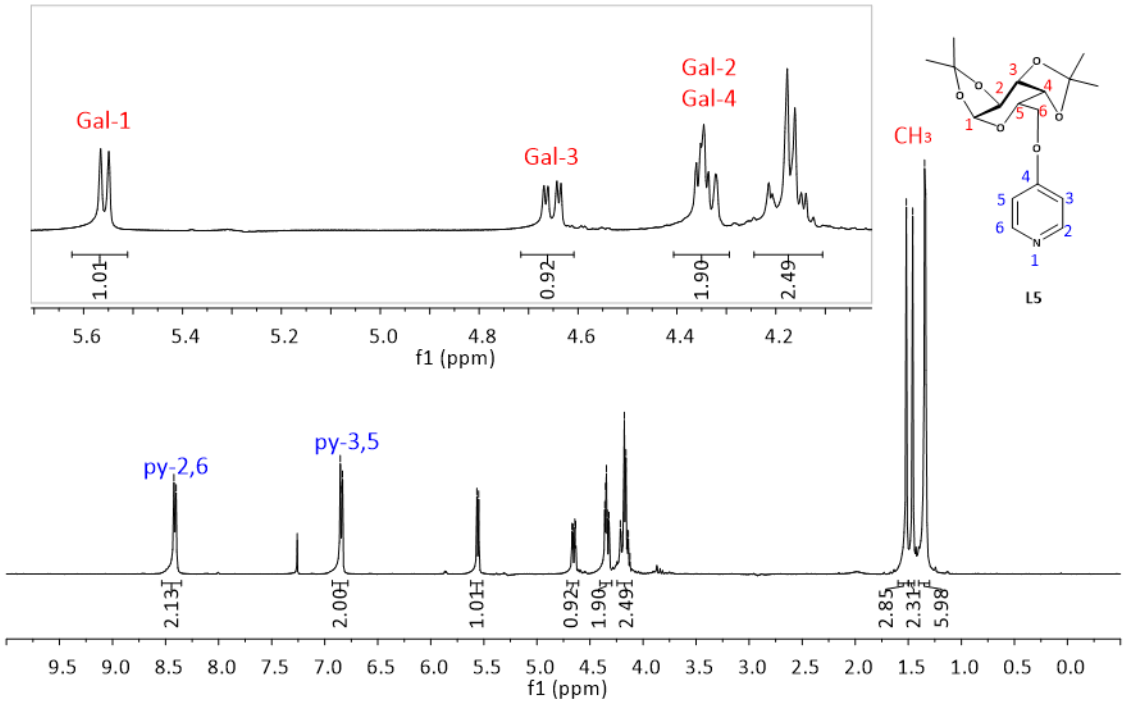

Figure 36 – ^{1}H NMR spectrum of **L5** in $CDCl_3$.

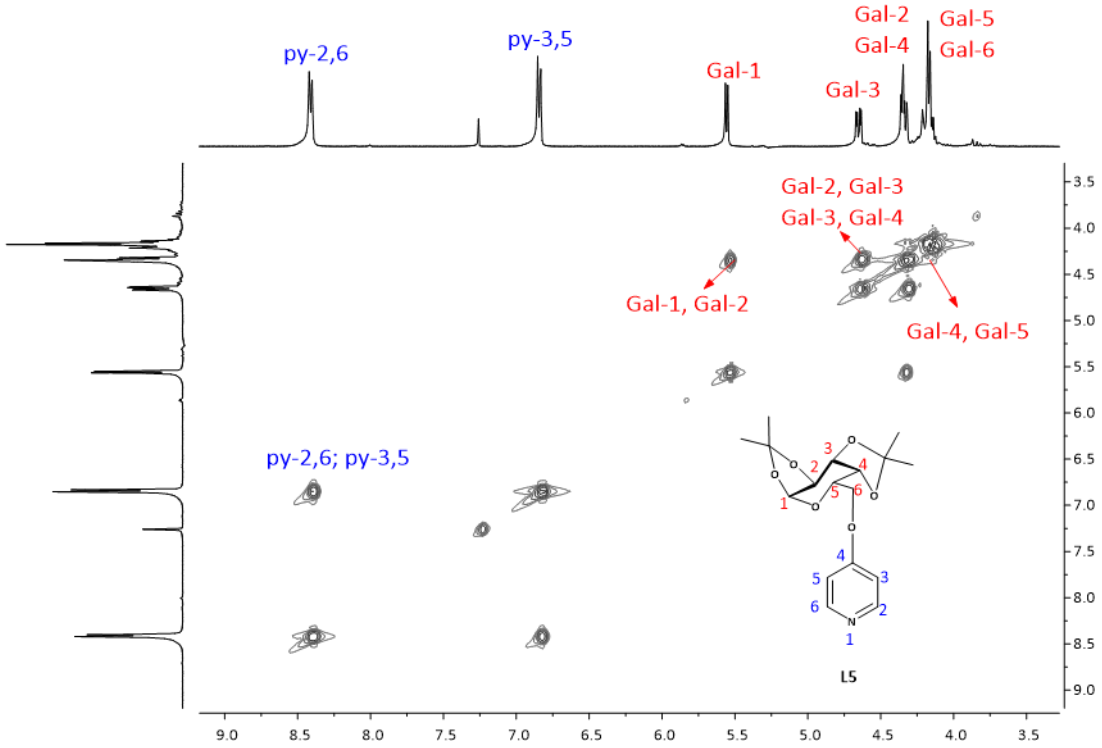

Figure 37 – COSY NMR spectrum of **L5** in $CDCl_3$.

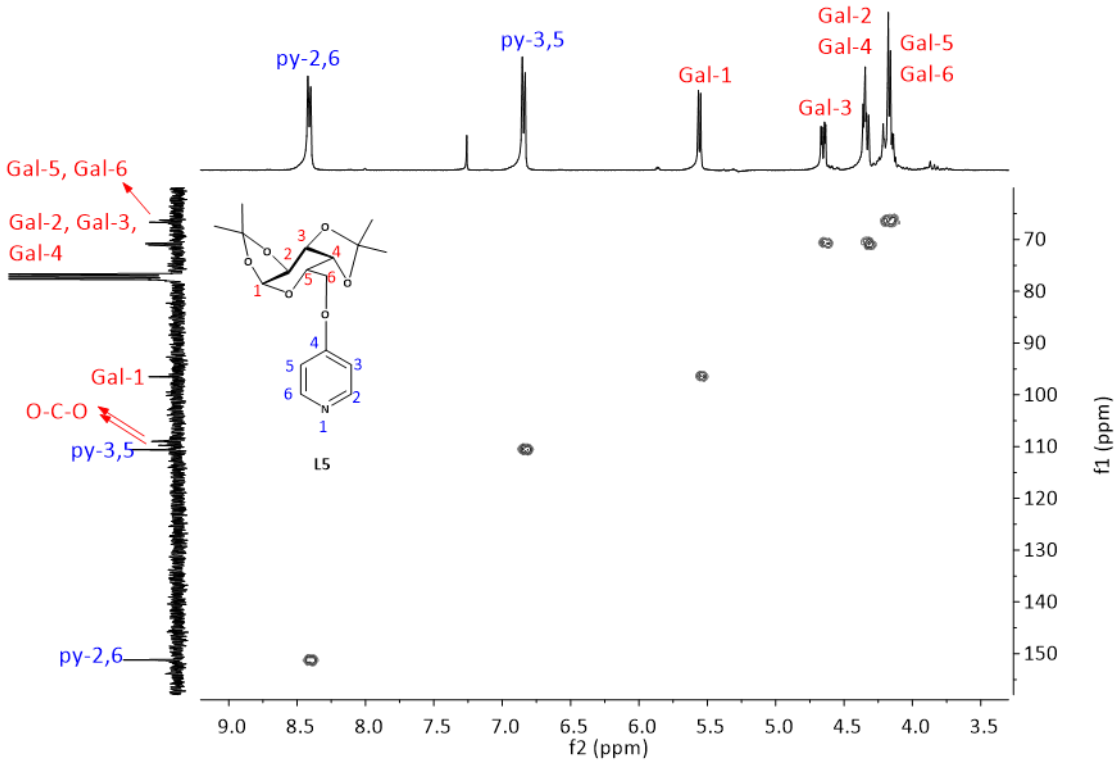

Figure 38 – Detail of the HMQC NMR spectrum of **L5** in $CDCl_3$.

In **Figure 39** the ^1H NMR spectrum in $CDCl_3$ of **L6** is represented. Man-H^1 appears as a singlet at δ 5.70 ppm. The lack of Man-H^1–Man-H^2 coupling probably arrises from their geometrical disposition, forming a dihedral angle of 90°, and thus exhibiting a $^3J_{HH} = 0$. The doublet of doublet of doublets (ddd) at δ 4.41 ppm is assigned to Man-H^5, since it is the only proton coupled to three different protons (Man-H^4 and the two non-equivalent Man-H^6 protons). The remaining resonances were asigned by comparison of the coupling constants of Man-H^5 with the others. Man-H^6 shows two double of doublets, one at 4.08 ppm ($^3J_{5,6}$ = 6.3 Hz) and the other one at 3.94 ppm ($^3J_{5,6}$ = 4.1 Hz). The two Man-H^6 protons display a large geminal coupling constant ($^2J_{6,6}$ = 8.8) and appear at 4.08 and 3.94 ppm. Man-H^4 shows a double of doublets at 4.02 ppm, with Man-H^4–Man-H^5 and Man-H^4–Man-H^3 coupling constants of $^3J_{4,5}$ = 7.7 Hz and $^3J_{3,4}$ = 3.3 Hz, respectively. Man-H^3 exhibits a double of doublets at 4.91 ppm, with a Man-H^3–Man-H^2 coupling constant of $^3J_{2,3}$ = 5.9 Hz. Finally, the doublet at 4.8 ppm can be attributed to Man-H^2. These correlations were confirmed by COSY NMR (**Figure 39** and **Figure 40**).

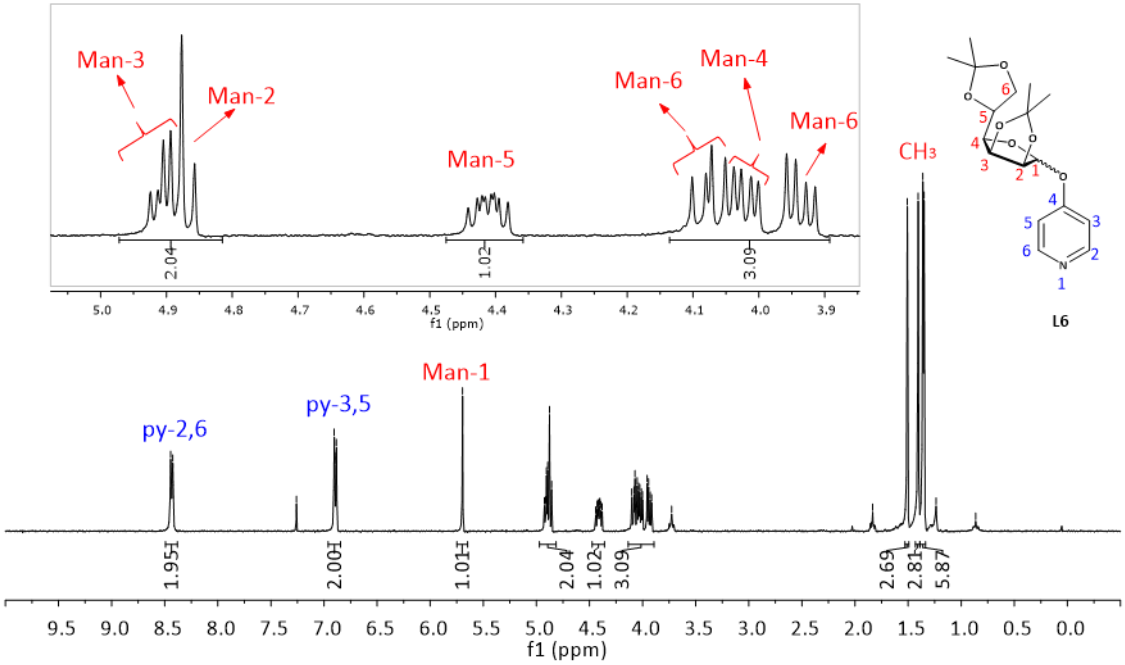

Figure 39 - ^{1}H NMR spectrum in $CDCl_3$ of **L6**.

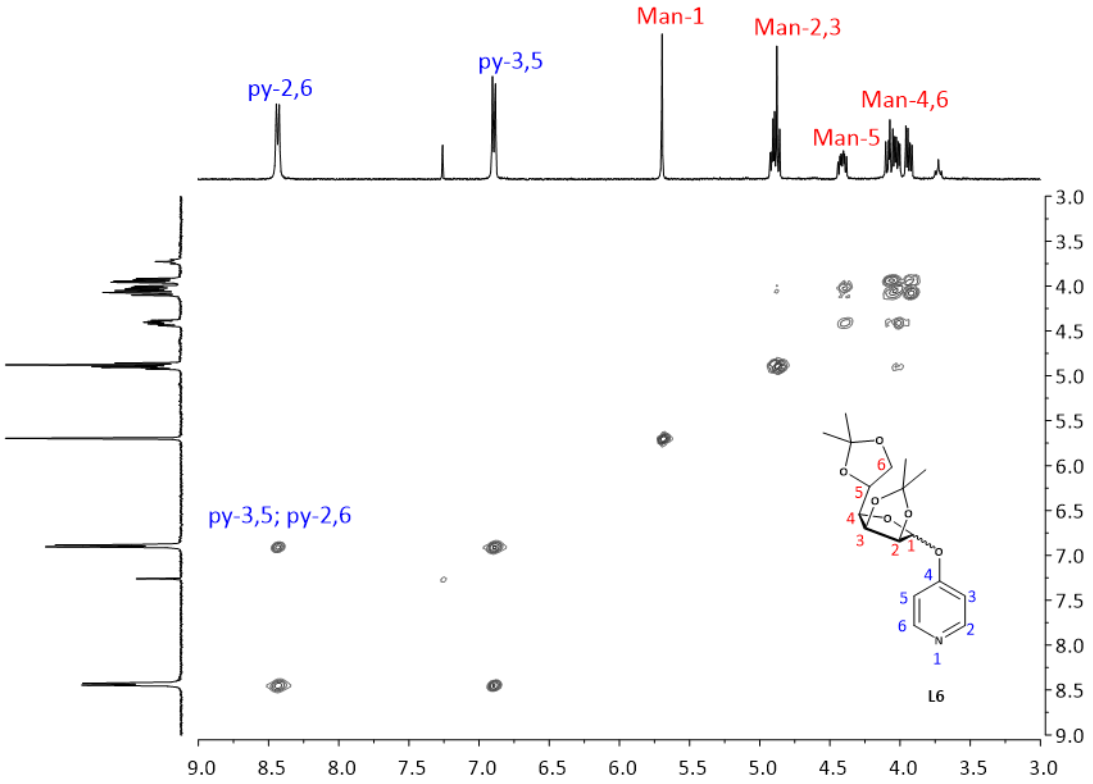

Figure 40 – COSY NMR spectrum of **L6** in $CDCl_3$.

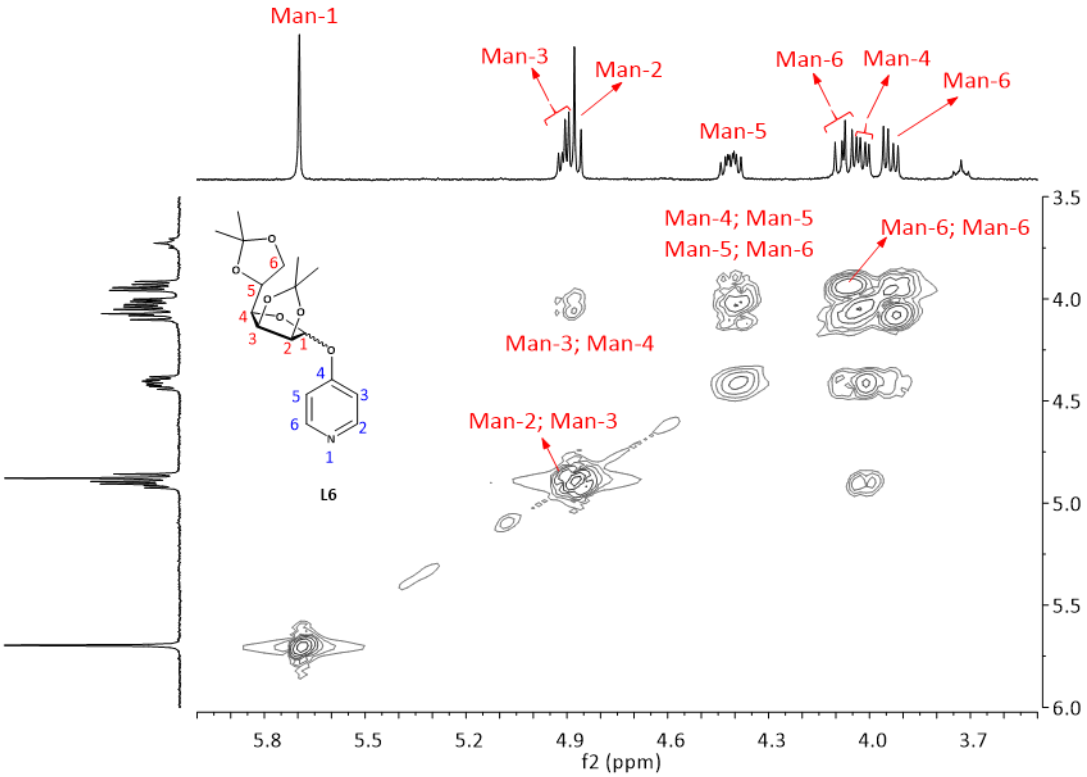

Figure 41 – Detail of the COSY NMR spectrum of **L6** in $CDCl_3$.

The HMQC NMR spectrum of **L6** is represented in **Figure 42**, where it was possible to assign all the signals corresponding to the pyridine unit and the mannose moiety. Once again, the peaks with no correlation, at 162.46 ppm (not seen in the HMQC spectrum), 113.41 ppm and 109.54 ppm, correspond to the H^4 pyridyl carbon and to the two ketal carbons, respectively.

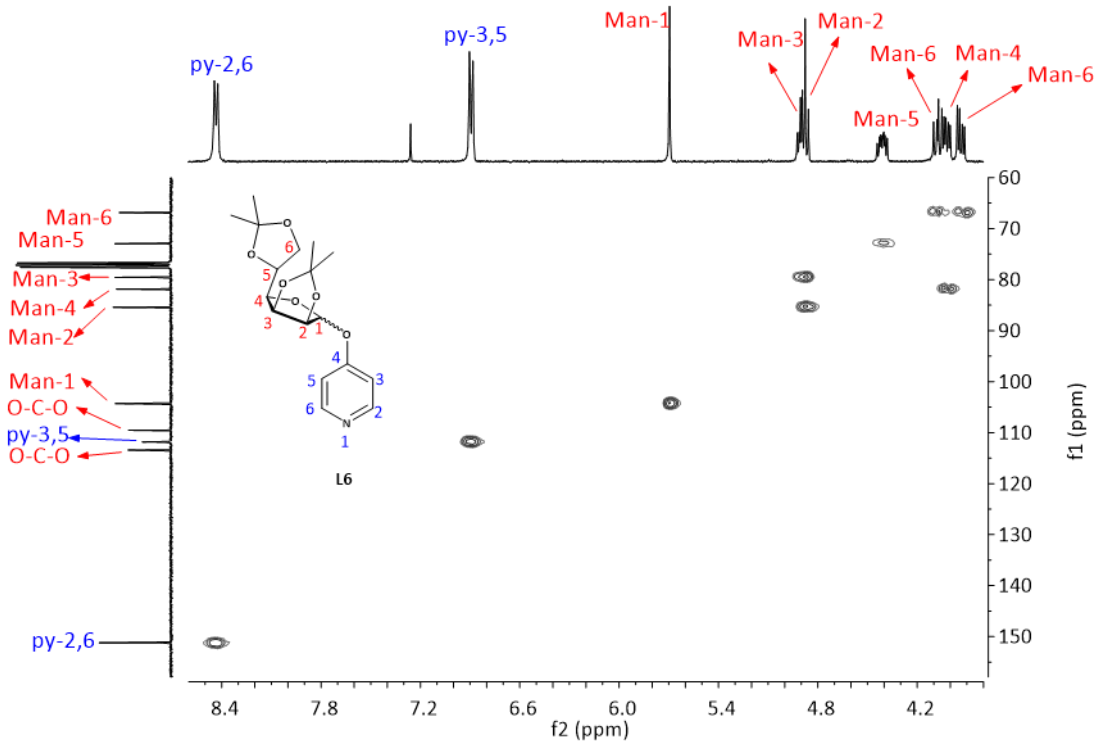

Figure 42 – Detail of the HMQC NMR spectrum of **L6** in $CDCl_3$.

For the deprotection of carbohydrates, **L4-6** were dissolved in a 1:1 mixture of TFA/H_2O and stirred at room temperature for 4 hours to afford the corresponding pyridine-based ligands functionalized with deprotected carbohydrate units (**L7-9**, **Scheme 16**). The characterization of these compounds was carried out by NMR spectroscopy and MS.

Usually, D-glucose, being an aldohexose, is more stable as the pyranose than as the furanose form. In fact, in aqueous solution, D-glucose usually exists as a mixture consisting on about one-third of α-pyranose, two-thirds of β-pyranose, and very small amounts (<0.19% at 43 °C) of furanose forms.[289] In **L4**, the glucose unit is fixed in its α-furanose configuration, arising from the commercially available 1,2:5,6-di-*O*-isopropylidene-α-D-glucofuranose. However, upon the deprotection reaction the ring could be rearranged to a more stable configuration. In order to verify the configuration of the Glu moiety in **L7**, we proceeded with its acetylation in the presence of DMAP and pyridine (**Scheme 17**), as described in the literature.[290] The acetylated ligands were analyzed by NMR spectroscopy.

[289] Brimacombe, J. S. In Carbohydrate Chemistry (A specialist Periodic Report), Vol. 11; The Chemical Sociey, Burlington House: London, 1979; pp 162.
Nelson, D. L.; Lehninger, A. L.; Cox, M. M. In *Lehninger Principles of Biochemistry*; W. H. Freeman: New York, 2008; pp 238–272.

[290] Durantie, E.; Bucher, C.; Gilmour, R. *Chem. Eur. J.* **2012**, *18* (26), 8208–8215.

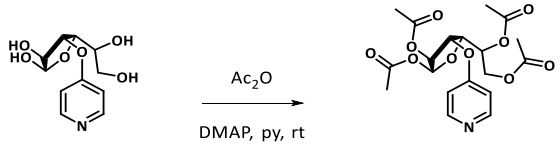

L7 **L7a**

Scheme 17 – Acetylation of **L7**.

Figure 43 shows the ^{1}H NMR spectrum of acetylated **L7**. The presence of a mixture of isomers, namely, α-D-glucofuranose, β-D-glucopyranose and β-D-glucopyranose is evidenced. In particular, the three doublets at 6.38, 5.99 and 5.78 ppm correspond to the protons connected to the anomeric carbons of the three different isomers, since they are deshielded due to their connection to two oxygen atoms. In the β-pyranose configuration, both Glu-H^{1} and Glu-H^{2} are in the axial positions. Thus, the signal at 5.78 ppm with the highest coupling constant (^{3}J = 8.31 Hz) corresponds to the anomeric proton of the β-pyranose form. The doublets at 6.38 and 5.99 ppm with the smaller coupling constants of ^{3}J = 3.67 and 3.65 Hz, respectively, are characteristic of both α-furanose and α-pyranose isomers. Among these two signals, we assigned the resonance at 5.99 ppm to the anomeric proton of the α-furanose form, since it is close to the chemical shift of the ketal protected α-furanose (**L4**). The remaining doublet, at 6.38 ppm, should therefore correspond to the anomeric proton of the α-pyranose isomer.

We have estimated the relative amount of each isomer by integrating these three signals. As expected, the β-D-glucopyranose was the major isomer (54%), followed by the α-D-glucofuranose (41%) and, finally, the α-D-glucopyranose isomer (5%).

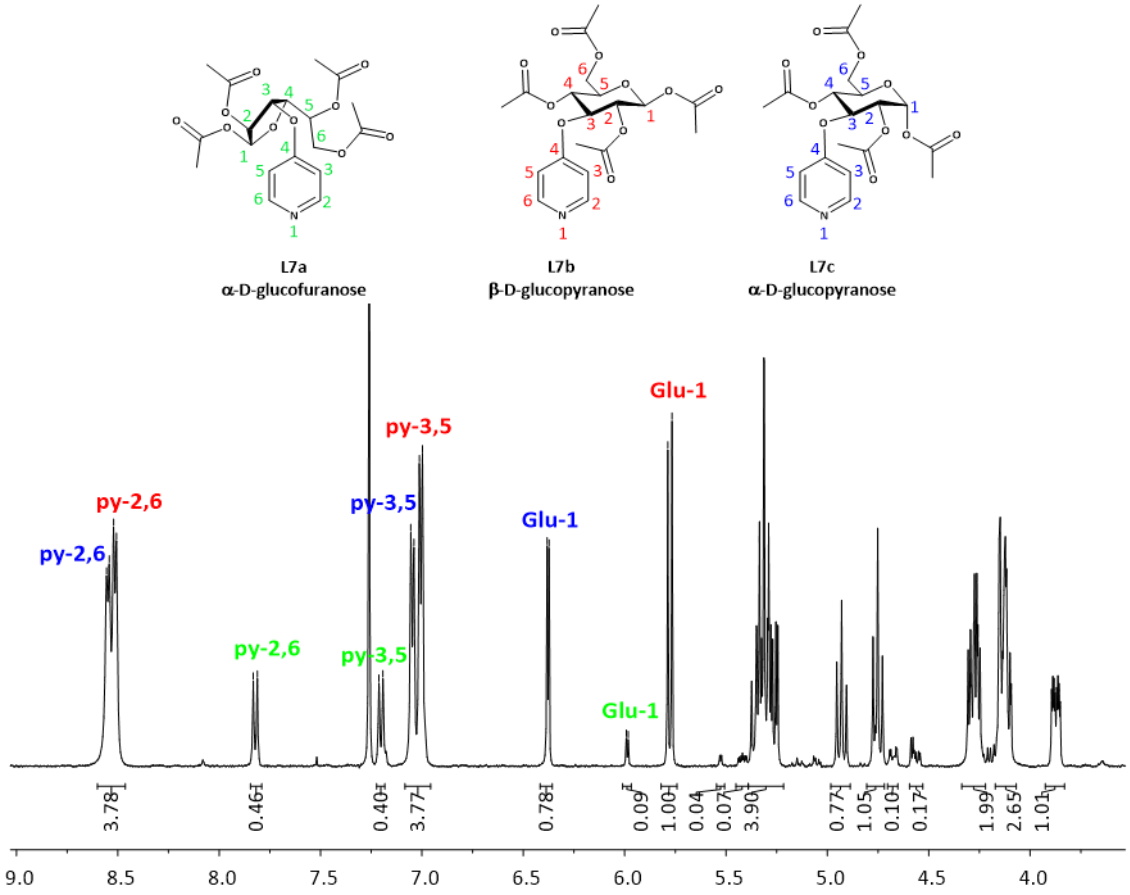

Figure 43 – ^{1}H NMR spectra in $CDCl_3$ of acetylated **L7** (**L7a-c**).

2.2.2. Coordination reactions to RuPc A and RuPc B

2.2.2.1. Coordination of pyridyl-based ligands functionalized with protected carbohydrate units

The three pyridine-based ligands functionalized with protected monosaccharide units (**L4-6**) were coordinated to **RuPc A** and **RuPc B** following the procedure described in section 1.3.2. The coordination reactions were carried out in $CHCl_3$, at 50 °C, in the absence of light (**Scheme 18**). The final PSs were purified by size exclusion chromatography in BioBeads. For PSs containing **RuPc A**, toluene was used as eluent, whereas for the compounds obtained from axial substitution on **RuPc B,** DCM was used.

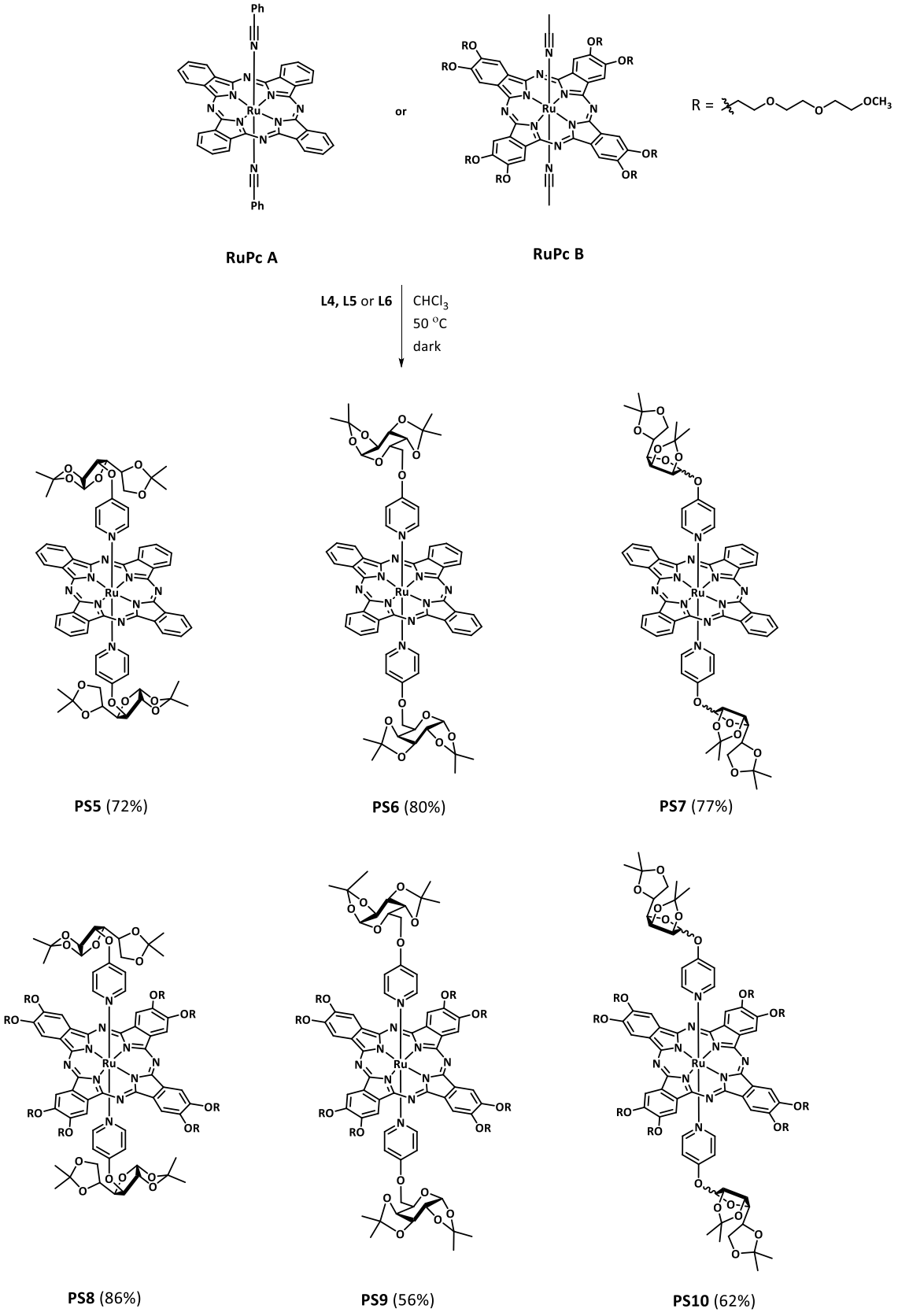

Scheme 18 – Preparation of **PS5-10**.

The characterization of **PS5-10** was performed by ^{1}H, MS and FT-IR.

Figure 44 represents the ^{1}H NMR spectrum of **PS5**. The doublet at 2.35 ppm, which corresponds to the $H^{2,6}$ pyridyl protons, appears 6.13 ppm upfield shifted, while the peak corresponding to $H^{3,5}$ pyridyl protons only move by 2.06 ppm, appearing also as a doublet at 4.85 ppm (**Figure 46**). Likewise, the peaks assigned to the carbohydrate unit are shifted to high field, with the signal corresponding to the anomeric proton appearing at 5.31 ppm as a doublet (upfield shifted by 0.62 ppm). Surprising to us, the other signals of the Glu moiety overlap upfield in a single multiplet, with the exception of the resonance for Glu-H^{2}, which appears as a doublet at 3.44 ppm. The later was assigned based on its coupling constant (J = 3.1 Hz, as in Glu-H^{1}) and by COSY NMR spectroscopy (**Figure 45**).

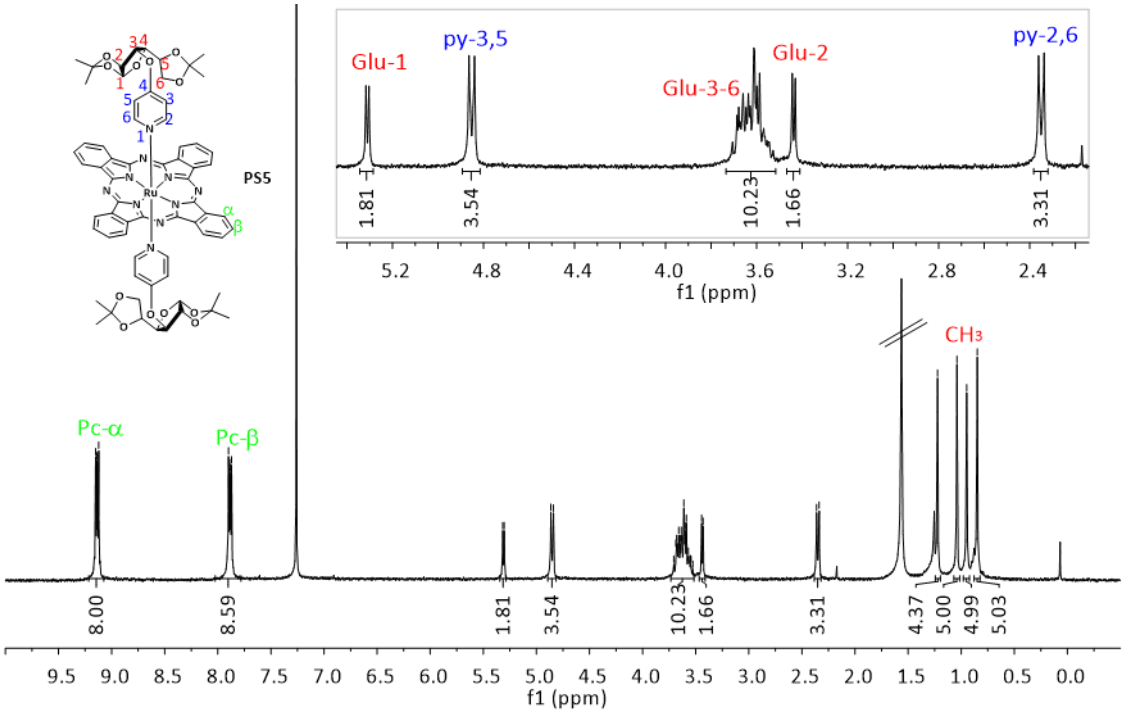

Figure 44 - ^{1}H NMR spectrum in $CDCl_3$ of **PS5**.

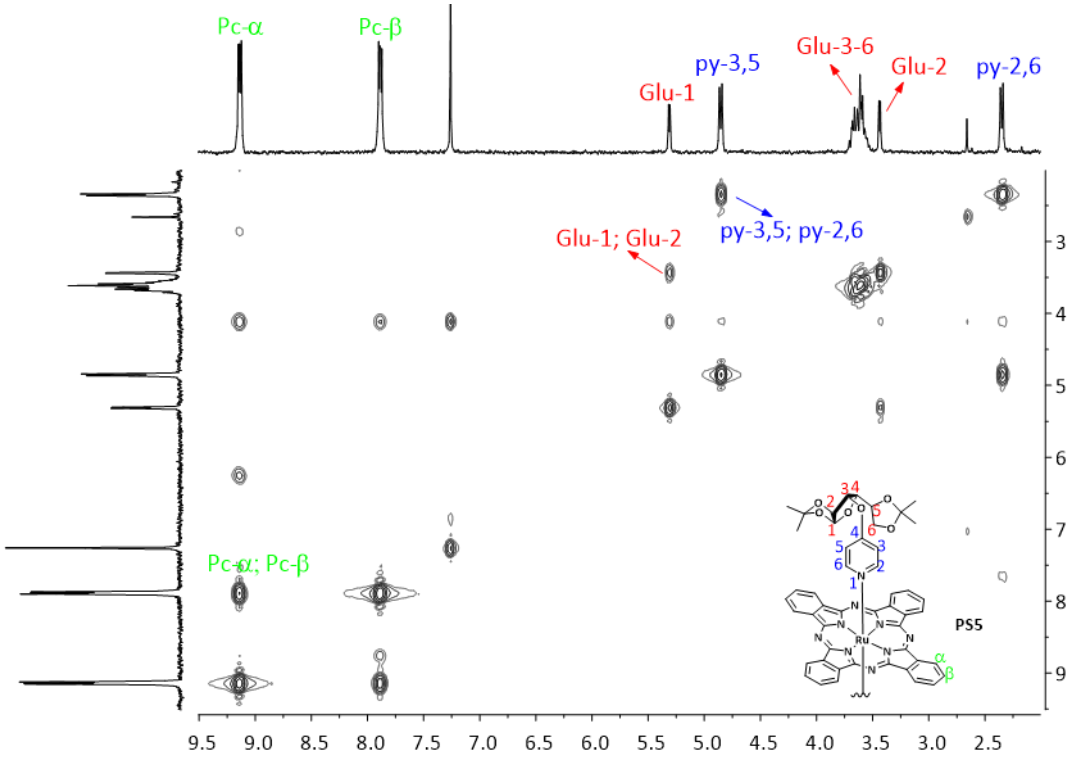

Figure 45 – COSY NMR spectrum of **PS5** in $CDCl_3$.

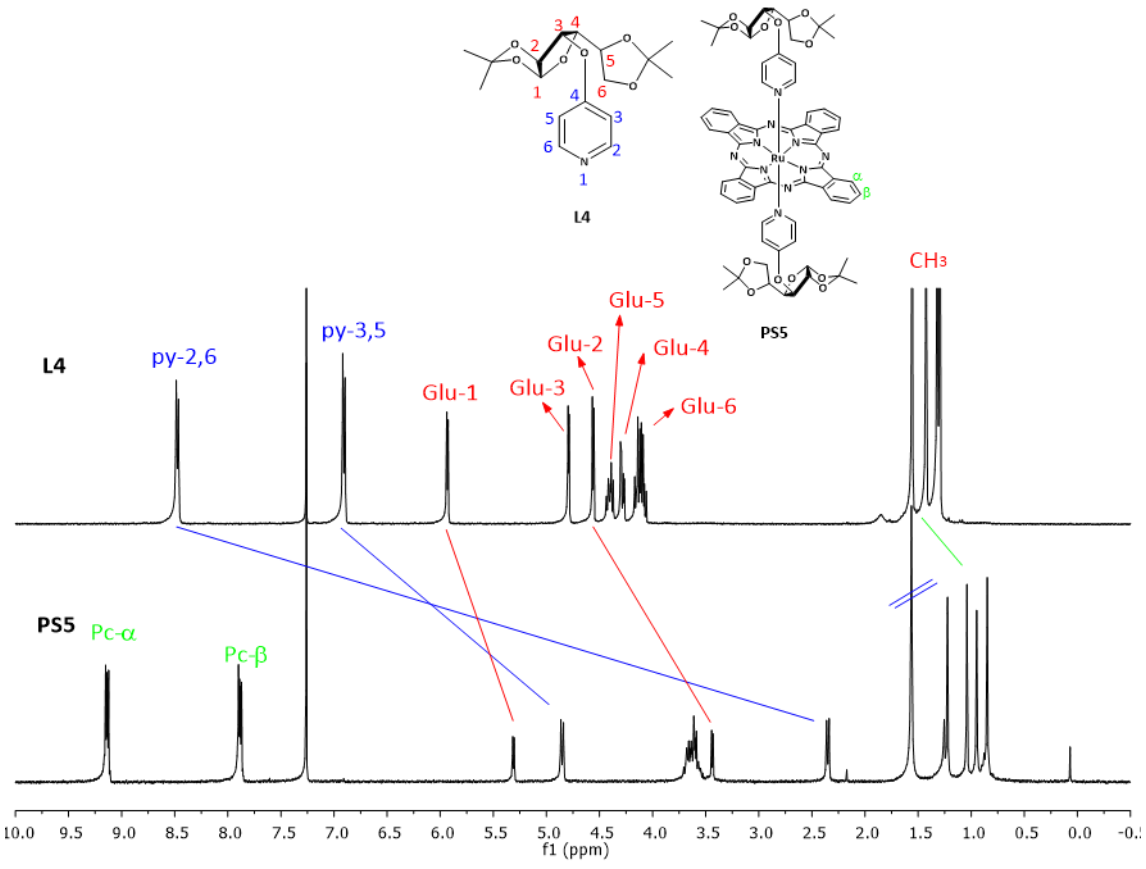

Figure 46 – Comparative ^1H NMR spectra in $CDCl_3$ of non-coordinated **L4** and **PS5**.

The ^{1}H and COSY NMR spectra of **PS6** are represented in **Figure 47** and **Figure 48** respectively. Upon coordination to **RuPc A**, the signals of **L5** suffered upfield shifts (**Figure 49**) as those observed for **PS5**. The H^{2} and H^{6} pyridyl protons, which appear at 2.35 ppm, exhibited the largest shift, of 6.06 ppm, followed by the H^{3} and H^{5} pyridyl protons with a displacement of 1.99 ppm, appearing at 4.85 ppm. Gal-H^{1} and Gal-H^{3} peaks were moved to higher field by 0.45 and 0.37 ppm, respectively. The remaining signals of the pyranose ring, which were overlapped in two multiplets in **L5**, were also shifted to higher fields and are now separated in individual peaks. The coupling constants and the COSY NMR spectrum allowed the identification of each signal. Hence, the two doublets of doublets at 4.04 ppm and 3.66 ppm correspond to Gal-H^{2} and Gal-H^{4}, respectively. Gal-H^{5} appears at 3.33 ppm as a triplet of doublets (the coupling constants with the two Gal-H^{6} protons are the same) and Gal-H^{6} protons correspond to the two double of doublets at 3.18 and 3.07 ppm. Finally, the methyl protons also experienced an upfield shift of about 0.4 ppm.

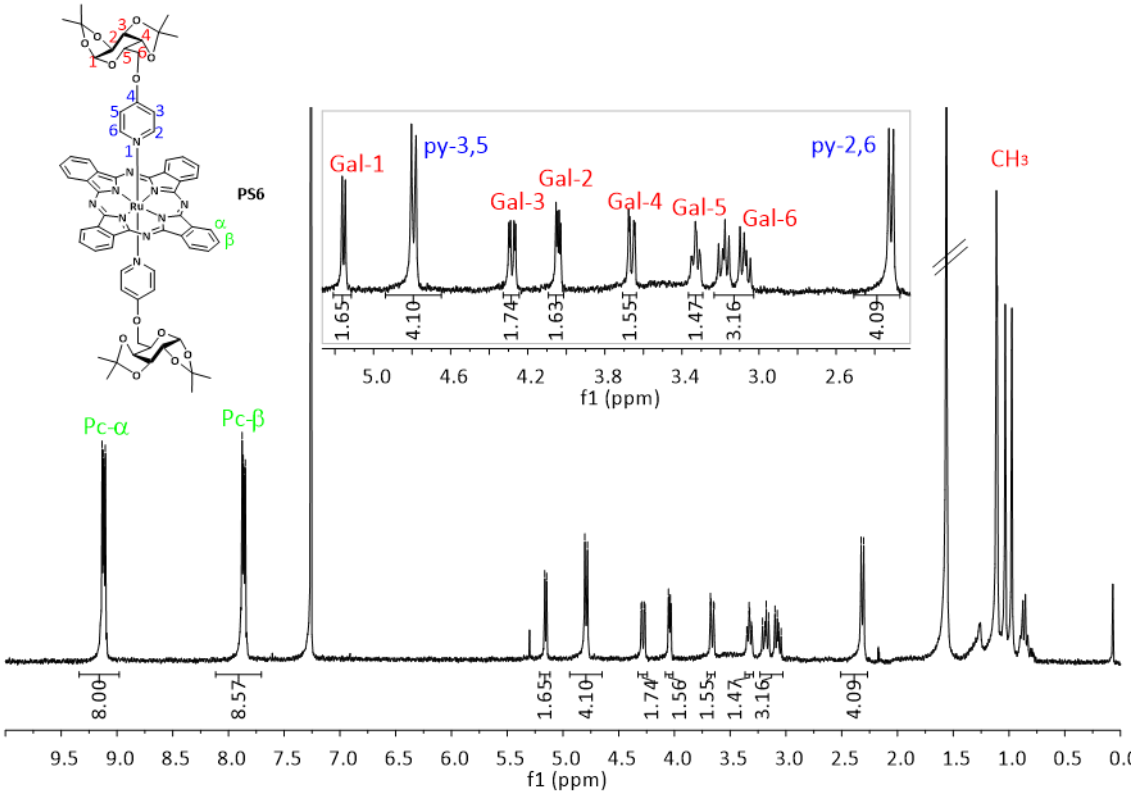

Figure 47 – ^{1}H NMR spectrum in $CDCl_3$ of **PS6**.

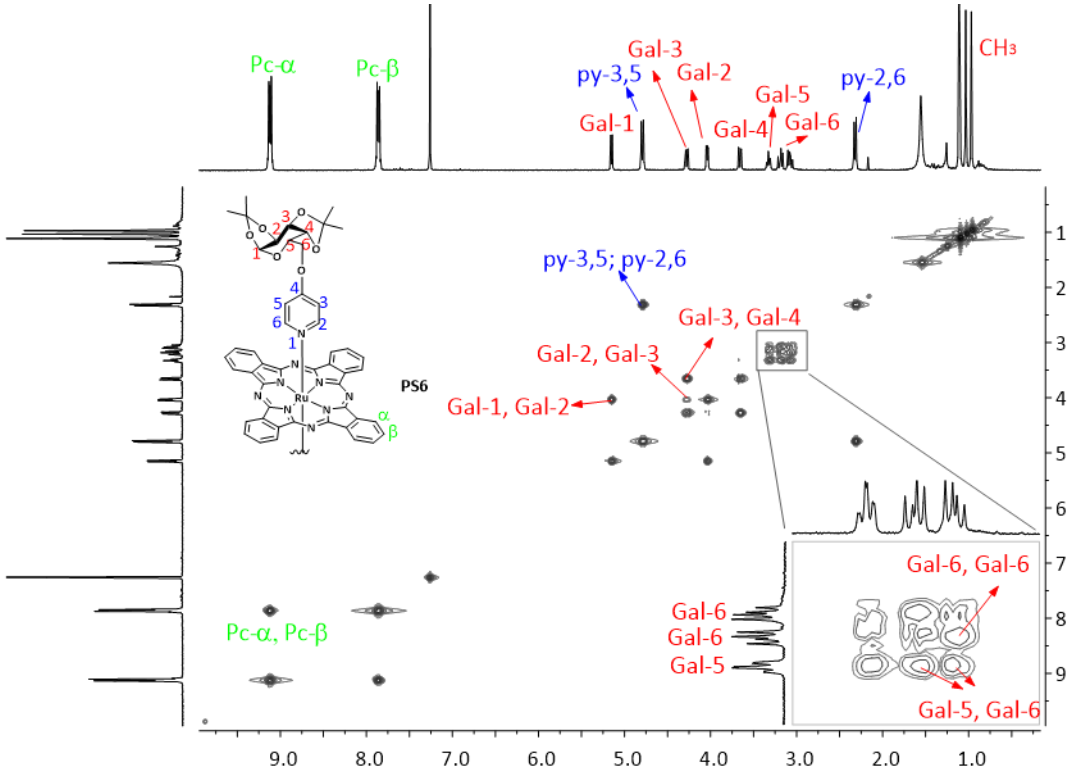

Figure 48 – COSY NMR spectrum of **PS6**.

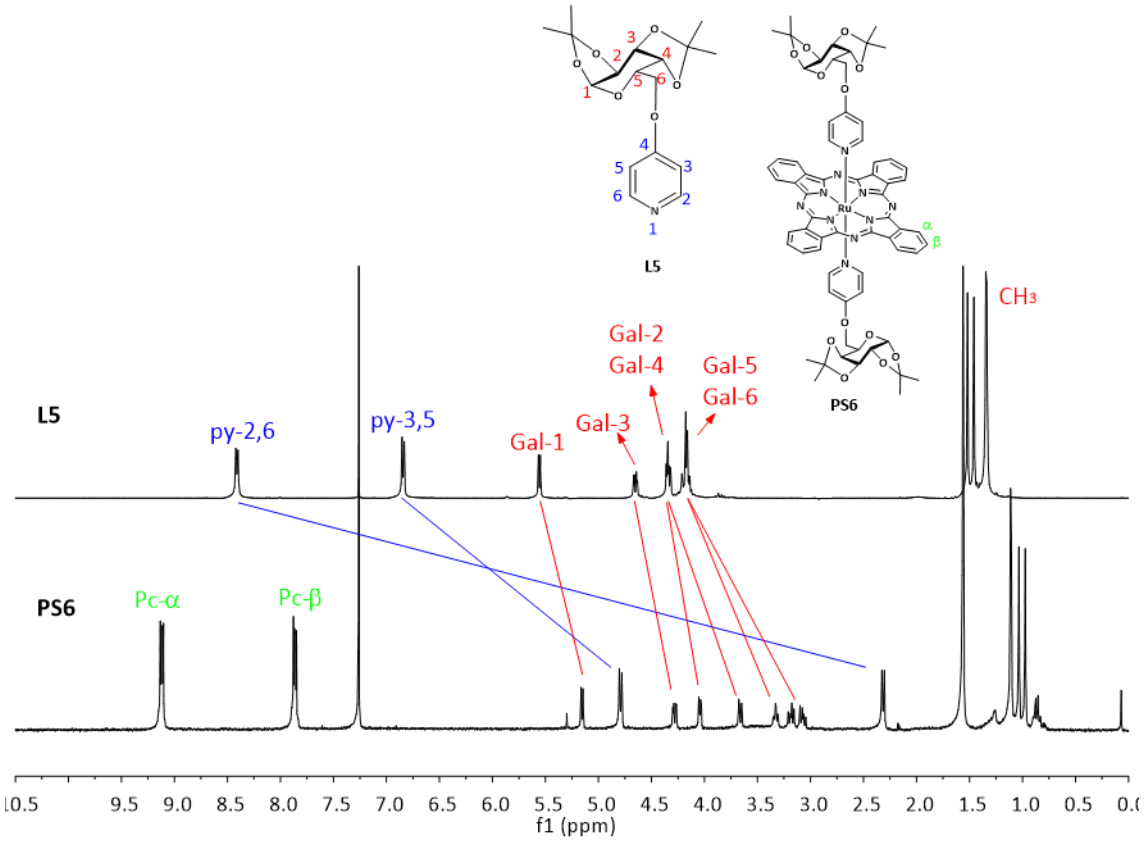

Figure 49 – Comparative ^{1}H NMR spectra in $CDCl_3$ of non-coordinated **L34** and **PS6**.

Figure 50 and **Figure 51** represent the ^{1}H and COSY NMR spectra of **PS7**, respectively. Again, upon coordination the protons of **L6** unit are influenced by the anisotropic effect of the macrocycle upon coordination, appearing upfield shifted with respect to the non-coordinated ligand (**Figure 52**). Thus, $H^{2,6}$ and $H^{3,5}$ pyridyl protons appear at 2.32 and 4.84 ppm, that is, shifted by 6.11 and 2.05 ppm, respectively. The signals corresponding to the mannose unit are shifted by 1.18–0.71 ppm. The assignment of the signals corresponding to the mannose unit was performed according to the characterization of **L6**, explained above. Thus, protons H^{1}, H^{3}, H^{2} and H^{5} of the mannose unit appear at 4.52, 4.39, 4.12 and 3.96 ppm, respectively. One of the Man-H^{6} protons displays a doublet of doublets at 3.68 ppm ($^{3}J_{5,6}$ = 6.3 Hz and $^{2}J_{6,6}$ = 8.8 Hz), while the other Man-H^{6} proton appears also as a doublet of doublets at 3.31 ppm ($^{3}J_{5,6}$ = 4.6 Hz and $^{2}J_{6,6}$ = 8.8 Hz). Finally, the Man-H^{4} protons exhibit a doublet of doublets at 3.23 ppm ($^{3}J_{3,4}$ = 3.7 Hz and $^{3}J_{4,5}$ = 7.9 Hz). The ketal methyl protons were shielded by 0.3 ppm, approximately.

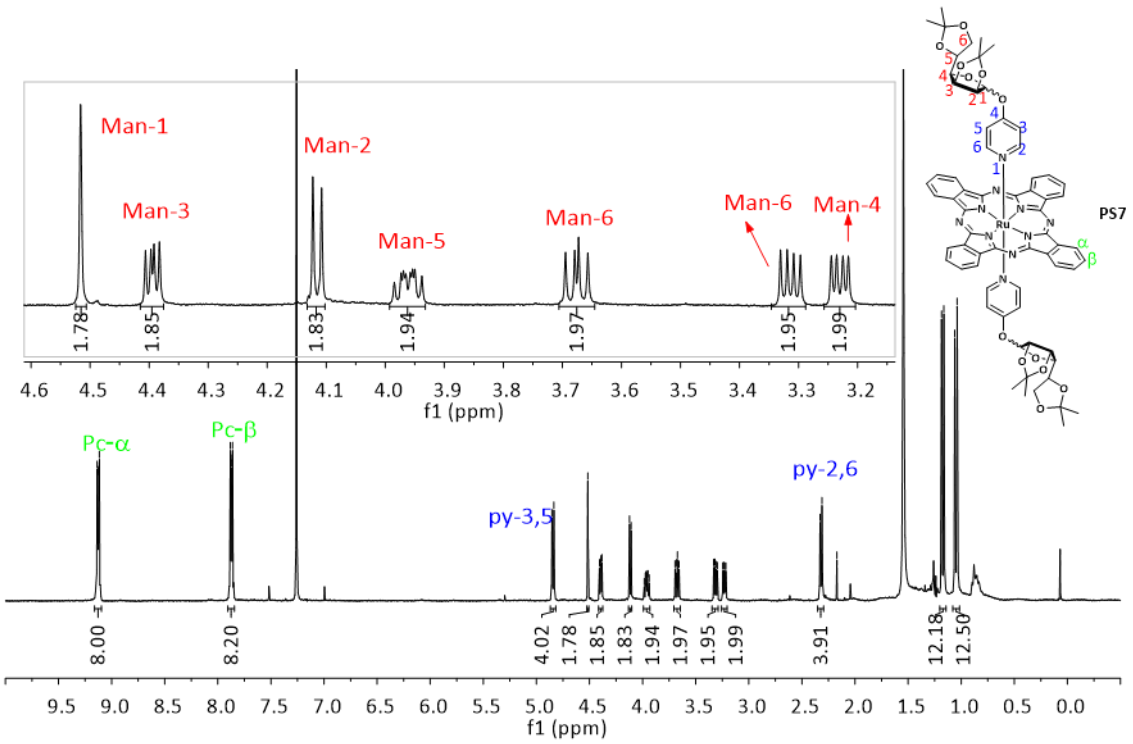

Figure 50 - ^{1}H NMR spectrum in $CDCl_3$ of **PS7**.

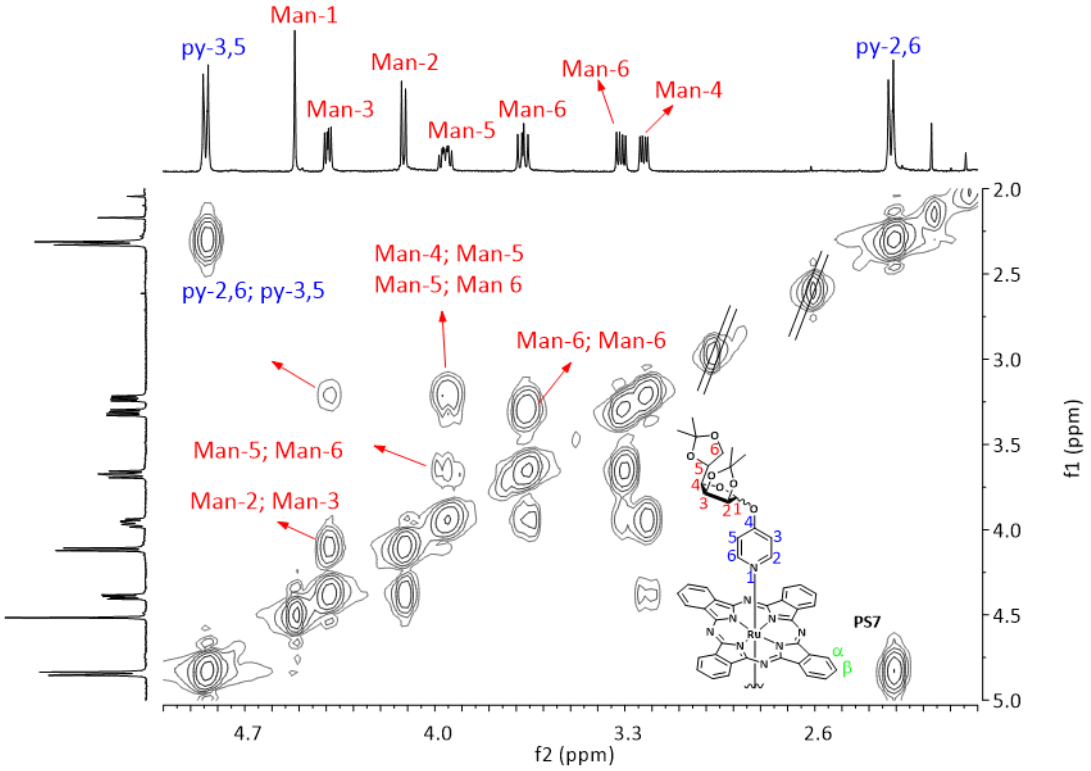

Figure 51 – Detail of the COSY NMR spectrum of **PS7** in $CDCl_3$.

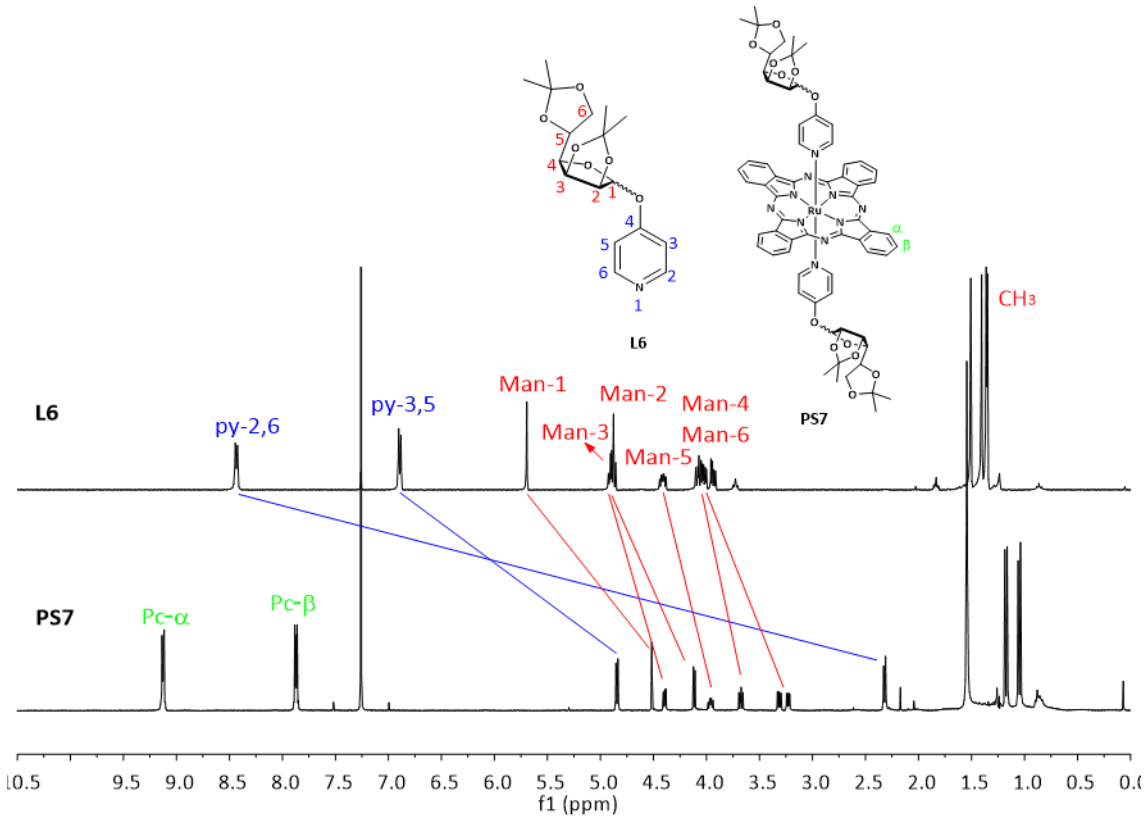

Figure 52 – Comparative ^{1}H NMR spectra in $CDCl_3$ of non-coordinated **L 35** and **PS 7**.

PS8-10 display similar chemical shifts to those observed for **PS5-7**.

The deprotection of the galactose units in **PS6** was attempted by stirring **PS6** in a 9:1 mixture of TFA/H_2O for 6h at room temperature (**Scheme 19**). However, this resulted in the formation of a large number of products that were observed by reverse phase chromatography using a 1:1 mixture of THF/H_2O as the eluent. Therefore, this route was discarded, and RuPcs bearing deprotected carbohydrate units at axial positions were prepared by coordination of pyridyl ligands with the previously deprotected carbohydrate moieties (**L7-9**).

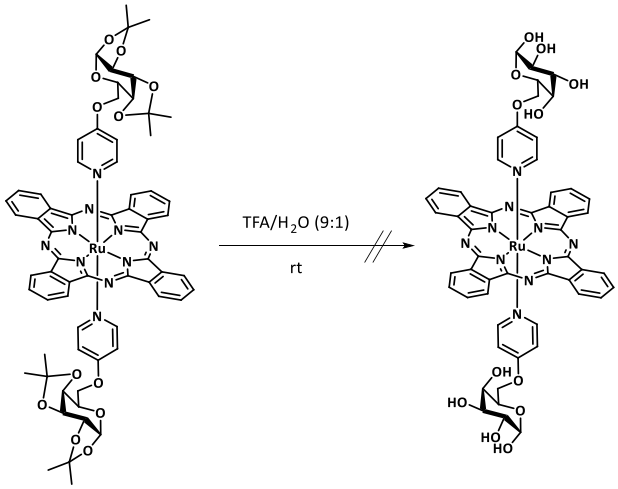

Scheme 19 – Attempt to deprotect the galactose units of **PS6**.

2.2.2.2. Coordination of pyridyl-based ligands functionalized with deprotected carbohydrate units

Owing to the low solubility of ligands **L7-9** in $CHCl_3$, a more polar solvent, able to dissolve such ligands, as well as **RuPc A** and **RuPc B**, was necessary for the coordination reactions.

Coordination of **L8** to **RuPc A** was first essayed using THF as solvent, at 50 °C and protected from light. Under these conditions, no coordination was observed, probably due to the low solubility of **L8** in this solvent.

Next, we performed the same coordination reaction in DMSO, at room temperature and in the dark. Under these conditions, coordination of **L8** to **RuPc A** took place. The coordination product was isolated by gel permeation chromatography on biobeads with THF as the eluent. Surprisingly, the isolated product was a RuPc bearing **L8** at one of its axial positions, and one molecule of DMSO

coordinated at the other axial site (**PS12**, **Scheme 20**), as it was verified by ^{1}H NMR and ESI^{+}. The ESI^{+}-MS spectrum of **PS12** displayed a peak at 950.2 corresponding to $[M + H]^{+}$.

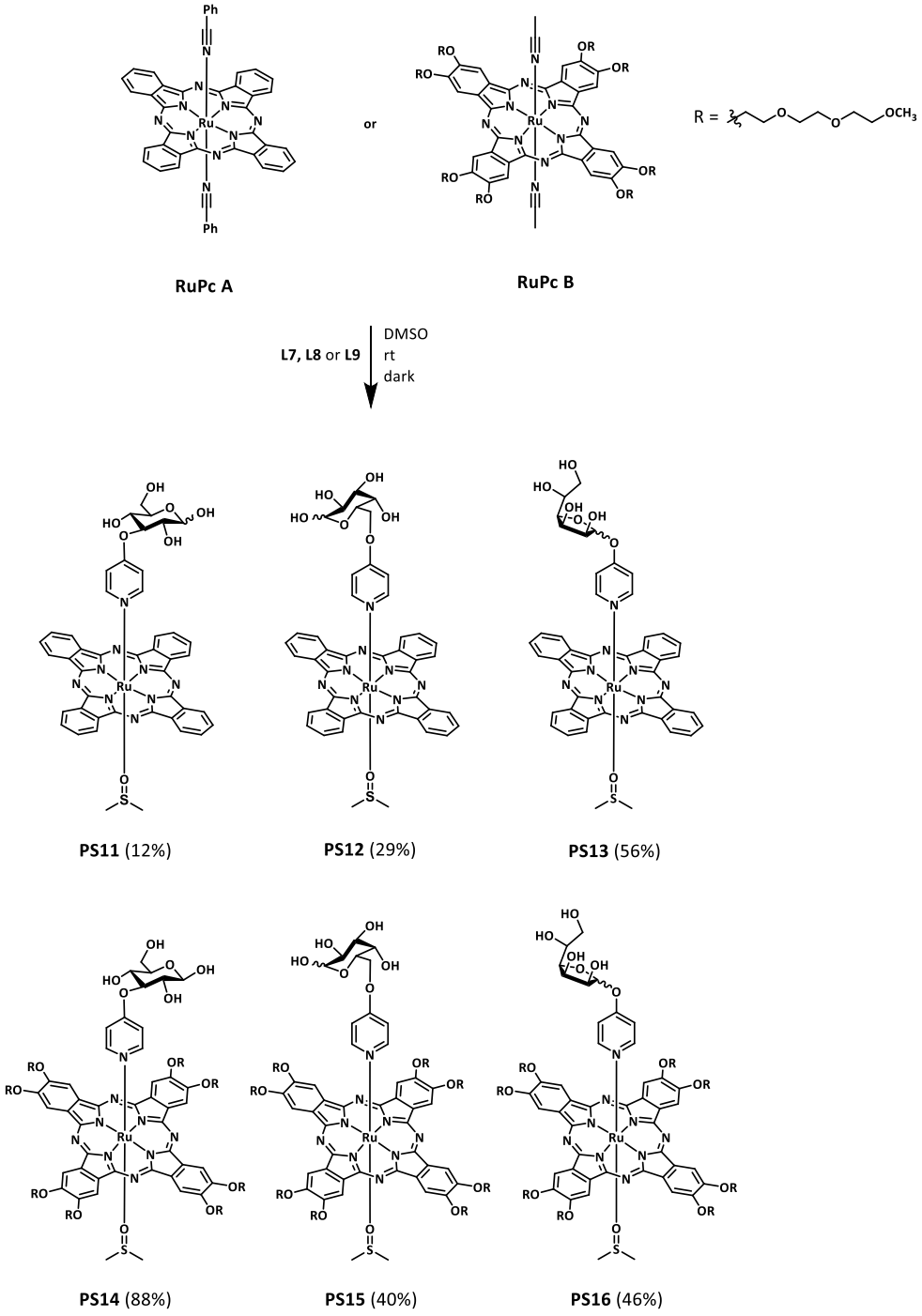

Scheme 20 – Preparation of **PSs 11-16**.

Figure 53 represents comparative ^{1}H NMR spectra of **L8** in DMSO-d_6, **PS12** in a mixture of DMSO-d_6 and D_2O and **PS12** in DMSO-d_6. The coordinated DMSO molecule is strongly influenced by

the Pc diamagnetic current, appearing as singlet at –1.09 ppm.[45] The integration of this signal does not match the six expected protons of the DMSO ligand due to the partial replacement by DMSO-d_6. As observed in the previous coordination reactions, the coordination of **L8** to **RuPc A** also produces an upfield shift of the resonances corresponding to **L8**. The closest protons to the Pc core, i.e. H^2 and H^6 pyridyl protons, moved by 6.86 ppm, while H^3 and H^5 pyridyl protons shifted by 2.27 ppm. The upfield shift of the anomeric proton was less pronounced (0.45 ppm). When recording the spectrum of **PS12** in a mixture of DMSO-d_6 and D_2O, the replacement of the exchangeable hydroxyl protons by deuterium atoms took place, this allowing for the identification of the signals corresponding to the hydroxyl groups of the galactose moiety, which appear at 6.29, 5.86, 4.40 and 4.25 ppm. Finally, integration of the pyridyl protons, in the spectrum of **PS12** in DMSO-d_6, indicates the presence of only one pyridyl ligand at the axial position of the RuPc.

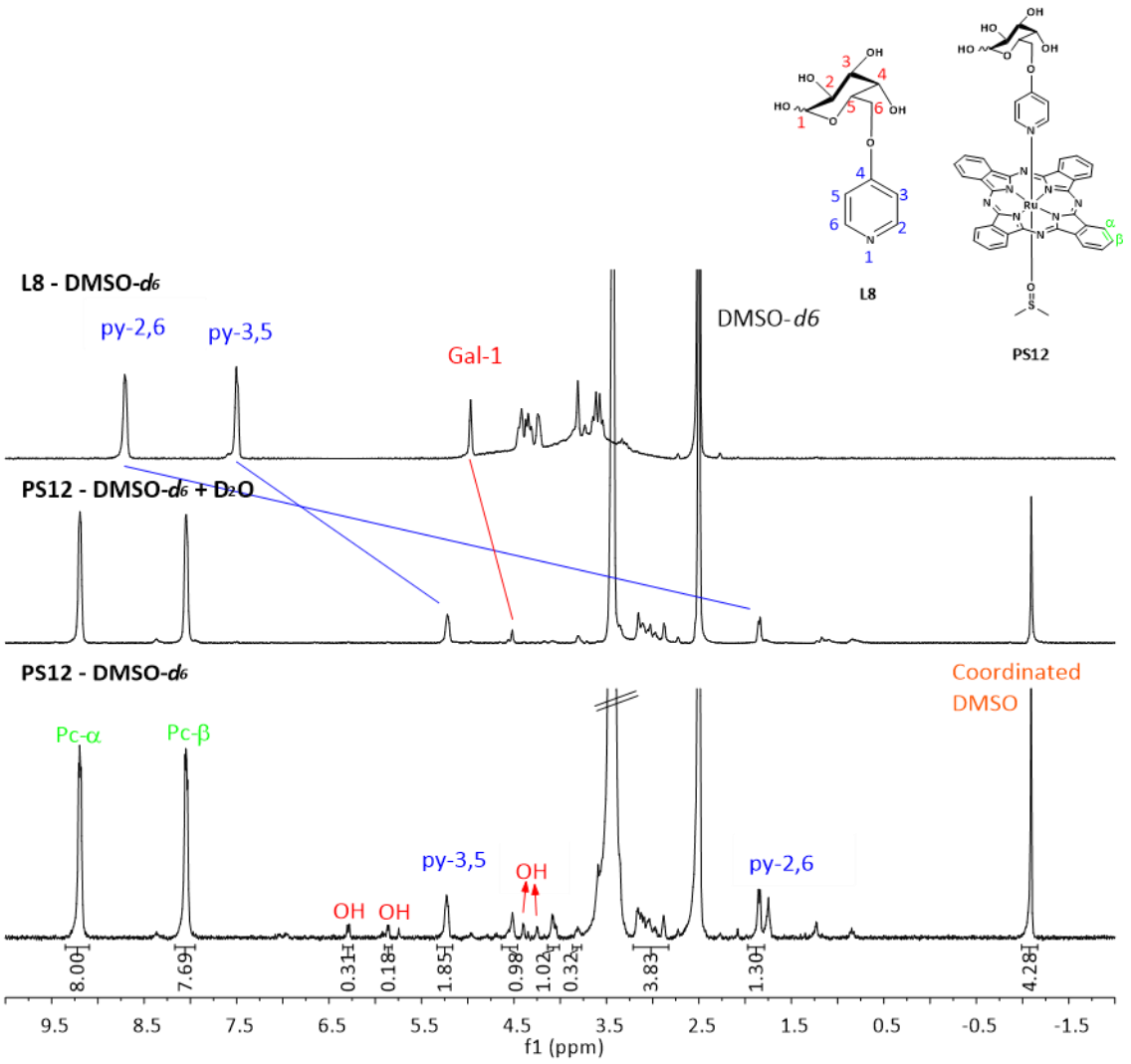

Figure 53 – Comparative ^{1}H NMR spectra of **L8** in DMSO-d_6, **PS12** in DMSO-d_6 + D_2O and **PS 12** in DMSO-d_6.

The coordination reactions of **L7** and **L9** to **RuPc A** and of **L7-9** to **RuPc B** were carried out under the same conditions, affording **PS11** and **PS13-16** in good yields (**Scheme 20**). The isolation was also done by size exclusion chromatography using THF as eluent, and their characterization was performed by ^{1}H NMR and ESI^{+}. Concerning the ^{1}H NMR spectra, comparable features were observed for signals of **L7** and **L9** signals upon coordination to **RuPc A** (**Figure 54** and **Figure 55**) and to **RuPc B**, as well as the signals for the DMSO ligands.

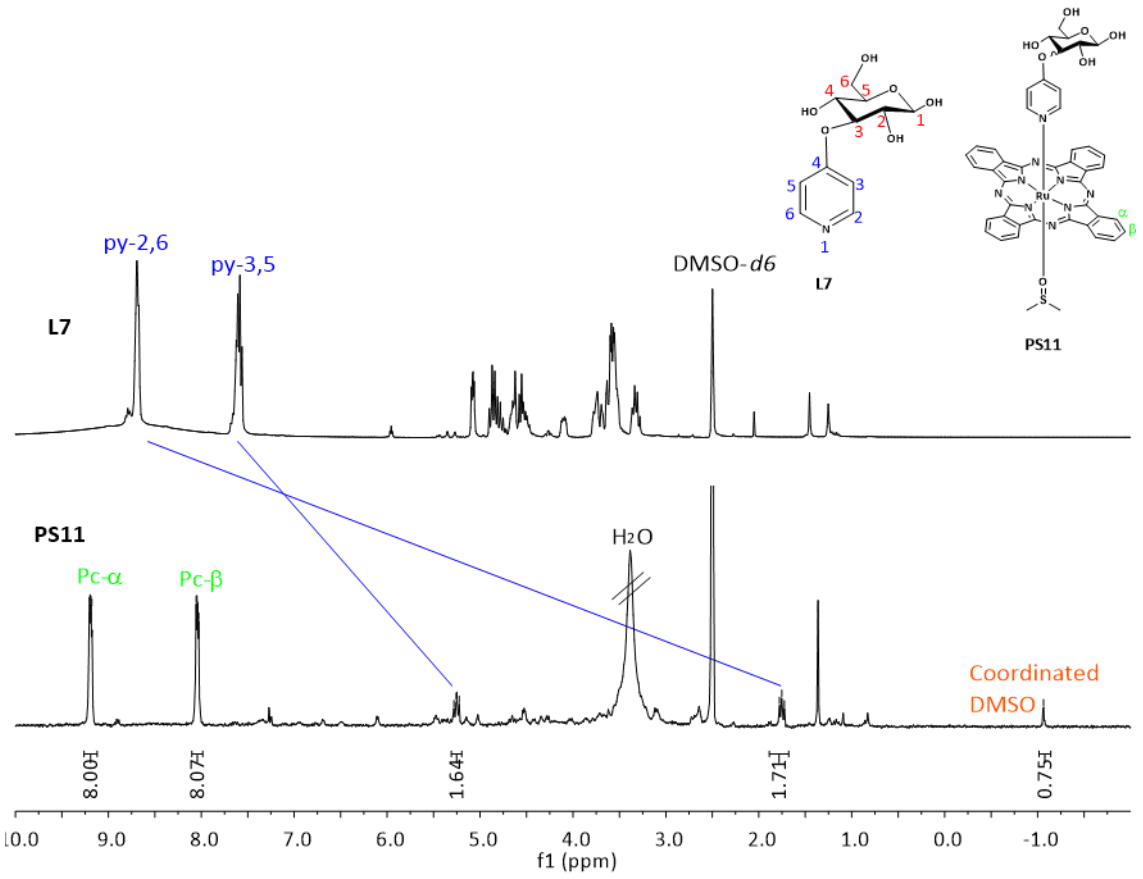

Figure 54 – Comparative ^{1}H NMR spectra of **L7** and **PS11** in DMSO-d_6.

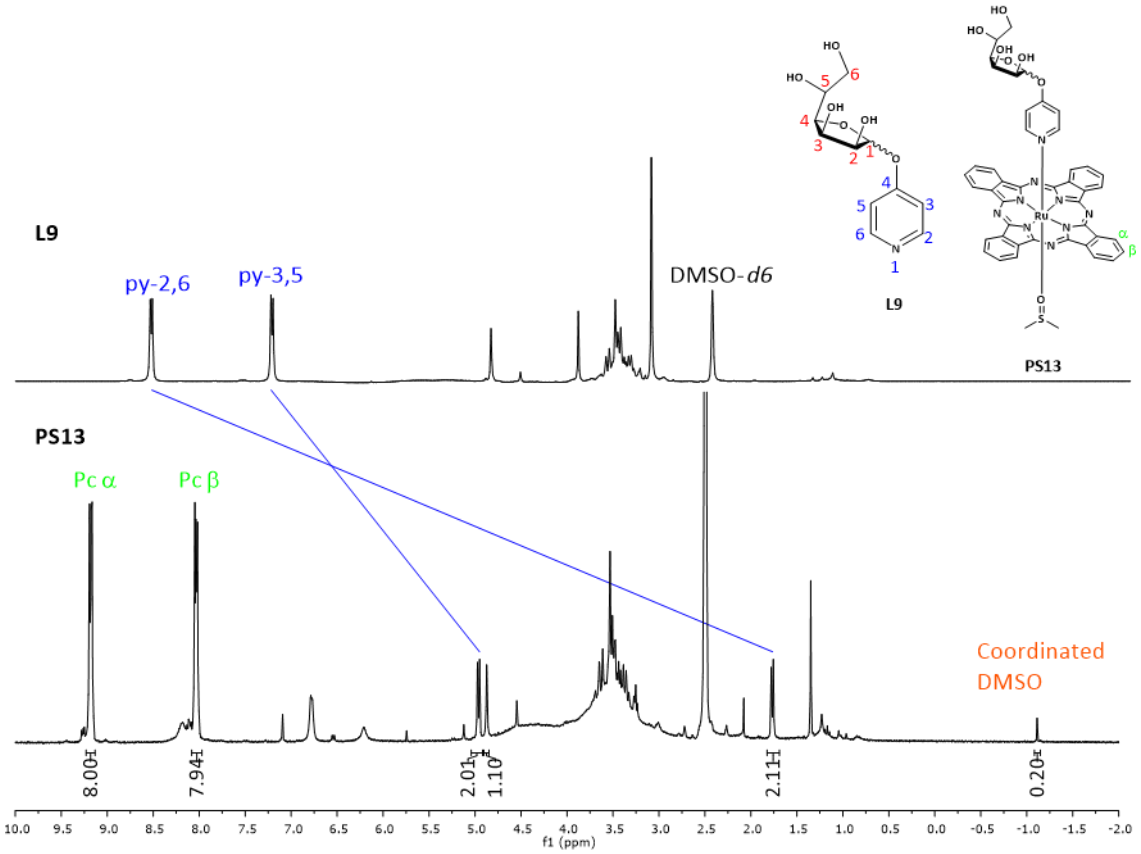

Figure 55 – Comparative ^{1}H NMR spectra of **L9** and **PS13** in DMSO-d_6.

2.2.3. Studies on the purity of PS11-16

The purity of **PS11-16** was further assessed using reverse phase HPLC. The chromatograms obtained for **PS11-16** were compared with the chromatograms of the non-coordinated ligands **L7-9**. **Table 7** describes the retention times of compounds bearing glucose units (**L7**, **PS11** and **PS14**), galactose units (**L8**, **PS12** and **PS15**) and mannose units (**L9**, **PS13** and **PS16**). HPLC was carried out using different mixtures of MeCN/H_2O, such as 50:50, 60:40 and 80:20, and at different flow rates, namely 0.3 and 0.5 mL/min. Detection was performed by UV-Vis at 280 nm, corresponding to the absorption of the free ligands, and at 640 nm, to detect the absorption of RuPcs. For example, when using a 60:40 mixture of MeCN/H_2O at a flow rate of 0.5 mL/min, **PS11** showed only one peak with a retention time of 12.02 min absorbing at 640 nm and at 280 nm, while no peak with a retention time of 7.94 min, corresponding to the free ligand, is observed.

Table 7 – Retention times (min) of **L7-9** and **PS11-16** upon reverse-phase HPLC analysis using a 60:40 mixture of MeCN/H_2O at a flow rate of 0.5 mL/min.

λ	Glucose			Galactose			Mannose		
	L7	**PS11**	**PS14**	**L8**	**PS12**	**PS15**	**L9**	**PS13**	**PS16**
280 nm	7.94	12.02	8.24	7.95	10.67	8.85	7.53	14.62	8.88
640 nm		12.02	8.24		10.67	8.85		14.62	8.88

2.2.4. Studies on the coordination site of DMSO of PS11-16

One of the aspects to be considered in the structure of complexes **PS11-16** is the coordination site of the DMSO. There are few examples in the literature of RuPcs bearing DMSO molecules as axial ligands and, usually, no reference is done with respect to the coordination site to which they are attached, namely S–Ru or O–Ru.[45,291]

One of the models used to explain the coordination of sulfoxides is based on the assumption that DMSO is a resonance hybrid with three canonical forms, which are represented in **Scheme 21**. According to this model, form **A** is considered the best representation of DMSO and, therefore, DMSO is expected to bind Lewis acids by the O atom, which bears a negative charge. The latter is true for the majority of complexes.[292] Nevertheless, S–bonding, which is sterically more demanding, may also occur, as in the case of coordination to soft acids, where the orbital overlap is more favorable with the diffuse σ-orbital of sulfur. Whereas S–bonding involves donation from the σ-orbital of sulfur, O–bonding comprises donation from the π-orbital of oxygen, being more favorable for the coordination with hard acids.[292,293]

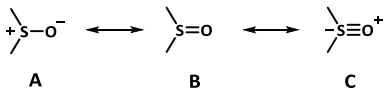

Scheme 21 – Canonical forms contributing to the resonance hybrid of DMSO.

The sulfur atom of DMSO is a moderate π-acceptor that is able to stabilize metals in low oxidation states. For electronic reasons, the coordination to Ru(II) usually occurs *via* the sulfur atom, especially in the presence of pure σ and/or π-donor ligands, although mild π-acceptor ligands

[291] Dolphin, D.; James, B. R.; Murray, A. J.; Thornback, J. R. *Can. J. Chem.* **1980**, *58* (11), 1125–1132.

[292] Davies, J. A. In *Advances in Inorganic Chemistry and Radiochemistry*; Emeléus, H. J., Sharpe, A. G., Eds.; Elsevier B.V, 1981; Vol. 24, pp 115–187.

[293] Alessio, E. *Chem. Rev.* **2004**, *104* (9), 4203–4242.

are also accepted. In contrast, O–bonding occurs if strong π-acceptor ligands are coordinated to the Ru(II), such as CO or NO.[293]

The coordination site of DMSO can be studied by IR spectroscopy. The $\nu_{S=O}$ stretching of free DMSO appears at 1050 cm^{-1}. Coordination through the sulfur atom shifts this frequency to values close to 1100 cm^{-1} (more triple bond character, form **C**), while O–coordination shifts this frequency to values around 915 cm^{-1} (more single bond character, form **A**).[294-296] Comparison between the IR spectra of DMSO complexes **PS11-16** with the corresponding **PSs 5-10**, bearing two carbohydrate units, (**Figure 56** and **Figure 57**) shed no light about the DMSO coordination site.

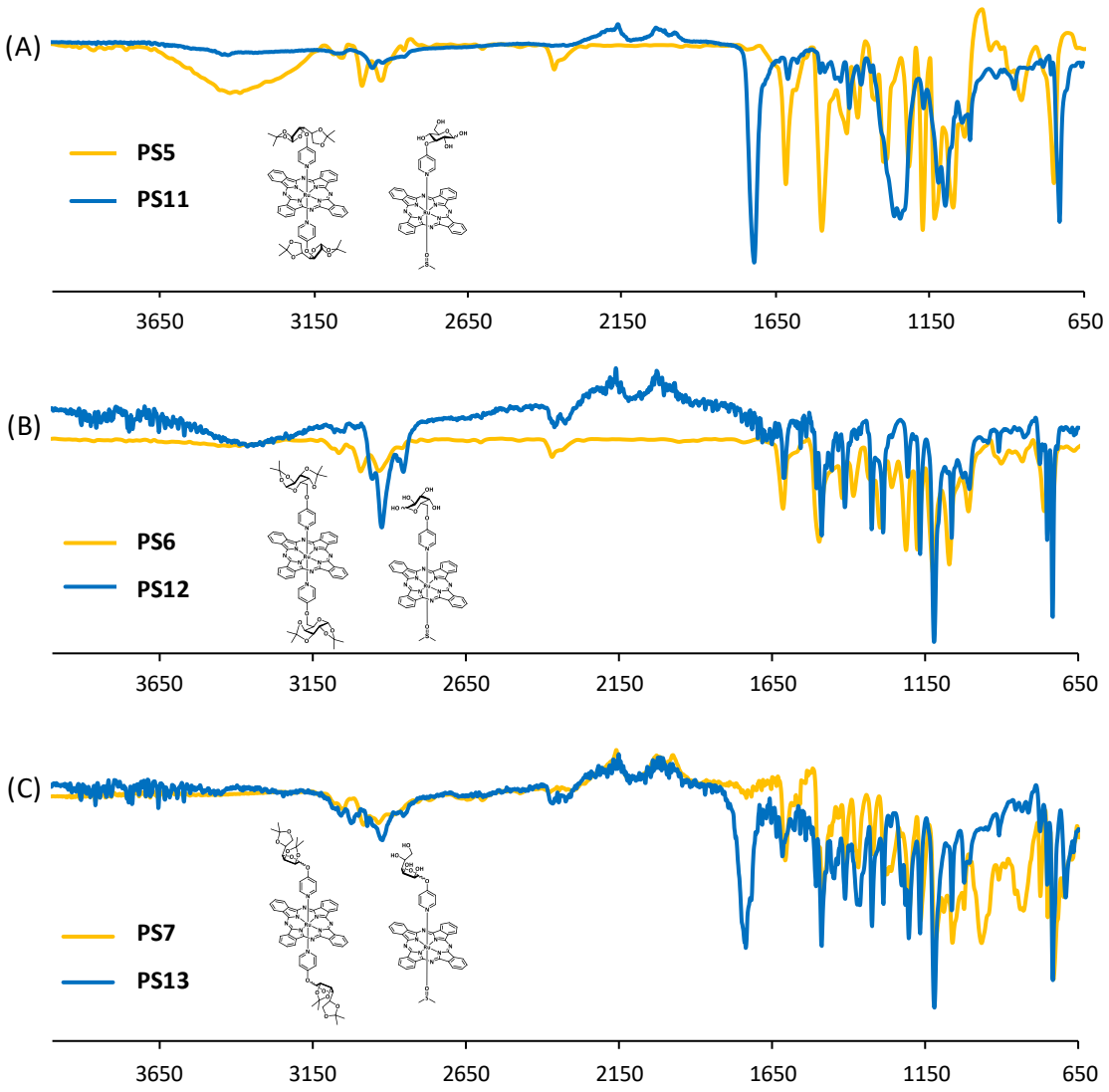

Figure 56 – Comparative IR spectra of (A) **PS5** and **PS11**, (B) **PS6** and **PS12**, (C) **PS7** and **PS13**.

[294] Hudali, H. A.; Kingston, J. V; Tayim, H. A. *Inorg. Chem.* **1979**, *18* (5), 1391–1394.
[295] Rhodes, L. F.; Sorato, C.; Venanzi, L. M.; Bachechi, F. *Inorg. Chem.* **1988**, *27* (4), 604–610.
[296] Alessio, E.; Milani, B.; Calligaris, M.; Bresciani-Pahor, N. *Inorganica Chim. Acta* **1992**, *194* (1), 85–91.

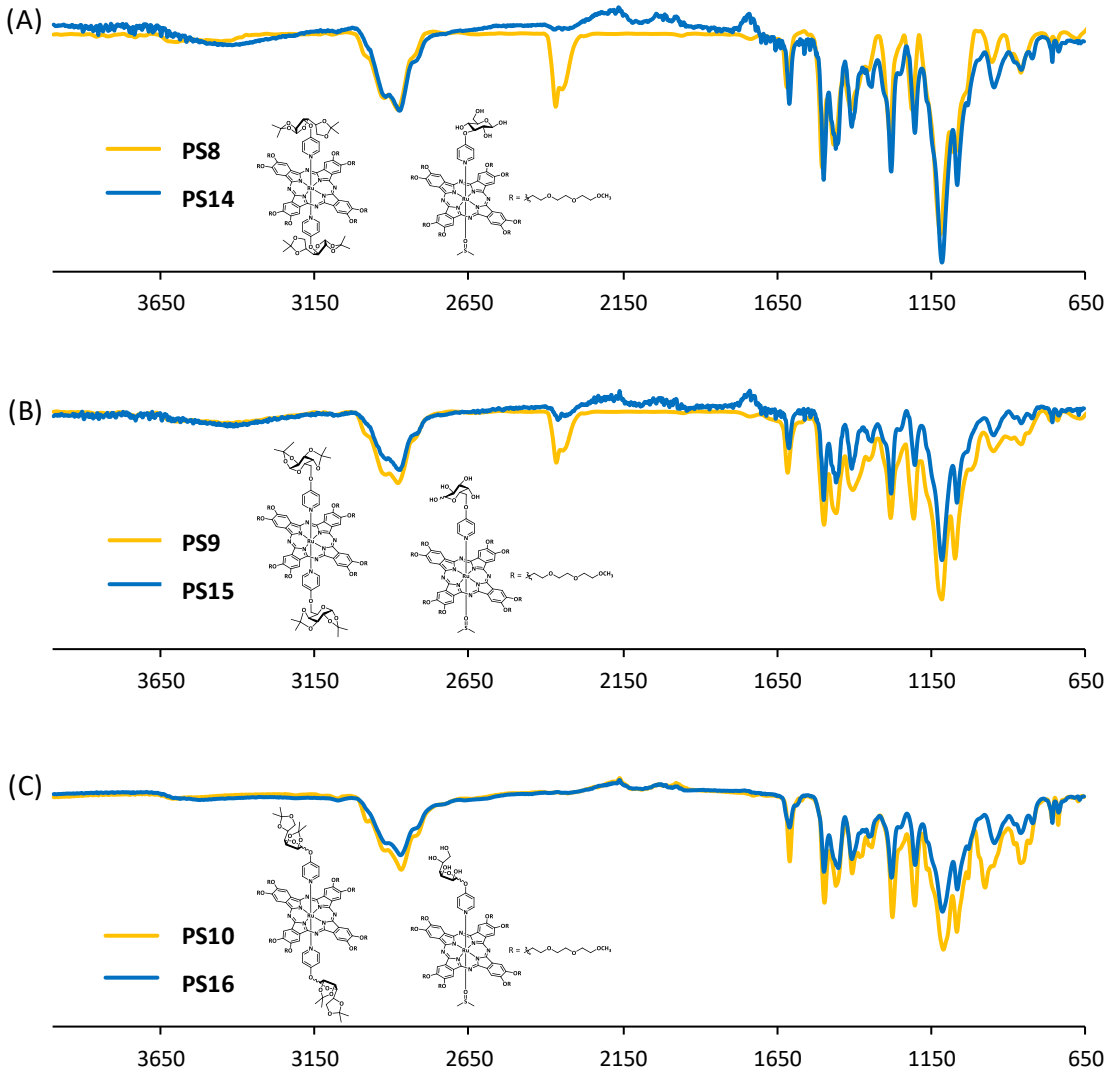

Figure 57 – Comparative IR spectra of (A) **PS8** and **PS14**, (B) **PS9** and **PS15**, (C) **PS10** and **PS16**.

The coordination site of DMSO can also be studied by ^{1}H NMR since this produces distinct effects on the chemical shift of the DMSO methyl protons. While the corresponding resonances appear at 2.53 ppm for free DMSO, S–coordinated DMSO usually exhibits an upfield shift of about 1 ppm. On the other hand, O–coordination has a weaker effect, and the methyl protons usually aren't shifted by more than 0.5 ppm.[292,295,296] As mentioned before, for **PS11-16**, the peak corresponding to coordinated DMSO appears at –1.11 ppm, a much larger upfield shift (3.64 ppm) than that expected for S–coordinated complexes (1 ppm). This strong shift arises from two different effects that could not be quantified separately, namely, coordination of DMSO to Ru(II) and placement of the DMSO ligand in the shielding cone of the diamagnetic RuPc. However, taking into account the magnitude of the upfield shift, (3.64 ppm) and comparing this value with that observed

for Ru-coordinated pyridyl ligands, that is, ~6.8 ppm for three-bond H–Ru distance, and 2.3 ppm for four-bond H–Ru distance (see for example **Figures 54** and **55**), we find very reasonable the DMSO is coordinated to RuPcs through the oxygen atom. This should produce signals for the DMSO protons shifted upfield by ca. 2.8 ppm, very close to those observed experimentally, contrasting to values expected for S–coordination (7.8 upfield shifts), very far from the experimental values.

2.2.5. UV-Vis spectra of PSs and aggregation studies

As described in chapter 1.3.4., the hydrophilicity of **PS5-16** was attested through the UV-Vis spectroscopy in DMSO and water. The absorption spectra of **PS5-10**, which were recorded in DMSO, H_2O/DMSO (99:1) and, in the case of **PS8-10**, in neat water, are represented in **Figure 58**. The corresponding Q-band absorption maxima and absorption coefficients (ε) are listed in **Table 8**.

As observed before for **PS1**, **PS2** and **PS4**, the position of the Q-band in **PS5-7** is maintained with respect to **RuPc D**, therefore neither the presence of electron-withdrawing nor electron-donating groups influences the Q-band of RuPcs.

Due to the presence of eight TEG chains at the periphery of the macrocycles, **PS8-10** were more soluble in the 99:1 mixture of H_2O/DMSO and in neat water, when compared with unsubstituted **PS5-7**, which partially precipitated in the same mixture of solvents. However, the solubility of **PS8-10** in water is still limited, judging by the lower absorption intensities of both Soret and Q-bands, which indicate partial precipitation in these media.

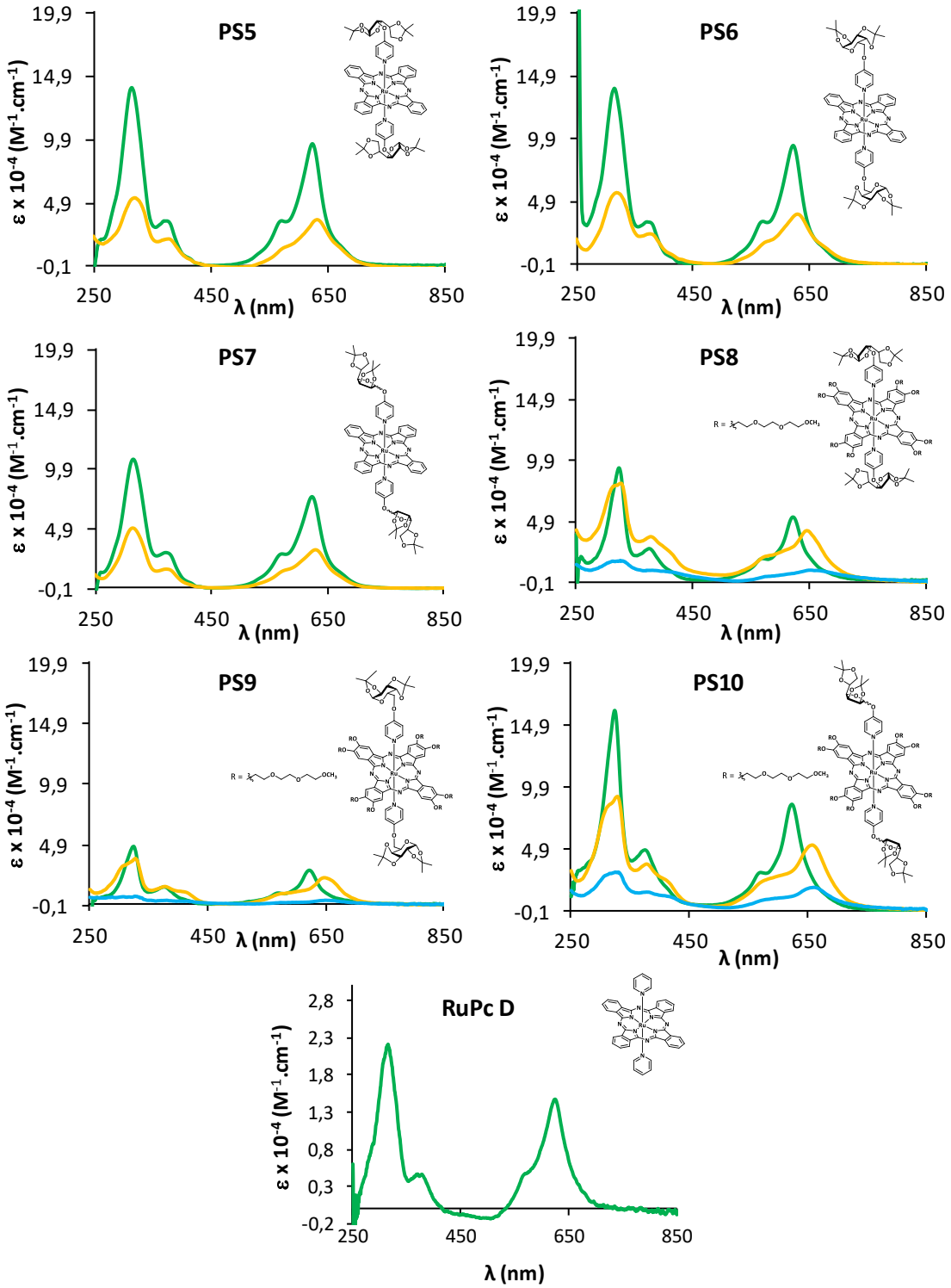

Figure 58 – Absorption spectra of **PS5-10** and **RuPc D** in DMSO (green line), in a 99:1 mixture of H_2O/DMSO (orange line) and in H_2O (blue line).

Furthermore, for **PS8-10** the Q-band maxima show a pronounced red-shift of 24-26 nm upon increasing the solvent polarity. This phenomenon has been assigned to positive solvatochromism and suggests that the polar solvents stabilize the excited state of the PSs.[297]

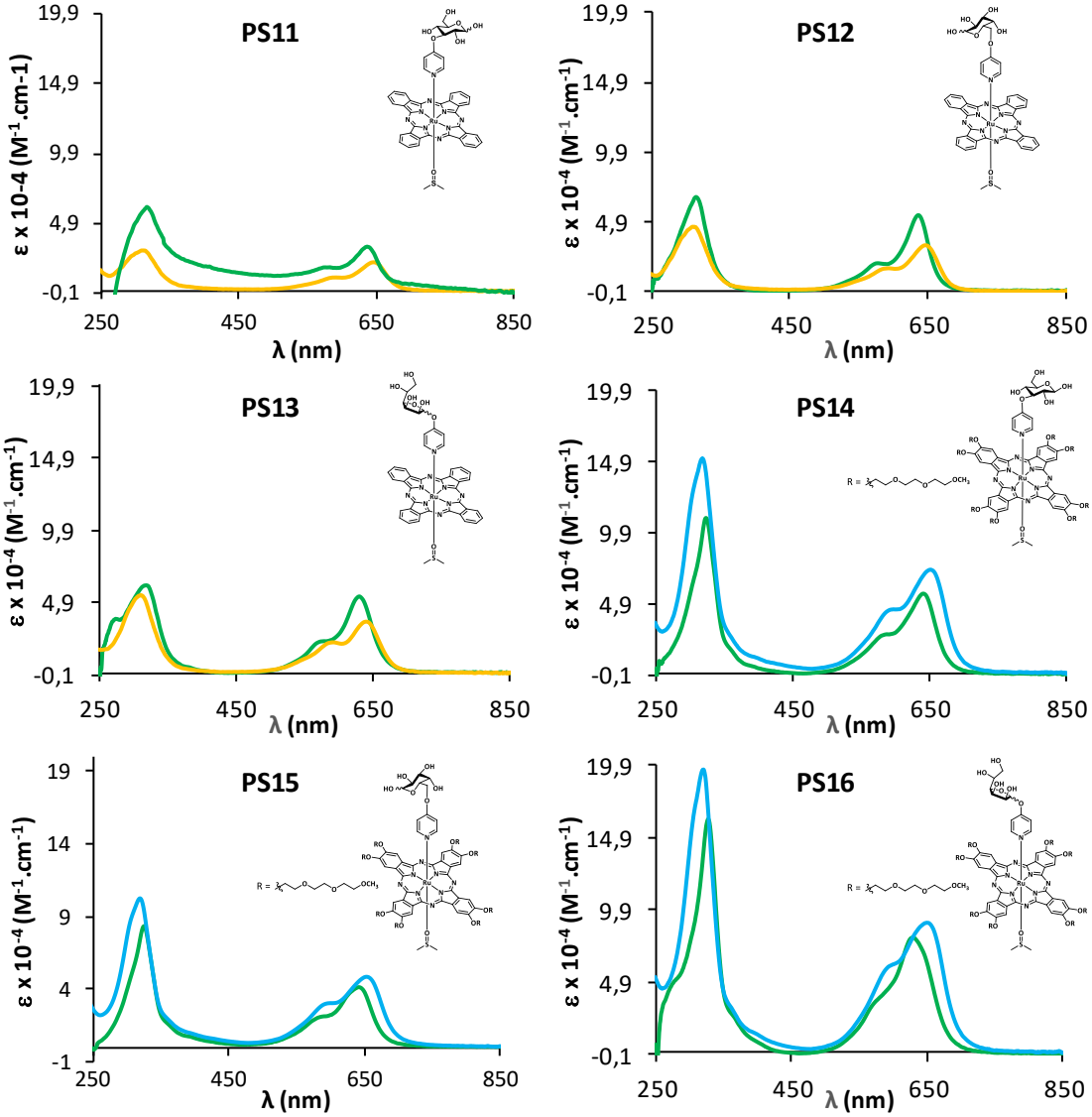

Figure 59 – Absorption spectra of **PS11-16** in DMSO (green line), in a 99:1 mixture of H_2O/DMSO (orange line) and in H_2O (blue line).

Compounds bearing deprotected carbohydrate units (**PS11-13**) exhibited a red-shifted Q-band (8-13 nm) when compared with **RuPc D**. The coordination of DMSO to RuPc is likely responsible for this displacement of the Q-band, since this effect was not observed for the corresponding **PS5-7** bearing two carbohydrate units.

[297] Randles, E. G.; Bergethon, P. R. *J. Phys. Chem. B* **2013**, *117* (35), 10193–10202.

Furthermore, (**Figure 59**) **PS11-13** showed some precipitation in a 99:1 mixture of H_2O/DMSO, although to a lesser extent than that observed for **PS5-7**. **PS14-16**, functionalized with eight TEG chains at their peripheral positions, exhibited the greatest solubility in water, with absorption coefficients even higher in water than in DMSO. Overall **PS11-16** proved to be more soluble in water than **PS5-10**, evidencing the importance of the deprotection of the monosaccharide moieties in order to increase the hydrophilicity of these compounds.

Table 8 – Absorption spectra data and singlet oxygen quantum yields (Φ_Δ) for **PS5-16** and **RuPc D**.

PS	Q-band maximum, nm (ε x 10^{-4}, $M^{-1}.cm^{-1}$)		
	DMSO	**H_2O/DMSO (99:1)**	**H_2O**
5	623 (9.55)	631 (3.25)	
6	623 (9.38)	630 (3.89)	
7	623 (7.62)	629 (3.20)	
8	622 (5.27)	644 (4.17)	652 (0.94)
9	622 (2.79)	649 (2.22)	649 (0.36)
10	623 (8.52)	657 (5.23)	658 (1.82)
11	637 (3.21)	646 (2.06)	
12	638 (5.38)	649 (3.25)	
13	633 (5.29)	642 (3.28)	
14	643 (5.59)		654 (7.31)
15	643 (7.26)		654 (6.27)
16	630 (7.97)		651 (8.96)
RuPc D	625 (1.48)		

In order to assess the aggregation properties of the PSS, dilution studies on **PS5** and **PS8** (**Figure 60**), and of **PS13** and **PS14** (**Figure 61**) were also recorded in a 99:1 mixture of H_2O-DMSO using concentrations ranging from 100 μM to 0.5 μM. It can be seen that, while **PS5** and **PS13**, with no peripheral substituents, follow the Lambert-Beer law up to the concentration of 15 μM, while for **PS8** and **PS14**, with PEG chains at the periphery, the regressing line fits up to 25 μM. Further studies on the aggregation of **PS11-16** are described in Chapter 4.

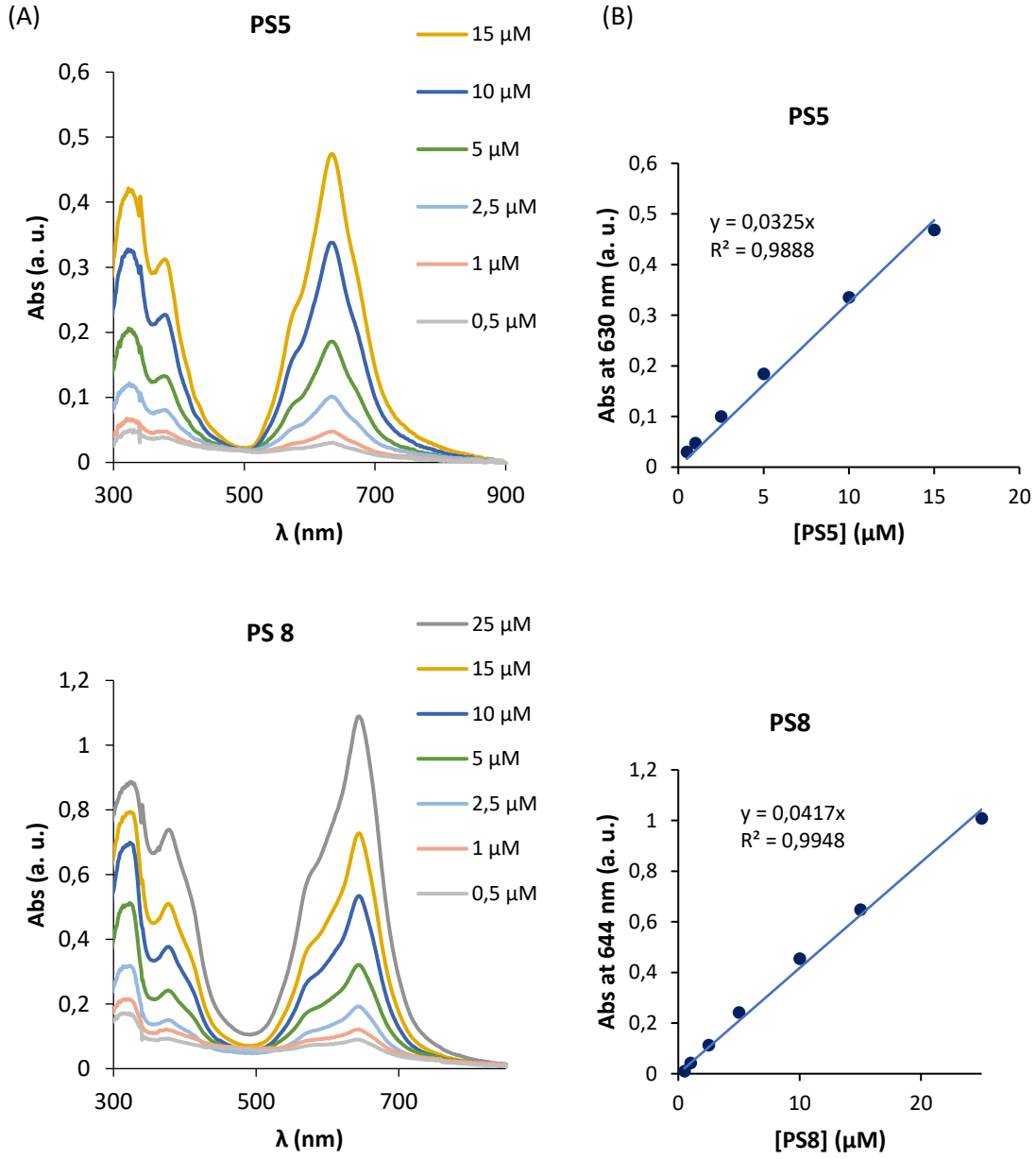

Figure 60 – UV-Vis dilution studies of **PS5** and **PS8** a 99:1 mixture of H_2O/DMSO.

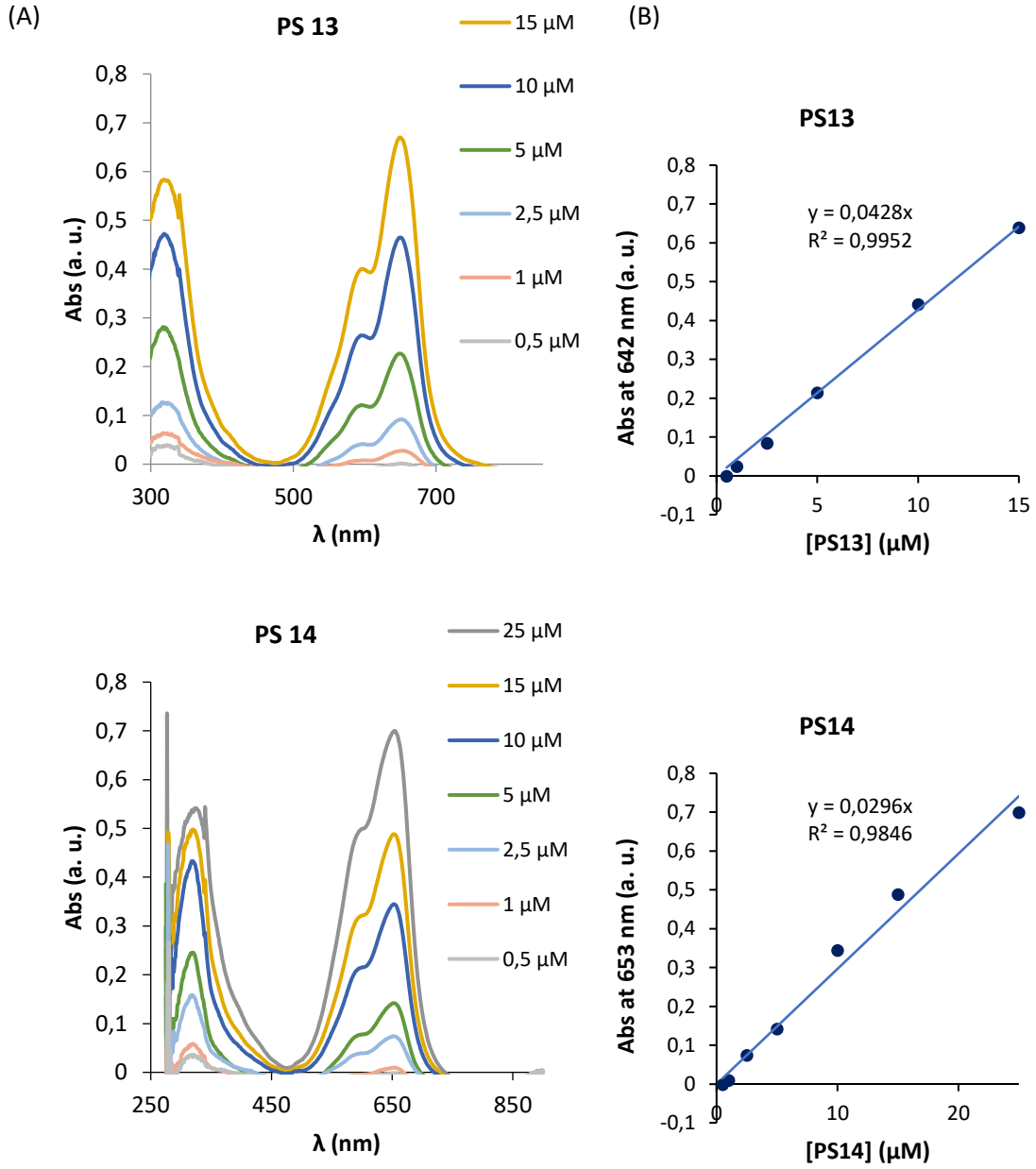

Figure 61 – UV-Vis dilution studies of **PS13** and **PS14** a 99:1 mixture of H_2O/DMSO.

2.2.6. Photostability studies

The photostability of **PS5-16** (**Table 9**) were studied under the same conditions as those used for **PS1-4**.

The photobleaching of the less hydrophilic compounds, **PS5-13**, was measured in DMSO. All of the PSs showed high photostability in this solvent (**Figure 62** and **Figure 63**), with **PS8** being the least stable one, with a decrease in Q-band intensity of 7%.

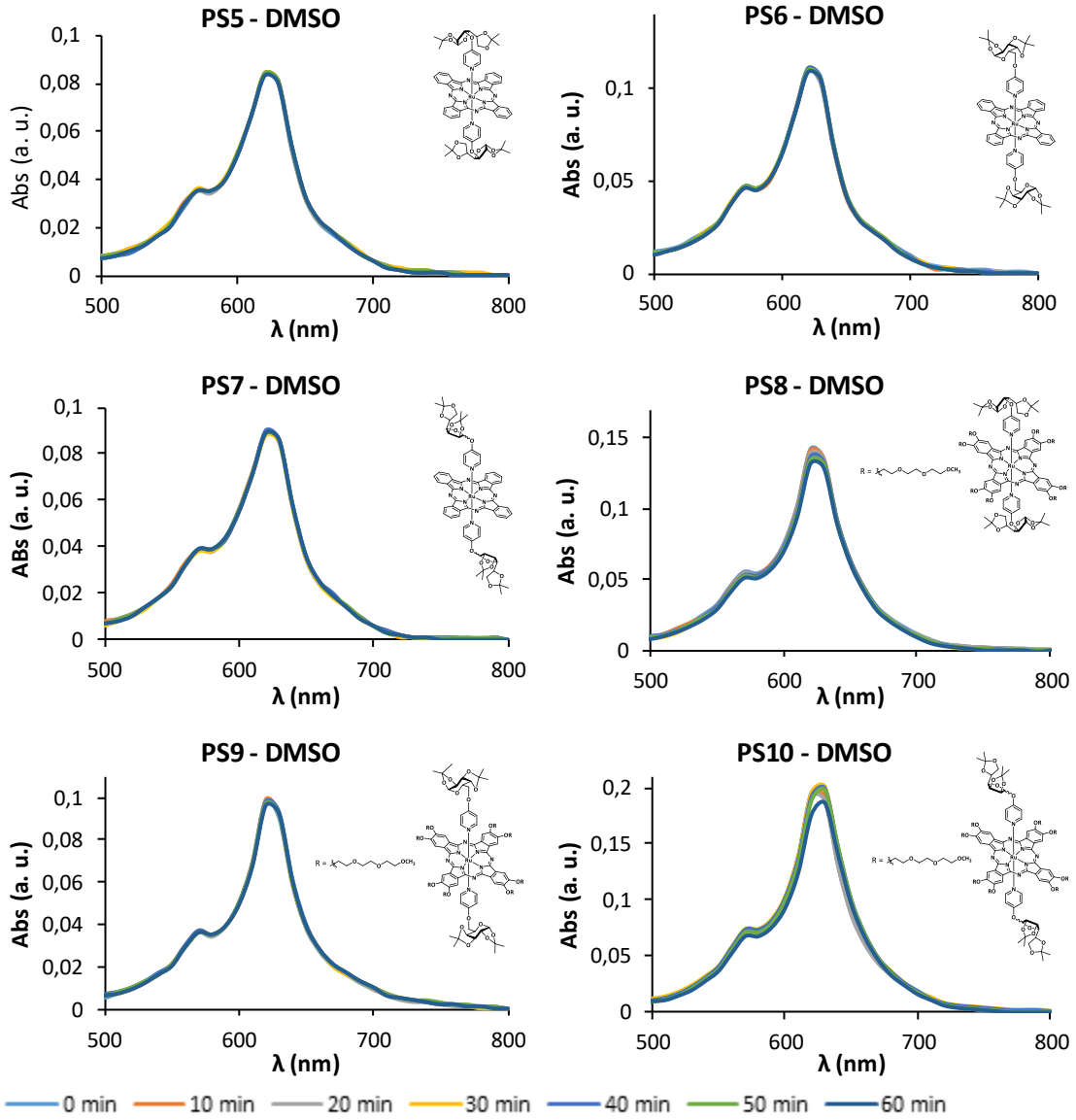

Figure 62 – Photostability of **PS5-10** (5μM solutions in DMSO) after irradiation with red light at a fluence rate of 20 mW/cm^2 at intervals of 10 min, for a total of 60 min.

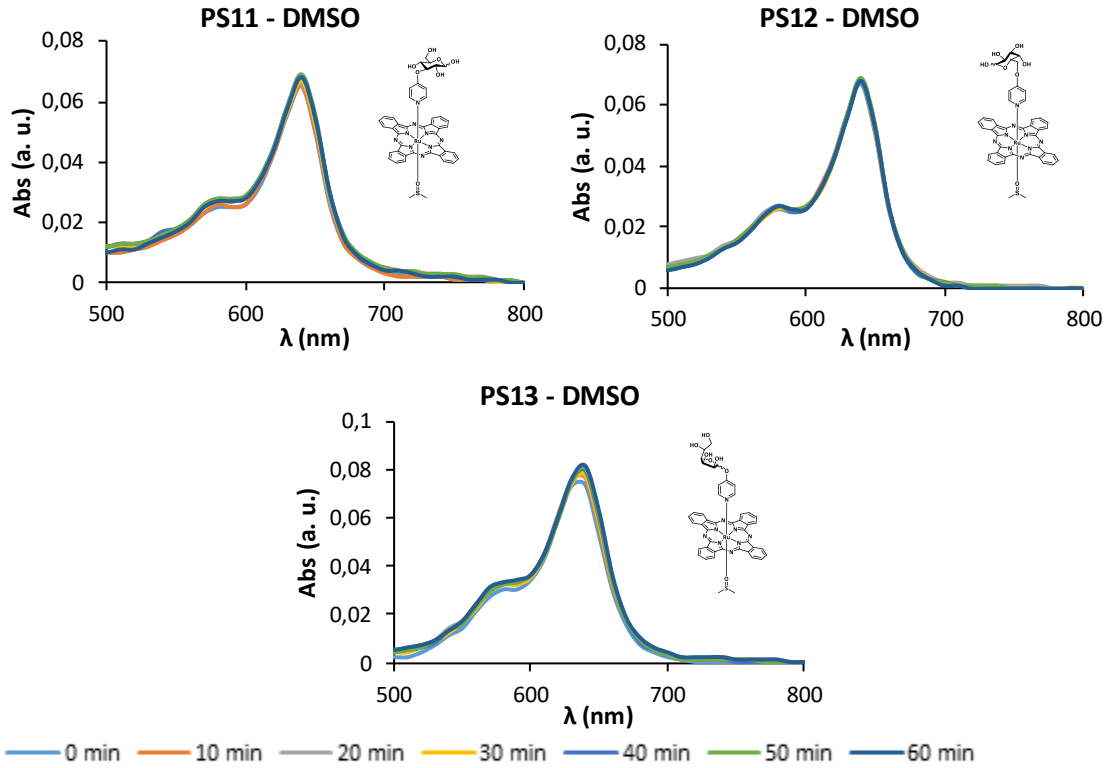

Figure 63 – Photostability of **PS11-13** (5µM solutions in DMSO) after irradiation with red light at a fluence rate of 20 mW/cm^2 at intervals of 10 min, for a total of 60 min.

Among **PS14-16**, which also exhibit high photostability in DMSO solutions (**Figure 64**), **PS16** showed the most significant decrease (5%) in its absorption intensity. In PBS, these compounds were slightly less photostable (9-11% decrease in absorption), although still much more stable than **PS2a**, **PS3** and **PS4**.

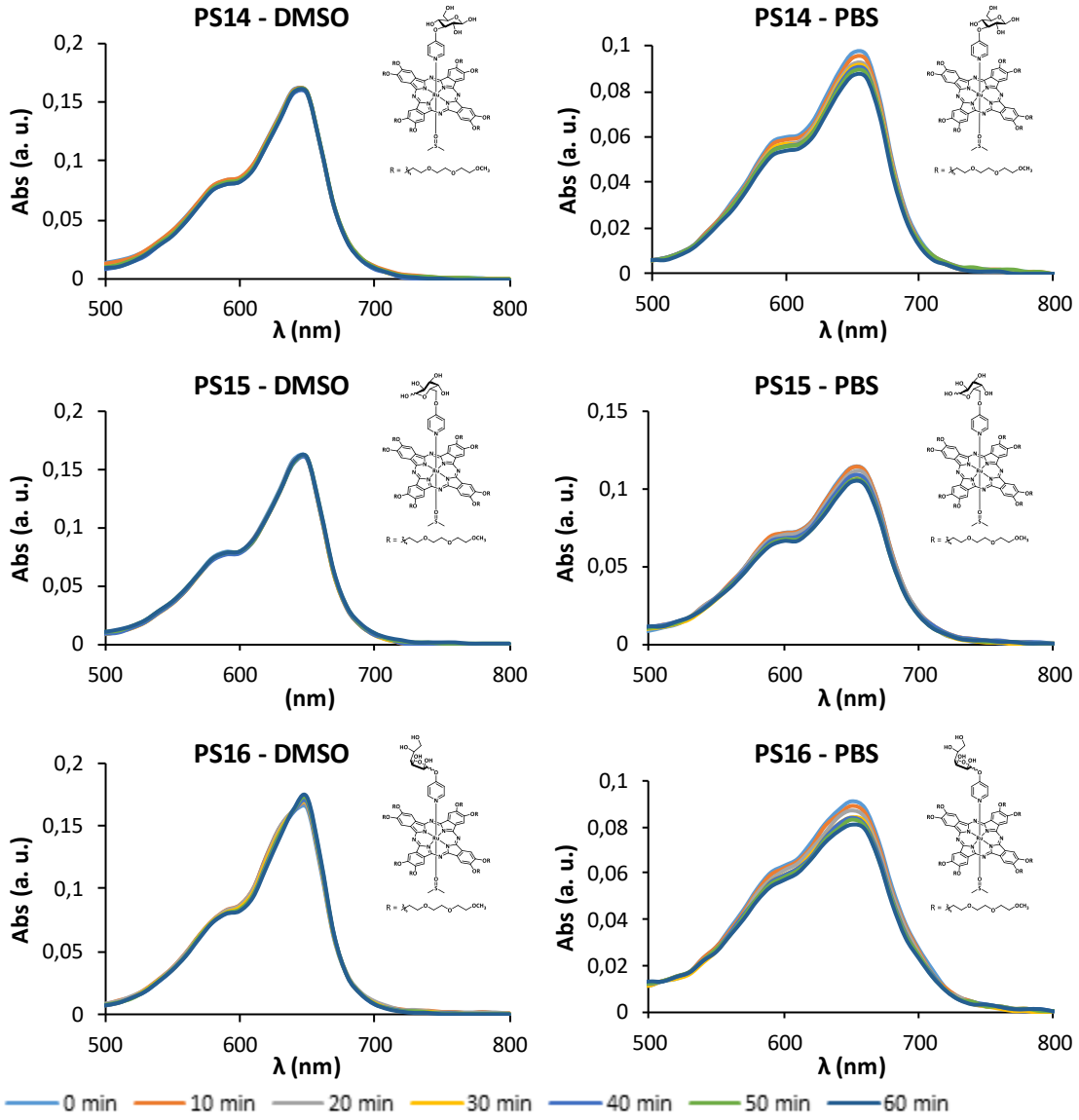

Figure 64 – Photostability of **PS14-16** (5µM solutions in DMSO and in PBS) after irradiation with red light at a fluence rate of 20 mW/cm^2 at intervals of 10 min, for a total of 60 min.

Table 9 – Photostability of **PS5-16** in 5μM solutions in DMSO (for all PSs) and in PBS (for **PS14-16**) after irradiation with red light at a fluence rate of 20 mW/cm^2 at intervals of 10 min, for a total of 60 min. Results are given as % from Abs at t = 0 min.

PS	Solvent	Time (min)						
		0	10	20	30	40	50	60
5	DMSO	100	100	99	100	99	100	99
6	DMSO	100	100	101	101	101	100	99
7	DMSO	100	100	100	100	100	100	100
8	DMSO	100	99	98	96	96	94	93
9	DMSO	100	101	100	99	99	99	98
10	DMSO	100	100	99	99	98	96	90
11	DMSO	100	100	100	100	100	100	100
12	DMSO	100	99	99	99	99	99	99
13	DMSO	100	100	100	100	100	100	100
14	DMSO	100	99	99	99	99	99	99
	PBS	100	98	95	94	93	92	90
15	DMSO	100	100	100	100	100	100	100
	PBS	100	99	96	95	95	92	91
16	DMSO	100	99	99	98	97	96	95
	PBS	100	98	96	92	92	91	89

2.2.7. Generation of singlet oxygen

Due to the low solubility in water of **PS5-10**, their singlet oxygen quantum yields were only measured in DMSO (**Table 10**). As observed in chapter 1.3.5., the highest Φ_Δ values were obtained for peripherally unsubstituted RuPcs (**PS5-7**). The Φ_Δ values varied from 0.16 to 0.21, compared to values of 0.08 for the PSs substituted at the periphery with TEG chains (**PS8-10**).

Overall, compounds functionalized with two protected carbohydrates at the axial positions (**PS5-10**) were less efficient in the production of singlet oxygen (Φ_Δ = 0.08 - 0.21) than compounds bearing PEG chains at axial positions (**PS1-4**, Φ_Δ = 0.20 - 0.79). Moreover, **PS5-7**, with quantum yields around 0.2, were less efficient than **RuPc D** (Φ_Δ = 0.56) to produce singlet oxygen, in contrast with **PS1**, **PS2** and **PS4**, which exhibited higher Φ_Δ values, around 0.8. This further supports our first assumption that pyridyl ligands functionalized with electron-withdrawing groups increase the singlet oxygen quantum yields, while pyridyl ligands endowed with π-electron-donating groups decrease it.

Among **PS11-16** functionalized with one deprotected carbohydrate unit and one DMSO molecule, compounds without peripheral functionalization (**PS10-13**) displayed the maximum yield

of singlet oxygen generation (**Table 10**). Their Φ_Δ values ranged from 0.80 to 0.99, whereas peripherally TEG donated **PS14-16** showed values between 0.52 and 0.74.

The singlet oxygen quantum yields of **PS14-16** were also measured in D_2O. As expected, a decrease in Φ_Δ was observed on going from DMSO to water. Still, the observed Φ_Δ values, which varied between 0.35 and 0.59, are very promising, being even higher than those obtained previously for **PS2a, PS3** and **PS4**. Among PSs bearing deprotected carbohydrate units, **PS13** and **PS16**, with a mannose unit, registered the lowest Φ_Δ values.

Summarizing, **PS11-16** containing a carbohydrate and a DMSO axial ligand, are the most efficient photosensitizers, with efficiencies in DMSO ranging from 0.52 to 0.99, and in water from 0.35 to 0.59. Therefore, DMSO as axial ligand seems to strongly increase the capacity of the photosensitizer to produce singlet oxygen.

Table 10 – Singlet oxygen quantum yields (Φ_Δ) for **PS5-16.**

PS	Φ_Δ	
	DMSO	**D_2O**
5	0.21	
6	0.16	
7	0.21	
8	0.08	
9	0.08	
10	0.08	
11	0.99	
12	0.95	
13	0.80	
14	0.74	0.58
15	0.74	0.59
16	0.52	0.35

2.3. Mixed RuPcs donated with axial pyridyl ligands functionalized with PEG chains and carbohydrate units

2.3.1. Coordination reactions to RuPc A and RuPc B

With the purpose of conjugating the hydrophilicity provided by the polyether chains and the selectivity delivered by the carbohydrate units, PSs with two different axial ligands were prepared. Coordination reaction were carried out in chloroform at 50 °C and protected from light, using different combinations of ligands **L1-2** and ligands **L4-6**, giving rise to mixed **PS17-28** in moderate yields (5-35%) (**Scheme 22**).

PS17-28 were isolated by column chromatography on silica gel. In this way, it was possible to separate the three products of each coordination reaction: a RuPc bearing *i)* two carbohydrate units; *ii)* one carbohydrate unit and two PEG chains; and *iii)* four PEG chains.

PS17-28 were characterized by ^{1}H NMR and MS spectrometry. All PSs exhibited peaks corresponding to $[M + H]^+$ in their ESI^+ spectra. **Figure 65** shows the ^{1}H NMR spectra in $CDCl_3$ of **L1**, **L4** and **PS17** as an illustrative example. Coordination of ligands **L1** and **L4** to **RuPc A** shifted their resonances similarly to that described above for symmetrical compounds **PS1** and **PS5**. The pyridyl protons of **L1,** H^2 and H^6, exhibited high field doublets at 3.23 ppm, upfield shifted by 6.19 ppm, while H^4, which is further apart from the macrocycle, appeared at 7.24 ppm, upfield shifted by 1.68 ppm, with respect to the free ligand. Signals corresponding to the axial PEG chains were also influenced by the diamagnetic RuPc, with the closest $COOCH_2$ displaying their resonance shifted to high field by δ 0.65 ppm. Coordination of **L4** also produced shielding of its resonances. In particular, signals of H^2 and H^6 pyridyl protons moved by 6.22 ppm, whereas peaks of H^3 and H^5 pyridyl protons were shielded by 2.06 ppm. The signals of the glucose moiety were also shifted, with the anomeric carbon showing a displacement of 0.62 ppm. **PS18-28** displayed comparable features in their ^{1}H NMR spectra.

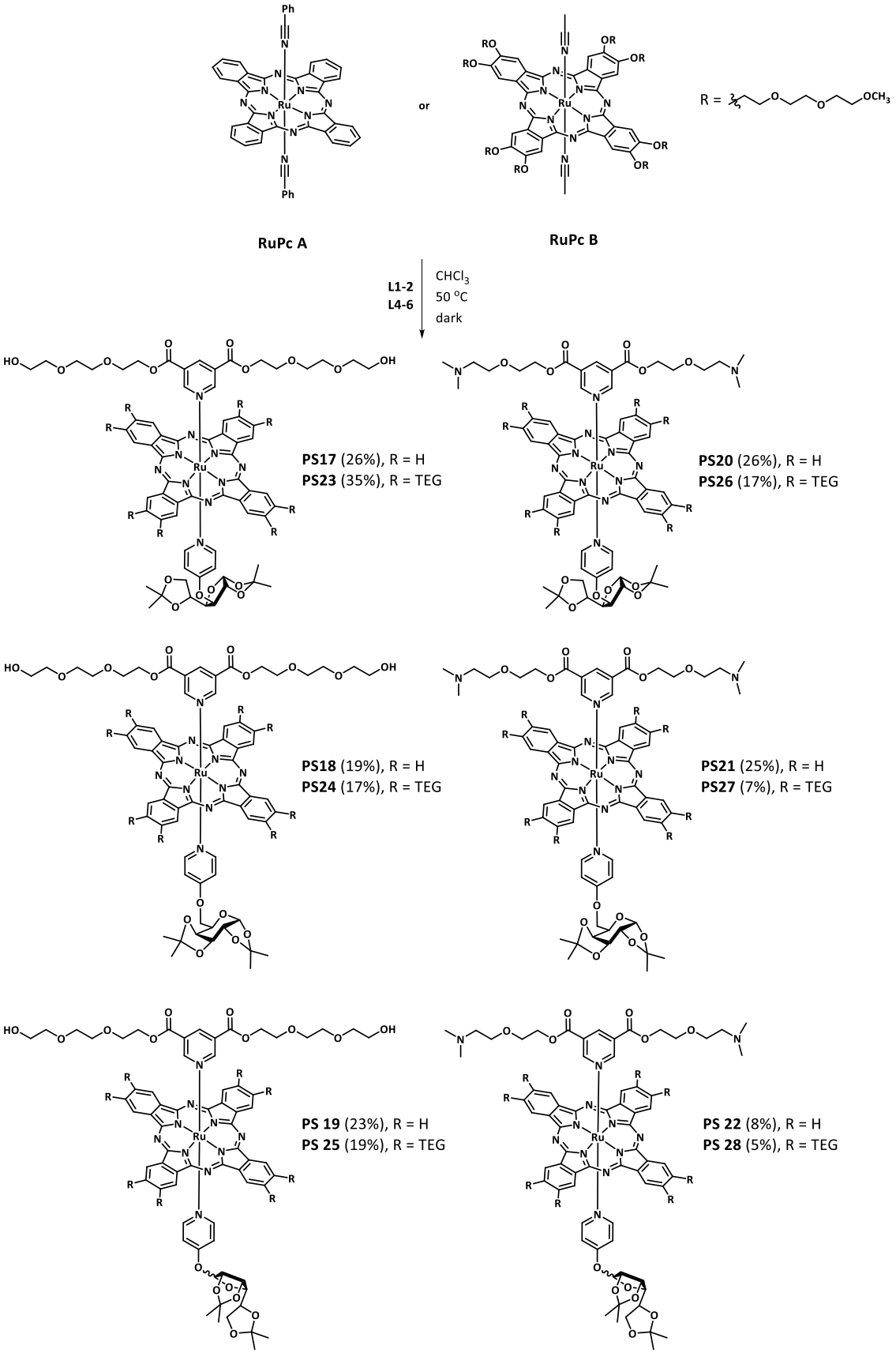

Scheme 22 – Preparation of **PSs 17-28**.

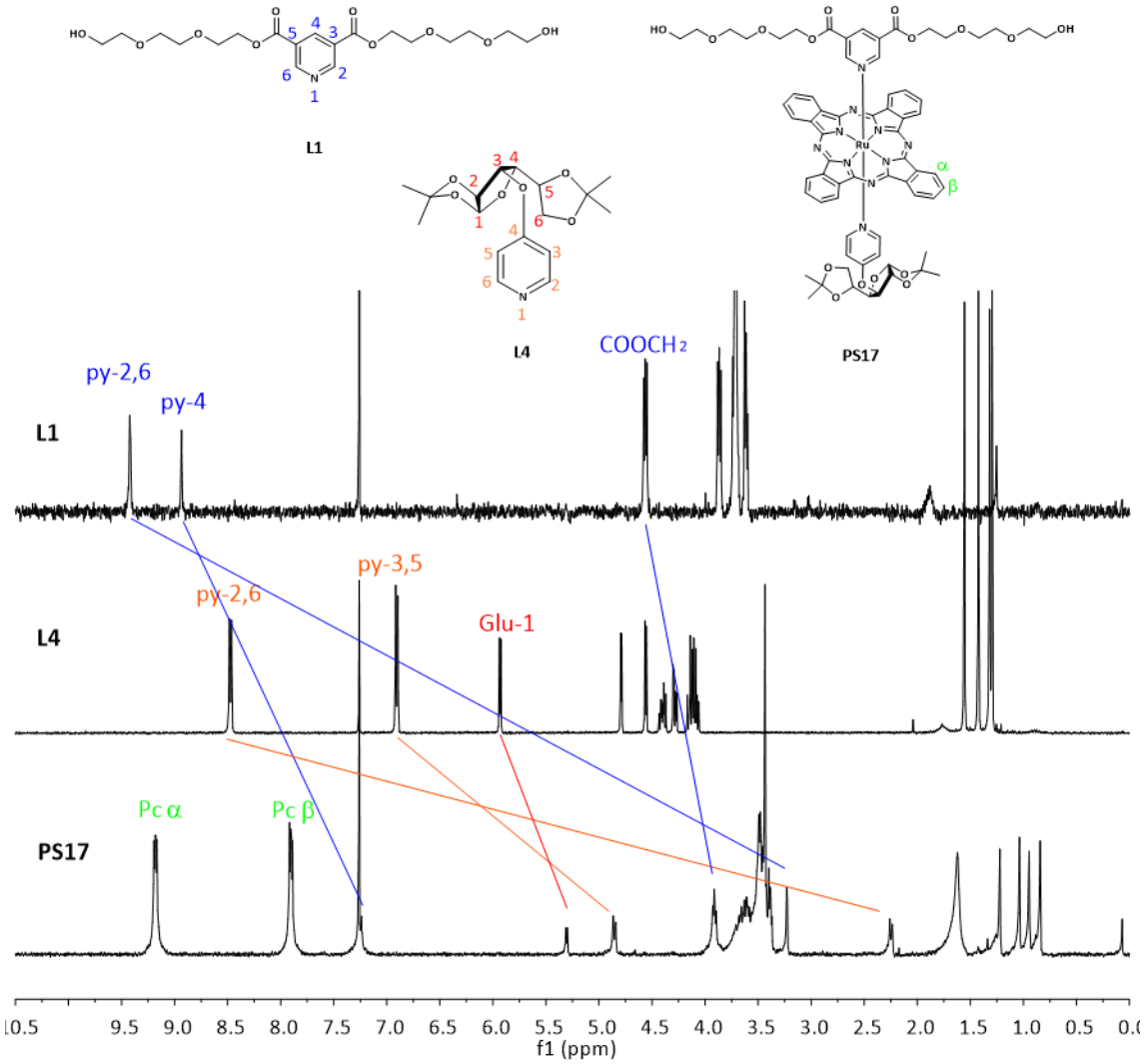

Figure 65 – Comparative ^{1}H NMR spectra in $CDCl_3$ of **L1**, **L4** and **PS17**.

2.3.2. UV-Vis spectra of PSs and aggregation studies

The UV-Vis spectra of unsubstituted RuPcs (**PS17-22**) were recorded in DMSO and in a 99:1 mixture of H_2O/DMSO (**Figure 66** and **Table 11**). The latter produced a decrease in both Soret and Q-band intensities with respect to neat DMSO, due to their partial precipitation in the presence of water, as observed before for compounds with no peripheral substituents.

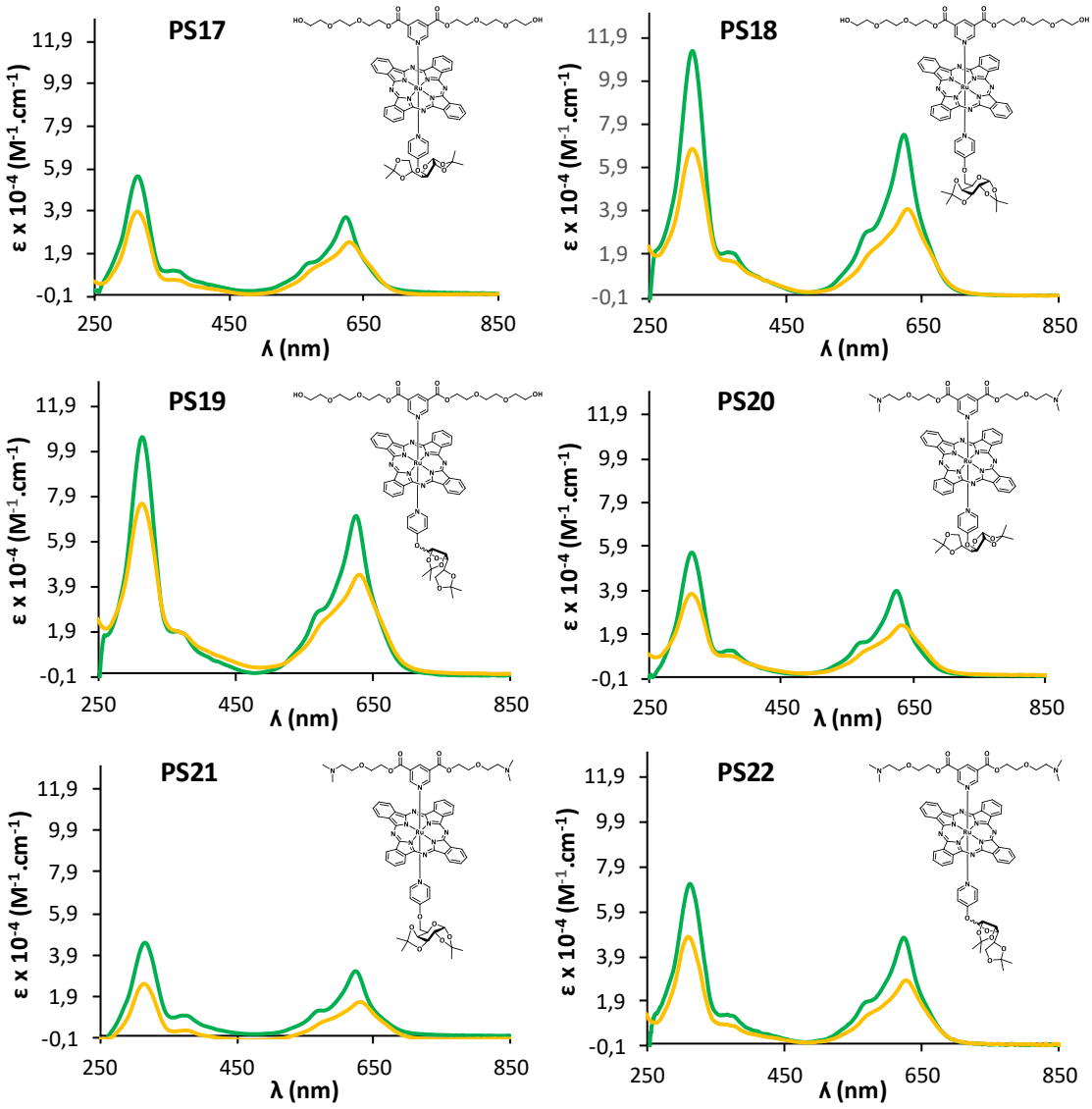

Figure 66 – Absorption spectra of **PS17-22** in DMSO (green line) and in 99:1 mixtures of H_2O/DMSO (orange line).

Figure 67 shows the UV-Vis spectra of **PS23-28**, bearing PEG chains at the periphery, which were measured both in DMSO and in neat H_2O. Absorption coefficients are only slightly smaller in water than in DMSO for all of them. The solubility is significantly higher than that of the corresponding RuPcs functionalized with two protected carbohydrate units (**PS8-10**), although considerably lower than that of **PS3**, which bears four PEG chains at the axial positions. Therefore, we concluded that the introduction of protected carbohydrate units reduces the hydrophilicity of RuPcs, whereas the functionalization with polyether chains greatly increases their solubility in aqueous solutions. The reduced solubility in water, related to that in DMSO, is less marked in **PS26-28**, with terminal amino groups, than in **PS23-25**, with terminal alcohol functions.

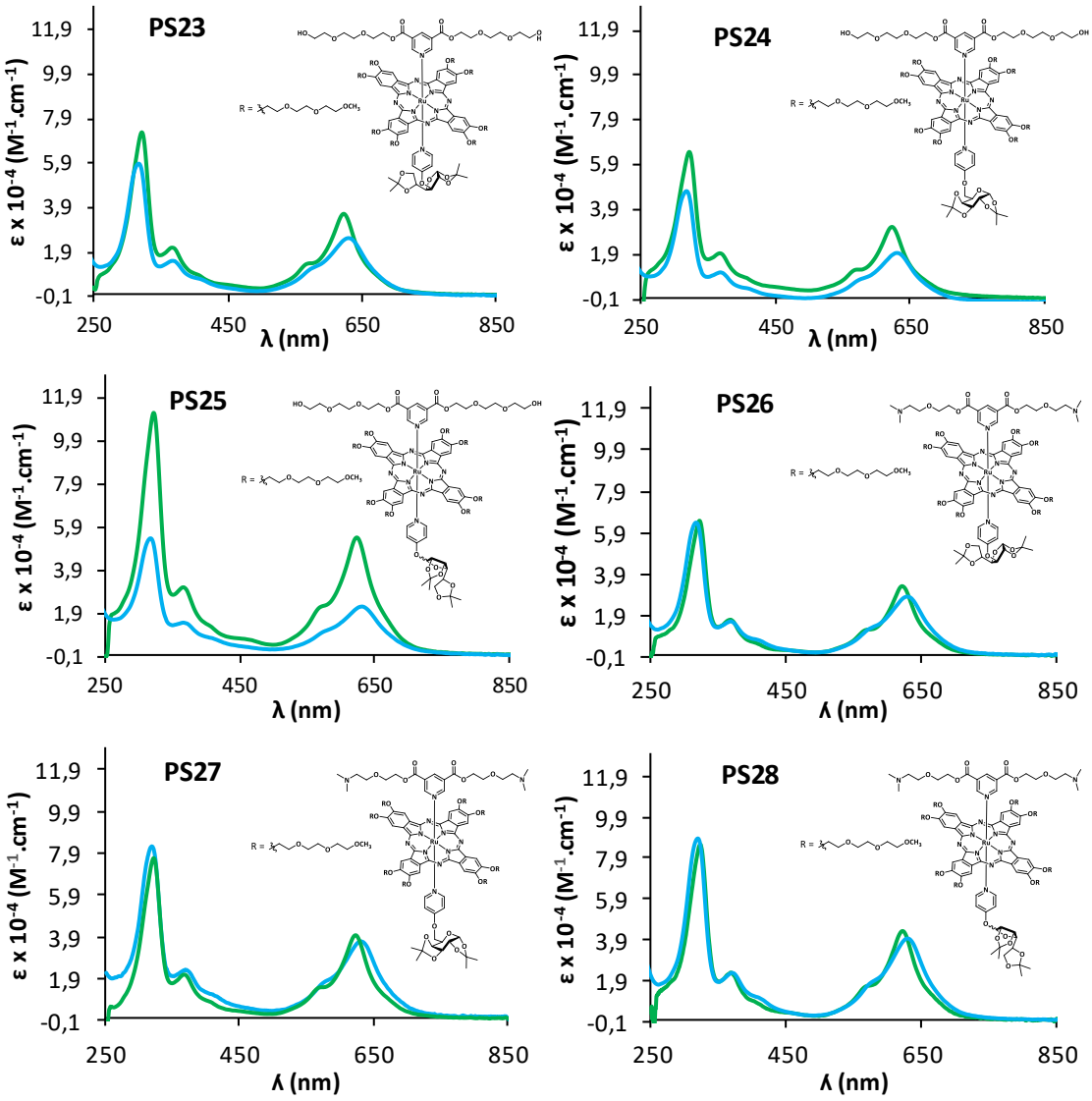

Figure 67 – Absorption spectra of **PS23-28** in DMSO (green line) and in H_2O (blue line).

Table 11 – Absorption spectra data for **PS17-28**.

PS	Q-band maximum, nm (ε x 10^{-4}, $M^{-1}.cm^{-1}$)		
	DMSO	H_2O/DMSO (99:1)	H_2O
17	624 (3.56)	630 (2.47)	
18	625 (7.42)	630 (3.96)	
19	625 (7.04)	630 (4.40)	
20	624 (3.85)	632 (2.27)	
21	624 (3.09)	630 (1.74)	
22	625 (4.75)	627 (2.83)	
23	623 (2.86)		630 (2.58)
24	623 (3.15)		631 (2.18)
25	623 (5.44)		631 (2.22)
26	623 (3.30)		631 (2.82)
27	623 (3.99)		630 (3.67)
28	623 (4.33)		630 (3.95)

2.3.3. Photostability studies

The photostability of **PS17-28** is summarized in **Table 12**. All compounds showed good photostabilities in DMSO solutions, with small reductions in the Q-band intensity only up to 7%. The photostability of RuPcs with PEG chains at the periphery (**PS23-28**) was also measured in PBS solutions. As observed in previous studies, the photobleaching in PBS was more important than in DMSO, with the Q-band intensities being reduced by 19-26%.

Table 12 – Photostability of **PS17-28** in 5μM solutions in DMSO (for all PSs) and in PBS (for **PS23-28**) after irradiation with red light at a fluence rate of 20 mW/cm^2 at intervals of 10 min, for a total of 60 min. Results are given as % from Abs at t = 0 min.

PS	Solvent	t (min)						
		0	**10**	**20**	**30**	**40**	**50**	**60**
17	DMSO	100	99	99	98	98	97	96
18	DMSO	100	100	100	100	100	100	100
19	DMSO	100	100	99	98	98	98	98
20	DMSO	100	100	99	99	99	98	97
21	DMSO	100	100	100	98	98	98	95
22	DMSO	100	100	98	98	98	98	97
23	DMSO	100	101	99	98	97	96	94
	PBS	100	97	92	91	87	84	81
24	DMSO	100	99	99	98	98	97	94
	PBS	100	95	90	85	83	78	75
25	DMSO	100	100	100	99	98	97	95
	PBS	100	96	91	87	82	81	77
26	DMSO	100	99	98	96	96	95	94
	PBS	100	92	89	84	82	79	74
27	DMSO	100	99	98	96	96	94	93
	PBS	100	95	91	87	83	79	75
28	DMSO	100	100	100	100	100	99	98
	PBS	100	93	88	83	80	76	72

2.3.4. Generation of singlet oxygen

Table 13 comprises the singlet oxygen quantum yields (Φ_Δ) measured for **PS17-28**. As for the symetrical **PS1-10**, the presence of TEG chains at the peripheral positions of the macrocycles decreases the efficiency in producing singlet oxygen. Thus, **PS17-22** showed Φ_Δ values ranging from 0.37 to 0.46, while the quantum yields for **PS23-28** did not exceeded 0.10.

Interestingly, the effect of each axial ligand in the production of singlet oxygen seems to be additive. Thus, mixed **PS17-28** exhibit Φ_Δ values that fall between those obtained for **PS1-4**, functionalized only with PEG chains at the axial positions, and those showed by **PS5-10**, bearing only carbohydrate functions as axial substituents. Again, it seems to be related to the overall electronic donation from the axial ligands to the Ru(II) ion.

The singlet oxygen quantum yields of **PS23-28** were also measured in D_2O, showing a reduced ability for generating singlet oxygen, related to that of **PS2a**, **PS3** and **PS4**, which are functionalized only with PEG chains connected through ester functions.

Table 13 – Singlet oxygen quantum yields (Φ_Δ) for **PS17-28**.

PS	Φ_Δ	
	DMSO	**D_2O**
17	0.40	
18	0.37	
19	0.46	
20	0.37	
21	0.38	
22	0.44	
23	0.08	0.03
24	0.09	0.03
25	0.10	0.03
26	0.08	0.03
27	0.07	0.02
28	0.08	0.03

2.4. RuPcs donated with axial pyridyl ligands functionalized with folic acid units

As mentioned before, a commonly used approach to afford selectivity towards tumor tissues is the use of folic acid (FA), which specifically binds to the folate receptor, whose expression is strongly increased in cancer tissues. Two main synthetic strategies were envisioned for the synthesis of RuPcs endowed with folic acid units at their peripheral positions. The first route (route A), involves the synthesis of a pyridyl ligand donated with a FA unit, using 4-(aminomethyl)pyridine as substrate for the amidation reaction with a FA molecule. This is followed by coordination of this ligand to the axial positions of **RuPc A** or **B**. In the second route (route B), **RuPc A** or **B** are first endowed with 4-(aminomethyl)pyridine, which is then used for the amidation reaction with FA.

2.4.1. Route A: Functionalization of pyridine with folic acid followed by coordination to a RuPc

A pyridine ligand functionalized with a folate unit was designed for its subsequent coordination to **RuPc A** or **B**. **Scheme 23** illustrates the synthetic approach that allowed the synthesis of such pyridine ligand (**L10**), based on a method commonly used for reactions with folic acid.[244,298,299] This methodology consists in an amidation reaction using N-hydroxyl-succinimide (NHS), in the presence of EDC, to activate the carbonyl function of folic acid, followed by the nucleophilic attack by the amine group in 4-(aminomethyl)pyridine, in the presence of TEA as a base. Although FA can be coupled *via* α or γ-carboxyl groups,[235] previous studies have shown that γ-carboxyl-linked conjugates are usually the major products of coupling reactions with amines.[300,301] In fact, only the formation of the corresponding γ-carboxyl-linked conjugates has been reported.[244,298,299] **L10** was characterized by ^{1}H and COSY NMR spectroscopies and by FAB^{+} spectrometry.

[298] Dong, R.; Chen, H.; Wang, D.; Zhuang, Y.; Zhu, L.; Su, Y.; Yan, D.; Zhu, X. *ACS Macro Lett.* **2012**, *1* (10), 1208–1211;.

[299] Sun, M.; Zhang, H.-Y.; Zhao, Q.; Hu, X.-Y.; Wang, L.-H.; Liu, B.-W.; Liu, Y. *J. Mater. Chem. B* **2015**, *3* (41), 8170–8179.

[300] Wang, S.; Lee, R. J.; Mathias, C. J.; Green, M. A.; Low, P. S. *Bioconjug. Chem.* **1996**, *7* (1), 56–62.

[301] Gravier, J.; Schneider, R.; Frochot, C.; Bastogne, T.; Schmitt, F.; Didelon, J.; Guillemin, F.; Barberi-Heyob, M. *J. Med. Chem.* **2008**, *51* (13), 3867–3877.

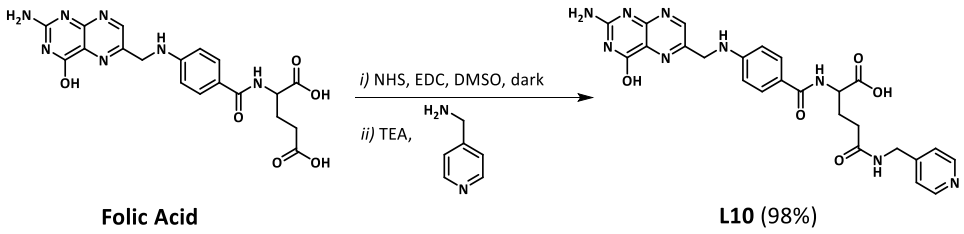

Scheme 23 – Synthesis of ligand **L10**.

Figure 68 shows the ^{1}H NMR spectrum of **L10** in DMSO-d_6. The assignment of all peaks was performed with the help of COSY NMR, and is in agreement with the characterization published in the literature.[298]

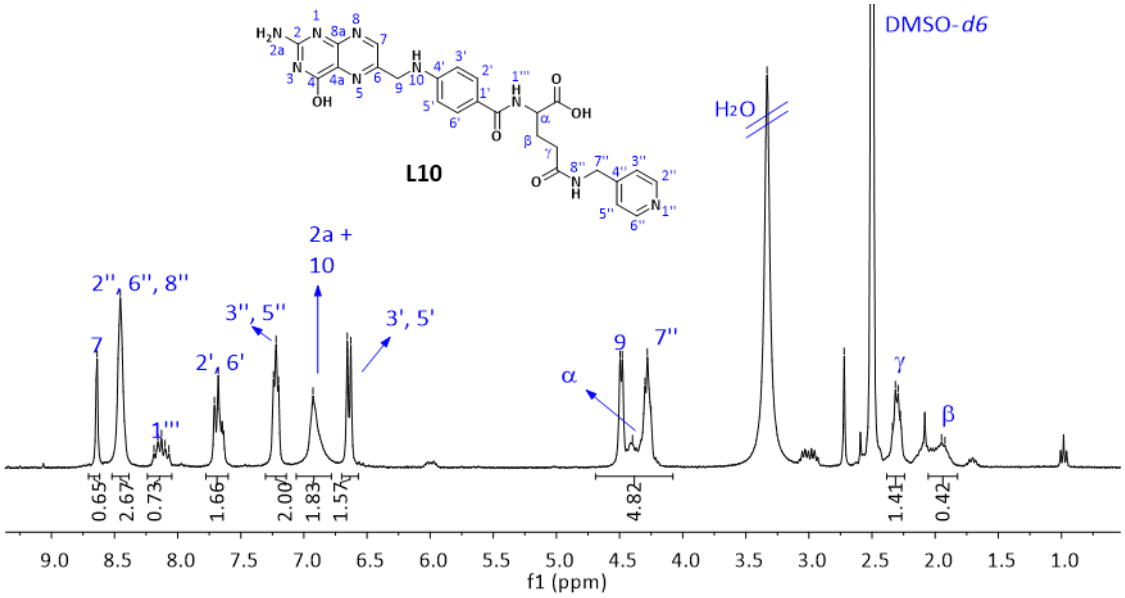

Figure 68 – ^{1}H NMR spectrum of **L10** in DMSO-d_6.

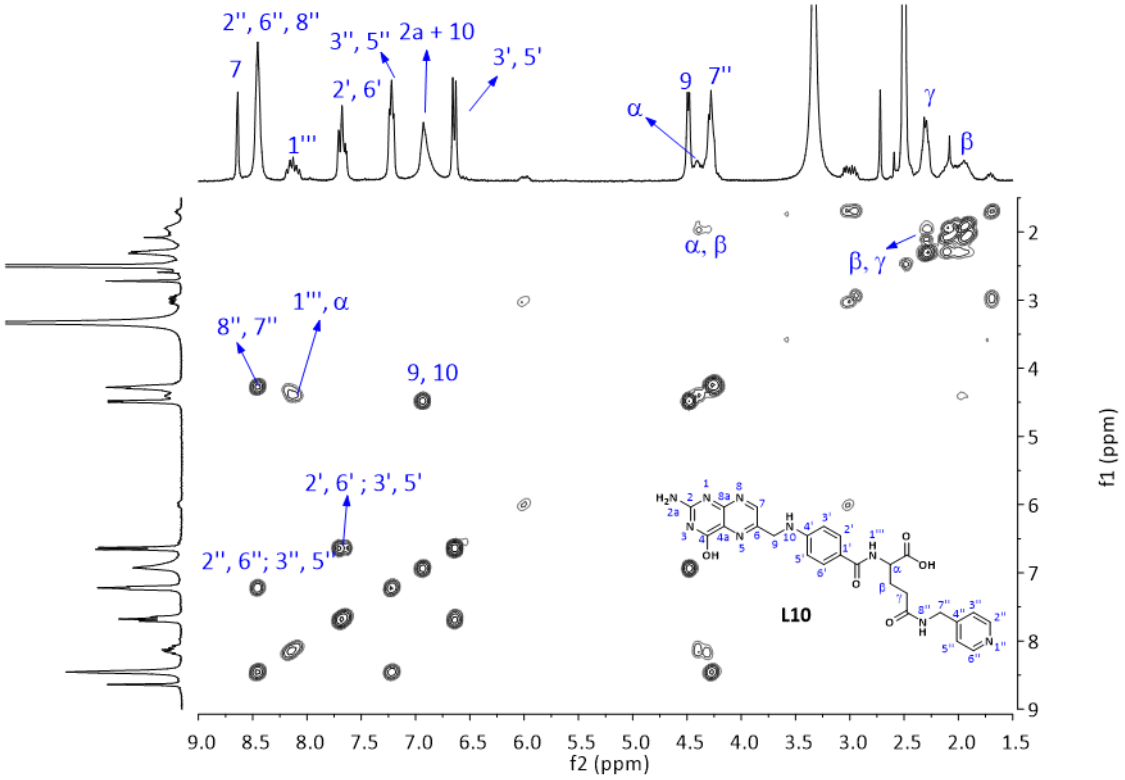

Figure 69 – COSY NMR spectrum of **L10** in DMSO-*d6*.

Owing to the poor solubility of **L10** in water, we decided to coordinate this ligand only to **RuPc B** and not to **RuPc A**, in order to obtain a PS with some solubility in water. In addition, **L10** was not soluble in chloroform, hence the coordination reaction was carried out in DMSO. The coordination of **L10** to **RuPc B** was performed by stirring overnight a DMSO solution of these two compounds, at room temperature and in the dark (**Scheme 24**). As for the carbohydrate-containing **PS11-16**, only one unit of **L10** was coordinated to one of the **RuPc B** axial positions, while one molecule of DMSO coordinated to the other Ru(II) axial coordination site. The isolation was carried out by gel permeation chromatography in BioBeads using DMF as eluent, affording **PS29** in good yields. The characterization of **PS29** was carried out by ^{1}H NMR spectroscopy and by MS spectrometry.

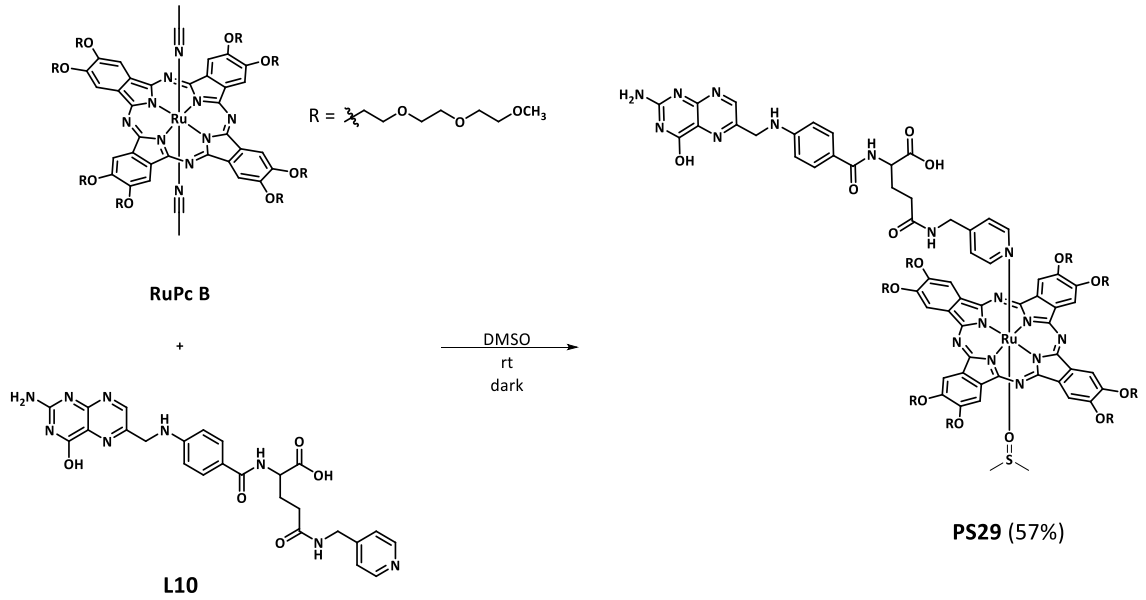

Scheme 24 – Preparation of **PS29**.

The coordination of **L10** to **RuPc B** was monitored by ^{1}H NMR spectroscopy (**Figure 70**). The characteristic signals of the coordinated pyridyl ligands appeared upfield shifted by 7.2 ppm for H^{2} and H^{6} protons and by 1.74 ppm for H^{3} and H^{5} protons. The FA unit located far apart from the macrocycle, showed no influence by the RuPc diatropic ring.

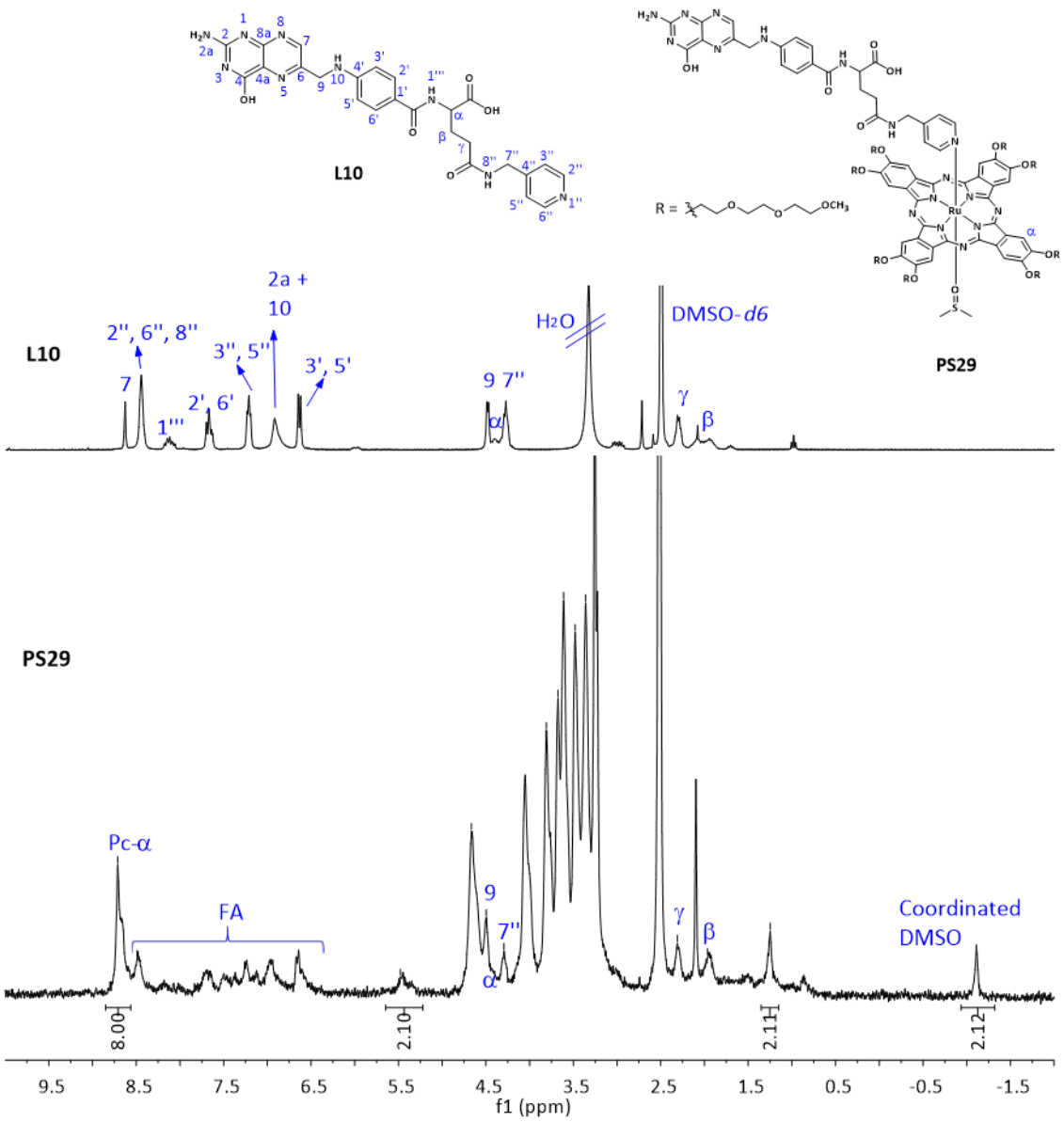

Figure 70 – Comparative ^{1}H NMR spectra in DMSO-d_6 of **L10** and **PS29**.

2.4.2. Route B: Coordination of 4-(aminomethyl)pyridine to RuPc followed by coupling to folic acid

In order to obtain a photosensitizer bearing two folate units at the axial positions, a distinct synthetic route was envisioned, consisting in the coordination of 4-(aminomethyl)pyridine to **RuPc B** followed by amination reaction with folic acid. Hence, a solution of **RuPc B** and 2.5 eq. of 4-(aminomethyl)pyridine in $CHCl_3$ was stirred at 50 °C, in the dark, overnight, to afford RuPc **11,** which

was purified by column chromatography on silica gel using a 9:1 mixture of $CHCl_3$/MeOH as the eluent. This compound was characterized by ^1H NMR and MS.

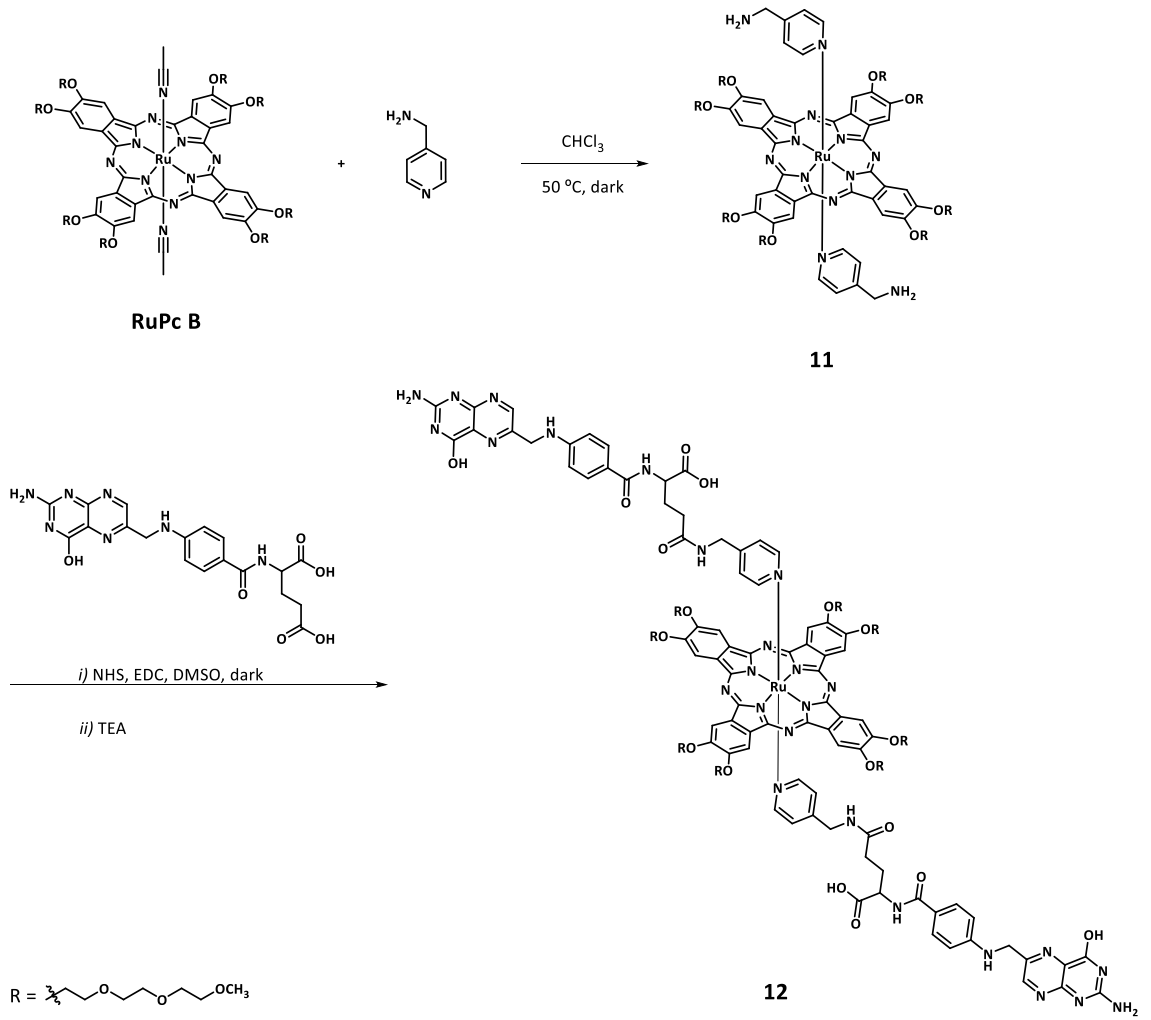

Scheme 25 – Synthesis of RuPc **12.**

The amidation reaction in the presence of NHS, EDC and TEA afforded RuPc **12**. The crude product was purified by size exclusion chromatography in BioBeads using DMF as eluent. By ^1H NMR (**Figure 71**) it seemed that we had the desired product, however, since FA signals do not show any displacement upon coordination to the RuPcs, it was not possible to confirm that no free FA was present.The analysis by MS (ESI^+, MeOH + 0.1% TFA) (**Figure 72**) revealed the presence of a peak at 1487.1 that we assigned to the molecular ion $[M + 2H]^{2+}$. However, another peak at 1275.0 revealed an incomplete amidation reaction, and this route was abandoned.

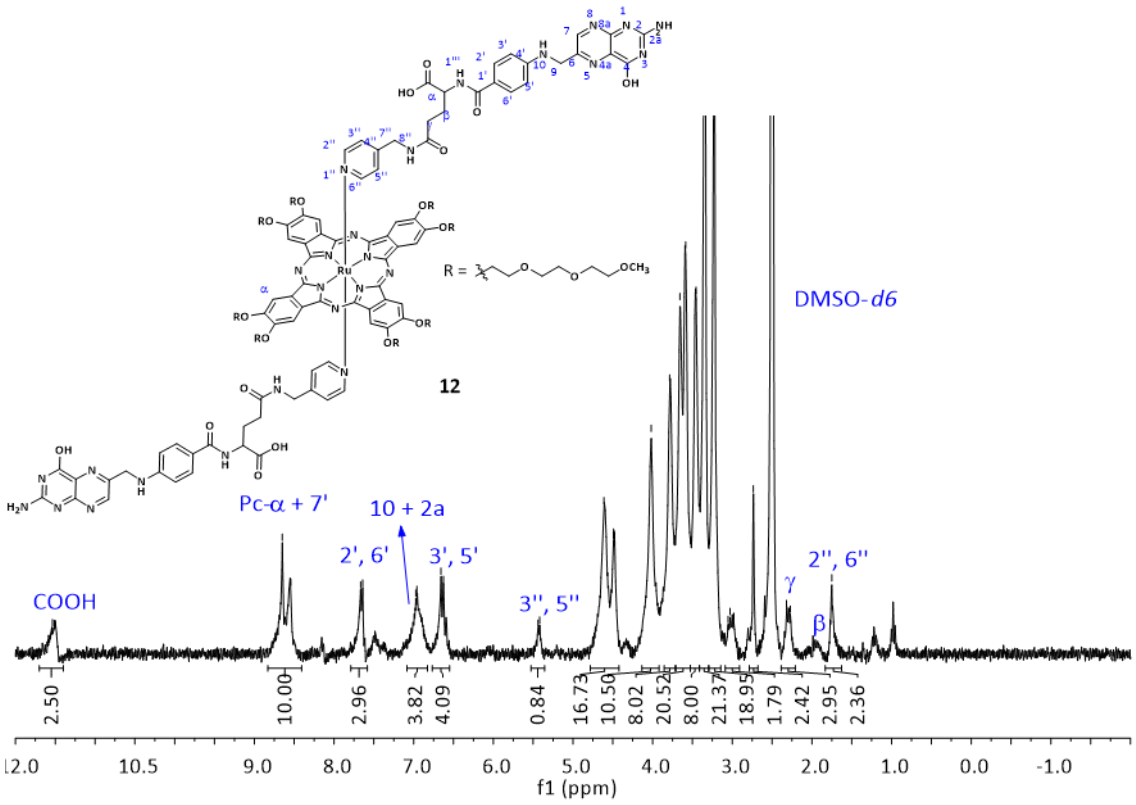

Figure 71 – ^{1}H NMR in DMSO-d_6 of **12**.

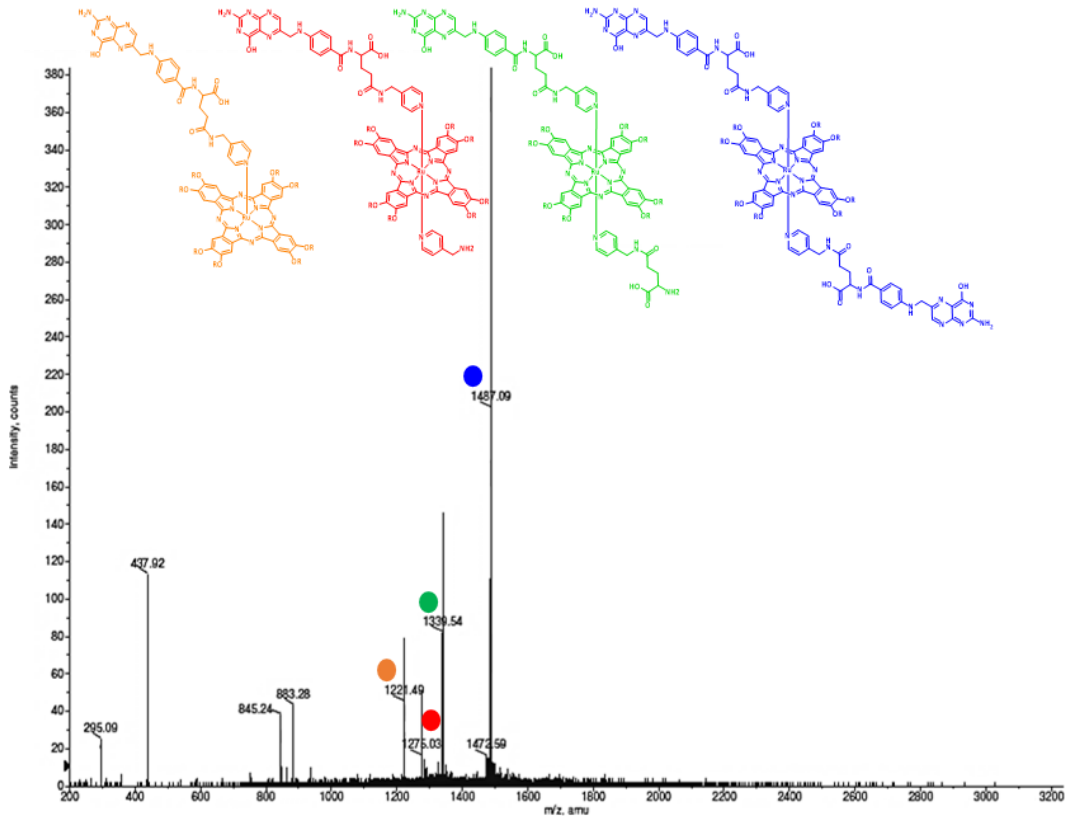

Figure 72 – MS (ESI^{+}, MeOH + 0.1% TFA) spectrum of **12**.

2.4.3. UV-Vis spectra of PSs and aggregation studies

The UV-Vis spectra of **PS29** was recorded in DMSO and in neat water (**Figure 73**). The spectrum in water showed only a slight decrease in absorbance when compared with the spectrum in DMSO, confirming a good solubility in water for this compound.

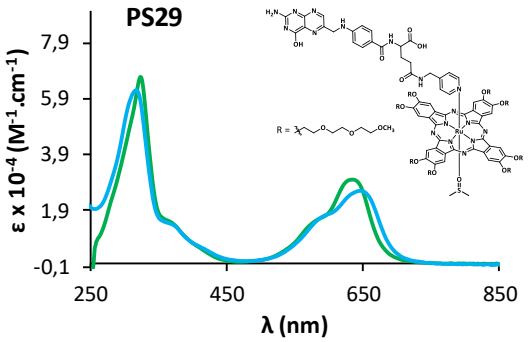

Figure 73 – UV-Vis spectra of **PS29** in DMSO (green) and water (blue).

Table 14 – Absorption spectra data for **PS29**.

Q-band maximum, nm (ε x 10^{-4}, $M^{-1}.cm^{-1}$)	
DMSO	**H_2O**
636 (2.99)	647 (2.24)

2.4.4. Photostability studies

PS29 presented high photostability both in DMSO and in PBS solutions (**Figure 74** and **Table 15**), with a decrease in the Q-band intensity of 2% and 8%, respectively, after irradiating for 60 min. Furthermore, no new bands are observed in the UV-Vis spectra, meaning that no phototransformation occurred.

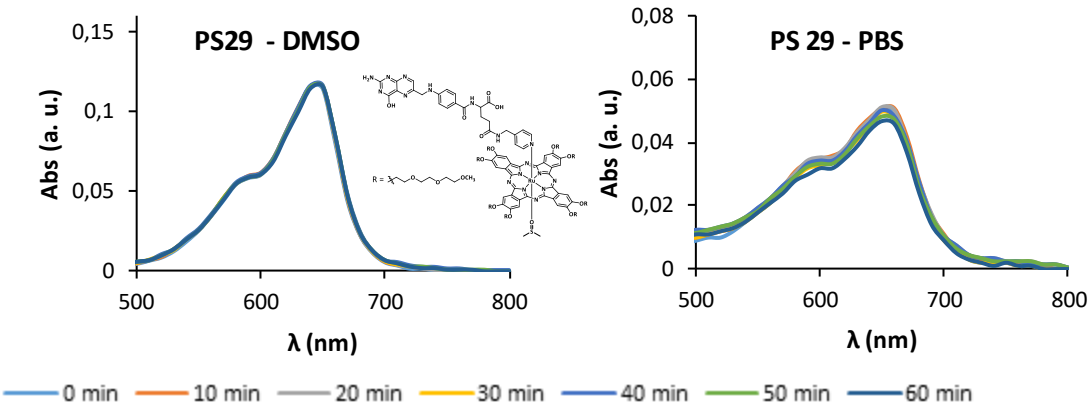

Figure 74 – Photostability of **PS29** (5µM solutions in DMSO and in PBS) after irradiation with red light at a fluence rate of 20 mW/cm^2 at intervals of 10 min, for a total of 60 min.

Table 15 – Photostability of **PS29** (5μM solutions in DMSO and in PBS) after irradiation with red light at a fluence rate of 20 mW/cm^2 at intervals of 10 min, for a total of 60 min. Results are given as % from Abs at t = 0 min.

Solvent	Time (min)						
	0	10	20	30	40	50	60
DMSO	100	99	99	99	99	99	98
PBS	100	100	100	98	98	94	92

2.4.5. Generation of singlet oxygen

The efficiency of **PS29** to generate singlet oxygen was measured in DMSO and in D_2O solutions, by the same methodology used for the previous compounds (**Table 16**). Comparing **PS29** with the previous RuPcs with PEG chains at the periphery, **PS29** showed higher singlet oxygen quantum yields than **PSs 3**, **8-10** and **23-28**, which bear two pyridyl ligands at the axial positions. The Φ_Δ values exhibited by **PS29** (see **Table 16**), similar to those obtained for **PS14-16**, which also have a DMSO molecule as axial ligand, support the idea that coordination of DMSO to Ru(II) increases the efficiency of the final PS to generate singlet oxygen.

Table 16 – Singlet oxygen quantum yields (Φ_Δ) for **PS29**.

DMSO	D_2O
0.74	0.36

2.5. RuPcs bearing a carbonyl group at one of the axial positions

In order to enhance their solubility in water, we focused on the synthesis of Pcs substituted by PEG functions at their periphery. The preparation of RuPcs **13-15** was attempted by treating **RuPc C** with excess of the corresponding **L1**, **L2** and **L4**, in chloroform, at room temperature and protected from light (**Scheme 26**).

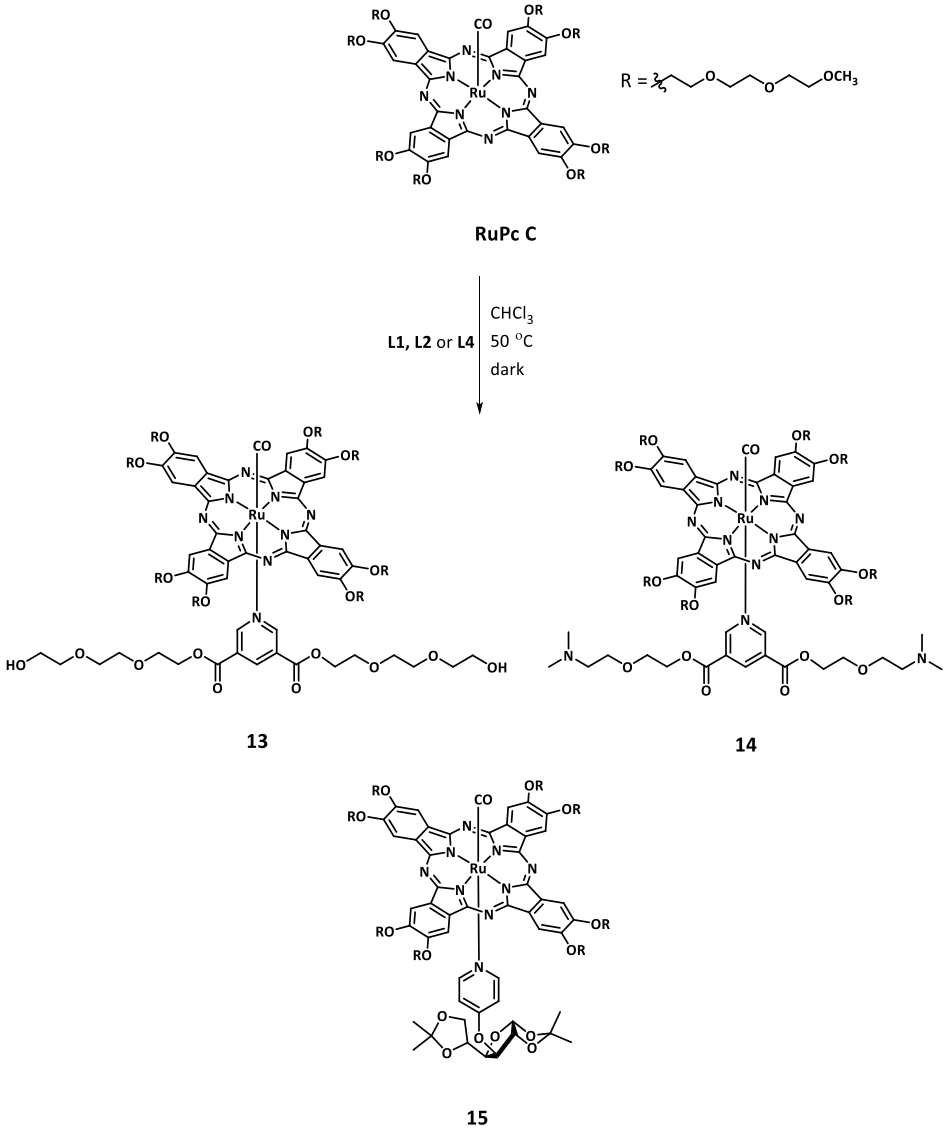

Scheme 26 – Synthesis of RuPcs **13-15**.

The reactions were monitored by ^{1}H NMR spectroscopy until completion. For **13** the ^{1}H NMR spectrum of the crude (**Figure 75**) shows a mixture of **13** and non-coordinated **L1.** Again, all the

protons corresponding to the coordinated axial ligand appear upfield shifted with respect to the non-coordinated ligand. In addition, the signal corresponding to the Pc α protons is considerably sharpened upon coordination of the second Ru coordination site with **L1**. This effect reflects an appreciable reduction of the aggregation phenomena for Pcs bearing two axial ligands, as they are unable to stack in a face-to-face manner. However, RuPcs **13** and **15** were highly unstable in solution. Thus, only starting material **RuPc C** was recovered after gel permeation chromatography in BioBeads using DCM and toluene as solvents. In the case of **14**, the purification was performed by precipitation with hexane, as done before with **PS2**. Once more, only the starting **RuPc C** was recovered.

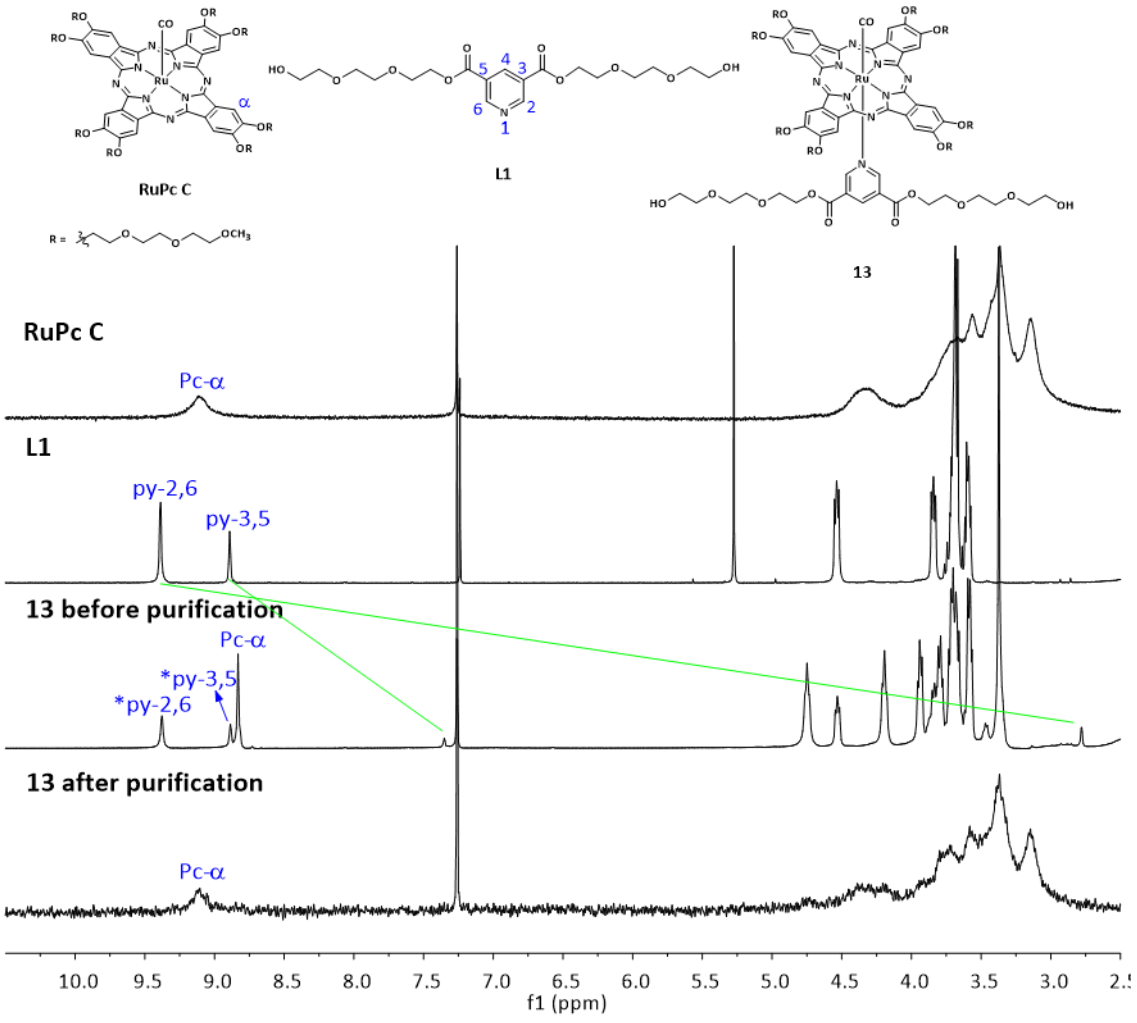

Figure 75 – Comparative ^{1}H NMR spectra in $CHCl_3$ of **RuPc C**, non-coordinated **L30** and **PS 42** before and after purification (*un-coordinated pyridine).

2.6. Summary and conclusions

In this chapter, pyridine-based ligands designed to confer selectivity towards tumor cells have been prepared. Their coordination to the axial positions of RuPcs has been accomplished with good yields.

- **PS5-29** were studied with respect to their solubility:
  - The introduction of eight TEG chains at the peripheral positions of RuPcs provides solubility in water for all compounds containing one polyether and one carbohydrate (**PS23-28**) at the axial positions as well as for **PS29**, containing folic acid and DMSO as axial ligands.
  - The ketal-protected carbohydrate moieties at the axial positions (**PS5-7**) do not confer solubility in neat water, although provide solubility in 99:1 mixtures of water and DMSO. In this case, even PSs containing eight TEG chains at the periphery (**PS8-10**) are insoluble in neat water.
  - Conversely, deprotected carbohydrate units provide enhanced hydrophilicity to both peripherally unsubstituted and TEG containing RuPcs (**PS11-16**).

- All the RuPcs show good photostability upon irradiation with red light of 20 mw/cm^2 during 60 min.

- All compounds are able to produce singlet oxygen upon light activation:
  - RuPcs bearing DMSO as one of the axial ligands show the highest singlet oxygen quantum yields. For PSs with no peripheral substituents (**PS11-13**) Φ_Δ values are between 0.80 and 0.99. The introduction of TEG chains at the peripheral positions (**PS14-16** and **PS29**) reduces the efficiency to produce singlet oxygen (Φ_Δ values ranging from 0.52 to 0.74).
  - PSs bearing two protected carbohydrate units at the two Ru axial coordination sites show less efficiency in the production of singlet oxygen, with peripherally unsubstituted **PS5-7** showing Φ_Δ values between 0.16 and 0.21, and the corresponding PEGylated derivatives **PS8-10** exhibiting quantum yields of 0.08.
  - The mixed derivatives (**PS17-28**), containing both PEG and protected carbohydrates, exhibited average Φ_Δ values related to the corresponding symmetric PSs. This supports

the additive nature of axial ligand coordination contributions to the ability to produce singlet oxygen.

▪ The differences in the generation of singlet oxygen provided by the axial ligands seem to be related to the electronic features of the pyridyl ligand, rather than the nature (carbohydrate or polyether) of the pendant functions. Thus, π-electron donor groups (alkoxy at the 4-pyridyl position) decrease Φ_Δ values, while π-electron withdrawing groups (ester at the 3,5-pyridyl positions) increase Φ_Δ values. Due to the lack of time, we could not confirm this hypothesis.

2.7. Experimental

2.7.1. General Remarks

UV-Vis spectra were recorded with a Jasco V-660 spectrometer. IR spectra were recorded with a Bruker Vector 22 spectrophotometer. EI-MS, MALDI-MS, ESI-MS and FAB-MS spectra were determined on GCT Agilent Technologies 6890N from Waters, Bruker Ultrareflex III, Applied Biosystems QSTAR and VG AutoSpec instruments, respectively. NMR spectra were recorded with a Bruker AV-300 instrument. Column chromatography was performed with Merck 60 (230-400mesh, 60 Å) silica gel and with Biobeads SX-3. Reagents were purchased from Sigma-Aldrich, AlfaAesar and Acros and used without further purification. Solvents were purchased from Carlo Erba Reagents. Anhydrous solvents were dried with molecular sieves of 0.4 nm purchased from Merk.

2.7.1. RuPcs endowed with axial pyridine ligands functionalized with carbohydrate units

2.7.2.1. Synthesis of pyridyl-based ligands functionalized with carbohydrate units

4-(1,2:5,6-Di-O-isopropylidene-alpha-D-glucofuranose)pyridine (L4)

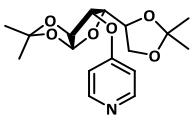

A solution of 1,2:5,6-Di-*O*-isopropylidene-alpha-D-glucofuranose (Diacetone-D-Glucose) (3.47 g, 13,3 mmol) and NaH (960.0 mg of a 60% mineral solution, 24.0 mmol) in dry DMF (30 ml) was stirred at 70 °C, under argon, for one hour. After the addition of 4-chloropyridine hydrochloride (1 g, 6.7 mmol), the reaction mixture was stirred at 40 °C, under argon, for 3 days. The resulting solution was diluted with DCM, transferred to a separatory funnel and washed with water. The organic phase was dried over anhydrous $MgSO_4$. After filtration and evaporation, the residue was chromatographed on silica gel using a 1:1 mixture of EtOAc/Heptane as the eluent. **L4** was obtained as a white solid in 78% yield.

^{1}H NMR (300 MHz, $CDCl_3$) δ_H 8.48 (dd, *J* = 4.8, 1.5 Hz, 2H, py Ar-$H^{2,6}$), 6.91 (dd, *J* = 4.8, 1.5 Hz, 2H, py Ar-$H^{3,5}$), 5.93 (d, 1H, *J* = 3.8 Hz, Glu-H^1), 4.79 (d, *J* = 3.0 Hz, 1H, Glu-H^3), 4.56 (d, *J* = 3.8 Hz, 1H, Glu-H^2), 4.40 (ddd, *J* = 8.1, 5.9, 5.2 Hz, 1H, Glu-H^5), 4.28 (dd, *J* = 8.1, 3.0 Hz, 1H, Glu-H^4), 4.14 (dd, *J* = 8.7, 5.9 Hz, 1H, Glu-H^6), 4.08 (dd, *J* = 8.7, 5.2 Hz, 1H, Glu-H^6), 1.56 (s, 3H, CH_3), 1.42 (s, 3H, CH_3), 1.32 (s, 3H, CH_3), 1.30 (s, 3H, CH_3);

^{13}C NMR (75.5 MHz, $CDCl_3$) δ_C 163.22 (py Ar-H^4), 151.48 (py Ar-$H^{2,6}$), 112.50 (O-C-O), 111.05 (py Ar-$H^{3,5}$), 109.53 (O-C-O), 105.36 (Glu-H^1), 82.27 (Glu-H^2), 80.39 (Glu-H^4), 79.74 (Glu-H^3), 72.07 (Glu-H^5), 67.33 (Glu-H^6), 27.02 (CH_3), 26.80 (CH_3), 26.36 (CH_3), 25.33 (CH_3);

MS (FAB, m-NBA) *m/z* 338.3 $[M + H]^+$.

4-(1,2:3,4-Di-O-isopropylidene-D-galactopyranose)pyridine (L5)

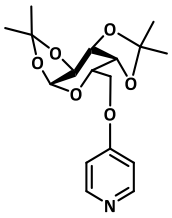

A solution of 1,2:3,4-Di-O-isopropylidene-D-galactopyranose (Diacetone-D-Galactose) (2.55 g, 9.8 mmol) and NaH (704.0 mg of a 60% mineral solution, 17.6 mmol) in dry DMF (25 mL) was stirred at 70 °C, under argon, for one hour. After the addition of 4-chloropyridine hydrochloride (734.8 mg, 4.9 mmol), the reaction mixture was stirred at 40 °C, under argon, for 3 days. The resulting solution was diluted with DCM, transferred to a separatory funnel and washed with water. The organic phase was dried over anhydrous $MgSO_4$. After filtration and evaporation of the solvent, the residue was chromatographed on silica gel using a 1:1 mixture of EtOAc/Heptane as the eluent. **L5** was obtained in 49% yield as a white solid.

^{1}H NMR (300 MHz, $CDCl_3$) δ_H 8.41 (dd, *J* = 4.9, 1.4 Hz, 2H, py Ar- $H^{2,6}$), 6.84 (dd, *J* = 4.9, 1.4 Hz, 2H, py Ar- $H^{3,5}$), 5.56 (d, *J* = 5.0 Hz, 1H, Gal-H^1), 4.65 (dd, *J* = 7.8, 2.3 Hz, 1H, Gal-H^3), 4.36-4.32 (m, 2H, Gal-$H^{2,4}$), 4.21-4.15 (3H, m, Gal-$H^{5,6}$), 1.52 (s, 3H, CH_3), 1.46 (s, 3H, CH_3), 1.35 (s, 3H, CH_3), 1.34 (s, 3H, CH_3);

^{13}C NMR (75.5 MHz, $CDCl_3$) δ_C 153.87 (py Ar- H^4), 151.21 (py Ar- $H^{2,6}$), 110.59 (py Ar- $H^{3,5}$), 109.01 (O-C-O), 108.99 (O-C-O), 96.49 (Gal-H^1), 71.03 (Gal-H), 70.78 (Gal-H), 70.68 (Gal-H), 66.65 (Gal-H), 66.22 (Gal-H), 26.21 (CH_3), 26.12 (CH_3), 25.06 (CH_3), 24.59 (CH_3);

MS $(EI)^+$ *m/z* 322.1 $[M - CH_3]^+$, 337.2 (M^+).

4-(2,3:5,6-Di-O-isopropylidene-alpha-D-mannofuranose)pyridine (L6)

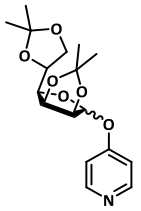

A solution of 2,3:5,6-Di-O-isopropylidene-alpha-D-mannofuranose (Diacetone-D-Mannose) (389.8 mg, 1.5 mmol) and NaH (90.0 mg of a 60% mineral solution, 2.2 mmol) in dry DMAC (7 mL) was stirred at 70 °C, under argon, for one hour. After the addition of 4-fluoropyridine hydrochloride (100.0 mg, 0.75 mmol), the reaction mixture was stirred at 70 °C, under argon, for 3 days. The solvent was evaporated under reduced pressure and the residue was dissolved in DCM, transferred to a separatory funnel, washed with water and dried over anhydrous $MgSO_4$. After filtration and evaporation of the solvent, the residue was chromatographed on silica gel using a 1:1 mixture of EtOAc/Heptane as the eluent. **L6** was obtained in 10% yield as a white solid.

^{1}H NMR (300 MHz, $CDCl_3$) δ_H 8.43 (dd, *J* = 4.8, 1.5 Hz, 2H, py Ar- $H^{2,6}$), 6.89 (dd, *J* = 4.8, 1.5 Hz, 2H, py Ar- $H^{3,5}$), 5.70 (s, 1H, Man-H^1), 4.91 (dd, *J* = 5.9, 3.3 Hz, 1H, Man-H^3), 4.80 (d, *J* = 5.9 Hz, 1H, Man-H^2), 4.41 (ddd, *J* = 7.7, 6.3, 4.1 Hz, 1H, Man-H^5), 4.08 (dd, *J* = 8.8, 6.3 Hz, 1H, Man-H^6), 4.02 (dd, *J* = 7.7, 3.3 Hz, 1H, Man-H^4), 3.94 (dd, *J* = 8.8, 4.1 Hz, 1H, Man-H^6), 1.51 (s, 3H, CH_3), 1.41 (s, 3H, CH_3), 1.36 (s, 3H, CH_3), 1.35 (s, 3H, CH_3);
^{13}C NMR (75.5 MHz, $CDCl_3$) δ_C 162.46 (py Ar- H^4), 151.21 (py Ar- $H^{2,6}$), 113.41 (O-C-O), 111.83 (py Ar- $H^{3,5}$), 109.54 (O-C-O), 104.32 (Man-H^1), 85.43 (Man-H^2), 81.87 (Man-H^4), 79.55 (Man-H^3), 72.95 (Man-H^5), 66.08 (Man-H^6), 27.00 (CH_3), 26.06 (CH_3), 25.28 (CH_3), 24.70 (CH_3);
MS (ESI+, MeOH + NaI) *m/z* 338.2 $[M + H]^+$, 360.1 $[M + Na]^+$.

4-(D-glucofuranose)pyridine (L7)

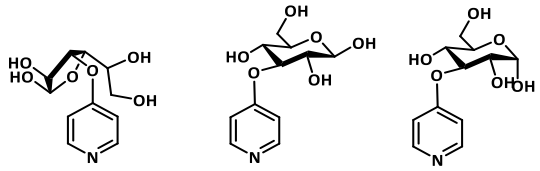

A solution of **L4** (200 mg, 0.59 mmol) in a 1:1 mixture of TFA/H_2O (40 mL) was stirred at room temperature overnight. The solvent was removed under reduced pressure to give **L7** in quantitative yield as a white solid.

^{1}H NMR (300Hz, DMSO-d_6) δ_H 8.68 (d, 2H, *J* = 5.5, py Ar-H^{2,6}), 7.62-7.56 (m, 2H, py Ar-H^{3,5}), 5.05 (d, *J* = 3.5, 0.5H, Glu-H$^{1\alpha}$), 4.85-4.74 (m, 1H, Glu-H^3), 4.54 (d, *J* = 7.7, 0.5H, Glu-H$^{1\beta}$), 3.75-3.48 (m, 4H, Glu-H^{2,5,6}), 3.35-3.25 (m, 1H, Glu-H^4);
MS (FAB, m-NBA) *m/z* 258.1 $[M + H]^+$.

4-(D-galactopyranose)pyridine (L8)

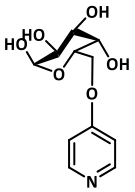

A solution of **L5** (200 mg, 0.59 mmol) in a 1:1 mixture of TFA/H_2O (40 mL) was stirred at room temperature overnight. The solvent was removed under reduced pressure and the residue was precipitated with $CHCl_3$ to give **L8** in quantitative yield as a white solid.

^{1}H NMR (300 MHz, DMSO-d_6) δ_H 8.71 (d, *J* = 6.0, 2H, py Ar-H^{2,6}), 7.53 (d, *J* = 6.0, 2H, py Ar-H^{3,5}), 5.02 (d, *J* = 3.2, 0.5H, Gal-H$^{1\alpha}$), 4.99 (d, *J* = 3.2, 0.5H, Gal-H$^{1\beta}$), 4.47-4.26 (m, 3H, Gal-H$^{3\text{-}5}$), 3.93-3.58 (m, 2H, Gal-H^6), 3.43-3.30 (m, 1H, Gal-H^2);
MS (FAB, m-NBA)$^+$ *m/z* 258.1 $[M + H]^+$.

4-(D-mannofuranose)pyridine (L9)

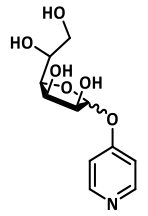

A solution of **L6** (200 mg, 0.59 mmol) in a 1:1 mixture of TFA/H_2O (40 mL) was stirred at room temperature overnight. The solvent was removed under reduced pressure and the residue was precipitated with $CHCl_3$ to give **L9** in quantitative yield as a white solid.

^{1}H NMR (300 MHz, DMSO-d_6) δ_H 8.54 (d, *J* = 6.6 Hz, 2H, py Ar- $H^{2,6}$), 7.24 (d, *J* = 6.6 Hz, 2H, py Ar-$H^{3,5}$), 4.88 (s, 1H, Man-H^1), 3.94 (s, 1H, Man-H), 3.71-3.28 (m, 5H, Man-H);
MS (ESI+, MeOH+NaI) m/z 129.0 $[M + 2H]^{2+}$; 203.1 $[Man + Na]^+$.

2.7.2.2. Coordination Reactions to RuPc A and RuPc B

2.7.2.2.1. Coordination of pyridyl-based ligands functionalized with protected carbohydrate units

*General procedure for the synthesis of **PS5-10**:* **RuPc A** or **RuPc B** (0.08 mmol) and the ligand (**L4-6**) (0.20 mmol) were stirred in $CHCl_3$ at 50 °C, under argon, and protected from light. The reaction was monitored by ^{1}H NMR in $CDCl_3$. When the reaction was complete, the solvent was removed under reduced pressure and the residue was treated as indicated below.

PS5

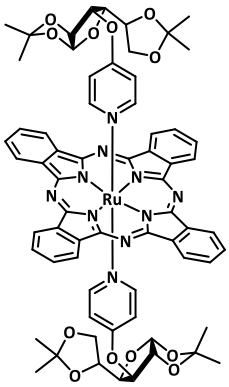

Prepared from **RuPc A** and **L4**. The crude was chromatographed on Biobeads using toluene as the eluent. The fraction containing **PS5** was precipitated with hexane, affording the pure product in 72% yield as a blue solid.

^{1}H NMR (300 MHz, $CDCl_3$) δ_H 9.14 (dd, *J* = 5.6, 3.0 Hz, 8H, Pc-H^{α}), 7.89 (dd, *J* = 5.6, 3.0 Hz, 8H, Pc-H^{β}), 5.31 (d, *J* = 3.9 Hz, 2H, Glu-H^1), 4.85 (d, *J* = 7.2 Hz, 4H, py Ar-$H^{3,5}$), 3.68-3.55 (m, 10H, Glu-H^{3-6}), 3.44 (d, *J* = 3.9 Hz, 2H, Glu-H^2), 2.35 (d, *J* = 7.2 Hz, 4H, py Ar-$H^{2,6}$), 1.22 (s, 6H, CH_3), 1.04 (s, 6H, CH_3), 0.95 (s, 6H, CH_3), 0.85 (s, 6H, CH_3);

^{13}C NMR (75.5 MHz, $CDCl_3$) δ_C 160.41, 150.84, 143.78, 140.92, 128.02, 121.44, 112.21, 110.04, 109.20, 104.80, 81.16, 79.60, 79.31, 77.36, 71.21, 66.97, 26.64, 26.41, 25.97, 24.77;

MS (ESI^+) *m/z* 1288.4 $[M + H]^+$;

UV-Vis (DMSO) λ_{max} nm (ε x 10^{-4}): 315 (14.0), 375 (3.46), 570 (3.47), 623 (9.55);

FT-IR (KBr) ν cm^{-1}: 2985, 2921, 1610, 1489, 1415, 1380,1323, 1289, 1207, 1167, 1124, 1067, 1027, 846, 754, 573.

PS6

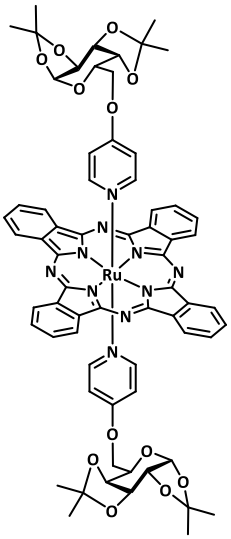

Prepared from **RuPc A** and **L5**. The crude was chromatographed on Biobeads using toluene as the eluent. The fraction containing **PS6** was precipitated with hexane, affording the pure product in 80% yield as a blue solid.

^{1}H NMR (300 MHz, $CDCl_3$) δ_H 9.12 (dd, *J* = 5.6, 3.0 Hz, 8H, Pc-H^{α}), 7.86 (dd, *J* = 5.6, 3.0 Hz, 8H, Pc-H^{β}), 5.15 (d, *J* = 5.0 Hz, 2H, Gal-H^1), 4.79 (d, *J* = 7.3 Hz, 4H, py Ar-$H^{3,5}$), 4.28 (dd, *J* = 8.0, 2.4 Hz, 2H, Gal-H^3), 4.04 (dd, *J* = 5.0, 2.4 Hz, 2H, Gal-H^2), 3.66 (dd, *J* = 8.0, 1.5 Hz, 2H, Gal-H^4), 3.33 (td, *J* = 6.3, 1.5 Hz, 2H, Gal-H^5), 3.18 (dd, 2H, *J* = 10.0, 6.3 Hz, Gal-H^6), 3.07 (dd, 2H, *J* = 10.0, 6.3 Hz, Gal-H^6), 2.31 (d, *J* = 7.3 Hz, 4H, py Ar-$H^{2,6}$), 1.11 (s, 12H, CH_3), 1.03 (s, 6H, CH_3), 0.97 (s, 6H, CH_3);

MS (ESI^+) *m/z* 1288.4 $[M + H]^+$;

UV-Vis (DMSO) λ_{max} nm (ε x 10^{-4}): 315 (13.9), 371 (3.31), 570 (3.34), 623 (9.38);

FT-IR (KBr) ν cm^{-1}: 3056, 2986, 2924, 1612, 1489, 1414, 1381, 1324, 1290, 1254, 1208, 1168, 1006, 898, 831, 754, 736, 665, 573, 512.

PS7

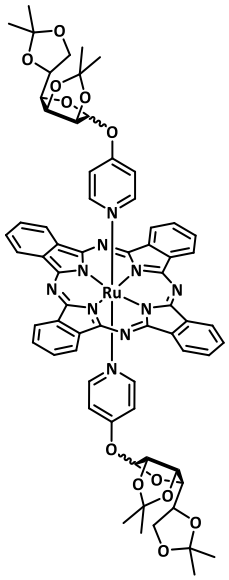

Prepared from **RuPc A** and **L6**. The crude was chromatographed on Biobeads using toluene as the eluent. The fraction containing **PS7** was precipitated with hexane, affording the pure product in 77% yield as a blue solid.

^{1}H NMR (300 MHz, $CDCl_3$) δ_H 9.13 (dd, *J* = 5.6, 3.0 Hz, 8H, Pc-H^{α}), 7.87 (dd, *J* = 5.6, 3.0 Hz, 8H, Pc-H^{β}), 4.84 (d, *J* = 7.4 Hz, 4H, py Ar-$H^{3,5}$), 4.52 (s, 2H, Man-H^{1}), 4.39 (dd, *J* = 5.8, 3.7 Hz, 2H, Man-H^{3}), 4.12 (d, *J* = 5.8 Hz, 2H, Man-H^{2}), 3.96 (ddd, *J* = 7.9, 6.3, 4.6 Hz, 2H, Man-H^{5}), 3.68 (dd, *J* = 8.8, 6.3 Hz, 2H, Man-H^{6}), 3.31 (dd, *J* = 8.8, 4.6 Hz, 2H, Man-H^{6}), 3.23 (dd, *J* = 7.9, 3.7 Hz, 2H, Man-H^{4}), 2.32 (d, *J* = 7.4 Hz, 4H, py Ar-$H^{2,6}$), 1.19 (s, 6H, CH_3), 1.16 (s, 6H, CH_3), 1.06 (s, 6H, CH_3), 1.04 (s, 6H, CH_3);
^{13}C NMR (75.5 MHz, $CDCl_3$) δ_C 159.65, 150.73, 143.78, 140.92, 127.96, 121.41, 113.16, 110.79, 109.27, 103.78, 84.60, 81.68, 78.97, 72.33, 66.63, 26.63, 25.77, 25.22, 24.48;
MS (ESI^+) *m/z* 615.1 $[(M - 2L) + H]^+$, 952.2 $[(M - L) + H]^+$, 1289.4 $[M + H]^+$;
UV-Vis (DMSO) λ_{max} nm (ε x 10^{-4}): 316 (10.7), 372 (2.97), 571 (2.86) 623 (7.62);
FT-IR (KBr) ν cm^{-1}: 3049, 2981, 2888, 1608, 1486, 413, 1370, 1322, 1287, 1204, 1166, 1120, 1063, 1025, 968, 842, 774.

PS8

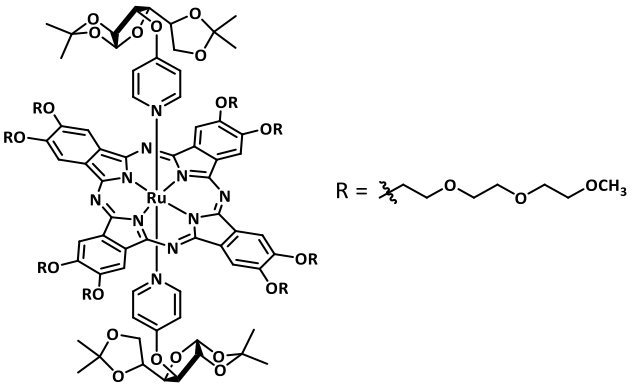

Prepared from **RuPc B** and **L4**. The crude was chromatographed on Biobeads using DCM as the eluent. The fraction containing **PS8** was precipitated with hexane, affording the pure product in 86% yield as a blue, waxy solid.

^{1}H NMR (300 MHz, $CDCl_3$) δ_H 8.55 (s, 8H, Pc-H^{α}), 5.32 (d, *J* = 4.0 Hz, 2H, Glu-H^{1}), 4.87 (d, *J* = 7.3 Hz, 4H, py Ar-$H^{3,5}$), 4.69 (t, *J* = 5.5 Hz, 16H, Pc-OCH_2), 4.17 (t, *J* = 5.2 Hz, 16H, Pc-OCH_2), 3.96-3.93 (m, 16H, Pc-OCH_2), 3.82-3.79 (m, 16H, Pc-OCH_2), 3.75-3.72 (m, 16H, Pc-OCH_2), 3.71-3.59 (m, 16H + 10H, Pc-OCH_2 + Glu-H^{3-6}), 3.44 (d, *J* = 4.0 Hz, 2H, Glu-H^{2}), 3.40 (s, 24H, OCH_3), 2.37 (d, *J* = 7.3 Hz, 4H, py Ar-$H^{2,6}$), 1.24 (s, 6H, CH_3), 1.07 (s, 6H, CH_3), 0.96 (s, 6H, CH_3), 0.90 (s, 6H, CH_3);

^{13}C NMR (75.5 MHz, $CDCl_3$) δ_C 160.19, 151.30, 150.11, 143.48, 134.48, 112.14, 109.86, 109.15, 105.88, 104.76, 81.08, 79.55, 79.21, 72.08, 71.14, 70.89, 70.72, 69.95, 69.23, 66.89, 59.16, 31.03, 26.63, 26.37, 25.94, 24.79;

MS (ESI^+, MeOH + 0.1% fomic acid) *m/z* 1293.5 $[M + 2H]^{2+}$, 2586.1 $[M + H]^+$;

UV-Vis (DMSO) λ_{max} nm (ε x 10^{-4}): 323 (9.31), 375 (2.68), 570 (1.86), 622 (5.27);

FT-IR (KBr) ν cm^{-1}: 2874, 1608, 1495, 1457, 1404, 1276, 1202, 1113, 1064, 944, 850, 734.

PS9

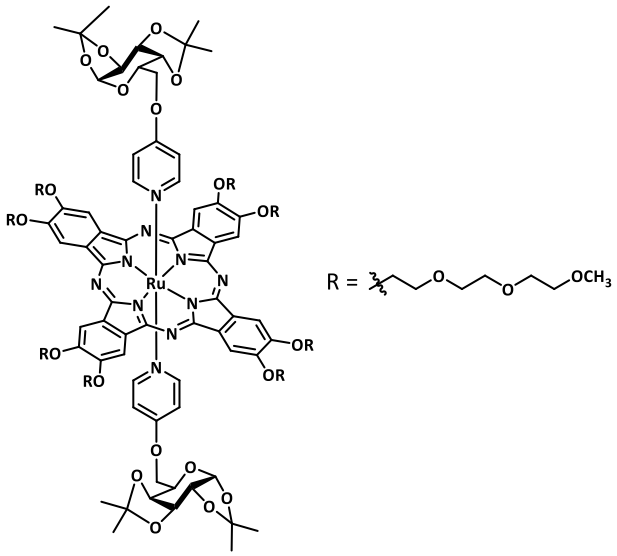

Prepared from **RuPc B** and **L5**. The crude was chromatographed on Biobeads using DCM as the eluent. The fraction containing **PS9** was precipitated with hexane, affording the pure product in 56% yield as a blue, waxy solid.

^{1}H NMR (300 MHz, $CDCl_3$) δ_H 8.54 (s, 8H, Pc-H^{α}), 5.16 (d, *J* = 4.9 Hz, 2H, Gal-H^1), 4.81 (d, *J* = 6.8 Hz, 4H, py Ar-$H^{3,5}$), 4.67 (t, *J* = 4.8 Hz, 16H, Pc-OCH_2), 4.29 (dd, *J* = 7.9, 2.2 Hz, 2H, Gal-H^3), 4.16 (t, *J* = 4.9 Hz, 16H, Pc-OCH_2), 4.05 (dd, *J* = 4.9, 2.2 Hz, 2H, Gal-H^2), 3.95-3.92 (m, 16H, Pc-OCH_2), 3.81-3.78 (m, 16H, Pc-OCH_2), 3.75-3.72 (m, 16H, Pc-OCH_2), 3.74-3.68 (m, 16H + 2H, Pc-OCH_2 + Gal-H^4), 3.61-3.57 (m, 16H, Pc-OCH_2), 3.39 (m broad signal, 24H + 2H, OCH_3 + Gal-H^5), 3.20-3.05 (m, 4H, Gal-H^6), 2.33 (d, *J* = 6.8 Hz, 4H, py Ar-$H^{2,6}$), 1.12 (s, 12H, CH_3), 1.05 (s, 12H, CH_3);

MS (ESI^+, MeOH + 0.1% fomic acid) *m/z* 1293.5 $[M+2H]^{2+}$, 1911.8 $[(M-2L)+H]^+$, 2248.9 $[(M – L) + H]^+$, 2586.1 $[M + H]^+$;

UV-Vis (DMSO) λ_{max} nm (ε x 10^{-4}): 324 (4.76), 376 (1.41), 571 (0.911) 622 (2.79);

FT-IR (KBr) ν cm^{-1}: 2874, 1609, 1495, 1457, 1405, 1275, 1202, 1112, 1066, 942, 854, 754, 733.

PS10

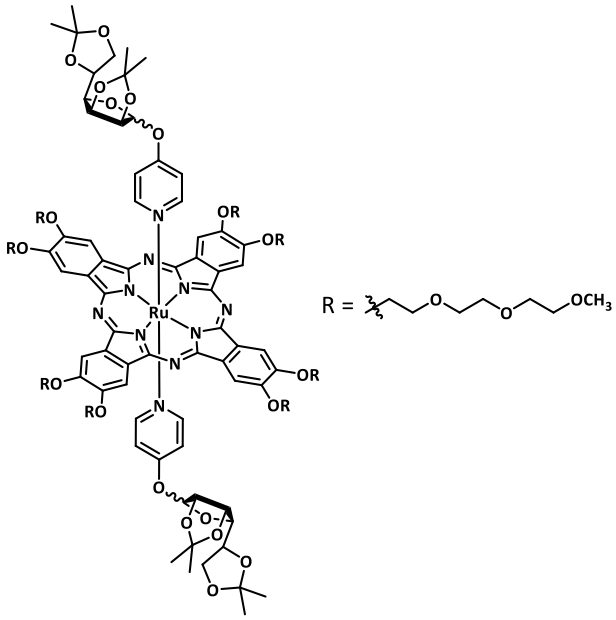

Prepared from **RuPc B** and **L6**. The crude was subjected to size exclusion chromatography on Biobeads using DCM as the eluent. The fraction containing **PS10** was precipitated with hexane, affording the pure product in 62% yield as a blue, waxy solid.

^{1}H NMR (300 MHz, $CDCl_3$) δ_H 8.54 (s, 8H, Pc-H$^{\alpha}$), 4.87 (d, *J* = 7.1 Hz, 4H, py Ar-H^{3,5}), 4.68 (t, *J* = 5.1 Hz, 16H, OCH_2), 4.54 (s, 2H, Man-H^1), 4.41 (dd, *J* = 5.8, 3.6 Hz, 2H, Man-H^3), 4.17 (t, *J* = 5.1 Hz, 16H, OCH_2), 4.13 (d, *J* = 5.8 Hz, 2H, Man-H^2), 3.96-3.93 (m, 16H + 4H, OCH_2 + Man-H^5), 3.82-3.78 (m, 16H, OCH_2), 3.75-3.72 (m, 16H, OCH_2), 3.70 (dd, *J* = 9.0, 6.0 Hz, 2H, Man-H^6), 3.62-3.59 (m, 16H, OCH_2), 3.40 (s, 24H, OCH_3), 3.32 (dd, *J* = 9.0, 4.2 Hz, 2H, Man-H^6), 3.25 (dd, *J* = 7.9, 3.6 Hz, 2H, Man-H^4), 2.33 (d, *J* = 7.1 Hz, 4H, py Ar-H^{2,6}), 1.20 (s, 6H, CH_3), 1.18 (s, 6H, CH_3), 1.08 (s, 12H, CH_3);

MS (ESI$^+$, MeOH + 1% TFA) *m/z* 338.2 $[L+H]^+$, 967.4 $[(M - 2L) + H + Na]^{2+}$, 1125.0 $[(M - L) + 2H]^{2+}$, 1293.6 $[M + 2H]^{2+}$, 1911.8 $[(M - 2L) + H]^+$, 2249.0 $[(M - L) + H]^+$, 2586.2 $[M + H]^+$;

UV-Vis (DMSO) λ_{max} nm (ε x 10^{-4}): 324 (16.1), 375 (4.84), 570 (3.02), 623 (8.52);

FT-IR (KBr) ν *cm^{-1}*: 2870, 1607, 1494, 1457, 1404, 1341, 1273, 1200, 1108, 1064, 972, 856, 754, 732.

2.7.2.2.2. Coordination of pyridyl-based ligands functionalized with deprotected carbohydrate units

*General procedure for the synthesis of **PS11-16**:* **RuPc A** or **RuPc B** (0.08 mmol) and the ligand (**L7-9**) (0.20 mmol) were stirred in DMSO at room temperature, overnight, under argon and protected from light. The solvent was removed under reduced pressure and the residue was chromatographed on Biobeads using THF as the eluent.

PS11

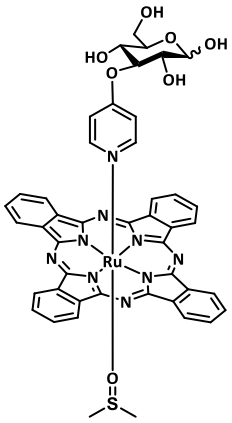

Prepared from **RuPc A** and **L7**. The fraction containing **PS11** was precipitated with hexane, affording the pure product in 12% yield as a blue solid.

^{1}H NMR (300 MHz, DMSO-d_6) δ_H 9.19 (dd, *J* = 5.5, 2.9 Hz, 8H, Pc-H$^{\alpha}$), 8.04 (dd, *J* = 5.5, 2.9 Hz, 8H, Pc-H$^{\beta}$), 6.10 (d, *J* = 3.9 Hz, 1H, Glu-H^1), 5.25 (dd, *J* = 9.7, 7.4 Hz, 2H, py Ar-H^{3,5}), 4.68-4.26 (m, 3H, Glu-H), 3.12-3.10 (m, 1H, Glu-H), 2.73-2.64 (m, 2H, Glu-H), 1.75 (m, 2H, py Ar-H^{2,6}), -1.11 (s, coordinated DMSO);

MS (ESI$^+$, MeOH + 0.5% TFA) *m/z* 258.1 [py-Glu + H]$^+$, 437.9 [(M – DMSO) + 2H]$^{2+}$, 614.1 [M – 2L]$^+$, 871.1 [(M – DMSO) + H]$^+$, 950.2 [M + H]$^+$, 956.2 [M with DMSO-d_6 + H]$^+$;

UV-Vis (DMSO) λ_{max} nm (ε x 10^{-4}): 316 (6.07), 637 (3.21);

FT-IR (KBr) ν *cm^{-1}*: 3343 (OH), 1718, 1608, 1408, 1263, 1244, 1167, 1120, 1097, 1042, 1017, 727.

PS12

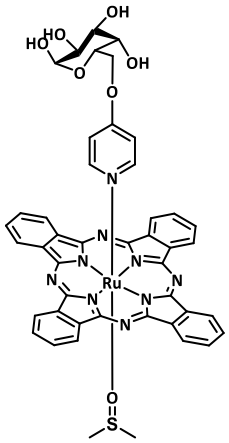

Prepared from **RuPc A** and **L8**. The fraction containing **PS12** was precipitated with hexane, affording the pure product in 29% yield as a blue solid.

^{1}H NMR (300 MHz, DMSO-d_6) δ_H 9.19 (dd, *J* = 5.3, 2.9, 8H, Pc-H$^{\alpha}$), 8.04 (dd, *J* = 5.3, 2.9, 8H, Pc-H$^{\beta}$), 5.23-5.21 (m, 2H, py Ar-H^{3,5}), 4.52 (broad s, 1H, Gal-H^1), 4.08-4.04 (m, 1H, Gal-H), 3.17-2.88 (m, 4H, Gal-H), 1.85 (d, *J* = 6.0, 2H, py Ar-H^{2,6}), -1.09 (s, coordinated DMSO);
MS (ESI$^+$, MeOH + 0.5% TFA) *m/z* 258.1 [py-Gal + H]$^+$, 437.9 [(M – DMSO) + 2H]$^{2+}$, 614.1 [M – 2L]$^+$, 872.1 [(M – DMSO) + H]$^+$, 950.2 [M + H]$^+$;
UV-Vis (DMSO) λ_{max} nm (ε x 10^{-4}): 316 (6.69), 638 (5.38);
FT-IR (KBr) ν *cm*$^{-1}$: 3360 (OH), 1610, 1489, 1412, 1325, 1289, 1121, 1065, 1008, 948, 754, 736.

PS13

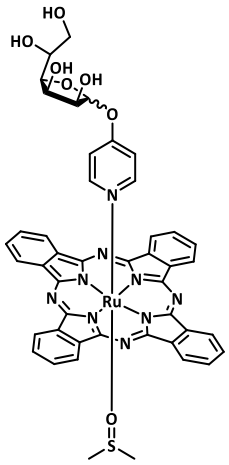

Prepared from **RuPc A** and **L9**. The fraction containing **PS13** was precipitated with hexane, affording the pure product in 56% yield as a blue solid.

^{1}H NMR (300 MHz, DMSO-d_6) δ_H 9.18 (dd, *J* = 5.6, 2.9, 8H, Pc-H$^{\alpha}$), 8.03 (dd, *J* = 5.6, 2.9, 8H, Pc-H$^{\beta}$), 4.96 (d, *J* = 6.9 Hz, 2H, py Ar-H^{3,5}), 4.87 (s, 1H, Man-H^1), 3.69-3.25 (m, 6H, Man-H), 1.77 (d, *J* = 6.9 Hz, 2H, py Ar-H^{2,6}), -1.11 (s, coordinated DMSO);
MS (ESI$^+$, MeOH + 0.5% TFA) *m/z* 309.0 [(M – 2L) + 2H]$^{2+}$, 437.9 [(M – DMSO) + 2H]$^{2+}$, 615.1 [(M – 2L) + H]$^+$, 693.1 [(M – L) + H]$^+$ 788.1 [(M – Man) + H]$^+$, 794.2 [(M with DMSO-d_6 – Man) + H]$^+$;
UV-Vis (DMSO) λ_{max} nm (ε x 10^{-4}): 318 (6.05), 633 (5.29);
FT-IR (KBr) ν *cm^{-1}*: 3342, 1740, 1617, 1508, 1489, 1448, 1413, 1373, 1325, 1205, 1169, 1122, 1065, 1025, 911, 754, 736, 695.

PS14

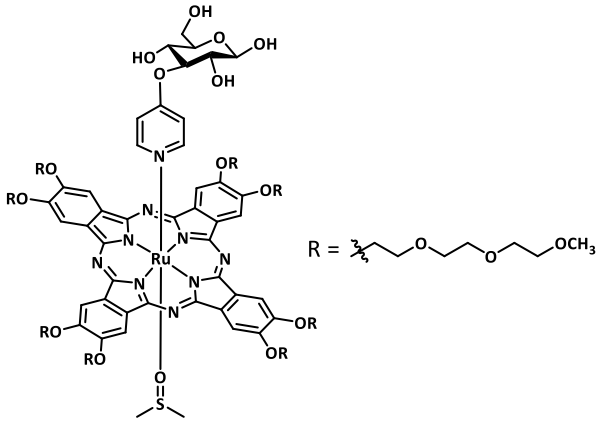

Prepared from **RuPc B** and **L7**. The fraction containing **PS14** was precipitated with hexane, affording the pure product in 88% yield as a blue, waxy solid.

^{1}H NMR (300 MHz, DMSO-d_6) δ_H 8.68 (s, 8H, Pc-H$^{\alpha}$), 6.10 (d, *J* = 3.9 Hz, 1H, Glu-H^1), 5.25 (m, 2H, py Ar-H^{3,5}), 4.66 (broad m, 16H, OCH_2), 4.55-4.18 (m, 3H, Glu-H), 4.05 (broad m, 16H, OCH_2), 3.81 (broad m, 16H, OCH_2), 3.67 (broad m, 16H, OCH_2), 3.61 (broad m, 16H, OCH_2), 3.48 (broad m, 16H, OCH_2), 3.26 (s, 24H, OCH_3), 3.11-3.14 (m, 1H, Glu-H), 2.73-2.68 (m, 2H, Glu-H), 1.74 (m, 2H, py Ar-H^{2,6}), -1.12 (s, coordinated DMSO);

MS (ESI$^+$, MeOH + 0.5% TFA) *m/z* 1084.9 [(M-DMSO)+2H]$^{2+}$, 1123.9 [M+2H]$^{2+}$, 1126.9 [(M with DMSO-d_6) +2H]$^{2+}$, 1989.8 [(M - py-Glu)+H]$^+$, 1995.8 [(M with DMSO-d_6 – py-Glu) + H]$^+$, 2246.9 [M + H]$^+$;

UV-Vis (DMSO) λ_{max} nm (ε x 10^{-4}): 325 (10.9), 643 (5.59);

FT-IR (KBr) ν *cm*$^{-1}$: 3420 (OH), 1068, 1496, 1457, 1405, 1341, 1277, 1200, 1112, 1063, 942, 854, 739.

PS15

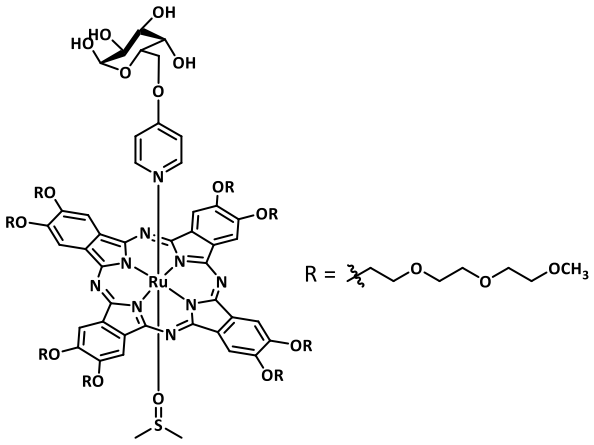

Prepared from **RuPc B** and **L8**. The fraction containing **PS15** was precipitated with hexane, affording the pure product in 40% yield as a blue, waxy solid.

^{1}H NMR (300 MHz, DMSO-d_6) δ_H 8.68 (s, 8H, Pc-H$^{\alpha}$), 5.22 (m, 2H, py Ar-H^{3,5}), 4.65 (broad m, 16H + 1H, OCH_2 + Gal-H^1), 4.05 (broad m, 16H + 4H, OCH_2 + Gal-H), 3.81-3.80 (m, 16H, OCH_2), 3.69-3.67 (m, 16H, OCH_2), 3.63-3.59 (m, 16H, OCH_2), 3.50-3.47 (m, 16H, OCH_2), 3.26 (s, 24H, OCH_3), 2.90 (m, 4H, Gal-H), 1.85 (m, 2H, py Ar-H^{2,6}), −1.13 (s, coordinated DMSO);

MS (ESI$^+$, MeOH + 0.5% TFA) *m/z* 258.1 [py-Gal + H]$^+$, 1084.9 [(M – DMSO) + 2H]$^{2+}$, 1123.9 [M + 2H]$^{2+}$, 1126.9 [M with DMSO-d_6 + 2H]$^{2+}$, 1989.8 [(M – py-Gal) + H]$^+$, 1995.8 [(M with DMSO-d_6 – py-Gal) + H]$^+$, 2246.9 [M + H]$^+$;

UV-Vis (DMSO) λ_{max} nm: 325 (14.1), 643 (7.97);

FT-IR (KBr) ν *cm*$^{-1}$: 3424 (OH), 1610, 1497, 1456, 1405, 1340, 1277, 1200, 1113, 1064, 943, 853, 752, 732.

PS16

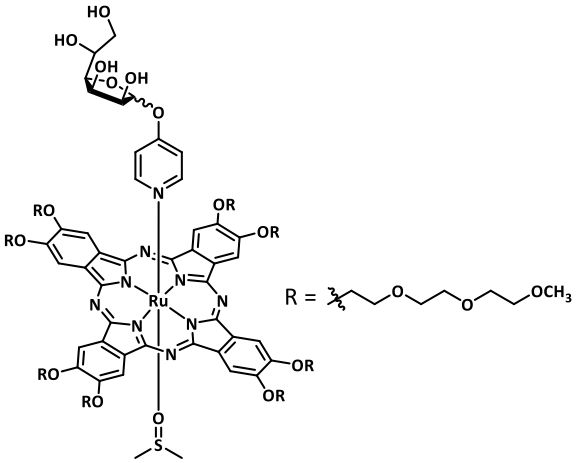

Prepared from **RuPc B** and **L9**. The fraction containing **PS16** was precipitated with hexane, affording the pure product in 46% yield as a blue, waxy solid.

^{1}H NMR (300 MHz, DMSO-d_6) δ_H 8.65 (s, 8H, Pc-H$^{\alpha}$), 4.98 (m, py Ar-H^{3,5}), 4.87 (s, 1H, Man-H^1), 4.64 (broad m, 16H, OCH_2), 4.04 (broad m, 16H, OCH_2), 3.81-3.79 (m, 16H, OCH_2), 3.67-3.65 (m, 16H, OCH_2), 3.69-3.25 (m, 6H, Man-H), 3.63-3.59 (m, 16H, OCH_2), 3.47-3.46 (m, 16H, OCH_2), 3.25 (s, 24H, OCH_3), 1.81 (m, 2H, py Ar-H^{2,6}), -1.15 (s, coordinated DMSO);
MS (ESI$^+$, MeOH + 0.5% TFA) *m/z* 1003.9 [(M – DMSO – Man) + 2H]$^{2+}$, 1043.0 [(M – Man) + 2H]$^{2+}$, 1046.0 [(M with DMSO-d_6 – Man) + 2H]$^{2+}$, 1989.8 [(M – py-Man)+H]$^+$, 1995.8 [(M with DMSO-d_6 – py-Man) +H]$^+$, 2084.9 [(M – Man) + H]$^+$, 2090.9 [(M with DMSO-d_6 – Man) + H]$^+$;
UV-Vis (DMSO) λ_{max} nm (ε x 10^{-4}): 328 (16.1), 630 (7.97);
FT-IR (KBr) ν *cm^{-1}*: 3442 (OH), 1610, 1497, 1456, 1405, 1340, 1277, 1200, 1113, 1064, 943, 853, 752, 732.

2.7.3. Mixed RuPcs donated with axial pyridyl ligands functionalized with PEG chains and carbohydrate units

2.7.3.1. Coordination reactions to RuPc A and RuPc B

*General procedure for the synthesis of **PS17-28**:* **RuPc A** or **RuPc B** (0.08 mmol) and the ligands (**L1-3** and **L4-6**) (0.20 mmol) were stirred in $CHCl_3$ at 50 °C, under argon, and protected from light. The

reaction was followed by ^{1}H NMR in $CDCl_3$. When the reaction was complete, the solvent was removed under reduced pressure and the residue was treated as indicated below.

PS17

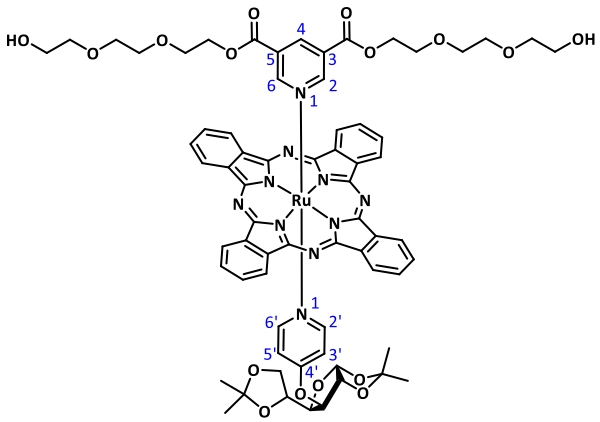

Prepared from **RuPc A**, **L1** and **L4**. The crude was chromatographed on silica gel using a 1:1 mixture of dioxane/heptane as the eluent. The fraction containing **PS17** was precipitated with hexane, affording the pure product in 26% yield as a blue solid.

^{1}H NMR (300 MHz, $CDCl_3$) δ_H 9.18 (dd, *J* = 5.6, 3.0 Hz, 8H, Pc-H$^{\alpha}$), 7.90 (dd, *J* = 5.6, 3.0 Hz, 8H, Pc-H$^{\beta}$), 7. 24 (t, *J* = 1.8 Hz, 1H, py Ar-H^{4}), 5.31 (d, *J* = 4.0 Hz, 1H, Glu-H^{1}), 4.85 (d, *J* = 7.1 Hz, 2H, py Ar-H$^{3',5'}$), 3.9 (t, *J* = 5.0 Hz, 4H, OCH_2), 3.71-3.55 (m, 5H, Glu-H$^{3-6}$), 3.49-3.37 (m, 2H + 20H, Glu-H^{2} + OCH_2), 3.23 (d, *J* = 1.8 Hz, 2H, py Ar-H^{2,6}), 2.25 (d, *J* = 7.1 Hz, 2H, py Ar-H$^{2',6'}$), 1.22 (s, 3H, CH_3), 1.04 (s, 3H, CH_3), 0.95 (s, 3H, CH_3), 0.84 (s, 3H, CH_3);

^{13}C NMR (75.5 MHz, $CDCl_3$) δ_C 161.08 (C=O), 160.60, 154.70, 150.62, 143.88, 140.86, 128.21, 125.20, 121.60, 112.24, 110.14, 109.22, 104.80, 81.17, 79.60, 79.38, 72.48, 71.19, 70.72, 70.35, 68.42, 66.98, 64.45, 61.73, 26.63, 26.40, 25.97, 24.76;

MS (ESI^{+}, MeOH + 1%TFA) *m/z* 1383.4 $[M + H]^{+}$;

UV-Vis (DMSO) λ_{max} nm (ε x 10^{-4}): 314 (5.49), 369 (1.06), 624 (3.56);

FT-IR (KBr) ν *cm^{-1}*: 1737 (C=O), 1610, 1489, 1414, 1373, 1324, 1289, 1238, 1208, 1168, 1122, 1066, 1025, 948, 885, 845, 779, 754, 738, 701.

PS18

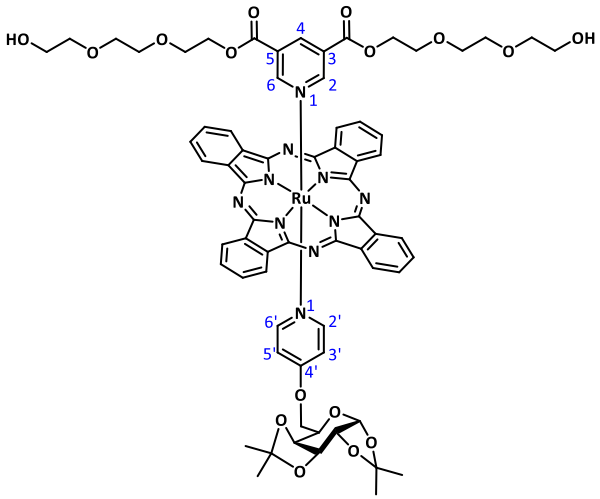

Prepared from **RuPc A**, **L1** and **L5**. The crude was chromatographed on silica gel using a 1:1 mixture of dioxane/heptane as the eluent. The fraction containing **PS18** was precipitated with hexane, affording the pure product in 19% yield as a blue solid.

^{1}HNMR (300 MHz, $CDCl_3$) δ_H 9.17 (dd, *J* = 5.6, 3.0 Hz, 8H, Pc-H^{α}), 7.89 (dd, *J* = 5.6, 3.0 Hz, 8H, Pc-H^{β}), 7.23 (t, *J* = 1.8 Hz, 1H, py Ar-H^4), 5.15 (d, *J* = 5.0 Hz, 1H, Gal-H^1), 4.81 (d, *J* = 7.2 Hz, 2H, py Ar-$H^{3',5'}$), 4.28 (dd, *J* = 7.8, 2.3 Hz, 1H, Gal-H^3), 4.04 (dd, *J* = 5.0, 2.3 Hz, 1H, Gal-H^2), 3.91 (t, *J* = 4.8 Hz, 4H, OCH_2), 3.66 (dd, *J* = 8.0, 5.0 Hz, 1H, Gal-H^4), 3.50-3.31 (m, 1H + 20H, Gal-H^5 + OCH_2), 3.22 (d, *J* = 1.8 Hz, 2H, py Ar-$H^{2,6}$), 3.21-3.04 (m, 2H, Gal-H^6), 2.22 (d, *J* = 7.2, 2H,py Ar-$H^{2',6'}$), 1.11 (6H, s, CH_3), 1.03 (3H, s, CH_3), 0.98 (3H, s, CH_3);

MS (ESI^+, MeOH + 1%TFA) *m/z* 1383.4 $[M + H]^+$;

UV-Vis (DMSO) λ_{max} nm (ε x 10^{-4}): 315 (11.3), 367 (1.99), 625 (7.42);

FT-IR (KBr) ν cm^{-1}: 1739 (C=O), 1613, 1489, 1414, 1381, 1324, 1289, 1240, 1208, 1169, 1123, 1066, 1006, 889, 833, 779, 754, 740, 700.

PS19

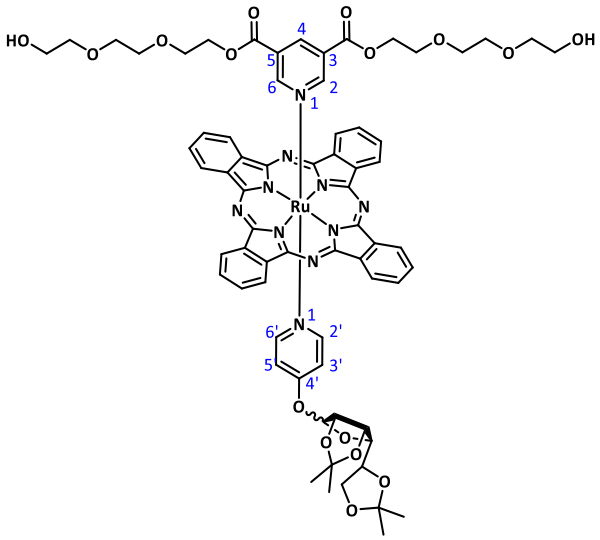

Prepared from **RuPc A**, **L1** and **L6**. The crude was chromatographed on silica gel using a 1:1 mixture of dioxane/heptane as the eluent. The fraction containing **PS19** was precipitated with hexane, affording the pure product in 23% yield as a blue solid.

^{1}HNMR (300 MHz, $CDCl_3$) δ_H 9.17 (dd, *J* = 5.6, 3.0 Hz, 8H, Pc-H$^{\alpha}$), 7.89 (dd, *J* = 5.6, 3.0 Hz, 8H, Pc-H$^{\beta}$), 7.23 (t, *J* = 1.8 Hz, 1H, py Ar-H^4), 4.88 (d, *J* = 7.4 Hz, 4H, py Ar-H^{3,5}), 4.52 (s, 2H, Man-H^1), 4.39 (dd, *J* = 5.8, 3.7 Hz, 1H, Man-H^3), 4.12 (d, *J* = 5.8 Hz, 1H, Man-H^2), 3.96 (ddd, *J* = 7.9, 6.3, 4.6 Hz, 1H, Man-H^5), 3.91 (t, *J* = 4.8 Hz, 4H, OCH_2), 3.67 (dd, *J* = 8.9, 6.3 Hz, 1H, Man-H^6), 3.50-3.37 (m, 20H, OCH_2), 3.31 (dd, *J* = 8.9, 4.6 Hz, 1H, Man-H^6), 3.23 (dd, *J* = 7.9, 3.7 Hz, 1H, Man-H^4), 3.20 (d, *J* = 1.8 Hz, 2H, py Ar-H^{2,6}), 2.25 (d, *J* = 7.4 Hz, 4H, py Ar-H^{2,6}), 1.18 (s, 3H, CH_3), 1.16 (s, 3H, CH_3), 1.06 (s, 3H, CH_3), 1.03 (s, 3H, CH_3);

MS (ESI$^+$, MeOH + 1%TFA) *m/z* 454.2 [py-PEG + Na]$^+$, 1383.4 [M + H]$^+$ 1405.4 [M + Na]$^+$;

UV-Vis (DMSO) λ_{max} nm: 315 (10.5), 367 (1.91), 625 (7.04);

FT-IR (KBr) ν *cm^{-1}*: 1738 (C=O), 1610, 1413, 1372, 1324, 1289, 1237, 1207, 1168, 1122, 1065, 976, 844, 779, 754, 738, 700, 682.

PS20

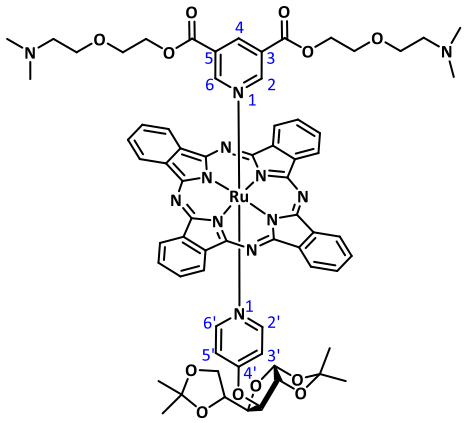

Prepared from **RuPc A**, **L2** and **L4**. The crude was chromatographed on silica gel using a 94:5:1 mixture of dioxane/MeOH/TEA as the eluent. After the evaporation of the fraction containing **PS20**, the residue was redissolved in DCM and washed with brine. The organic phase was evaporated and washed with hexane, affording the pure product in 26% yield as a blue solid.

^{1}HNMR (300 MHz, $CDCl_3$) 9.18 (dd, *J* = 5.0, 2.3 Hz, 8H, Pc-H^{α}), 7.92 (dd, *J* = 5.0, 2.3 Hz, 8H, Pc-H^{β}), 7.19 (t, *J* = 2.1 Hz, 1H, py Ar-H^4), 5.31 (d, *J* = 3.9, 1H, Glu-H^1), 4.86 (d, *J* = 6.0, 2H, py Ar-$H^{3',5'}$), 3.2 (t, *J* = 3.3 Hz, 4H, OCH_2), 3.71-3.42 (m, 6H, Glu-H^{2-6}), 3.44 (t, *J* = 5.5 Hz, 8H, OCH_2), 3.21 (d, *J* = 2.1, 2H, py Ar-$H^{2,6}$), 2.34-2.33 (m, 4H + 12H + 2H, NCH_2 + py Ar-$H^{2',6'}$ + NCH_3), 1.22 (s, 3H, CH_3), 1.03 (s, 3H, CH_3), 0.95 (s, 3H, CH_3), 0.84 (s, 3H, CH_3);

MS (ESI^+, MeOH + 1%TFA) *m/z* 1349.5 $[M + H]^+$;

UV-Vis (DMSO) λ_{max} nm (ε x 10^{-4}): 315 (5.58), 370 (1.14), 625 (3.85);

FT-IR (KBr) ν cm^{-1}: 176, 1610, 1488, 1413, 1372, 1323, 1288, 1208, 1167, 1122, 1065, 1022, 911, 846, 779, 754, 738.

PS21

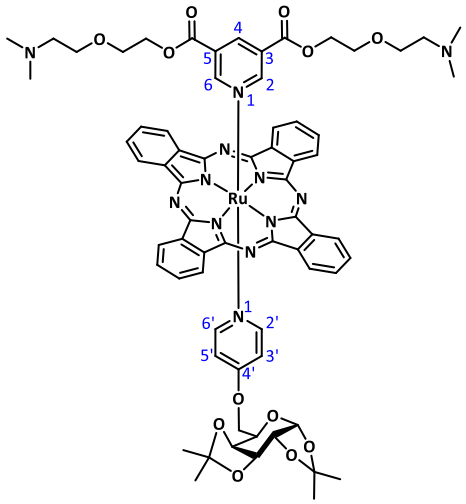

Prepared from **RuPc A**, **L2** and **L5**. The crude was chromatographed on silica gel using a 94:5:1 mixture of dioxane/MeOH/TEA as the eluent. After the evaporation of the fraction containing **PS21**, the residue was redissolved in DCM and washed with brine. The organic phase was evaporated and washed with hexane, affording the pure product in 25% yield as a blue solid.

^{1}HNMR (300 MHz, $CDCl_3$) δ_H 9.16 (dd, *J* = 5.5, 3.0 Hz, 8H, Pc-H^{α}), 7.89 (dd, *J* = 5.5, 3.0 Hz, 8H,Pc-H^{β}), 7.18 (t, *J* = 1.7, 1H, py Ar-H^4), 5.15 (d, *J* = 5.0, 1H, Gal-H^1), 4.80 (d, *J* = 7.4, 2H, py Ar-$H^{3',5'}$), 4.28 (dd, *J* = 7.9 and 2.3, 1H, Gal-H^3), 4.04 (dd, *J* = 5.0, 2.3 Hz, 1H, Gal-H^2), 3.89 (t, *J* = 5.2, 4H, OCH_2), 3.66 (dd, *J* = 7.9, 1.7 Hz, 1H, Gal-H^4), 3.46 (m, 8H, OCH_2), 3.33 (m, 1H, Gal-H^5), 3.20 (d, *J* = 1.7, 2H, py Ar-$H^{2,6}$), 3.20-3.15 (m, 1H, Gal-H^6), 3.00-3.05 (m, 1H, Gal-H^6), 2.44 (t, *J* = 5.3, 4H, NCH_2), 2.22 (m, 2H + 12H, py Ar-$H^{2',6'}$ + NCH_3), 1.11 (s, 6H, CH_3), 1.03 (s, 3H, CH_3), 0.98 (s, 3H, CH_3);

MS (ESI$^+$, MeOH + 1%TFA) *m/z* 952.2 [(M – py-PEG) + H]$^+$, 1349.5 [M + H]$^+$;

UV-Vis (DMSO) λ_{max} nm (ε x 10^{-4}): 315 (4.45), 370 (0.963), 625 (3.09);

FT-IR (KBr) ν *cm^{-1}*: 1735 (C=O), 1613, 1488, 1413, 1373, 1323, 1289, 1256, 1207, 1123, 1066, 1005, 832, 754, 738, 700.

PS22

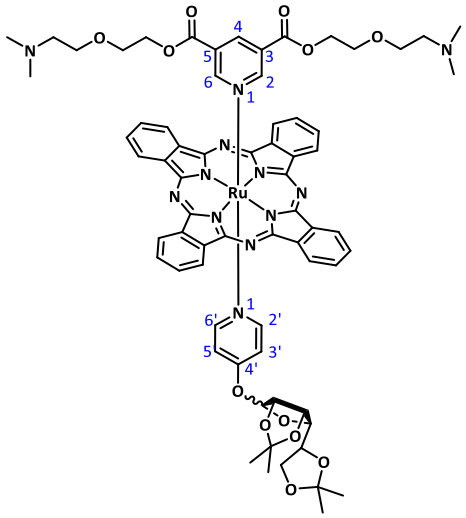

Prepared from **RuPc A**, **L2** and **L6**. The crude was chromatographed on silica gel using a 94:5:1 mixture of dioxane/MeOH/TEA as the eluent. After the evaporation of the fraction containing **PS21**, the residue was redissolved in DCM and washed with brine. The organic phase was evaporated and washed with hexane, affording the pure product in 8% yield as a blue solid.

^{1}HNMR (300 MHz, $CDCl_3$) δ_H 9.17 (broad m, 8H, Pc-H^{α}), 7.93 (broad m, 8H,Pc-H^{β}), 7.16 (m, 1H, py Ar-H^4), 4.88 (d, *J* = 6.7 Hz, 2H, py Ar-$H^{3,5}$), 4.52 (s, 1H, Man-H^1), 4.39 (m, 1H, Man-H^3), 4.12 (d, *J* = 5.6 Hz, 2H, Man-H^2), 3.96-3.90 (m, 1H + 4H, OCH_2 + Man-H^5), 3.76-3.48 (m, 1H + 8H, Man-H^6 + OCH_2), 3.30 (dd, *J* = 9.5, 4.2 Hz, 1H, Man-H^6), 3.23 (dd, *J* = 7.7, 4.1 Hz, 2H, Man-H^4), 3.18 (d, *J* = 2.2, 2H, py Ar-$H^{2,6}$), 2.47 (m, 4H, NCH_2), 2.23 (m, 2H, py Ar-$H^{2',6'}$), 2.18 (s, 12H, NCH_3), 1.18 (s, 3H, CH_3), 1.16 (s, 3H, CH_3), 1.06 (s, 3H, CH_3), 1.02 (s, 3H, CH_3);

MS (ESI^+, MeOH + 0.1% formic acid) *m/z* 1349.4 $[M + H]^+$;

UV-Vis (DMSO) λ_{max} nm (ε x 10^{-4}): 315 (7.12), 368 (1.34), 625 (4.75);

FT-IR (KBr) ν cm^{-1}: 1733 (C=O), 1610, 1489, 1413, 1372, 1323, 1288, 1261, 1207, 1168, 1122, 1065, 1029, 977, 912, 861, 779, 755, 738.

PS23

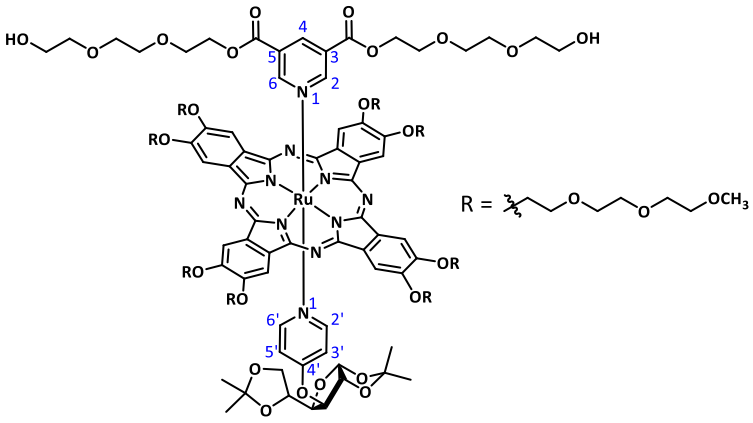

Prepared from **RuPc B**, **L1** and **L4**. The crude was chromatographed on silica gel using a 99:1 mixture of THF/MeOH as the eluent. The fraction containing **PS23** was evaporated, dissolved in the minimum amount of DCM and precipitated with hexane, affording the pure product in 35% yield as a blue, waxy solid.

^{1}H NMR (300 MHz, $CDCl_3$) δ_H 8.61 (8H, s, Pc-H^{α}), 7.22 (1H, m broad signal, py Ar-H^4), 5.31 (d, *J* = 3.6, 1H, Glu-H^1), 4.86 (d, *J* = 6.5, 2H, py Ar-$H^{3',5'}$), 4.69 (m broad signal, 16H, Pc-OCH_2), 4.17 (t, *J* = 4.5, 16H, Pc-OCH_2), 3.95-3.92 (m, 16H + 4H, Pc-OCH_2 + py-OCH_2), 3.81-3.58 (48H + 5H, m, Pc-OCH_2 + Glu-H^{3-6}), 3.49-3.39 (24H + 20H + 1H, m, Pc-OCH_3 + py-OCH_2 + Glu-H^2), 3.26 (m broad signal, 2H, py Ar-$H^{2,6}$), 2.22 (2H, d, *J* = 6.5, py Ar-$H^{2',6'}$), 1.23 (s, 3H, CH_3), 1.06 (s, 3H, CH_3), 0.95 (s, 3H, CH_3), 0.88 (s, 3H, CH_3);

MS (ESI$^+$, MeOH + 1%TFA) *m/z* 1340.6 $[M + 2H]^{2+}$, 1911.7 $[(M - 2L) + H]^+$, 2248.9 $[(M - py\text{-}PEG) + H]^+$, 2679.1 ($M^+$), 2680.1 $[M + H]^+$;

UV-Vis (DMSO) λ_{max} nm (ε x 10^{-4}): 323 (5.72), 369 (1.55), 623 (2.86);

FT-IR (KBr) ν cm^{-1}: 1731 (C=O), 1609, 1496, 1453, 1406, 1276, 1200, 1112, 1064, 942, 851, 745, 730.

PS24

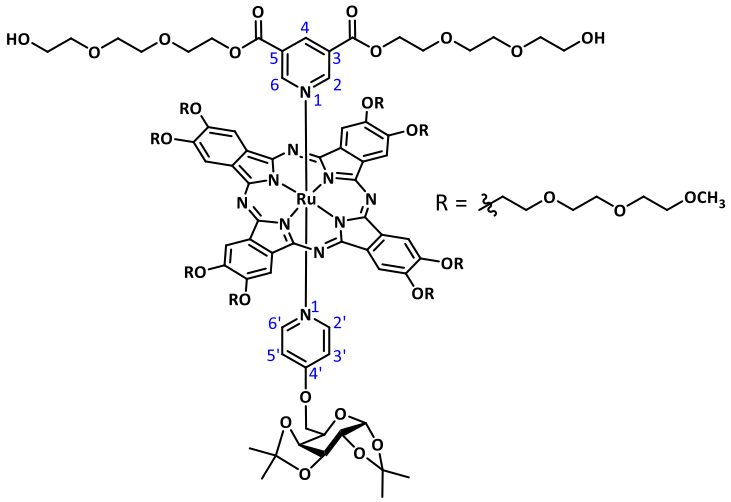

Prepared from **RuPc B**, **L1** and **L5**. The crude was chromatographed on silica gel using a 99:1 mixture of THF/MeOH as the eluent. The fraction containing **PS24** was evaporated, dissolved in the minimum amount of DCM and precipitated with hexane, affording the pure product in 17% yield as a blue, waxy solid.

^{1}H NMR (300 MHz, $CDCl_3$) δ_H ^{1}H NMR (300Hz, $CDCl_3$) δ_H 8.61 (8H, s, Pc-H$^{\alpha}$), 7.22 (m broad signal, 1H, py Ar-H^4), 5.17 (d, *J* = 4.8 Hz, 1H, Gal-H^1), 4.82 (d, *J* = 6.6 Hz, 2H, py Ar-H$^{3',5'}$), 4.70 (m broad signal, 16H, Pc-OCH_2), 4.30 (dd, *J* = 8.0, 2.0 Hz, 1H, Gal-H^3), 4.18 (m broad signal, 16H, Pc-OCH_2), 4.05 (m, 1H, Gal-H^2), 3.95-3.92 (m broad signal, 16H + 4H, Pc-OCH_2 + py-OCH_2), 3.79 (t, *J* = 4.7 Hz, 16H, Pc-OCH_2), 3.74-3.71 (m, 16H + 1H, Pc-OCH_2 + Gal-H^4), 3.60 (t, *J* = 4.7 Hz, 16H, Pc-OCH_2), 3.50-3.39 (24H + 20H + 1H, m, Pc-OCH_3 + py-OCH_2 + Gal-H^5), 3.26 (m broad signal, 2H, py Ar-H^{2,6}), 3.16-2.98 (m, 2H, Gal-H^6), 2.20 (d, *J* = 6.6 Hz, 2H, py Ar-H$^{2',6'}$), 1.42 (6H, s, CH_3), 1.12 (3H, s, CH_3), 1.06 (3H, s, CH_3);

MS (ESI$^+$, MeOH + 1%TFA) *m/z* 1340.58 $[M + 2H]^{2+}$, 2248.94 $[(M – py\text{-}PEG) + H]^+$, 2680.11 $[M + H]^+$;

UV-Vis (DMSO) λ_{max} nm (ε x 10^{-4}): 323 (6.47), 368 (1.98), 623 (3.15);

FT-IR (KBr) ν *cm^{-1}*: 1736 (C=O), 1609, 1495, 1451, 1406, 1275, 1199, 1102, 1064, 943, 819, 753.

PS25

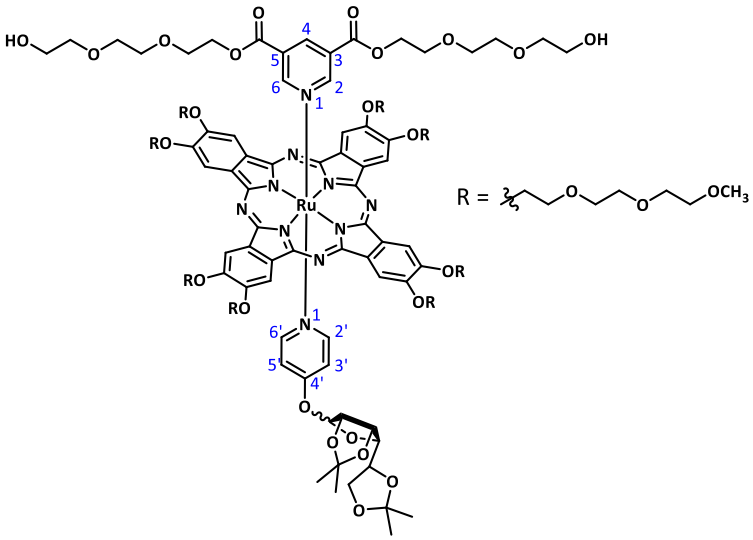

Prepared from **RuPc B**, **L1** and **L6**. The crude was chromatographed on silica gel using a 98:2 mixture of THF/MeOH as the eluent. The fraction containing **PS25** was evaporated, dissolved in the minimum amount of DCM and precipitated with hexane, affording the pure product in 19% yield as a blue, waxy solid.

^{1}H NMR (300 MHz, $CDCl_3$) δ_H ^{1}H NMR (300Hz, $CDCl_3$) δ_H 8.61 (8H, s, Pc-H$^{\alpha}$), 7.21 (t, *J* = 2.0 Hz,, 1H, py Ar-H^4), 4.87 (d, *J* = 7.3 Hz, 2H, py Ar-H^{3,5}), 4.68 (m broad signal, 16H, Pc-OCH_2), 4.53 (s, 1H, Man-H^1), 4.40 (dd, *J* = 5.8, 3.3 Hz, 1H, Man-H^3), 4.16 (t, *J* = 5.0, 16H, Pc-OCH_2), 4.12 (d, *J* = 5.9 Hz, 1H, Man-H^2), 3.95-3.92 (m, 16H + 4H + 2H, Pc-OCH_2 + py-OCH_2 + Gal-H^{2,5}), 3.81-3.78 (m, 16H, Pc-OCH_2), 3.74-3.71 (m, 16H, Pc-OCH_2), 3.70-3.66 (m, 1H, Man-H^6), 3.61-3.58 (m, 16H, Pc-OCH_2), 3.51-3.29 (m, 24H + 20H + 1H, Pc-OCH_3 + py-OCH_2 + Man-H^6), 3.26-3.22 (m, 2H + 1H, py Ar-H^{2,6} + Man-H^4), 2.23 (d, *J* = 7.3 Hz, 2H, py Ar-H$^{2',6'}$), 1.19 (s, 3H, CH_3), 1.16 (s, 3H, CH_3), 1.07 (s, 6H, CH_3);

MS (ESI$^+$, MeOH + 0.1% formic acid) *m/z* 1340.5 $[M + 2H]^{2+}$, 2680.1 $[M + H]^+$;

UV-Vis (DMSO) λ_{max} nm (ε x 10^{-4}): 322 (11.2), 366 (3.12), 623 (5.44);

FT-IR (KBr) ν *cm*$^{-1}$: 1735 (C=O), 1609, 1488, 1413, 1372, 1323, 1288, 1208, 1167, 1122, 1064, 1023, 948, 855, 764.

PS26

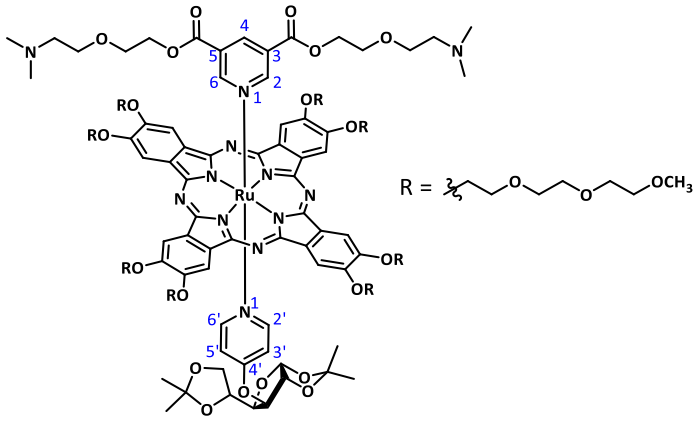

Prepared from **RuPc B**, **L2** and **L4**. The crude was chromatographed on silica gel using a 94:5:1 mixture of THF/MeOH/TEA as the eluent. After the evaporation of the fraction containing **PS26**, the residue was redissolved in DCM and washed with brine. The organic phase was evaporated, dissolved in the minimum amount of DCM and precipitated with hexane, affording the pure product in 17% yield as a blue, waxy solid.

^{1}H NMR (300 MHz, $CDCl_3$) δ_H 8.60 (s, 8H, Pc-H$^{\alpha}$), 7.15 (t, *J* = 1.6 Hz, 1H, py Ar-H^4), 5.31 (d, *J* = 4.3, 1H, Glu-H^1), 4.88 (d, *J* = 7.2, 2H, py Ar-H$^{3',5'}$), 4.69 (t, *J* = 1.6 Hz, 16H, Pc-OCH_2), 4.17 (t, *J* = 4.9, 16H, Pc-OCH_2), 3.98-3.91 (m, 16H + 4H, Pc-OCH_2 + py-OCH_2), 3.79 (t, *J* = 4.8 Hz, 16H, Pc-OCH_2), 3.73 (t, *J* = 4.7 Hz, 16H, Pc-OCH_2), 3.61-3.58 (m, 16H + 5H, Pc-OCH2 + Glu-H$^{3-6}$), 3.49-3.47 (m, 8H, py-OCH_2), 3.43 (d, *J* = 3.9, 1H, Glu-H^2), 3.40 (s, 24H, Pc-OCH_3), 3.18 (d, *J* = 1.6, 2H, py Ar-H^{2,6}), 2.94-2.91 (m, 4H, py-NCH_2), 2.57 (s, 12H, py-NCH_3), 2.25 (d, *J* = 7.2, 2H, py Ar-H$^{2',6'}$), 1.23 (3H, s, CH_3), 1.06 (3H, s, CH_3), 0.96 (3H, s, CH_3), 0.88 (3H, s, CH_3);

MS (ESI$^+$, MeOH + 1%TFA) *m/z* 1323.6 $[M + 2H]^{2+}$, 1911.8 $[(M – 2L) + H]^+$ 2249.0 $[(M – py\text{-}PEG) + H]^+$;

UV-Vis (DMSO) λ_{max} nm (ε x 10^{-4}): 323 (6.44), 369 (1.69), 623 (3.30);

FT-IR (KBr) ν *cm^{-1}*: 1734 (C=O), 1606, 1495, 1406, 1276, 1241, 1200, 1111, 1064, 944, 850, 757, 732, 697.

PS27

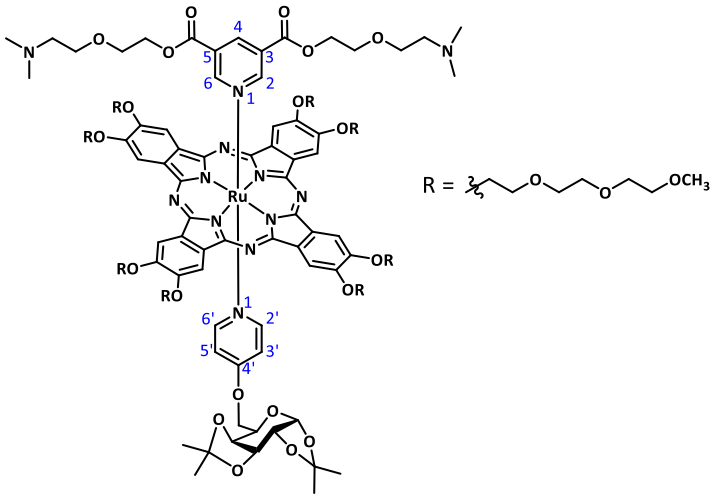

Prepared from **RuPc B**, **L2** and **L5**.The crude was chromatographed on silica gel using a 94:5:1 mixture of THF/MeOH/TEA as the eluent. After the evaporation of the fraction containing **PS27**, the residue was redissolved in DCM and washed with brine. The organic phase was evaporated, dissolved in the minimum amount of DCM and precipitated with hexane, affording the pure product in 7% yield as a blue, waxy solid.

^{1}H NMR (300 MHz, $CDCl_3$) δ_H 8.60 (s, 8H, Pc-H$^{\alpha}$), 7.16 (m broad signal, 1H, py Ar-H^4), 5.17 (d, *J* = 5.0, 1H, Gal-H^1), 4.83 (d, *J* = 7.3 Hz, 2H, py Ar-H$^{3',5'}$), 4.69 (m, 16H, Pc-OCH_2), 4.30 (dd, *J* = 8.0, 2.0 Hz, 1H, Gal-H^3), 4.17 (t, *J* = 5.3, 16H, Pc-OCH_2), 4.06 (dd, *J* = 5.0, 2.4 Hz, 2H, Gal-H^2), 3.97 (m broad signal, 4H, py-OCH_2), 3.94-3.92 (m, 16H, Pc-OCH_2), 3.81-3.79 (m, 16H, Pc-OCH_2), 3.74-3.72 (m, 16H, Pc-OCH_2), 3.69 (dd, J = 8.0, 1.7 Hz, 1H, Gal-H^4), 3.61-3.59 (m, 16H, Pc-OCH_2), 3.48 (m broad signal, 4H, py-OCH_2), 3.40 (s, 24H, Pc-OCH_3), 3.37 (m, 1H, Gal-H^5), 3.18 (d, J = 1.5 Hz, 2H, py-Ar-H^{2,6}), 3.20-3.06 (m, 2H, Gal-H^6), 2.91 (m broad signal, 4H, py-NCH_2), 2.5 (s, 12H, py-NCH_3), 2.24 (d, *J* = 7.3 Hz, 2H, py Ar-H$^{2',6'}$), 1.12 (6H, s, CH_3), 1.06 (3H, s, CH_3), 1.05 (3H, s, CH_3);

MS (ESI$^+$, MeOH + 0.1% formic acid) *m/z* 1323.6 $[M+2H]^{2+}$, 1911.8 $[(M - 2L) + H]^+$ 2248.9 [(M – py-PEG) + H]$^+$;

UV-Vis (DMSO) λ_{max} nm (ε x 10^{-4}): 322 (7.69), 368 (2.09), 623 (3.99);

FT-IR (KBr) ν *cm^{-1}*: 1735 (C=O), 1609, 1494, 1450, 1405, 1274, 1199, 1109, 1063, 941, 854, 753, 730.

PS28

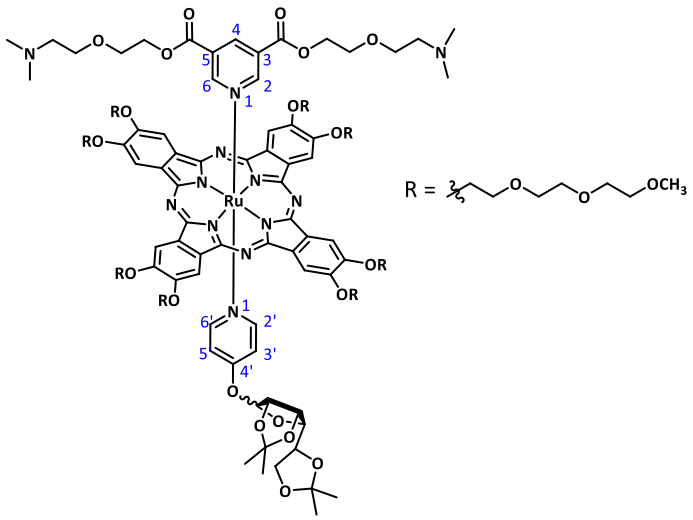

Prepared from **RuPc B**, **L2** and **L6**.The crude was chromatographed on silica gel using a 94:5:1 mixture of THF/MeOH/TEA as the eluent. After the evaporation of the fraction containing **PS28**, the residue was redissolved in DCM and washed with brine. The organic phase was evaporated, dissolved in the minimum amount of DCM and precipitated with hexane, affording the pure product in 5% yield as a blue, waxy solid.

^{1}H NMR (300 MHz, $CDCl_3$) δ_H 8.59 (s, 8H, Pc-H$^{\alpha}$), 7.15-7.14 (m, 1H, py Ar-H^4), 4.87 (d, *J* = 7.6 Hz, 2H, py Ar-H$^{3',5'}$), 4.70-4.65 (m, 16H, Pc-OCH_2), 4.53 (s, 1H, Man-H^1), 4.41-4.38 (m, 1H, Man-H^3), 4.16 (t, *J* = 4.9, 16H, Pc-OCH_2), 4.12 (d, *J* = 5.7 Hz, 1H, Man-H^2), 3.99-3.95 (m, 1H + 4H, Man-H^5 + py-OCH_2), 3.93-3.90 (m, 16H, Pc-OCH_2), 3.80-3.77 (m, 16H, Pc-OCH_2), 3.73-3.70 (m, 16H, Pc-OCH_2), 3.70-3.66 (m, 1H, Man-H^6), 3.60-3.57 (m, 16H, Pc-OCH_2), 3.48-3.45 (m, 4H, py-OCH_2), 3.38 (s, 24H, Pc-OCH_3), 3.34-3.32 (m, 1H, Man-H^6), 3.23 (dd, *J* = 8.3, 3.4 Hz, 1H, Man-H^4), 3.18 (d, J = 1.5 Hz, 2H, py-Ar-H^{2,6}), 2.94-2.91 (m, 4H, py-NCH_2), 2.56 (s, 12H, py-NCH_3), 2.23 (d, *J* = 7.6 Hz, 2H, py Ar-H$^{2',6'}$), 1.18 (s, 3H, CH_3), 1.16 (s, 3H, CH_3), 1.06 (s, 6H, CH_3);

MS (ESI$^+$, MeOH + 0.1% formic acid) *m/z* 500.7 [(M - 2L) + 4Na]$^{4+}$, 772.3 [(M – py-PEG) + 3Na]$^{3+}$, 1125.0 [(M – py-PEG) + 2H]$^{2+}$, 1136.0 [(M – py-PEG) + Na + H]$^{2+}$, 1147.0[(M – py-PEG) + 2Na]$^{2+}$, 1324.1 [M + 2H]$^{2+}$;

UV-Vis (DMSO) λ_{max} nm (ε x 10^{-4}): 323 (8.59), 369 (2.29), 623 (4.33);

FT-IR (KBr) ν *cm*$^{-1}$: 1732 (C=O), 1609, 1496, 146, 1407, 1378, 1275, 1201, 1112, 1064, 945, 856, 819, 755, 730, 693.

2.7.4. RuPcs donated with axial pyridyl ligands functionalized with folic acid units

2.7.4.1. Route A: Functionalization of pyridine with folic acid followed by coordination to a RuPc

4-(folic acid) pyridine (L10)

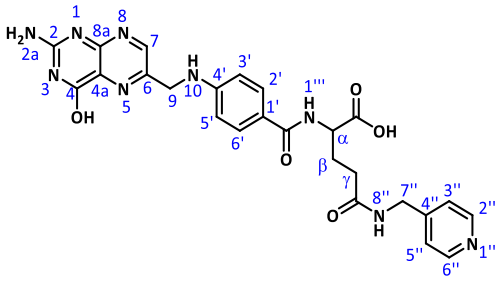

To a solution of folic acid (1 g, 2.3 mmol) in dry DMSO (100 mL) N-hydroxysuccinimide (310.7 mg, 2.7 mmol) and EDC (517.6 mg, 2.7 mmol) were added. After stirring at room temperature, in the dark, under argon, for an hour, 4-(aminomethyl)pyridine (0.275 mL, 2.7 mmol) and TEA (0.96 mL, 6.9 mmol) were added. The reaction mixture was stirred at room temperature, under argon, for 2 days. The resulting solution was evaporated under reduced pressure and the residue was precipitated with acetone, filtrated and washed with water, $CHCl_3$ and acetone, affording **L10** in 98% yield as an orange solid.

^{1}H NMR (300 MHz, DMSO-d_6) δ_H 11.45 (s, 1H, CO_2H), 8.64 (s, 1H, pyrazine Ar-H^{7}), 8.45 (broad m, 2H+1H, py Ar-H$^{2'',6''}$ + NH$^{8''}$), 8.18-8.07 (m, 1H, NH$^{1'''}$), 7.69 (d, *J* = 9.0 Hz, 2H, Ar-H$^{2',6'}$), 7.24-7.20 (m, 2H, py Ar-H$^{3'',5''}$), 6.93 (broad m, 2H + 1H, NH_2^{2a} + NH^{10}), 6.64 (d, *J* = 9.0, 2H, Ar-H$^{3',5'}$), 4.49 (d, *J* = 5.5, 2H, H^{9}), 4.42-4.40 (m, 1H, H$^{\alpha}$), 4.29 (d, *J* = 5.6, 2H, H$^{7''}$), 2.31 (d, *J* = 6.6 Hz, 2H, H$^{\gamma}$), 2.08-1.92 (m, 2H, H$^{\beta}$);

MS (FAB+, m-NBA+TFA) *m/z* 532.3 $[M + H]^+$.

PS29

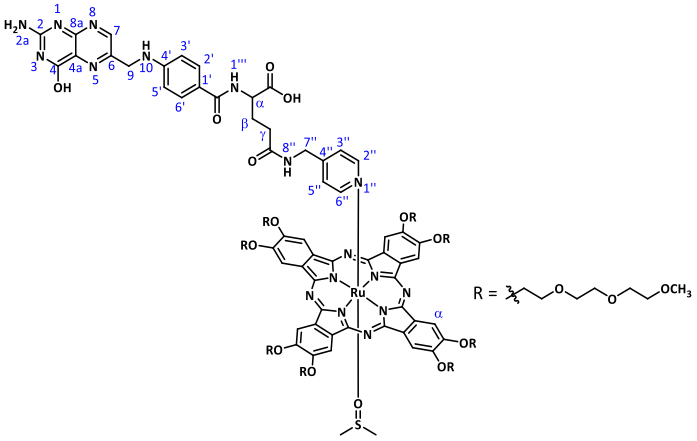

A solution of **RuPc B** (43.7 mg, 0.022 mmol) and **L10** (29.1 mg, 0.055 mmol) in DMSO (3 mL) was stirred overnight, at room temperature, under argon and protected from light. The resulting solution was evaporated under reduced pressure and the crude was subjected to size exclusion chromatography on Biobeads using DMF as the eluent. The fraction containing **PS29** was evaporated, dissolved in the minimum amount of DCM and precipitated with hexane, affording **PS29** in 57% yield as a blue, waxy solid.

^{1}H NMR (300 MHz, DMSO-d_6) δ_H 8.71 (s, 8H, Pc-H$^{\alpha}$), 8.64 (s, 1H, pyrazine Ar-H^{7}), 8.45 (broad s, 1H, NH$^{8''}$), 8.22-8.15 (m, 1H, NH$^{1'''}$), 7.71-6.63 (m, 7H, Ar-H$^{2',6'}$ + NH_2^{2a} + NH^{10} + Ar-H$^{3',5'}$), 5.48-5.46 (m, 2H, py-H$^{3'',5''}$), 4.66 (broad m, 16H, OCH_2), 4.50-4.40 (m, 2H + 1H, H^9 + H$^{\alpha}$), 4.31-4.27 (m, 2H, H$^{7''}$), 4.05 (broad m, 16H, OCH_2), 3.81 (broad m, 16H, OCH_2), 3.61 (broad m, 16H, OCH_2), 3.48 (broad m, 16H, OCH_2), 3.36 (broad m, 16H, OCH_2), 3.25 (s, 24H, OCH_3), 2.30-2.31 (m, 2H, H$^{\gamma}$), 2.10-1.97 (m, 2H, H$^{\beta}$) 1.26-1.25 (m, 2H, py-H$^{2'',6''}$), -1.11 (s, coordinated DMSO);

MS (ESI$^+$, MeOH + 0.5% TFA) *m/z* 1222.0 [(M-DMSO) + 2H]$^{2+}$, 1261.0 [M + 2H]$^{2+}$, 1264.0 [M with DMSO-d_6 + 2H]$^{2+}$, 1911.8 [(M – 2L) + H]$^+$, 1989.8 [(M – py-FA) + H]$^+$;

UV-Vis (DMSO) λ_{max} nm (ε x 10^{-4}): 323 (6.64), 636 (2.99);

FT-IR (KBr) ν *cm^{-1}*: 1647, 1605, 1492, 1441, 1402, 1340, 1272, 1196, 1090, 1057, 938, 850, 820, 753, 732.

2.7.4.2. Route B: Coordination of 4-(aminomethyl)pyridine to RuPc followed by coupling to folic acid

Ru(bis-4-(aminomethyl)pyridine)phthalocyanine (11)

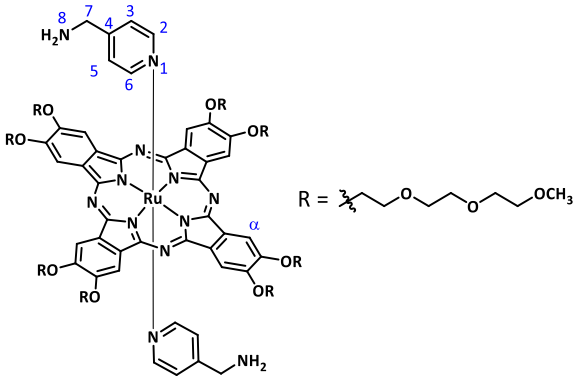

A mixture of **RuPc B** (47.3 mg, 0.024 mmol) and 4-(aminomethyl)pyridine (6.0 μL, 0.059 mmol) in CHCl3 (3 mL) was stirred overnight at 50 °C, under argon, in the dark. The resulting solution was evaporated under reduced pressure and the residue was chromatographed on neutral silica gel (previously neutralized by stirring overnight in a 95:5 mixture of $CHCl_3$/TEA, followed by filtration and washing with $CHCl_3$) using a 9:1 mixture of $CHCl_3$/MeOH as the eluent. The fraction containing **11** was evaporated and redissolved in the minimum amount of EtOAc. Hexane was added and the resulting precipitate was filtrated to afford **11** in 46% yield as a blue, waxy solid.

^{1}H NMR (300 MHz, $CDCl_3$) δ_H 8.64 (s, 8H, Pc-H$^{\alpha}$), 5.31 (d, *J* = 6.9 Hz, 4H, py Ar-H^{3,5}), 4.58 (broad m, 16H,OCH_2), 4.08 (broad m, 16H, OCH_2), 4.08 (broad m, 16H, OCH_2) 3.86 (broad m, 16H, OCH_2), 3.67 (broad m, 32H, OCH_2), 3.35 (s, 24H, OCH_3), 2.79 (s, 4H, NCH_2^7) 2.48 (d, *J* = 6.9 Hz, 4H, py Ar-H^{2,6}); **MS** (ESI$^+$, MeOH + 1% formic acid) *m/z* 967.4 [(M – 2L) + 2H]$^{2+}$, 1010.4 [(M – L) + 2H]$^{2+}$, 1064.5 [M + 2H]$^{2+}$, 1911.8 [(M – 2L) + H]$^+$, 2019.9 [(M – L) + H]$^+$, 2128.0 [M + H]$^+$.

RuPc 12

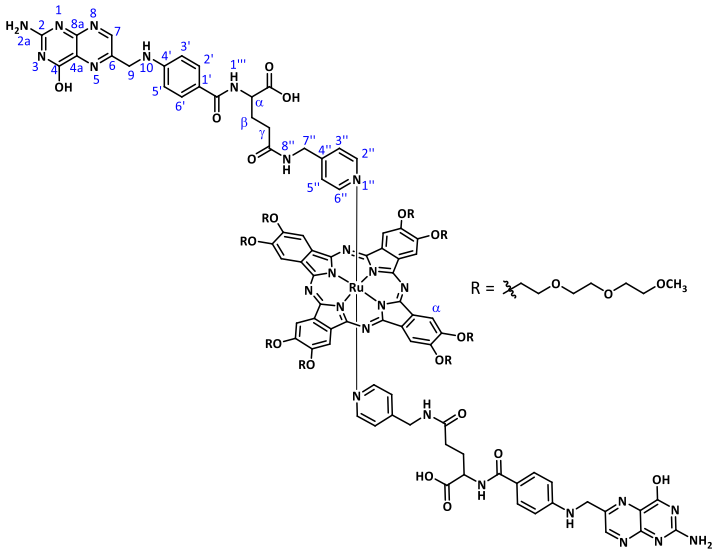

To a solution of folic acid (12.3 mg, 0.028 mmol) in dry DMSO (1 mL) N-hydroxysuccinimide (3.8 mg, 0.033 mmol) and EDC (6.3 mg, 0.033 mmol) were added. The reaction mixture was stirred at room temperature, in the dark, under argon, for an hour. TEA (11.7 µL, 0.084 mmol) and **11** (23.4 mg, 0.011 mmol) were added and the reaction mixture was stirred at room temperature for 2 days. The resulting solution was evaporated under reduced pressure and the residue was washed with THF to give a blue, waxy solid.

^{1}H NMR (300 MHz, DMSO-d_6) δ_H 11.54 (2H, s, CO_2H), 8.65 (s, 8H, Pc-H^{α}), 8.54 (s, 2H, pyrazine Ar-H^{7}), 7.65 (d, J = 8.1, 4H, Ar-$H^{2',6'}$), 6.96 (broad m, 2H + 1H, NH_2^{2a} + NH^{10}), 6.64 (d, J = 8.1, 4H, Ar-$H^{3',5'}$), 5.43 (d, J = 6.2, 4H, py Ar-$H^{3'',5''}$), 4.61-4.48 (m, 16H + 2H +2H + 4H, OCH_2 + H^9 + H^{α} + $H^{7''}$), 4.02 (broad m, 16H, OCH_2), 3.79 (broad m, 16H, OCH_2), 3.66 (broad m, 16H, OCH_2), 3.59 (broad m, 16H, OCH_2), 3.45 (broad m, 16H, OCH_2), 3.35 (24H, s, OCH_3), 2.32-2.27 (m, 4H, H^{γ}), 1.98-1.93 (m, 4H, H^{β}) 1.75-1.73 (m, 4H, py-$H^{2'',6''}$).

MS (ESI$^+$, MeOH + 0.1% TFA) *m/z* 1221.5 $[(M - L) + 2H]^{2+}$, 1275.0 $[(M - FA) + 2H]^{2+}$, 1487.1 $[M + 2H]^{2+}$.

Chapter 3 – Design, Synthesis and Characterization of Ruthenium Phthalocyanines Containing Axial Phosphine Ligands

3.1. Overview

The preparation of RuPcs endowed with phosphines as axial ligands has been reported by treatment of the so-called "crude RuPc", prepared from phthalonitrile and either $Ru_3(CO)_{12}$ or $RuCl_3.3H_2O$, with an excess of phosphine ligand.[49,302] There are also some reports on the coordination of phosphine ligands to the axial positions of RuPcs by replacement of other ligands, namely benzonitrile,[260,261] DMSO,[50] or even pyridyl ligands.[303] Alternatively, RuPcs functionalized with phosphine ligands have been prepared by cyclotetramerization of phthalonitrile in the presence of a Ru-phosphine complex.[49]

As mentioned in the introduction, a RuPc functionalized at the axial positions with phosphine ligands bearing sulphonate units (**Figure 19**a) has been prepared by replacing axial benzonitrile from a RuPc. The latter showed good solubility in water, reduced aggregation and promising photophysical properties and *in vitro* results as photosensitizer for PDT.[56,260,261]

The objectives of this chapter were the synthesis of triphenylphosphine-based ligands bearing functional groups at the benzene rings that could be converted into cationic functions, either before or after the coordination to **RuPc A**, that we would carry out by replacement of the two benzonitrile ligands. In addition, anionic phosphine ligands would be prepared from triphenylphosphine units bearing carboxylic acids.

3.2. RuPcs bearing positively charged phosphine ligands

3.2.1. RuPcs bearing six ammonium salts

The synthesis of a phosphine ligand bearing three amino functions amenable of quaternization, before or after coordination to **RuPc A**, started with the preparation of the corresponding trimethylsilyl (TMS) protected tris(3-aminophenyl)phosphine (**16**). The reaction of the 3-[bis(trimethylsilyl)amino]phenylmagnesium chloride with phosphorus trichloride (**Scheme 27**) was accomplished in good yield according to a reported procedure.[304] Characterization was done by MS,

[302] Doeff, M. M.; Sweigart, D. A. *Inorg. Chem.* **1981**, *20* (6), 1683–1687.

[303] Boucher, L. J.; Rivera, P. *Inorg. Chem.* **1980**, *19* (6), 1816–1818.

[304] Hessler, A.; Stelzer, O.; Dibowski, H.; Worm, K.; Schmidtchen, F. P. *J. Org. Chem.* **1997**, *62* (8), 2362–2369.

^{1}H (**Figure 76**), ^{13}C, ^{31}P, COSY (**Figure 77**) and HMQC (**Figure 78**) NMR. In all the NMR spectra the typical couplings with phosphorous are observed.

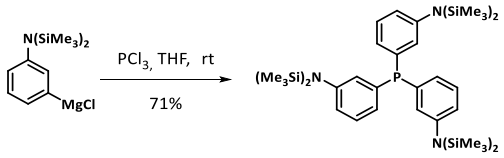

16

Scheme 27 – Synthesis of phosphine **16**.

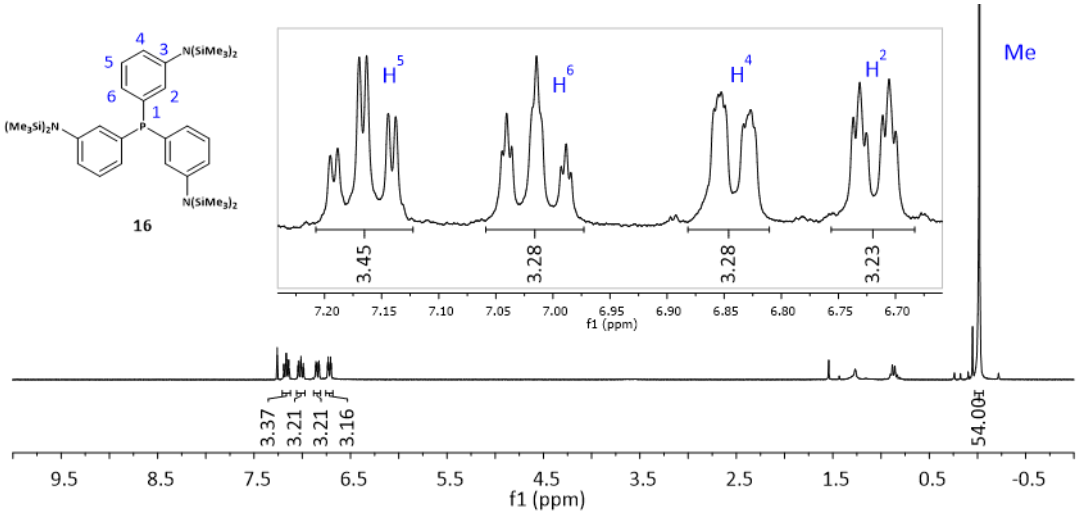

Figure 76 – ^{1}H NMR spectrum of **16** in $CDCl_3$.

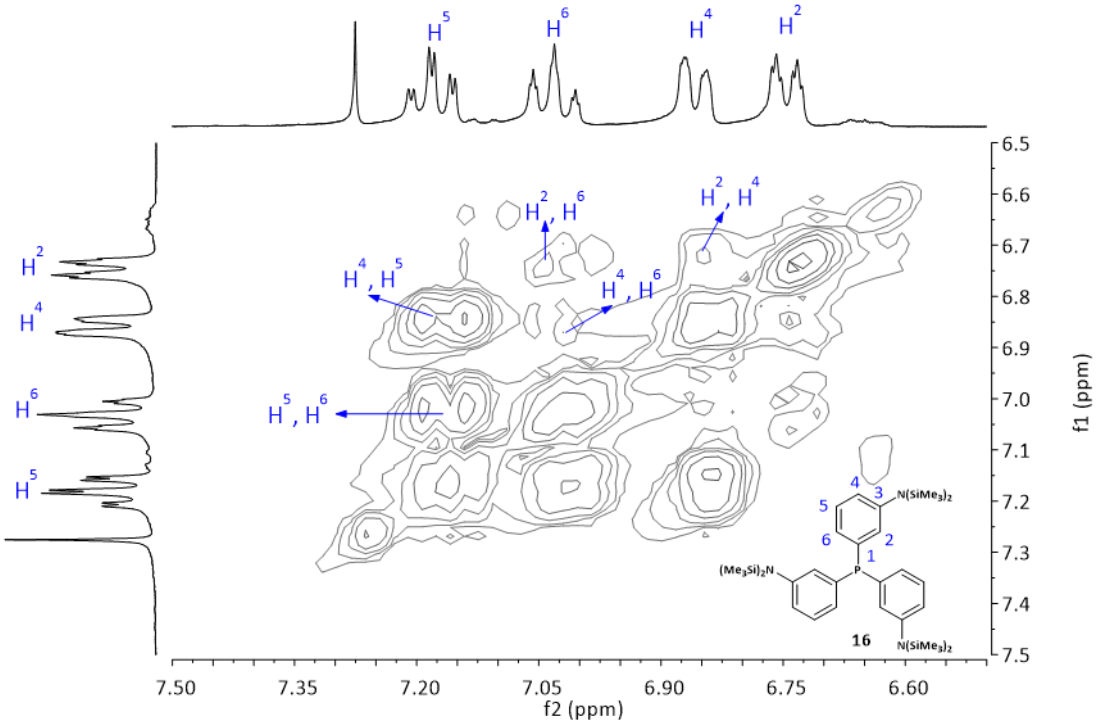

Figure 77 – Detail of the COSY NMR spectrum of **16** in $CDCl_3$.

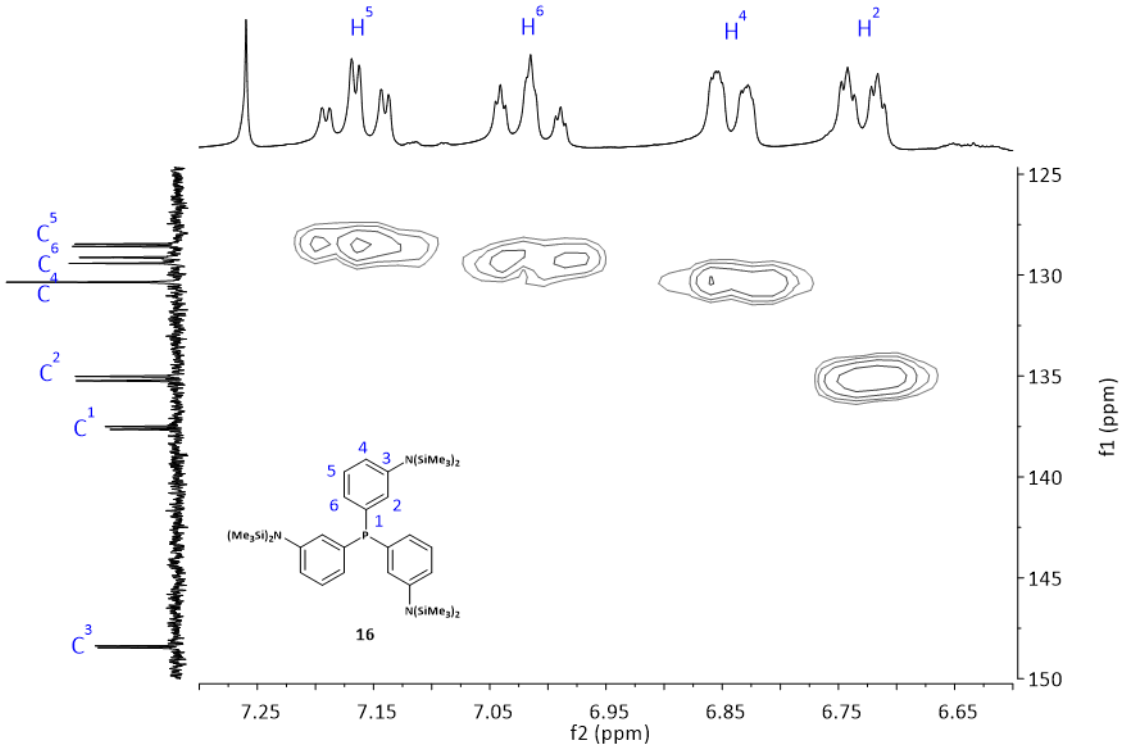

Figure 78 – Detail of the HMQC NMR spectrum in of **16** $CDCl_3$.

The synthetic routes essayed for the assembly of RuPc **21** are illustrated in **Scheme 28**.

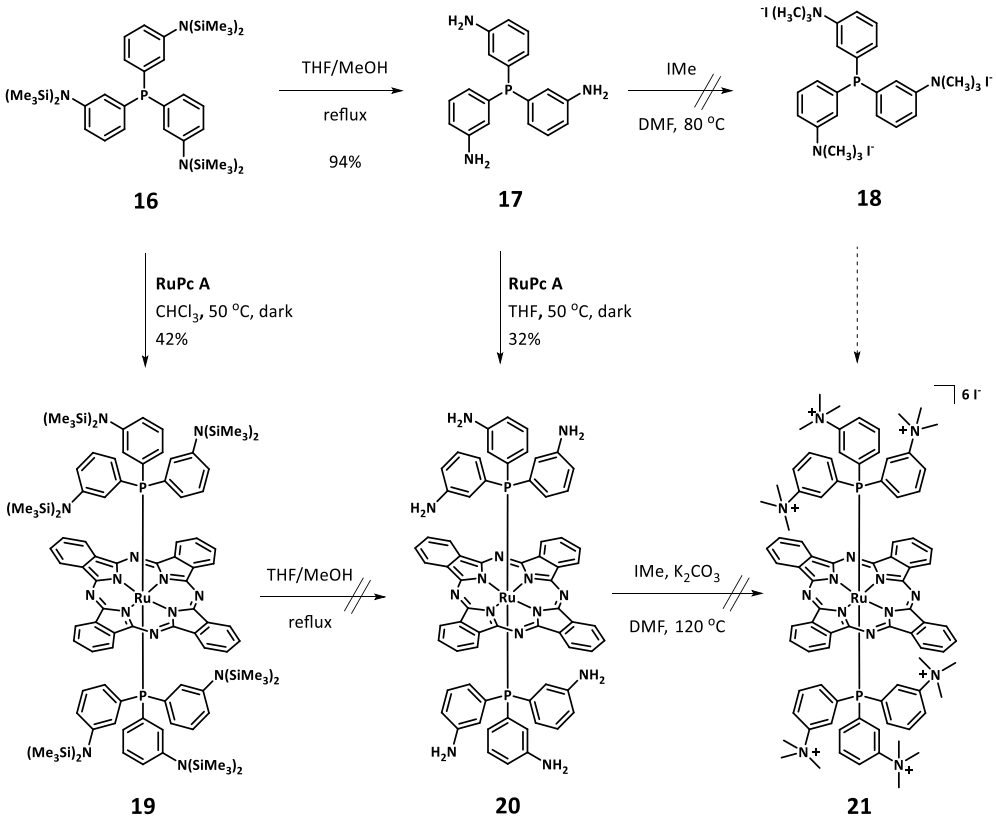

Scheme 28 – Synthetic approaches for the synthesis of **21**.

We first essayed the coordination of **16** to **RuPc A**, followed by deprotection and quaternization of the amino functions. Thus, **16** and **RuPc A** were stirred at 50 °C in chloroform in the dark, affording RuPc **19** with 42% yield, after purification by size exclusion chromatography in Biobeads, using toluene as the eluent. This compound was characterized by ^{1}H, ^{13}C, ^{31}P and COSY NMR (**Figure 79**), MS-ESI and IR. As for any RuPc axial ligand, the signals corresponding to the coordinated triphenylphosphine ligands in the ^{1}H NMR are upfield shifted with respected to those exhibited by the free ligands (**Figure 80**). The closest H^2 and H^6 protons are expected to show the highest upfield shift, corresponding to signals at 4.24 and 3.63 ppm. Thus, the multiplet at 6.16 ppm corresponds to H^4 and H^5 protons, which experienced a smaller shielding, of 0.68 and 1.01 ppm, respectively. The larger coupling constant in the COSY NMR, corresponding to the H^4–H^6 and H^5–H^6 couplings, allowed the assignment of the peak at 3.63 ppm to H^6 (upfield shifted by 3.38 ppm), while the smaller coupling constant corresponds to the H^2–H^4 coupling and thus, H^2 corresponds to the signal at 4.24 ppm (upfield shifted by 2.48 ppm).

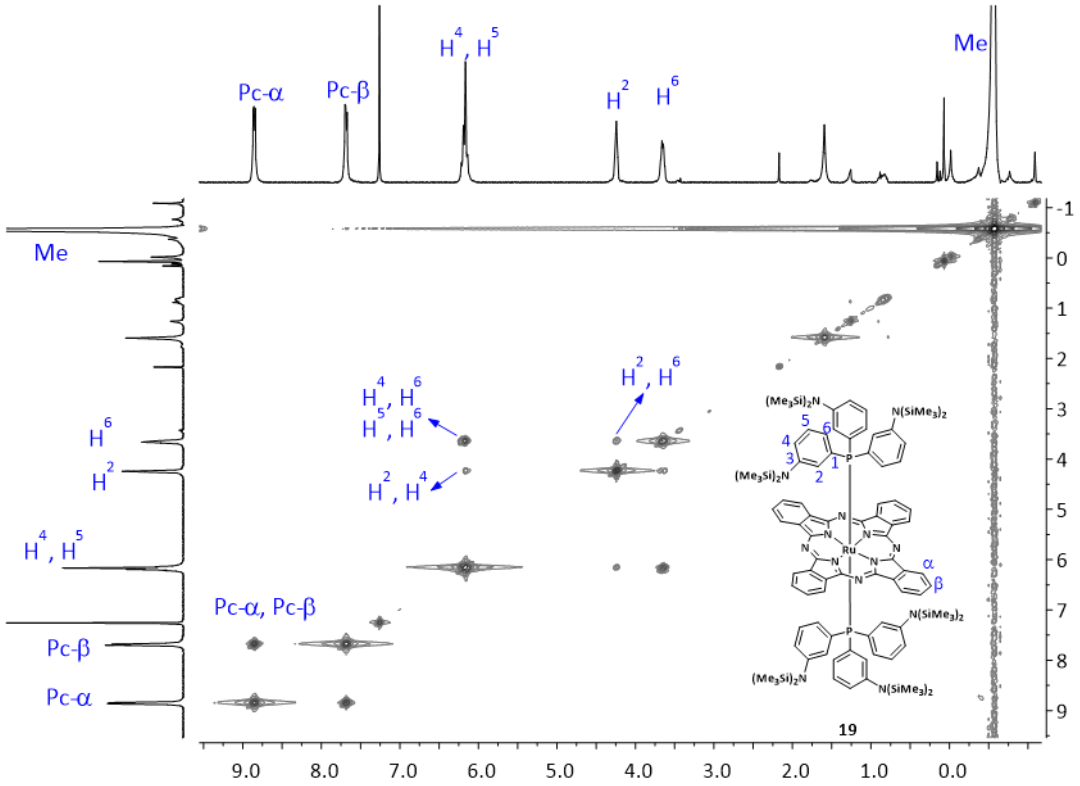

Figure 79 – Detail of the COSY NMR of RuPc **19** in $CDCl_3$.

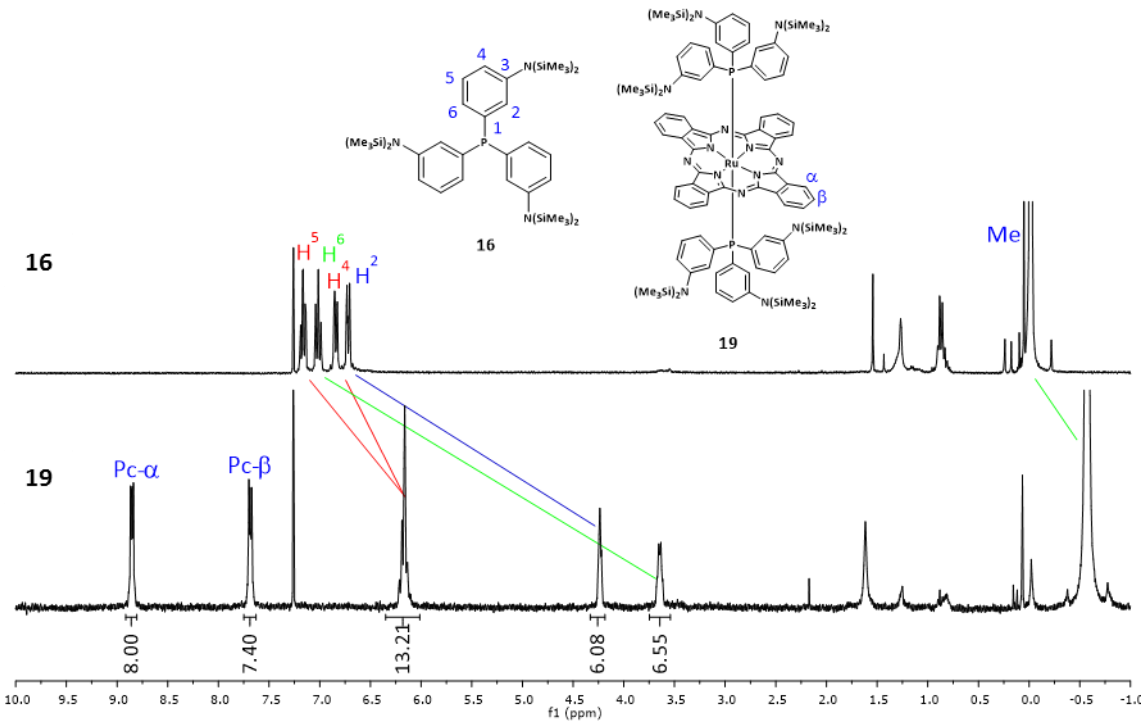

Figure 80 – Comparative ^1H NMR spectra in $CDCl_3$ of ligand **16** and RuPc **19**.

Removal of the trimethylsilyl (TMS) groups of **19** was attempted by stirring **19** in a mixture of THF and MeOH at reflux, according to a reported procedure.[304] However, this resulted in the decoordination of the phosphine ligands from the RuPc.

Hence, the removal of the TMS groups was performed prior to the coordination of the phosphine to **RuPc A**. Deprotection of the amino groups was accomplished by stirring **16** in a mixture of THF and methanol, resulting in tris-(3-aminophenyl)phosphine **17**.[304] This compound was characterized by ^{1}H, ^{13}C and ^{31}P NMR spectroscopies. Coordination of **17** to **RuPc A** was performed in THF leading to RuPc **20** (**Scheme 28**). Purification was accomplished by gel permeation chromatography in Sephadex using a 99:1 mixture of MeOH/HCl(1M) as the eluent, affording RuPc **20** in 30% yield as a blue solid. The coordination reaction was confirmed by ^{1}H NMR (**Figure 81**). Here, typical upfield shifts for the axial triphenylphosphine ligand can be observed. In particular, the closer H^2 and H^6 protons showed the highest shift of ~3 ppm, whereas the further H^4 and H^5 protons were displaced only by ~1 ppm. Integration of these peaks suggests that only one phosphine is coordinated to RuPc. In spite of our suspicion, we proceeded with the methylation reaction. Thus, "**20**" was treated with an excess of methyl iodide, in the presence of sodium carbonate, in order to quaternize the primary amines. However, a complex mixture of products was obtained and attempts of purification by gel permeation chromatography in Sephadex failed.

Alternatively, we attempted methylation of ligand **17** before the coordination reaction to **RuPc A**. However, treatment of **17** with MeI also resulted in the formation of several products of difficult purification and characterization.

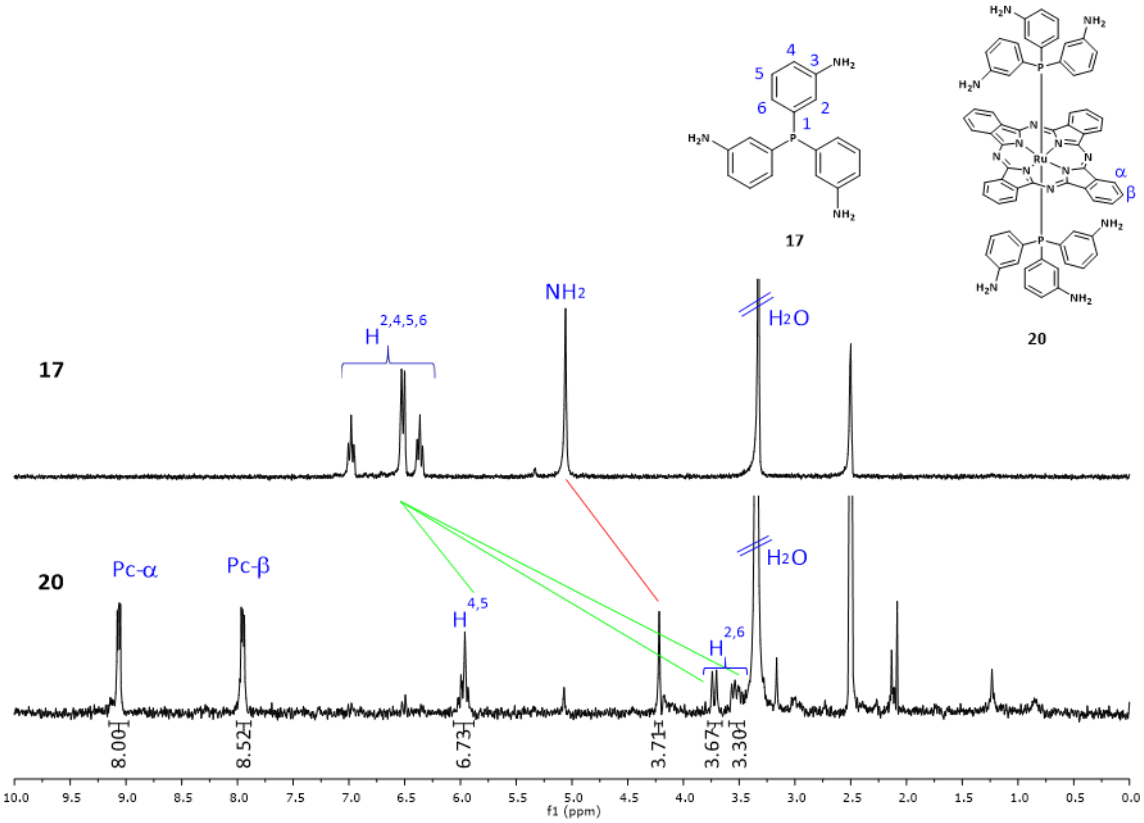

Figure 81 – Comparative ^{1}H NMR spectra in DMSO-d_6 of ligand **56** and RuPc **59**.

Next, we envisioned the synthesis of RuPc **24** by using a phosphine ligand already functionalized with tertiary amines (**22**, **Scheme 29**). The latter should reduce the necessary methylation reaction to one per each nitrogenated function.

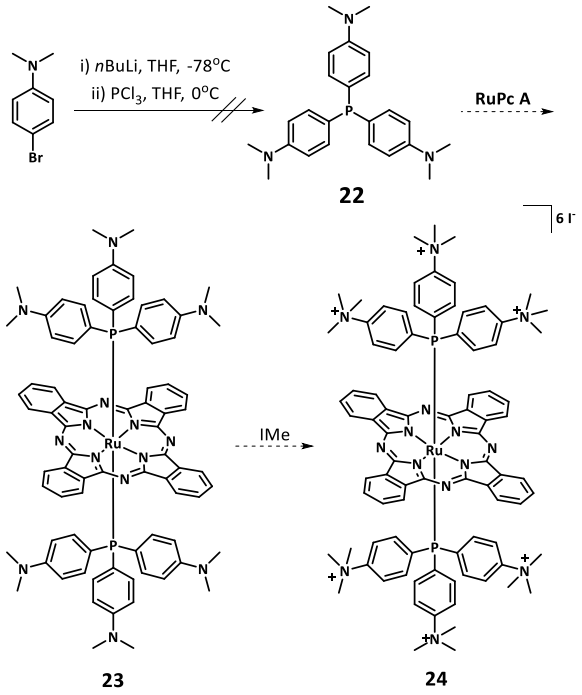

Scheme 29 – Synthetic approach to the synthesis of RuPc **24** from 4-bromo-*N*,*N*-dimethylaniline.

For the synthesis of phosphine **22**, 4-bromo-*N*,*N*-dimethylaniline was treated with *n*-butyl lithium, and to the resulting anion species phosphorus trichloride was added, following reported procedures.[305,306] This reaction resulted in a complex mixture of products, which were separated by column chromatography on silica gel using a 1:3 mixture of dioxane/heptane as the eluent. Analysis of the isolated products by ^{1}H NMR, ^{31}P NMR and MS did not provide enough evidences for the formation of **22**. Therefore, this route was discarded.

3.2.2. RuPcs bearing six guanidinium salts

Triphenylphosphine **17**, bearing primary amines, was also used as precursor to prepare triphenylphosphine **26**, containing three guanidinium salts. Thus, according to a reported procedure,[304] **17** was converted into the corresponding ammonium salt **25** by treatment with hydrochloric acid in water. **25** was then dissolved in dimethylcyanamide and stirred at 100 °C overnight, leading to the tris(guanidiniumphenyl)phosphine **26** in high yield. These compounds where characterized by ^{1}H NMR (see experimental section). Several attempts to coordinate **26** to

[305] Kang, Y.; Song, D.; Schmider, H.; Wang, S. *Organometallics* **2002**, *21* (12), 2413–2421;

[306] Ding, J.; Wang, Q.; Zhao, L.; Ma, D.; Wang, L.; Jing, X.; Wang, F. *J. Mater. Chem.* **2010**, *20* (37), 8126–8133.

RuPc A were performed, both in chloroform and in THF. Analysis by ^{1}H NMR did not provide any evidence for the formation of RuPc **27**.

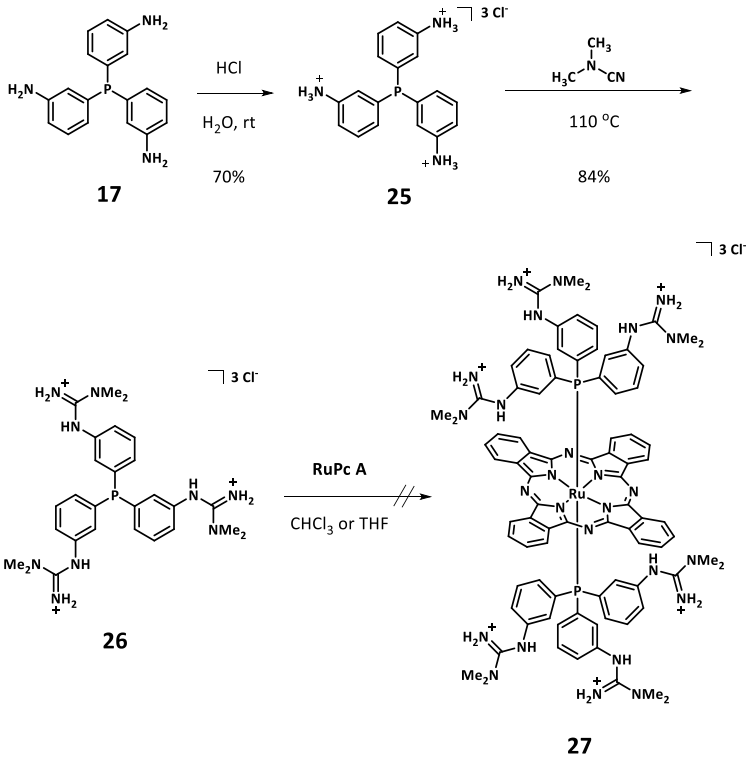

Scheme 30 – Synthetic approach for the synthesis of RuPc **27**.

3.3. RuPcs bearing negatively charged phosphine ligands

As negatively charged function we chose carboxylate functions. Therefore, we tackled the synthesis of a triphenyphosphine ligand endowed with three carboxylic functions (**29**).[307]

The first synthetic approach to the synthesis of **29** is represented in **Scheme 31**. Tris-*p*-bromotriphenylphosphine (**28**) was prepared as described in the literature,[307,308] through substitution reaction of phosphorous trichloride with (4-bromophenyl)lithium, which was generated *in situ* by treating 1,4-dibromobenzene with *n*BuLi. Compound **28** was characterized by ^{1}H and ^{31}P NMR and MS (EI^{+}). Subsequently, we attempted a triple carboxylation reaction using *n*BuLi and dry ice, to obtain the corresponding lithiated trianion **29**, as reported in the literature.[307] Despite all the efforts to prepare **29**, a mixture of mono-, di- and tri- carboxylated products that was not possible to separate, was always obtained.

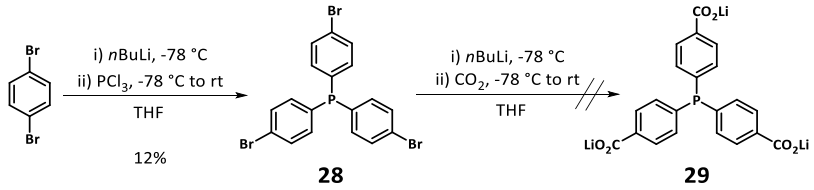

Scheme 31 – Synthetic approach to the synthesis of **29** through carboxylation of phenyl bromides.

We then designed a different approach to prepare **29**, involving protected carboxylic acids. Hence, methyl 4-bromobenzoate was converted into *t*-butyl 4-bromobenzoate (**31**, **Scheme 32**) *via* hydrolysis with sodium hydroxide, followed by esterification with *t*-butanol in the presence of carbonyldiimidazole (CDI) and DBU.[309] Next, the anion obtained by treatment of **31** with *n*BuLi was used to react with phosphorous trichloride, following a typical procedure to prepare triarylphosphines. Under these conditions, a complex mixture of products was obtained, probably arising from transesterification reactions at the carboxylic function.

[307] Borobia, O. B.; Guionneau, P.; Heise, H.; Köhler, F. H.; Ducasse, L.; Vidal-Gancedo, J.; Veciana, J.; Golhen, S.; Ouahab, L.; Sutter, J.-P. *Chem. – A Eur. J.* **2005**, *11* (1), 128–139;

[308] Amengual, R.; Genin, E.; Michelet, V.; Savignac, M.; Genêt, J.-P. *Adv. Synth. Catal.* **2002**, *344* (3–4), 393–398.

[309] Görmer, K.; Bürger, M.; Kruijtzer, J. A. W.; Vetter, I.; Vartak, N.; Brunsveld, L.; Bastiaens, P. I. H.; Liskamp, R. M. J.; Triola, G.; Waldmann, H. *ChemBioChem* **2012**, *13* (7), 1017–1023;

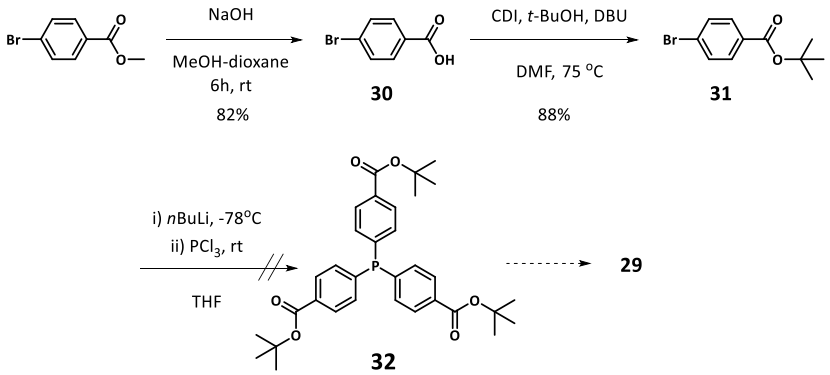

Scheme 32 – Synthetic approach to the synthesis of **29** through the corresponding *t*-butyl ester.

In order to prevent transesterification reactions, we replaced the carboxylic acid protecting group by a OBO-ester (4-methyl-2,6,7-trioxabicyclo[2.2.2]octyl derivative) (**Scheme 33**). These protecting groups are stable against nucleophiles and bases.

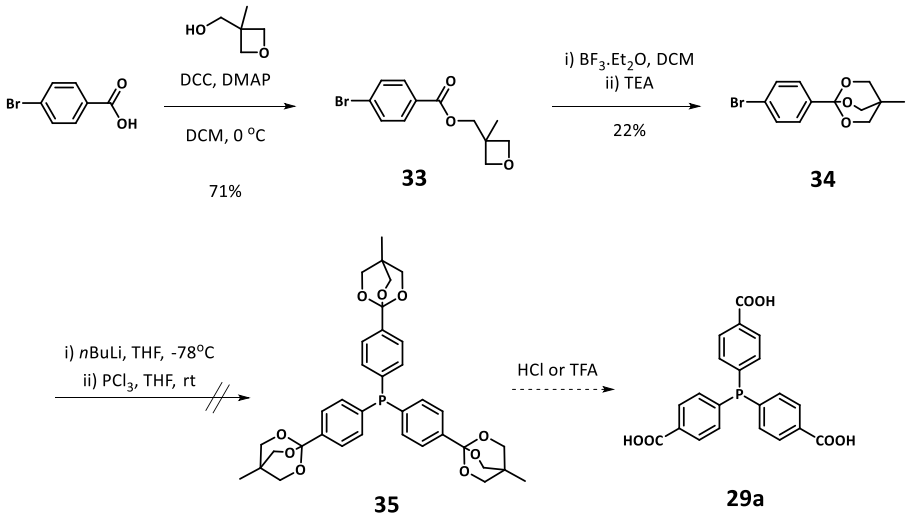

Scheme 33 – Synthetic approach to prepare **29a** *via* the corresponding OBO esters.

4-bromobenzoate ester of 3-methyl-3-(hydroxymethyl)oxetane **33** was prepared following a procedure described in the literature,[310] involving the esterification reaction of *p*-bromobenzoic acid with 3-methyl-3-oxetanemethanol in the presence of DCC and DMAP. OBO-ester **34** was prepared upon treatment with boron trifluoride, which acts as a catalyst for the rearrangement of the corresponding 3-methyl-3-(hydroxymethyl)oxetane ester **33**. **Table 17** describes several

[310] Zhdanko, A. G.; Nenajdenko, V. G. *J. Org. Chem.* **2009**, *74* (2), 884–887.

reaction conditions tested for the synthesis of **34.**[310-312] From these, only entry 4 resulted in the formation of the desired compound.[312]

Table 17 – Synthetic procedures tested for the synthesis of **34**.

Entry	Equiv. of $BF_3.Et_2O$	Solvent	T (°C)	Time (h)	Workup	Purification	Yield	Ref.
1	0.1	DCM	rt	6.5	Method A[a]	Method C[c]	N.D.[e]	310
2	0.04	DCM	0-rt	43	Method A[a]	Method C[c]	N.D.[e]	311
3	0.25	DCM	0-rt	16	Method B[b]	Method C[c]	N.D.[e]	312
4	0.25	DCM	0-rt	16	Method B[b]	Method D[d]	22%	312

[a] Method A: treatment with TEA and washing with a base; [b] Method B: treatment with TEA and filtration through a plug of Celite; [c] Method C: Column chromatography on silica gel; [d] Recrystallization; [e] N.D.: Not detected.

34 was lithiated with *n*BuLi and treated with PCl_3 in THF at room temperature (**Scheme 33**). This afforded a complex mixture of products, the analysis of which did not provide any evidence of the formation of **35**.

Alternatively, the preparation of **29a** was essayed through oxidation of tri(*p*-tolyl)phosphine into the corresponding phosphine oxide **36** (**Scheme 34**), containing three carboxylic acid functions, with potassium permanganate.[313] Usually, the phosphine oxide can be selectively reduced by treatment with $HSiCl_3$. The reduction reaction was monitored by ^{31}P NMR, since the peak corresponding to the phosphine oxide appears around 25 ppm, while the signal corresponding to the phosphine appears around −5 ppm. However, analysis of the reaction product by ^{31}P NMR of the reaction product showed three different signals: one at −6.30, corresponding to the **29a**, another at 24.53 ppm, assigned to the starting material (**36**) and a third one at 41.68 ppm. We were unable to lead the reaction to completion even after prolonged reaction times.

[311] Rose, N. G. W.; Blaskovich, M. A.; Wong, A.; Lajoie, G. A. *Tetrahedron* **2001**, *57* (8), 1497–1507.

[312] Frid, M.; Pérez, D.; Peat, A. J.; Buchwald, S. L. *J. Am. Chem. Soc.* **1999**, *121* (40), 9469–9470.

[313] Václavík, J.; Servalli, M.; Lothschütz, C.; Szlachetko, J.; Ranocchiari, M.; van Bokhoven, J. A. *ChemCatChem* **2013**, *5* (3), 692–696.

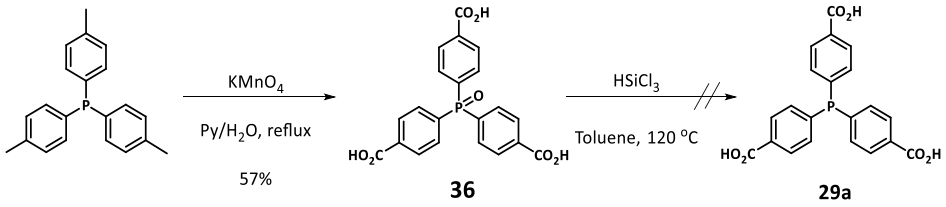

Scheme 34 – Synthetic approach to the synthesis of **29a** through oxidation of tri(*p*-tolyl)phosphine.

3.4. Summary and conclusions

In this chapter, the synthesis of RuPcs endowed with charged phosphine-based ligands was attempted.

- Two novel RuPcs were prepared from the coordination of triphenylphosphine ligands bearing TMS protected amine functions (**19**) and primary amines (**20**). However, deprotection and/or quaternization of the amine functions to afford positively charged PSs proved unsuccessful.
- A phosphine ligand endowed with guanidinium functions (**26**) was prepared according to reported procedures. Its coordination to **RuPc A** was unsuccessful probably due to the different solubility of the two reagents.
- All attempts to prepare phosphine ligands containing carboxylate functions were unsuccessful.

As a conclusion, phosphines are quite unstable ligands when compared to pyridine-based ligands, and their synthesis proved to be difficult and tedious, resulting in air sensitive products of difficult purification.

3.5. Experimental

3.5.1. General remarks

UV-Vis spectra were recorded with a Jasco V-660 spectrometer. IR spectra were recorded with a Bruker Vector 22 spectrophotometer. EI-MS, MALDI-MS, ESI-MS and FAB-MS spectra were determined on GCT Agilent Technologies 6890N from Waters, Bruker Ultrareflex III, Applied Biosystems QSTAR and VG AutoSpec instruments, respectively. NMR spectra were recorded with a Bruker AV-300 instrument. Column chromatography was performed with Merck 60 (230-400mesh, 60 Å) silica gel, with Biobeads SX-3 or with Sephadex G-10. Reagents were purchased from Sigma-Aldrich, AlfaAesar and Acros and used without further purification. Solvents were purchased from Carlo Erba Reagents. Anhydrous solvents were dried with molecular sieves of 0.4 nm purchased from Merk.

3.5.2. RuPcs bearing positively charged phosphine ligands

3.5.2.1. RuPcs bearing six ammonium salts

Tris([N,N-bis(trimethylsilyl)amino]phenyl)phosphine (16)

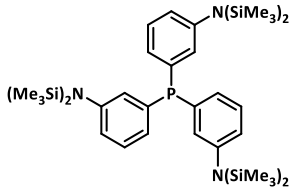

It was synthesized by the procedure already described.[304] To a solution of freshly distilled PCl_3 (1.0 g, 7.3 mmol) in dry THF (9.7 mL) 3-[bis(trimethylsilyl)amino]phenylmagnesium chloride (24.3 mL of a 1.0 M solution in THF) was added. The reaction mixture was stirred at room temperature, for 3.5 hours, under argon atmosphere. Then, the solution was evaporated under reduced pressure and the residue was dissolved in petroleum ether, washed with 5 mL of water and dried over anhydrous $MgSO_4$. After filtration and evaporation, the crude was chromatographed

on silica gel using a 1:1 mixture of EtOAc/heptane as the eluent. Evaporation of the fraction containing **16** afforded the pure product in 71% yield as a white solid.

^{1}H NMR (300Hz, $CDCl_3$) δ_H 7.17 (dt, *J* = 7.6 and 2.0, 3H, Ar-H^5), 7.01 (tt, *J* = 7.8 and 1.3, 3H, Ar-H^6), 6.84 (ddd, *J* = 5.6, 2.8 and 1.3, 3H, Ar-H^4), 6.72 (td, *J* = 7.7 and 1.8, 3H, Ar-H^2), 0.02 (s, 54H, $SiCH_3$);
^{13}C NMR (75.5 MHz, $CDCl_3$) δ_C 148.42 (d, J^3_{CP} = 6.74, Ar-H^3), 137.58 (d, J^1_{CP} = 11.11, Ar-H^1), 135.13 (d, J^2_{CP} = 15.90, Ar-H^2), 130.35 (s, Ar-H^4), 129.27 (d, J^2_{CP} = 22.09, Ar-H^6), 128.52 (d, J^3_{CP} = 8.67, Ar-H^5), 2.29 (s, $SiCH_3$);
^{31}P NMR (121 MHz, $CDCl_3$) −6.04;
MS (FAB, *m*-NBA) *m/z* 740.2 $[M+H]^+$.

Tris(3-aminophenyl)phosphine (17)

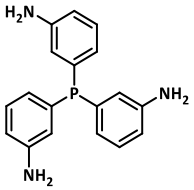

This compound was prepared according to the literature.[304] **16** (500 mg, 0.67 mmol) was dissolved in a mixture of MeOH (1mL) and THF (0.7 mL) and stirred at reflux, under argon, for 8h. The resulting solution was evaporated under reduced pressure and the residue washed with petroleum ether and filtrated to afford **17** in 94% yield.

^{1}H NMR (300Hz, DMSO-d_6) δ_H 6.98 (t, *J* = 7.4 Hz, 3H, Ar-H), 6.52 (d, *J* = 8.12 Hz, 6H, Ar-H), 6.36 (t, *J* = 7.7 Hz, 3H, Ar-H), 5.06 (s, 6H, NH_2);
^{13}C NMR (75.5 MHz, $CDCl_3$) δ_C 148.43 (d, J^3_{CP} = 8.89, Ar-H^3), 137.64 (d, J^1_{CP} = 9.76, Ar-H^1), 128.70 (d, J^3_{CP} = 7.64, Ar-H^5), 120.69 (d, J^2_{CP} = 18.04, Ar-H^2), 118.67 (d, J^2_{CP} = 22.36, Ar-H^6), 114.15 (s, Ar-H^4);
^{31}P NMR (121 MHz, $CDCl_3$) δ_P −3.34.

RuPc 19

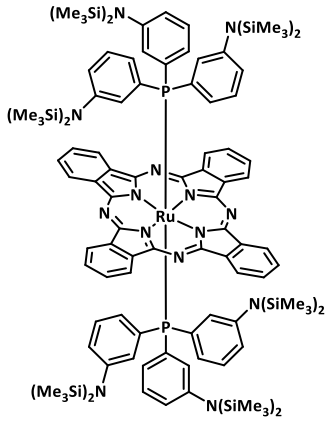

A mixture of **RuPc A** (20 mg, 0.024 mmol) and **16** (41.8 mg, 0.056 mmol) in $CHCl_3$ (3 mL) was stirred at 50 °C, in the dark, under argon, overnight. The resulting solution was evaporated under reduced pressure and the crude was subjected to size exclusion chromatography on BioBeads using toluene as the eluent. The fraction containing **19** was evaporated and the residue washed with MeOH and filtrated, affording **19** in 30% yield as a blue powder.

^{1}H NMR (300 MHz, $CDCl_3$) δ_H 8.85 (dd, J = 5.5 and 3.0 Hz, 8H, Pc-H^{α}), 7.68 (dd, J = 5.5 and 3.0 Hz, 8H, Pc-H^{β}), 6.22-6.18 (m, 12H, Ar-$H^{4,5}$), 4.25-4.22 (m, 6H, Ar-H^{2}), 3.66-3.63 (m, 6H, Ar-H^{6}), -0.57 (108H, s, $SiCH_3$);

^{13}C NMR (75.5 MHz, $CDCl_3$) δ_C 146.83, 143.46, 142.07, 130.93, 130.20, 129.06, 126.70, 126.17, 123.82, 121.22, 1.6;

MS (ESI+) *m/z* 614.1 $[RuPc]^+$, 921.2 $[Ru(L\text{-}TMS)Pc + H]^+$, 1228.3 $[M\text{-}TMS + H]^+$;

UV-Vis ($CHCl_3$) λ_{max} nm (ε x 10−4): 309 (0.64), 642 (0.45);

FT-IR (KBr) ν cm^{-1}: 3056, 2954, 1739, 1577, 1489, 1463, 1413, 1325, 1288, 1251, 1219, 1168, 1065, 967, 931, 886, 864, 753, 705, 682, 622, 573, 496.

RuPc 20

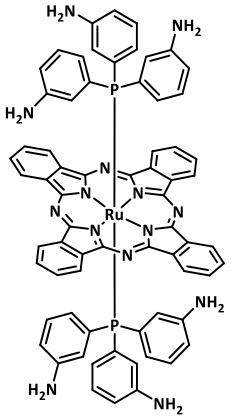

A mixture of **RuPc A** (15 mg, 0.018 mmol) and **17** (13.6 mg, 0.044 mmol) in THF (3 mL) was stirred at 50 °C, in the dark, under argon, for 4h. The resulting solution was evaporated under reduced pressure and the crede was subjected to size exclusion chromatography on Sephadex using a 99:1 mixture of MeOH/HCl(1M) as the eluent. Evaporation of the fraction containing **20** afforded the pure compound in 32% yield, as a dark blue solid.

^{1}H NMR (300 MHz, DMSO-d_6) δ_H 9.06 (dd, J = 5.5 and 3.0 Hz, 8H, Pc-H$^{\alpha}$), 7.95 (dd, J = 5.5 and 3.0 Hz, 8H, Pc-H$^{\beta}$), 6.02-5.93 (m, 6H, Ar-H), 3.74-3.70 (m, 3H, Ar-H), 3.57-3.50 (m, 3H, Ar-H).

3.5.2.2. RuPcs bearing six guanidinium salts

[Tris(3-aminophenyl)phosphine] trihydrochloride (25)

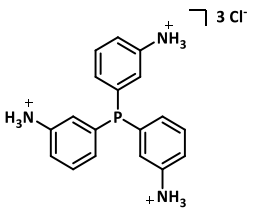

The synthesis was performed as described in the literature.[304] To a suspension of **17** (100 mg, 0.33 mmol) in H_2O (3.6 mL) HCl 2N (0.49 mL) was added. The reaction mixture was stirred at

room temperature, for 4h. The precipitate was filtered off and the filtrate was evaporated under reduced pressure to give **25** in 70% yield as a white solid.

^{1}H NMR (300 MHz, DMSO-d_6) δ_H 7.66-7.46 (m, 6H, Ar-H), 7.37-7.28 (m, 6H, Ar-H);
^{31}P NMR (121 MHz, DMSO-d_6) δ_P −6.06.

[Tris(3-(N,N-dimethylguanidino)phenyl)phosphine] trihydrochloride (26)

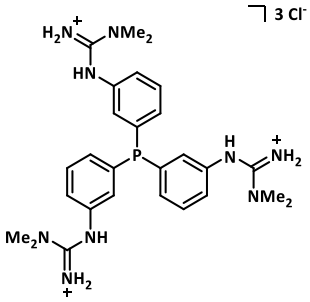

This compound was prepared according to a reported procedure.[304] To a sealed tube containing dimethylcyanamide (0.32 mL, 3.9 mmol) **25** (120 mg, 0.29 mmol) was added and the reaction mixture was stirred at 110 °C, overnight, under argon. Diethyl ether was added to the resulting solution, and the resulting precipitate was filtrated to afford **26** in 84% yield.

^{1}H NMR (300 MHz, DMSO-d_6) δ_H 9.92 (s, 1H, NH), 7.88 (s, 2H, NH_2), 7.47-7.14 (m, 12H, Ar-H), 3.07 (s, 18H, NCH_3).

3.5.3. RuPcs bearing negatively charged phosphine ligands

Tri(4-bromophenyl)phosphine (28)

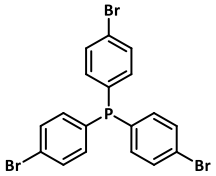

The synthesis was accomplished as described in the literature.[307,308] All the material was dried with a hot air gun (550 °C) under an argon stream and cooled down under argon. To a solution of 1,4-dibromobenzene (5g, 21.2 mmol) in dry THF (42 mL), at −78 °C, under argon, *n*BuLi (21.2 mmol in 0.62 mL of THF) was added dropwise. After stirring for 30 min, freshly distilled phosphorous trichloride (0.62 mL, 7.1 mmol) was added and the reaction mixture was stirred at room temperature for 2h. The resulting solution was diluted with diethyl ether and transferred to a separatory funnel, washed with brine and dried over anhydrous $MgSO_4$. After filtration and evaporation of the solvent, the residue was chromatographed on silica gel using a 1:19 mixture of DCM/heptane as the eluent. The fraction containing 28 was evaporated under reduced pressure and the residue redissolved in DCM, precipitated with methanol and filtrated, to afford 28 in 12% yield as a white solid.

^{1}H NMR (300 MHz, DMSO-d_6) δ_H 7.48 (d, J = 8.12 Hz, 6H, Ar-H), 7.12 (t, J = 7.72 Hz, 6H, Ar-H);
^{31}P NMR (121 MHz, DMSO-d_6) δ_P -8.40;
MS (EI+) *m/z* 497.82 (M^+).

4-Bromobenzoic acid (30)[309]

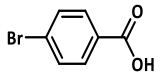

Methyl 4-bromobenzoate (500 mg, 2.3 mmol) was dissolved in a mixture of NaOH 4M (aq) (0.50 mL), MeOH (1.25 mL) and dioxane (3.5 mL) and the reaction mixture was stirred at room temperature for 8 h. the resulting solution was evaporated under reduced pressure and residue was dissolved in EtOAc, transferred to a separatory funnel, washed with HCl (10%) and with brine, and dried over anhydrous $MgSO_4$. After filtration and evaporation of the solvent, the residue was washe with hexane to afford **30** in 82% yield as a white solid.

^{1}H NMR (300 MHz, DMSO-d_6) δ_H 13.19 (broad s, 1H, OH), 7.86 (d, J = 8.5 Hz, 2H, Ar-H), 7.71 (d, J = 8.5 Hz, 2H, Ar-H).

t-Butyl 4-bromobenzoate (31)[309]

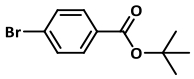

A mixture of 4-bromobenzoic acid (350 mg, 1.7 mmol) and CDI (310.6 mg, 1.9 mmol) in dry DMF (1.8 mL) was stirred at 75 °C for 1h. Then, *t*-BuOH (0.32 mL, 3.4 mmol) and DBU (0.28 mL, 1.9 mmol) were added and the reaction mixture was stirred at 75 °C for 3h. The reaction solution was diluted with EtOAc, transferred to a separatory funnel, washed with HCl (aq., 10%), K_2CO_3 (aq., 20%) and water, and dried over anhydrous $MgSO_4$. After filtration and evaporation of the solvent, the residue was chromatographed on silica gel using a 95:5 mixture of petroleum ether/EtOAc as the eluent. Evaporation of the fraction containing **31** afforded the pure product in 88% yield as a white solid.

^{1}H NMR (300 MHz, $CDCl_3$) δ_H 7.88 (d, *J* = 8.5 Hz, 2H, Ar-H), 7.54 (d, *J* = 8.5 Hz, 2H, Ar-H), 1.59 (s, 9H, CH_3).

4-bromobenzoate ester of 3-methyl-3-(hydroxymethyl)oxetane (33)[312]

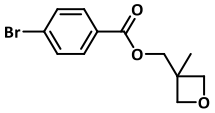

To a solution of 3-methyl-3-oxetanemethanol (0.12 mL, 1.2 mmol), DCC (225.8 mg, 1.1 mmol) and DMAP (12.2 mg, 0.099 mmol) in dry DCM (1.5 mL), at 0 °C, under argon, was added **30** (200 mg, 0.99 mmol) portion wise. The reaction mixture was stirred, under argon, at 0 °C for 1h15min. The resulting solution was diluted with DCM and the dicyclohexylurea (DCU) was filtered off. The filtrate was transferred to a separatory funnel, washed with water, HCl 0.01M (aq) and brine, and dried over anhydrous Na_2SO_4. After filtration and evaporation, the crude was chromatographed on silica gel using a 1:3 mixture of EtOAc/heptane as the eluent. Evaporation of the fraction containing **33** afforded the pure product in 71% yield as a white solid.

^{1}H NMR (300 MHz, $CDCl_3$) δ_H 7.85 (d, *J* = 8.5 Hz, 2H, Ar-H), 7.52 (d, *J* = 8.5 Hz, 2H, Ar-H), 4.57 (d, *J* = 6.0 Hz, 2H, oxetane-OCH_2), 4.40 (d, *J* = 6.0 Hz, 2H, oxetane-OCH_2), 4.34 (s, 2H, $COOCH_2$), 1.36 (s, 3H, CH_3).

^{13}C NMR (75.5 MHz, $CDCl_3$) δ_C 165.36 (C=O), 131.74 (Ar-H), 131.07 (Ar-H), 128.77 (Ar-H), 128.20 (Ar-H), 79.41 (oxetane-OCH_2), 69.16 ($COO\underline{C}H_2$), 39.23 (oxetane-C), 21.18 (CH_3).

1-(4-Bromophenyl)-4-methyl-2,6,7-trioxobicyclo[2,2,2]octane (34)[312]

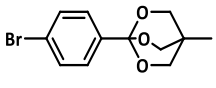

33 (4.49g, 15.8 mmol) was placed in a 50 mL round bottom flask and dried in vacuum at 50 °C. It was then cooled to 0 °C, under argon, and dissolved in dry DCM (28 mL). $BF_3.Et_2O$ (0.50 mL, 4.0 mmol) was added and the reaction mixture was stirred at 0 °C for 30 min and then at room temperature overnight. Dry TEA (2.2 mL, 15.8 mmol) was added and the reaction mixture was stirred at room temperature for 3h. The resulting solution was diluted with 40 mL of diethylether and filtrated through a plug of Celite. The solvent was evaporated under reduced pressure and the residue was recrystallized in EtOAc/hexane, affording **34** in 22% yield as a white solid.

^{1}H NMR (300 MHz, $CDCl_3$) δ_H 750-7.46 (m, 4H, Ar-H), 4.07 (s, 6H, CH_2), 0.88 (s, 3H, CH_3);

4,4',4''-phosphinetriyltribenzoic acid oxide (36)

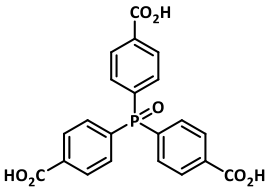

It was synthesized according to the literature.[313] To a solution of tri(*p*-tolyl)phosphine (100 mg, 0.33 mmol) in a mixture of pyridine (0.8 mL) and H_2O (1.6 mL) at reflux, potassium permanganate (1.06g, 6.7 mmol) was added portion wise. The reaction mixture was stirred at reflux for 40h. The resulting manganese dioxide was filtered off and the desired compound was extracted with hot water. The filtrate was acidified with sulfuric acid (50%) and the resulting white precipitate

was filtered and redissolved in the minimum amount of sodium hydroxide 2M. The solution was transferred to a separatory funnel, washed with a mixture of THF/EtOAc and the aqueous phase was again acidified with sulfuric acid (50%) to give **36** in 57% yield as a white solid.

^{1}H NMR (300 MHz, DMSO-d_6) δ_H 8.19 (dd, $^{3}J_{HH}$ = 8.2 Hz and $^{4}J_{PH}$ = 2.2 Hz, 6H, Ar-H), 7.78 (dd, $^{3}J_{HH}$ = 8.2 Hz and ^{3}J = 11.6 Hz, 6H, Ar-H);

^{31}P NMR (121 MHz, DMSO-d_6) δ_P 24.68.

MS (ESI^{+}, MeOH + 1% TFA) *m/z* 411.1 $[M+H]^{+}$.

Chapter 4 – *In Vitro* Studies of Ruthenium Phthalocyanines as Potential Photosensitizers for Photodynamic Therapy

4.1. Overview

The PSs prepared in the previous chapters were tested *in vitro* as photosensitizers for PDT applications. All compounds were studied, with the exception of RuPcs bearing two protected carbohydrate units at their axial positions (**PS5-10**), owing to their low solubility in aqueous solutions. *In vitro* evaluation of **PS1-4** and **PS11-29** was performed in HT-1376 bladder cancer cells. Bladder cancer is especially suited for PDT since bladder is a round shaped transparent organ, easily accessible using an endoscope, thus allowing for its easy and homogeneous illumination.[314]

Three important parameters concerning the application of PSs as photosensitizers were measured. These include *i)* the ability of PSs to accumulate inside HT-1376 bladder cancer cells, *ii)* their toxicity in the absent of light and *iii)* the toxic effects induced upon light excitation. The former was measured in terms of cellular uptake of PSs after incubation for determined periods of time. The last two parameters were measured in terms of cellular metabolic activity, which consists on an appropriate parameter to evaluate the cellular survival after treatment with PSs.

The *in vitro* studies were performed at the Institute for Biomedical Imaging and Life Sciences (IBILI) in the Faculty of Medicine of the University of Coimbra, in Portugal, under the supervision of Dra. Rosa Fernandes. The protocols applied for these studies were optimized and published by this laboratory.[232] The NIR measurements for the cellular uptake studies were performed at the Department of Chemistry of the University of Coimbra with the help of Dr. João Pina.

For the *in vitro* studies, stock solutions of each PS were made in DMSO and then, different dilutions were made with PBS to obtain the final working solutions. Such dilutions were made in such a way that the percentage of DMSO was kept under 0.45%. The final concentrations were of 0.5 μM, 2.5 μM, 5 μM, 9 μM and 12.5 μM.

[314] Shackley, D. C.; Briggs, C.; Whitehurst, C.; Betts, C. D.; O'Flynn, K. J.; Clarke, N. W.; Moore, J. V. *Expert Rev. Anticancer Ther.* **2001**, *1* (4), 523–530.

4.2. *In vitro* study of RuPcs bearing axial PEG chains

The PSs studied in this section are shown in **Figure 82**.

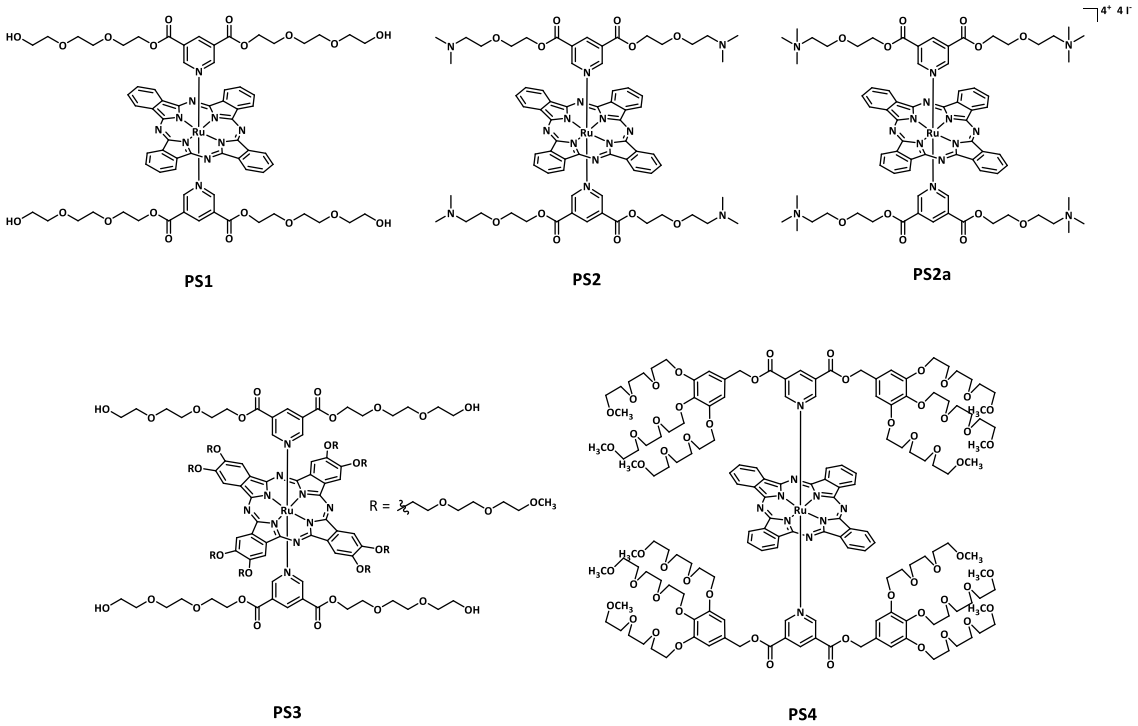

Figure 82 – Structure of PSs containing axial polyether chains studied in this section.

Aggregation studies of **PS1**, **PS2**, **PS3** and **PS4** were conducted in PBS containing up to 0.45% of DMSO, using a range of concentrations between 0.5 and 12.5 µM, which were achieved by sequential dilutions of stock solutions of each PS. For the verification of the Lambert-Beer law, an analysis of linear regression between the intensity of the Q-band and the concentration of the RuPcs was performed. The results show that the Lambert-Beer was fulfilled for all of the tested PSs (**Figure 83**), with R^2 values of 0.96 or greater. Hence, **PS1**, **PS2**, **PS3** and **PS4** seem to be non-aggregated in the PBS/DMSO mixture and the concentration range used for the *in vitro* studies.

Due to the lower solubility in water of **PS1** and **PS2**, the maximum concentration used for these compounds was 5 µM.

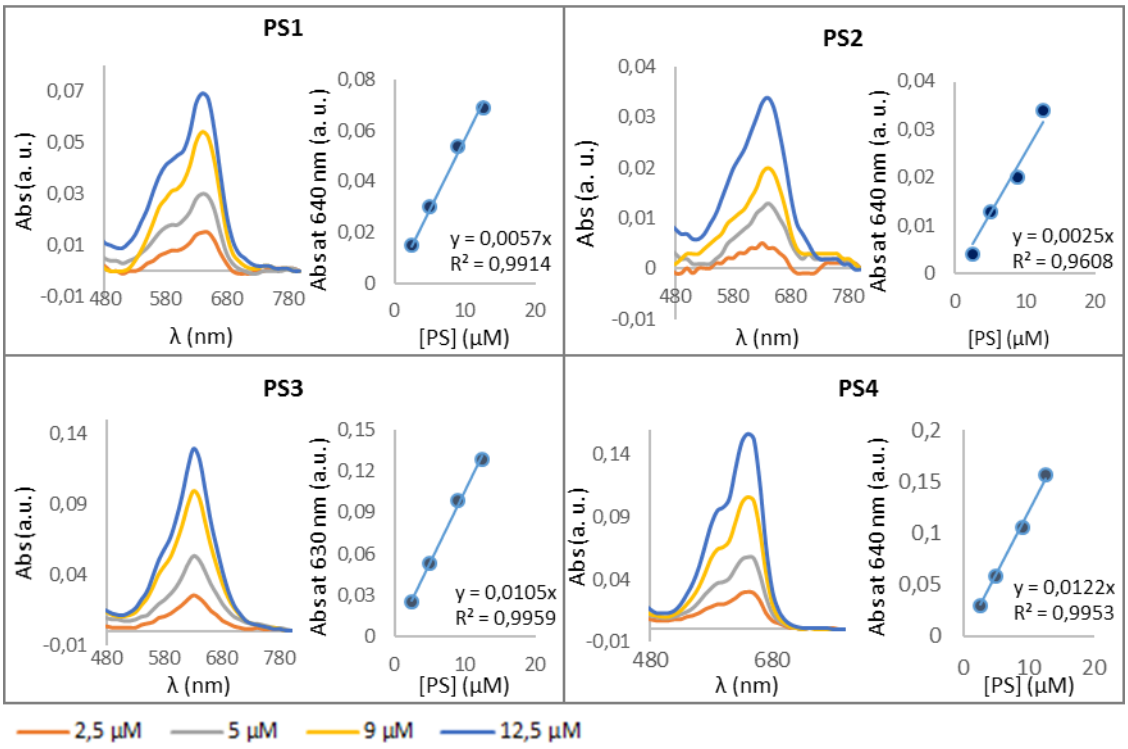

Figure 83 – UV-Vis dilution studies of **PS1-4** in physiologically relevant medium (PBS containing 0.45% of DMSO).

4.2.1. Cellular uptake

In order to measure the cellular uptake of **PS1-4**, HT-1376 cells were incubated for 2 hours, with PBS solutions of such compounds with different concentrations. This was followed by disruption of cellular membranes with a sodium dodecyl sulfate (SDS) solution. The concentration of PS was measured by Near Infra-Red (NIR) spectrofluorimetry and the results were normalized by the amount of protein, which was determined by the BCA method.

Figure 84 and **Table 18** show the determined cellular uptake of **PS1-4**. Values represent the mean value ± S.E.M. (standard error of mean) of at least two different experiments.

The cellular uptake of **PS1** and **PS2** is similar, showing values of 0.86 ± 0.06 and 1.14 ± 0.02 nmol of PS/mg of protein, respectively, after incubation with 5 μM solutions. The cationic analogue **PS2a** showed the highest cellular uptake, of 2.3 ± 0.2 nmol of PS/mg of protein after incubation with 5 μM solution and of 7.6 ± 0.07 nmol of PS/mg of protein for the highest concentration tested (12.5 μM). This is in agreement with previous findings, where the introduction of positively charged

functions enhanced the cellular uptake of the corresponding PSs.[315-318] This effect may arise from the characteristic slight negative charge of mammalian cellular membranes, which can interact with positively charged PSs *via* electrostatic interactions, resulting in the internalization of the compounds by endocytosis.

PS3 and **PS4** show a much lower cellular uptake than **PS1**, **PS2** and **PS2a**. The cellular uptake for the highest concentration tested (12.5 µM) of **PS4** is 0.69 ± 0.04 nmol of PS/mg of protein. **PS3** exhibit a cellular uptake even lower, of 0.1993 ± 0.07 nmol of PS/mg of protein for the 12.5 µM solution. For this compound, no phosphorescence was detected for the incubations with 0.5 and 2.5 µM solutions. These observations suggest that the presence of a higher number of PEG chains is responsible for a decrease in the cellular uptake by HT-1376 cells. The reduced cellular internalization of PEGylated PSs has been observed before,[319,320] which may arise from the difficulty of these hydrophilic molecules to diffuse across the hydrophobic cellular membrane. Therefore, the incubation time of **PS3** was extended to 4 hours, this leading to a slight increase in the amount of PS absorbed by the cells. Specifically, the incubation for 4 hours with a 12.5 µM solution of **PS3** resulted in a cellular uptake of 0.5 ± 0.1 nmol of PS/mg of protein, which is still lower than the cellular uptake of the other PSs.

[315] Ongarora, B. G.; Zhou, Z.; Okoth, E. A.; Kolesnichenko, I.; Smith, K. M.; Vicente, M. G. H. *J. Porphyr. Phthalocyanines* **2014**, *18* (10–11), 1021–1033.

[316] Viola, E.; Donzello, M. P.; Sciscione, F.; Shah, K.; Ercolani, C.; Trigiante, G. *J. Photochem. Photobiol. B Biol.* **2017**, *169*, 101–109.

[317] Wang, A.; Zhou, R.; Zhou, L.; Sun, K.; Jiang, J.; Wei, S. *Bioorg. Med. Chem.* **2017**, *25* (5), 1643–1651;

[318] Gui, L.; Zhang, Q.; Wang, Y.; Fang, K.; Wang, A.; You, X.; Zhou, L.; Zhou, J.; Wei, S. *Inorg. Chem. Commun.* **2017**, *75*, 1–4.

[319] Lo, P.-C.; Leung, S. C. H.; Chan, E. Y. M.; Fong, W.-P.; Ko, W.-H.; Ng, D. K. P. *Photodiagnosis Photodyn. Ther.* **2007**, *4* (2), 117–123.

[320] Hofman, J.-W.; van Zeeland, F.; Turker, S.; Talsma, H.; Lambrechts, S. A. G.; Sakharov, D. V; Hennink, W. E.; van Nostrum, C. F. *J. Med. Chem.* **2007**, *50* (7), 1485–1494.

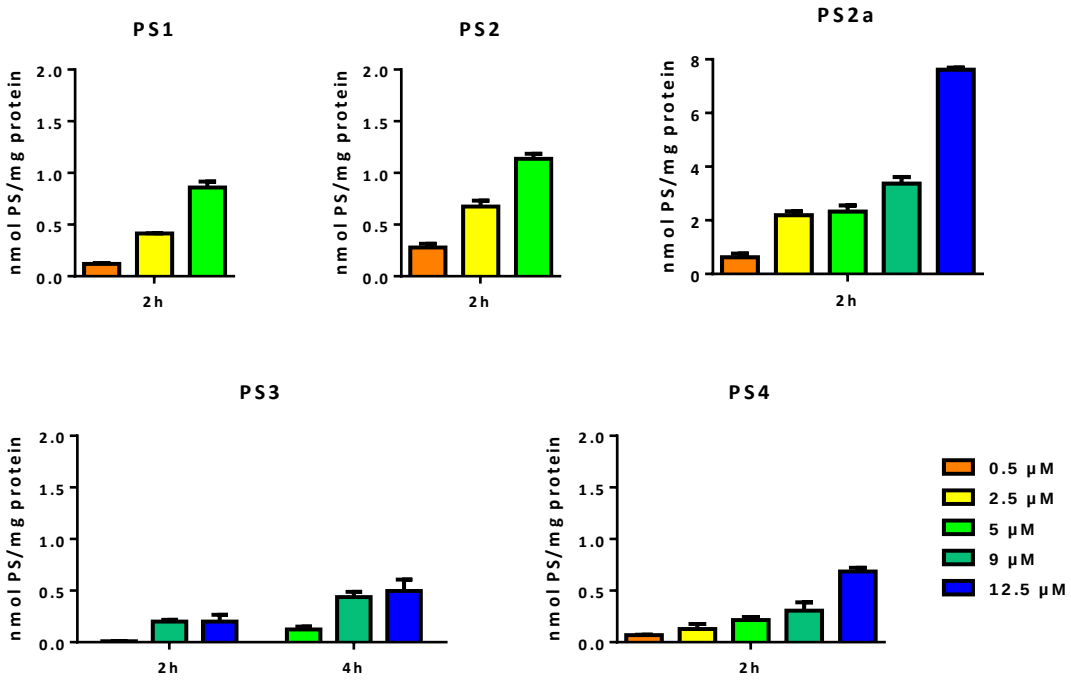

Figure 84 – Cellular uptake by HT-1376 cells after incubation for 2h with **PS1-4** and 4h with **PS3**. Data are the mean value ± S.E.M. of at least two different experiments.

Table 18 – Cellular uptake by HT-1376 cells after incubation for 2h with **PS1-4** and 4h with **PS3**. Data are represented as nmol of PS/mg of protein and are the mean value ± S.E.M. of at least two different experiments.

t	C (µM)	PS1	PS2	PS2a	PS3	PS4
2h	**0.5**	0.119 ± 0.009	0.28 ± 0.04	0.6 ± 0.1	N.D.	0.069±0.004
	2.5	0.415 ± 0.001	0.67 ± 0.06	2.2 ± 0.1	N.D.	0.13 ± 0.05
	5	0.86 ± 0.06	1.13 ± 0.05	2.3 ± 0.2	0.010±0.002	0.21 ± 0.03
	9			3.4 ± 0.2	0.20 ± 0.02	0.31 ± 0.08
	12.5			7.62 ± 0.07	0.20 ± 0.07	0.69 ± 0.04
4h	**5**				0.12 ± 0.03	
	9				0.44 ± 0.05	
	12.5				0.5 ± 0.1	

N.D.: not detected.

4.2.2. Phototoxic effect

Before testing the PDT effects of **PS1-4**, their dark toxicity was first evaluated to ensure that none of the compounds is toxic without irradiation. For this, HT-1376 cells were incubated with solutions of each PS with different concentrations. After 2h of incubation, the solution of PS was

removed and cells were incubated in culture medium RPMI-1640 for 24h. The cell metabolic activity was determined by MTT assay.

Figure 85 and **Table 19** show the dark toxicity of **PS1-4**, evaluated after incubation with solutions of concentrations of 0.5 µM, 2.5 µM, 5 µM, 9 µM and 12.5 µM. The percentage of MTT reduction was calculated relatively to control cells (untreated cells). Data are the mean value ± S.E.M. of at least three independent experiments performed in triplicates.

None of the compounds showed toxicity in dark conditions, with the exception of the two highest concentrations of PS **2a** (9 and 12.5 µM) which caused a significant reduction on cell metabolic activity (94 ± 3 % from control). This dark toxicity of **PS 2a** may be correlated with its high cellular uptake.

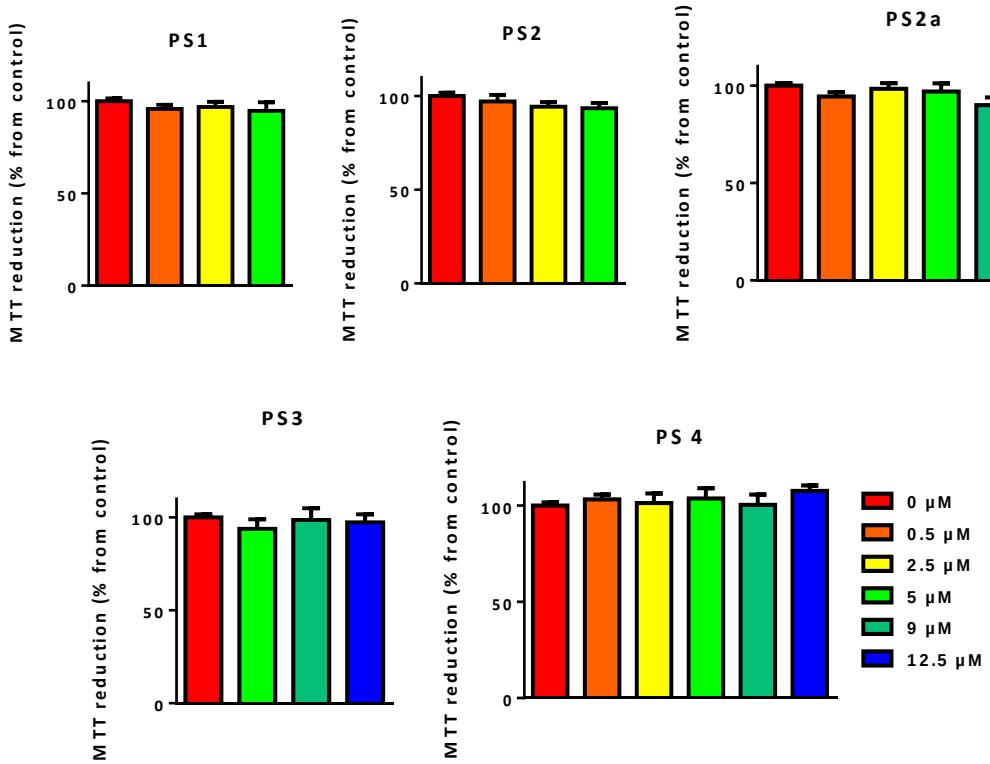

Figure 85 – Dark toxicity evaluated 24h after incubation with **PS1-4** for 2h using the MTT assay. The percentage of toxicity was calculated relatively to control cells. Data are the mean value ± S.E.M. of at least three independent experiments performed in triplicates. *(p≤0.05), **(p≤0.01), ***(p≤0.001), **** (p≤0.0001) significantly different from control cells.

Table 19 – Dark toxicity evaluated 24h after incubation with **PS1-4** for 2h using the MTT assay. The percentage of toxicity was calculated relatively to control cells. Data are the mean value ± S.E.M. of at least three independent experiments performed in triplicates.

C (μM)	PS1	PS2	PS2a	PS3	PS14
0	100 ± 2	100 ± 2	100 ± 1	100 ± 2	100 ± 2
0.5	96 ± 2	97 ± 3	94 ± 2		103 ± 2
2.5	97 ± 3	94 ± 2	98 ± 3		101 ± 5
5	95 ± 5	94 ± 3	97 ± 4	94 ± 5	104 ± 5
9			90 ± 4	99 ± 6	100 ± 5
12.5			88 ± 2	97 ± 4	108 ± 3

Once confirmed the lack of dark toxicity of **PS1-4**, their phototoxic effects were evaluated, using the same experimental conditions as for the studies in the dark. Therefore, HT-1376 cells were plated in 96-well microplates and, after 24h, they were incubated with solutions of **PS1-4** of different concentrations for 2h. Immediately after removal of PS solution and addition of culture medium RPMI-1640, cells were irradiated with red light at a fluence rate of 20 mW/cm^2 for 40 min. The MTT assay was performed 24h after treatment. The results obtained for **PS1-4** are described in **Figure 86** and **Table 20**, where data are the mean value ± S.E.M. of at least three independent experiments performed in triplicates.

Incubation with **PS1**, **PS2**, **PS2a** and **PS4** led to a reduction of the cell metabolic activity in a concentration-dependent manner. **PS1** and **PS2** show similar phototoxic effects, with a decrease in cell viability to 40 ± 4 and 43 ± 3 % from control, respectively, for the maximum concentration tested (5 μM). This correlates very well with the similar cellular uptake and singlet oxygen generation efficiency ($\Phi_{\Delta\ (DMSO)}$ = 0.76 for both compounds) verified for these two compounds. Although the singlet oxygen quantum yields of **PS2a** and **PS4** ($\Phi_{\Delta\ (DMSO)}$ = 0.79 for **PS2a**; $\Phi_{\Delta\ (DMSO)}$ = 0.77 for **PS4**) are equivalent to those of **PS1** and **PS2**, the former showed and improved phototoxic effect. Thus, incubation with 5 μM solutions of **PS2a** and **PS4** reduced metabolic activity to 7.8 ± 0.3 and 19 ± 2 % from control, respectively. In the case of **PS2a**, these observations can be justified by the increased cellular uptake displayed by this compound. Despite the lower cellular uptake of **PS4** related to **PS1** and **PS2**, it was able to produce a higher phototoxic effect. Such phenomenon suggests that some other factor is playing a role in the phototoxic effect of this compound, for instance, its increased solubility in water, compared to **PS1** and **PS2**. Furthermore, the improved phototoxicity of **PS2a** compared to **PS4** may also result from the higher singlet oxygen generation quantum yield in deuterated water ($\Phi_{\Delta\ (D_2O)}$ = 0.48 for **PS2a**; $\Phi_{\Delta\ (D_2O)}$ = 0.20 for **PS4**).

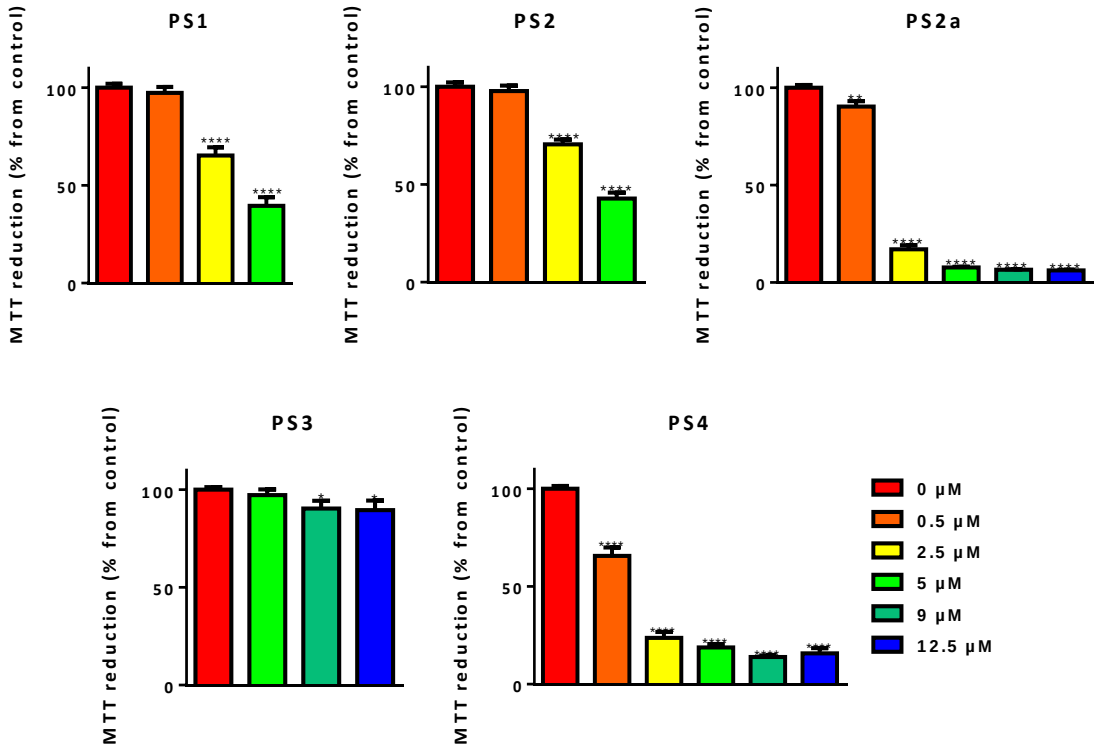

Figure 86 – Phototoxicity evaluated 24h after incubation with **PS1-4** for 2h and irradiation for 40 min at a fluence rate of 20 mW/cm^2. The percentage of toxicity was calculated relatively to control cells. Data are the mean value ± S.E.M. of at least three independent experiments performed in triplicates. *(p≤0.05), **(p≤0.01), ***(p≤0.001), **** (p≤0.0001) significantly different from control cells.

Table 20 – Phototoxicity evaluated 24h after incubation with **PS1-4** for 2h and irradiation for 40 min at a fluence rate of 20 mW/cm^2. The percentage of toxicity was calculated relatively to control cells. Data are the mean value ± S.E.M. of at least three independent experiments performed in triplicates.

C (µM)	PS1	PS2	PS2a	PS3	PS4
0	100 ± 2	100 ± 2	100 ± 1	100 ± 1	100 ± 1
0.5	97 ± 3	98 ± 3	90 ± 3		66 ± 4
2.5	65 ± 4	71 ± 2	17 ± 2		24 ± 3
5	40 ± 4	43 ± 3	7.8 ± 0.3	97 ± 3	19 ± 2
9			6.6 ± 0.2	90 ± 4	14.0 ± 0.7
12.5			6.3 ± 0.3	90 ± 5	16 ± 3

Little phototoxic effect was verified after incubation for 2h with **PS3** and irradiation for 40 min at 20 mW/cm^2. The highest concentration tested (12.5µM) resulted in a decrease of the cell metabolic activity to 90 ± 5 % from control. Since **PS3** displayed a slight higher cellular uptake after incubation for 4h, the phototoxic effects were also studied for this incubation time (**Figure 87**, **Table 21**). First, **PS3** showed no toxic effects. In order to optimize the irradiation conditions for **PS3**, three different experiments were carried out: *i)* irradiation for 40 min with red light of 20 mW/cm^2 (**Figure**

87, panel A); *ii)* two irradiations for 40 min each at a fluence rate of 20 mW/cm^2 with a time interval of 1.5 h (**Figure 87**, panel B); and *iii)* irradiation for 40 min with red light of 40 mW/cm^2 (**Figure 87**, panel C). The best results were obtained for the first set of conditions, where the metabolic activity was decreased to 73 ± 5 % from control. However, these results are less promising than those obtained for **PS1**, **PS2**, **PS2a** and **PS4.** The latter could be explained taking into account the low cellular uptake of **PS3** combined with its low singlet oxygen generation efficiency ($\Phi_{\Delta\ (DMSO)}$ = 0.20).

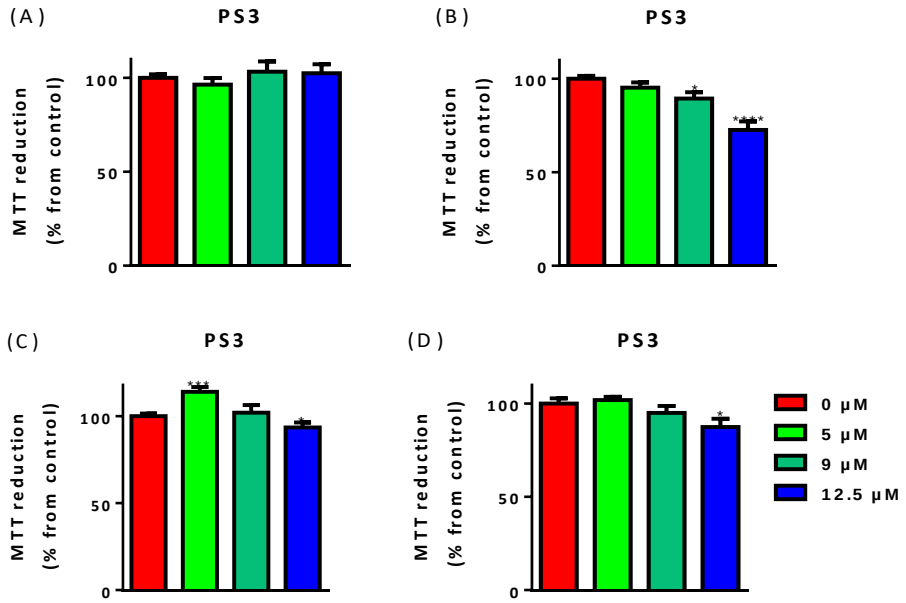

Figure 87 – Cell metabolic activity evaluated 24h after incubation with **PS3** for 4h; (A) dark toxicity; (B) phototoxicity after irradiation for 40 min at a fluence rate of 20 mW/cm^2; (C) phototoxicity after two irradiations for 40 min at a fluence rate of 20 mW/cm^2 with a time interval of 1.5 h; (D) phototoxicity after irradiation for 40 min at a fluence rate of 40 mW/cm^2. The percentage of toxicity was calculated relatively to control cells. Data are the mean value ± S.E.M. of at least three independent experiments performed in triplicates. *(p≤0.05), **(p≤0.01), ***(p≤0.001), **** (p≤0.0001) significantly different from control cells.

Table 21 – Cell metabolic activity evaluated 24h after incubation with **PS3** for 4h. The percentage of toxicity was calculated relatively to control cells. Data are the mean value ± S.E.M. of at least three independent experiments performed in triplicates.

C (µM)	**Dark**	**PDT** (40min irradiation; 20mW/cm^2)	**PDT** (PDT: two irradiations for 40 min with a time interval of 1.5 h; 20mW/cm^2)	**PDT** (40min irradiation; 40mW/cm^2)
0	100 ± 2	100 ± 2	100 ± 2	100 ± 3
5	96 ± 3	95 ± 3	114 ± 3	102 ± 2
9	103 ± 6	91 ± 3	102 ± 4	95 ± 4
12.5	103 ± 5	73 ± 5	94 ± 3	87 ± 4

4.3. *In vitro* study of PSs bearing axial carbohydrate units

RuPcs bearing pyridyl units functionalized with deprotected carbohydrates (**PS11-16**) were studied in this section (**Figure 88**). These compounds exhibited a very efficient generation of singlet oxygen and thus, were expected to produce promising results in the *in vitro* studies.

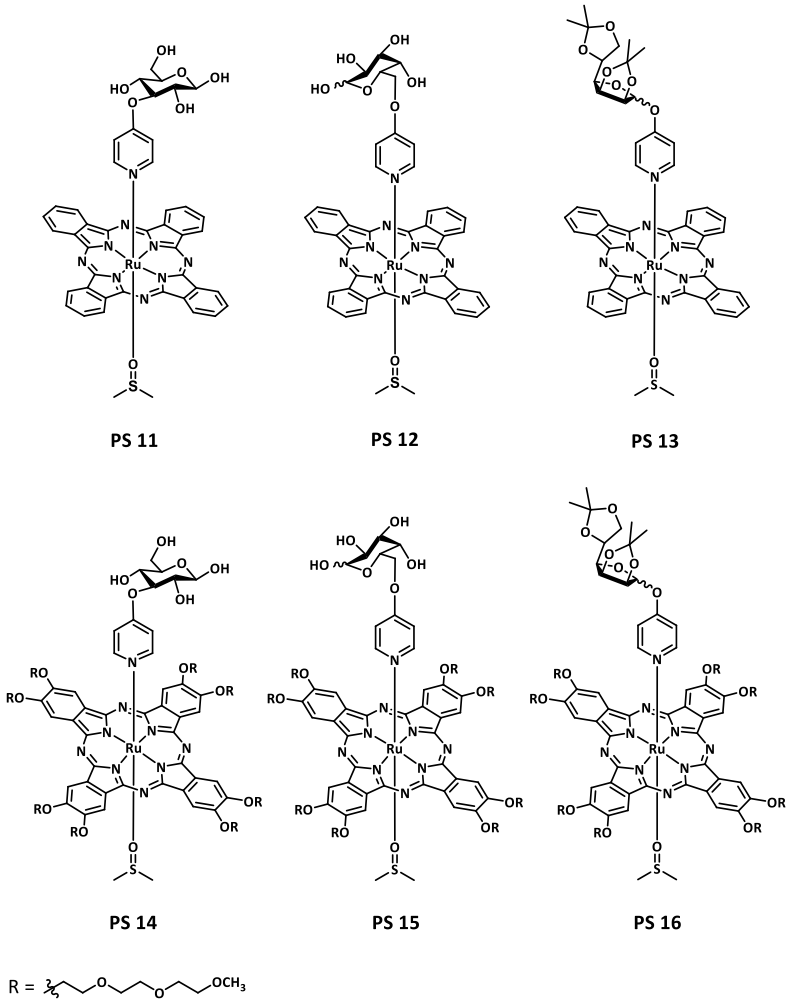

Figure 88 – Structure of PSs containing axial carbohydrate moieties studied in this section.

As illustrative examples, peripherally unsubstituted **PS12** and peripherally PEGylated **PS15** were studied regarding their aggregation behavior in PBS containing up to 0.45% of DMSO, as preformed for **PS1-4**. Given the lower solubility of **PS12**, 9 μM was the highest concentration used for this compound. The results show that the Lambert-Beer was fulfilled for both PSs (**Figure 89**), with R^2 values of 0.98 or greater, indicating that **PS12** and **PS15** are non-aggregated in the PBS/DMSO mixture in concentrations up to 9 μM and 12.5μM, respectively.

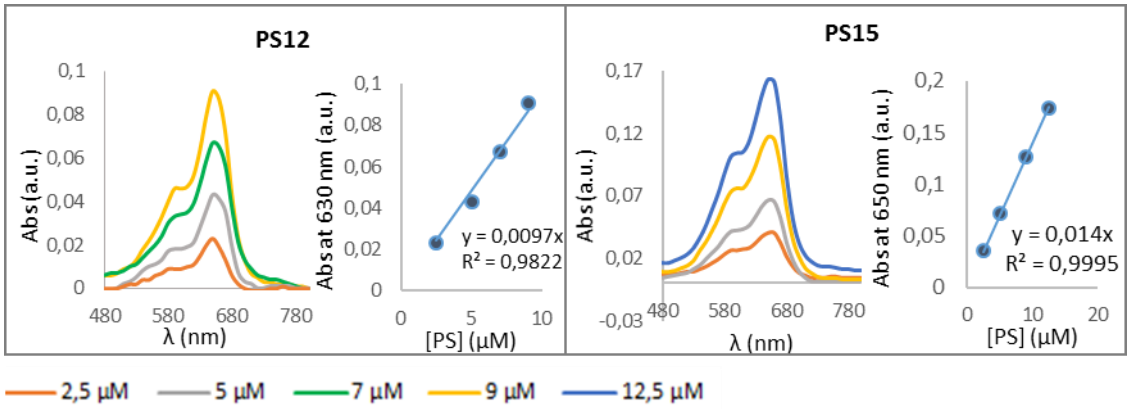

Figure 89 – UV-Vis dilution studies of **PS12** and **PS15** in physiologically relevant medium (PBS containing 0.45% of DMSO).

4.3.1. Cellular uptake

As in section 4.2., concentrations up to 5 µM were used for PSs with reduced solubility in water, namely RuPcs without peripheral substituents (**PS11-13**). Taking into account the low uptake exhibited by **PS3**, RuPcs with PEG chains as peripheral substituents (**PS14-16**) were incubated for 2h and 4h and with higher concentrations (5-12.5 µM).

As in section 4.2, PSs without peripheral substituents (**PS11-13**, **Figure 90** and **Table 22**) exhibit a significantly higher cellular uptake when compared to the ones with PEG chains at the periphery (**PS14-16**, **Figure 91** and **Table 23**).

Within **PS11-13**, the lowest cellular uptake was shown by **PS11**, bearing a glucose unit at the axial position, with a maximum cellular uptake of 0.75 ± 0.04 nmol of PS/mg of protein. **PS12** and **PS13** containing galactose and mannose units, respectively, didn't reveal significant differences between them, showing a cellular uptake of 1.3 ± 0.1 and 1.35 ± 0.09 nmol of PS/mg of protein, respectively, for the highest concentration tested.

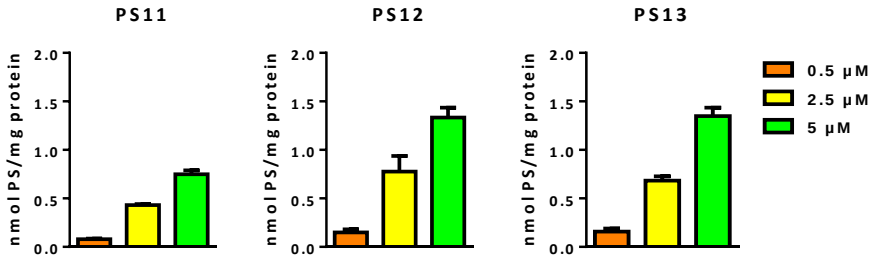

Figure 90 – Cellular uptake by HT-1376 cells of **PS11-13** after 2h incubation. Data are the mean value ± S.E.M. of at least two different experiments.

Table 22 – Cellular uptake by HT-1376 cells of **PS11-13** after 2h incubation. Data are represented as nmol of PS/mg of protein and are the mean value ± S.E.M. of at least two different experiments.

C (μM)	PS11	PS12	PS13
0.5	0.079 ± 0.007	0.15 ± 0.03	0.16 ± 0.03
2.5	0.43 ± 0.01	0.8 ± 0.2	0.68 ± 0.05
5	0.75 ± 0.04	1.3 ± 0.1	1.35 ± 0.09

PSs with PEG chains at the peripheral positions (**PS14-16**) showed the lowest cellular uptake among all the compounds tested so far. The decreasing cellular uptake followed the order: **PS14**, bearing a glucose unit at the axial position (0.25 ± 0.03 nmol of PS/ mg of protein); **PS16**, endowed with a mannose moiety (0.18 ± 0.06 nmol of PS/mg of protein); **PS15**, functionalized with a galactose unit (0.14 ± 0.03 nmol of PS/mg of protein).

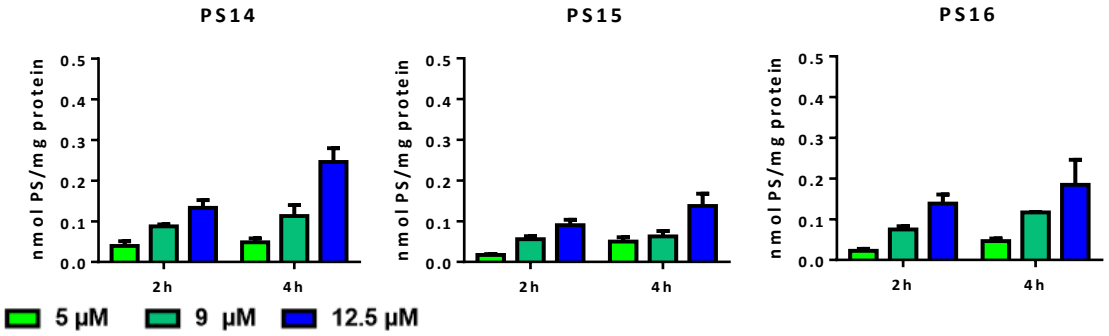

Figure 91 – Cellular uptake by HT-1376 cells of **PS14-16** after 2h and 4h incubation. Data are the mean value ± S.E.M. of at least two different experiments.

Table 23 – Cellular uptake by HT-1376 cells of **PS14-16** after 2h and 4h incubation. Data are represented as nmol of PS/mg of protein and are the mean value ± S.E.M. of at least two different experiments.

Time	C (μM)	PS14	PS15	PS16
2h	**5**	0.039 ± 0.01	0.017 ± 0.002	0.023 ± 0.005
	9	0.0876 ± 0.005	0.056 ± 0.007	0.075 ± 0.008
	12.5	0.13 ± 0.02	0.09 ± 0.01	0.14 ± 0.02
4h	**5**	0.05 ± 0.01	0.05 ± 0.01	0.046 ± 0.006
	9	0.11 ± 0.03	0.06 ± 0.01	0.1168 ± 0.0009
	12.5	0.25 ± 0.03	0.14 ± 0.03	0.18 ± 0.06

4.3.2. Phototoxic effect

The cytotoxic effects in the absence of light of PSs with no peripheral substituents (**PS11-13**) are described in **Figure 92** and **Table 24**. All the three compounds show toxic effects for the highest concentration tested (5 µM), with **PS12**, functionalized with a galactose unit, also being toxic for concentrations 0.5 and 2.5 µM. This led us to test lower concentrations, 0.1 and 0.25 µM, which proved to be non-toxic for all of the compounds.

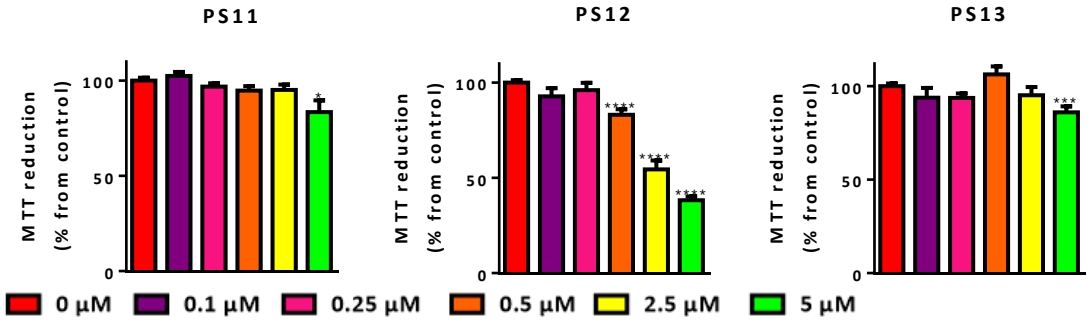

Figure 92 – Dark toxicity evaluated 24h after incubation with **PS11-13** for 2h using the MTT assay. The percentage of toxicity was calculated relatively to control cells. Data are the mean value ± S.E.M. of at least three independent experiments performed in triplicates. *(p≤0.05), **(p≤0.01), ***(p≤0.001), **** (p≤0.0001) significantly different from control cells.

Table 24 – Dark toxicity evaluated 24h after incubation with **PS11-13** for 2h using the MTT assay. Data are the mean value ± S.E.M. of at least three independent experiments performed in triplicates.

C (µM)	PS11	PS12	PS13
0	100 ± 2	100 ± 1	100 ± 1
0.1	103 ± 2	93 ± 4	94 ± 5
0.25	97 ± 2	96 ± 4	94 ± 2
0.5	95 ± 2	83 ± 3	106 ± 4
2.5	95 ± 3	55 ± 5	95 ± 4
5	83 ± 6	38 ± 2	86 ± 3

PSs bearing PEG chains at the periphery (**PS14-16**) did not show cytotoxic effects in the dark for none of the concentrations tested (5-12.5 µM, **Figure 93** and **Table 25**).

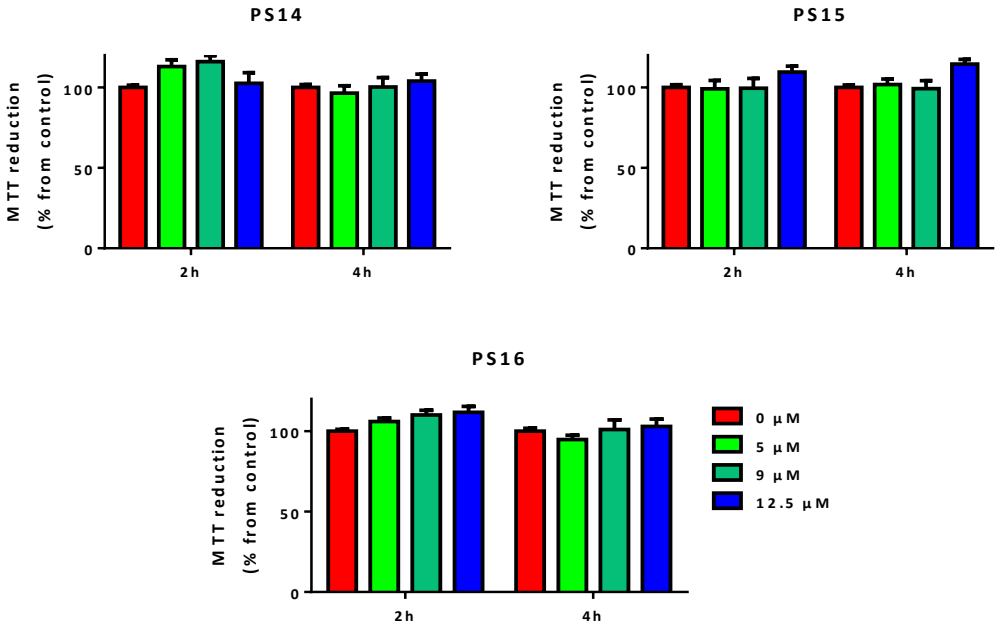

Figure 93 – Dark toxicity evaluated 24h after incubation with **PS14-16** for 2h and 4h using the MTT assay. The percentage of toxicity was calculated relatively to control cells. Data are the mean value ± S.E.M. of at least three independent experiments performed in triplicates. *(p≤0.05), **(p≤0.01), ***(p≤0.001), **** (p≤0.0001) significantly different from control cells.

Table 25 – Dark toxicity evaluated 24h after incubation with **PS14-16** for 2h and 4h using the MTT assay. The percentage of toxicity was calculated relatively to control cells. Data are the mean value ± S.E.M. of at least three independent experiments performed in triplicates.

Time	C (µM)	PS14	PS15	PS16
2h	**0**	100 ± 1	100 ± 2	100 ± 1
	5	108 ± 4	99 ± 5	106 ± 2
	9	105 ± 7	100 ± 6	110 ± 3
	12.5	103 ± 7	107 ± 3	112 ± 4
4h		100 ± 2	100 ± 2	100 ± 2
	5	96 ± 4	102 ± 3	95 ± 3
	9	100 ± 6	99 ± 5	101 ± 6
	12.5	104 ± 4	115 ± 3	103 ± 5

To evaluate the phototoxic effects of **PS11-13**, HT-1376 cells were incubated with solutions of these compounds of different concentrations for 2h, and, immediately after removal of PS solution and addition of culture medium RPMI-1640, cells were irradiated with red light at a fluence rate of 20 mW/cm^2 for 40 min. The MTT assay was performed 24h after treatment. The corresponding results are represented in **Figure 94** and **Table 26**.

All the three PSs proved to produce very effective phototoxic damage. **PS13**, bearing a mannose unit, is the most efficient one, with the lowest concentration tested (0.1 µM) already

reducing the cell metabolic activity to 20 ± 1 % from control, and the highest non-toxic concentration (2.5 µM) leading to a cell metabolic activity reduction to 16 ± 2% from control.

Next, **PS12**, functionalized with a galactose unit, which resulted in a decrease in cell metabolic activity to 29 ± 3 % from control upon the incubation with a 0.1 µM solution. It's highest non-toxic concentration (0.25 µM) led to a reduction in cell metabolic activity to 21 ± 2 % from control.

Finally, **PS11**, functionalized with a glucose unit, is the PS with the lowest phototoxic effect among the three compounds. The decrease in cell metabolic activity in this case ranged from 51 ± 3 % from control, for the lowest concentration tested (0.1 µM), to 16 ± 2 % from control, for the highest non-toxic concentration tested (2.5 µM). The lower phototoxic effect can be correlated with the lower cellular uptake displayed by **PS11**.

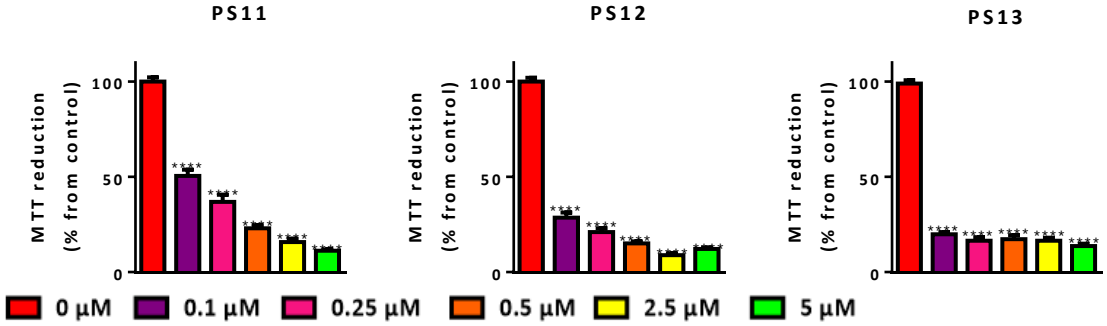

Figure 94 – Phototoxicity evaluated 24h after incubation with **PS11-13** for 2h and irradiation for 40 min at a fluence rate of 20 mW/cm^2. The percentage of toxicity was calculated relatively to control cells. Data are the mean value ± S.E.M. of at least three independent experiments performed in triplicates. *(p≤0.05), **(p≤0.01), ***(p≤0.001), **** (p≤0.0001) significantly different from control cells.

Table 26 – Phototoxicity evaluated 24h after incubation with **PS11-12** for 2h and irradiation for 40 min at a fluence rate of 20 mW/cm^2. The percentage of toxicity was calculated relatively to control cells. Data are the mean value ± S.E.M. of at least three independent experiments performed in triplicates.

C (µM)	PS11	PS12	PS13
0	100 ± 2	100 ± 2	100 ± 2
0.1	51 ± 3	29 ± 3	20 ± 1
0.25	37 ± 4	215 ± 2	17 ± 2
0.5	23 ± 2	15 ± 1	17 ± 2
2.5	16 ± 2	9.0 ± 0.9	16 ± 2
5	11.3 ± 0.7	12.2 ± 0.7	14 ± 1

The phototoxic effects of **PS14-16** were evaluated after 2h and 4h incubation and irradiation with light at a fluence rate of 20 mW/cm^2, and also upon two irradiations for 40 min with a time

interval of 1.5h at a fluence rate of 20 mW/cm^2 and irradiation for 40 min with light of 40 mW/cm^2, as done before for **PS3**. These results are collected in **Figure 95** and **Table 27**. All three compounds exhibit improved phototoxic damage after incubation for 4h and irradiation for 40 min at 40 mW/cm^2.

PS16, with a mannose moiety, was the most different in the four sets of experiments, as well as the most phototoxic PS. In particular, **PS16** achieved a reduction in cell metabolic activity of 19.6 ± 0.6 % from control for the highest concentration tested (12.5 μM).

PS15, which is functionalized with a galactose unit, is the second most effective compound, having reached a decrease in cell metabolic activity of 61 ± 5 % from control. However, this effect is much less effective than the one produced by **PS16**.

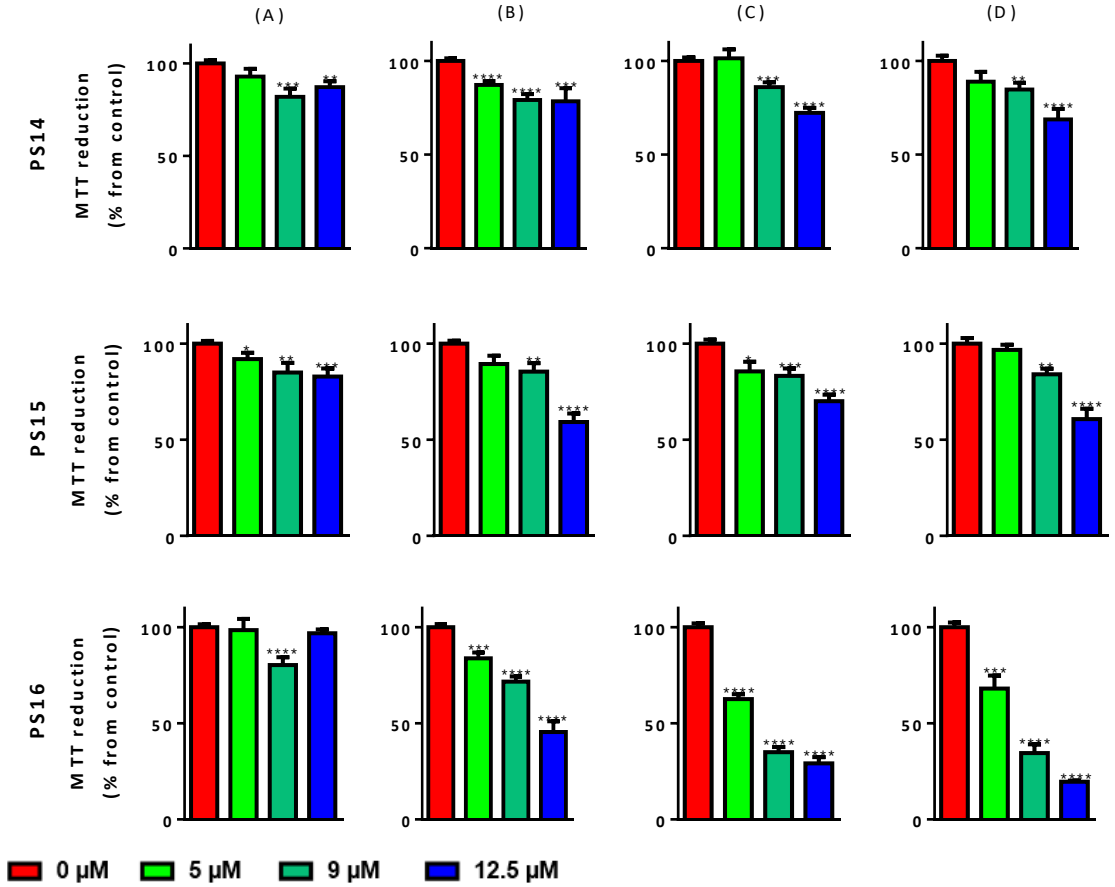

Figure 95 – Phototoxic effects of **PS14-16.** (A) incubation with PS for 2h and irradiation for 40 min at a fluence rate of 20 mW/cm^2; (B) incubation with PS for 4h and irradiation for 40 min at a fluence rate of 20 mW/cm^2; (C) incubation with PS for 4h and two irradiations for 40 min at a fluence rate of 20 mW/cm^2 with a time interval of 1.5 h; (D) incubation with PS for 4h and irradiation for 40 min at a fluence rate of 40 mW/cm^2. The percentage of toxicity was calculated relatively to control cells. Data are the mean value ± S.E.M. of at least three independent experiments performed in triplicates. *(p≤0.05), **(p≤0.01), ***(p≤0.001), **** (p≤0.0001) significantly different from control cells.

The least effective PS of this family was **PS14**, bearing a glucose unit. This compound reduced cell metabolic activity by only 69 ± 6 % from control.

In summary, among all six PSs bearing deprotected monosaccharides at one axial position and a DMSO ligand at the other one, PSs functionalized with a mannose unit were the most effective, followed by those containing a galactose moiety. PSs with a glucose unit were the least phototoxic compounds.

Table 27 – Phototoxic effects of **PS14-16.** The percentage of toxicity was calculated relatively to control cells. Data are the mean value ± S.E.M. of at least three independent experiments performed in triplicates.

		C (μM)	PS14	PS15	PS16
2h	40min irradiation; 20mW/cm^2	**0**	100 ± 2	100 ± 1	100 ± 2
		5	93± 4	92 ± 3	99 ± 6
		9	82 ± 4	85 ± 5	80 ± 4
		12.5	87 ± 3	83 ± 4	97 ± 2
4h	40min irradiation; 20mW/cm^2	**0**	100 ± 1	100 ± 1	100 ± 2
		5	87 ± 2	89 ± 4	84 ± 3
		9	79 ± 3	85 ± 4	74 ± 3
		12.5	79 ± 7	59 ± 4	45 ± 6
	2 irradiations for 40 min with 1.5h interval; 20mW/cm^2	**0**	100 ± 2	100 ± 2	100 ± 2
		5	101 ± 5	86 ± 5	62 ± 3
		9	86 ± 3	83 ± 4	35 ± 3
		12.5	72 ± 3	70 ± 3	29 ± 3
	40min irradiation; 40mW/cm^2	**0**	100 ± 3	100 ± 3	100 ± 2
		5	89 ± 5	97 ± 3	68 ± 8
		9	85 ± 4	84 ± 3	35 ± 5
		12.5	69 ± 6	61 ± 5	19.6 ± 0.6

4.4. *In vitro* study of mixed RuPcs bearing axial PEG chains and carbohydrate units

Mixed RuPcs bearing PEG chains and carbohydrate units (**PS17-28**) studied in this section are represented in **Figure 96**. As explained in section 2.3, the polyether chains were conjugated with carbohydrate moieties in order to combine both the hydrophilicity and the tumor selective properties provided by such functional groups, respectively. This series of PSs contain three distinct protected monosaccharides, glucose, galactose and mannose, and PEG chains with two different functional groups, namely alcohol and amine functions. Furthermore, PEG chains were also introduced at the peripheral positions to further improve the solubility in water of the final PSs.

RuPcs without peripheral substituents (**PS17-22**) were incubated for 2h with concentrations ranging from 0.5 to 5 μM, while compounds bearing polyether chains at their periphery (**PS23-28**) were incubated for 2h and 4h with concentration between 5 and 12.5 μM.

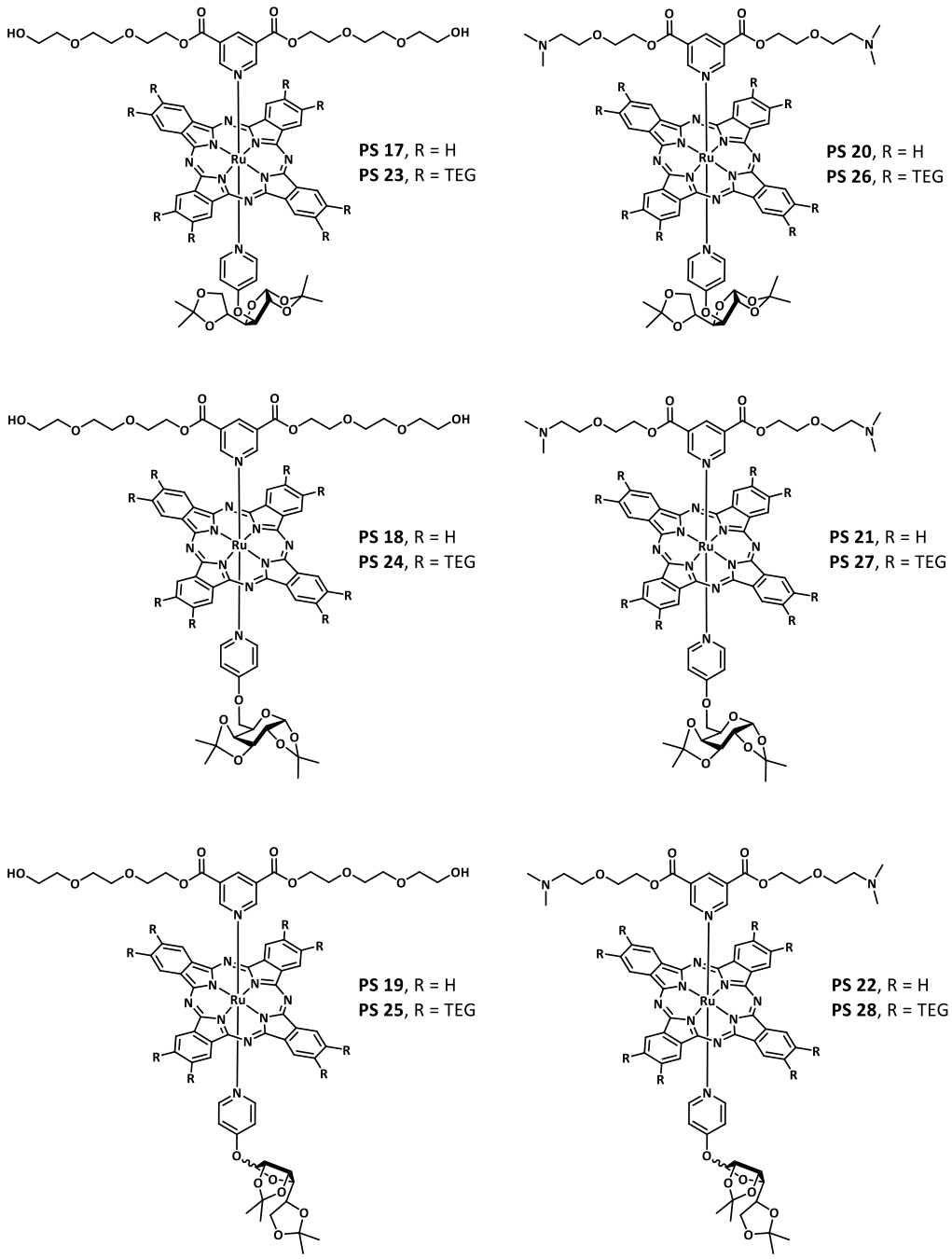

Figure 96 – Structure of mixed PSs containing axial polyether chains and carbohydrate units studied in this section.

As illustrative examples, aggregation studies in physiologically relevant medium (PBS containing 0.45% of DMSO) were performed for **PS18** and **PS24**, containing terminal alcohol functions, and for **PS21** and **PS27**, bearing terminal amino groups. Peripherally unsubstituted **PS18** and **PS21** were studied in concentrations between 2.5 and 9 μM, while peripherally PEGylated **PS24** and **PS27** were studied up to 12.5 μM. The results show that the Lambert-Beer was fulfilled for all

PSs (**Figure 97**), with R^2 values of 0.97 or greater, indicating that this family of compounds is non-aggregated in the PBS/DMSO mixture and in the concentrations that will be used for *in vitro* essays.

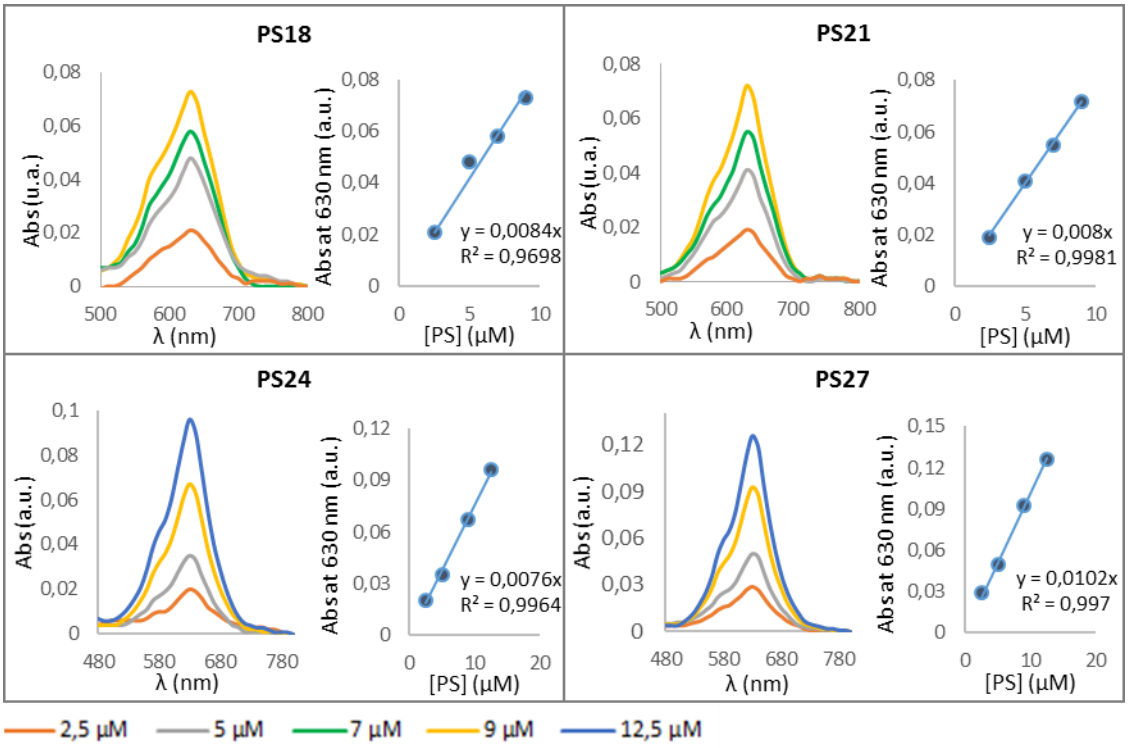

Figure 97 – UV-Vis dilution studies of **PS18**, **PS21**, **PS24** and **PS15** in physiologically relevant medium (PBS containing 0.45% of DMSO).

4.4.1. Cellular Uptake

The cellular uptake of RuPcs without peripheral functionalization (**PS17-22**) is depicted in **Figure 98** and **Table 28**.

Overall, the cellular uptake of **PS17-22** is similar to that of carbohydrate-free analogues **PS1** and **PS2**, respectively, indicating that the presence of one carbohydrate unit has little influence in the cellular uptake by HT-1376 cancer cells. As in the case of **PS1** and **PS2**, higher cellular uptake (from 1.13 ± 0.04 to 2.2 ± 0.2 nmol of PS/mg of protein) was verified for compounds bearing tertiary amino functions at the axial positions (**PS20-22**). The cellular uptake of RuPcs containing terminal alcohol functions oscillated between 0.8174 ± 0.03926 and 1.09 ± 0.09 nmol of PS/mg of protein, for the highest PS concentration tested.

Taking a closer look at the effect of the distinct carbohydrates, no significant changes are observed in the case of the RuPcs containing alcohol functions (**PS17-19**). Contrasting, in the family

of RuPcs with terminal amines, increased cellular uptake (2.2 ± 0.2 nmol of PS/mg of protein) is observed for the PS bearing a mannose unit (**PS22**), for the highest PS concentration tested.

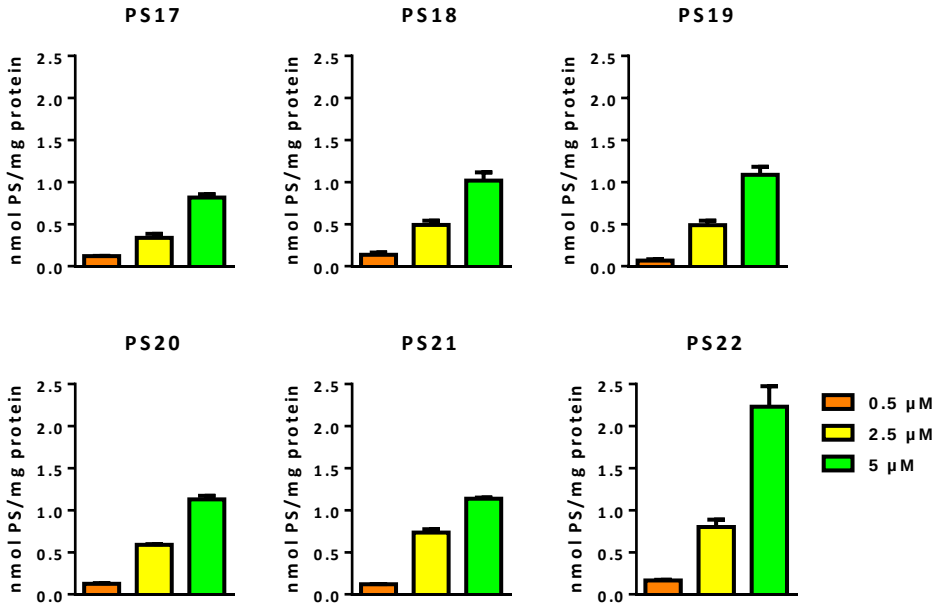

Figure 98 – Cellular uptake by HT-1376 cells of **PS17-22** after 2h incubation. Data are the mean value ± S.E.M. of at least two different experiments.

Table 28 – Cellular uptake by HT-1376 cells of **PS17-22** after 2h incubation. Data are represented as nmol of PS/mg of protein and are the mean value ± S.E.M. of at least two different experiments.

C (µM)	PS17	PS18	PS19
0.5	0.121 ± 0.003	0.14 ± 0.03	0.07 ± 0.02
2.5	0.34 ± 0.05	0.49 ± 0.05	0.49 ± 0.05
5	0.82 ± 0.04	1.0 ± 0.1	1.09 ± 0.09
	PS20	**PS21**	**PS22**
0.5	0.127 ± 0.007	0.122 ± 0.001	0.165 ± 0.009
2.5	0.589 ± 0.009	0.74 ± 0.04	0.80 ± 0.09
5	1.13 ± 0.04	1.14 ± 0.01	2.2 ± 0.2

The cellular uptake of RuPcs bearing PEG chains at peripheral positions (**PS23-28**) (**Figure 99** and **Table 29**) was lower than the corresponding unsubstituted analogues (**PS17-22**).

Contrary to what was observed for unsubstituted **PS17-22**, compounds bearing alcohol groups (**PS23-25**) showed higher cellular uptake (from 0.718 ± 0.003 to 1.71 ± 0.09 nmol of PS/mg of protein, for the highest PS concentration tested and 4h of incubation) than for compounds bearing amines (**PS26-28**, between 0.272 ± 0.009 and 1.16 ± 0.02 nmol of PS/mg of protein).

Besides, among peripherally functionalized RuPcs (**PS23-28**), those containing glucose units (**PS23** and **PS26**) show the maximum cellular uptake (1.71 ± 0.09 and 1.16 ± 0.02 nmol of PS/mg of protein), followed by those bearing mannose moieties (**PS25** and **PS28**, 1.1 ± 0.1 and 0.8 ± 0.1 nmol of PS/ mg of protein) and finally, those with galactose units (**PS24** and **PS27**, 0.718 ± 0.003 and 0.272 ± 0.009 nmol of PS/mg of protein).

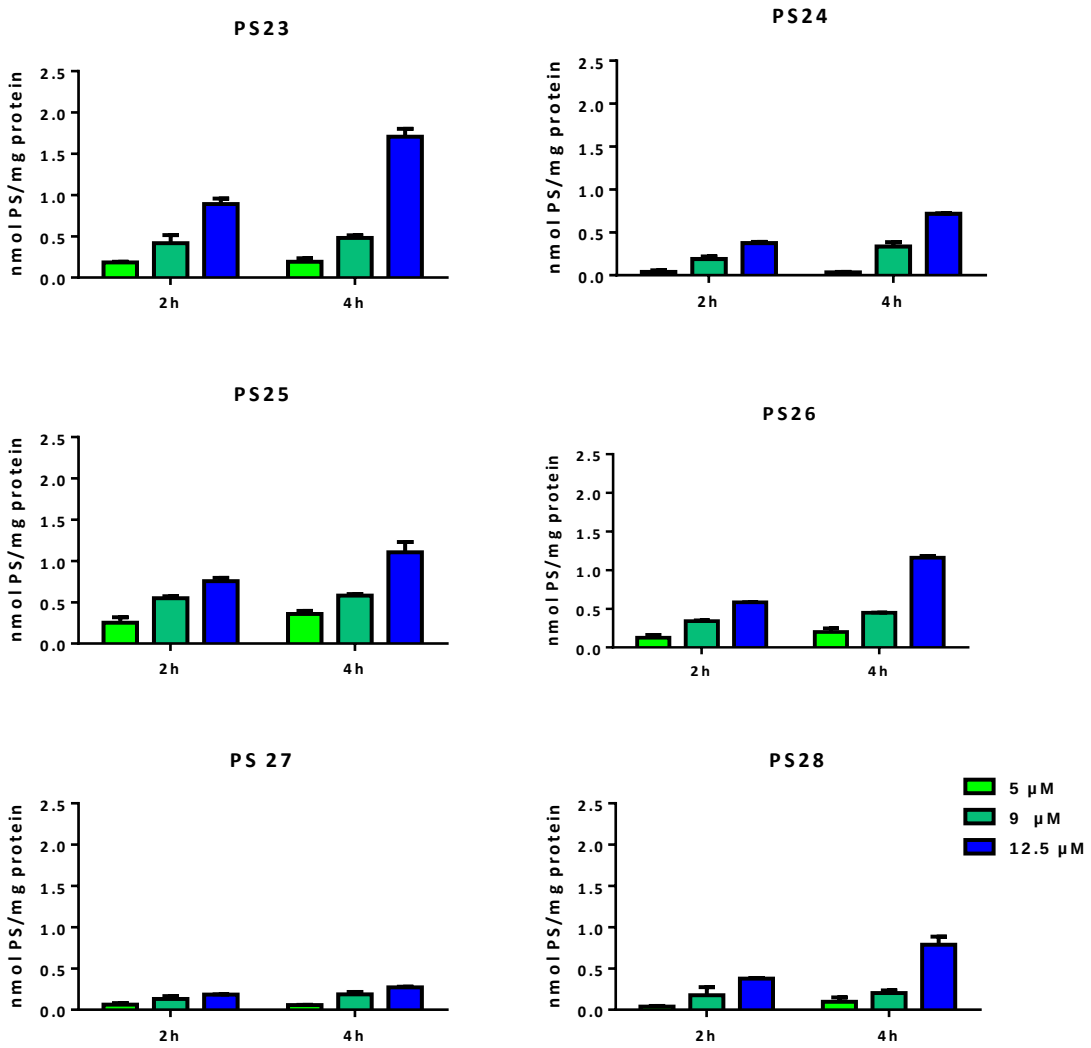

Figure 99 – Cellular uptake by HT-1376 cells of **PS23-28** after 2h and 4h incubation. Data are the mean value ± S.E.M. of at least two different experiments.

Table 29 – Cellular uptake by HT-1376 cells of **PS23-28** after 2h and 4h incubation. Data are represented as nmol of PS/mg of protein and are the mean value ± S.E.M. of at least two different experiments.

	C (μM)	PS23	PS24	PS25
2h	5	0.185 ± 0.008	0.04 ± 0.02	0.25 ± 0.07
	9	0.4 ± 0.1	0.19 ± 0.03	0.55 ± 0.02
	12.5	0.89 ± 0.07	0.37 ± 0.01	0.76 ± 0.04
4h	5	0.19 ± 0.04	0.032 ± 0.006	0.36 ± 0.04
	9	0.48 ± 0.03	0.33 ± 0.05	0.58 ± 0.02
	12.5	1.71 ± 0.09	0.718 ± 0.003	1.1 ± 0.1
		PS26	**PS27**	**PS28**
2h	5	0.13 ± 0.04	0.06 ± 0.02	0.038 ± 0.007
	9	0.34 ± 0.01	0.13 ± 0.03	0.2 ± 0.1
	12.5	0.584 ± 0.004	0.185 ± 0.002	0.377 ± 0.006
4h	5	0.20 ± 0.05	0.057 ± 0.002	0.10 ± 0.05
	9	0.449 ± 0.001	0.19 ± 0.03	0.20 ± 0.03
	12.5	1.16 ± 0.02	0.272 ± 0.009	0.8 ± 0.1

4.4.2. Phototoxic effect

The first step in the study of the effects of **PS17-28** on the metabolic activity of HT-1376 cells consisted on the evaluation of their dark toxicity. RuPcs with no peripheral substituents (**PS17-22**) were incubated for 2h (**Figure 100** and **Table 30**), whereas compounds bearing polyether chains at the periphery (**PS23-28**) were incubated for 2 and 4h (**Figure 101** and **Table 31**). With the exception of the highest concentrations (5 μM) of **PS21** and **PS22**, none of the compounds showed toxic effects in the dark.

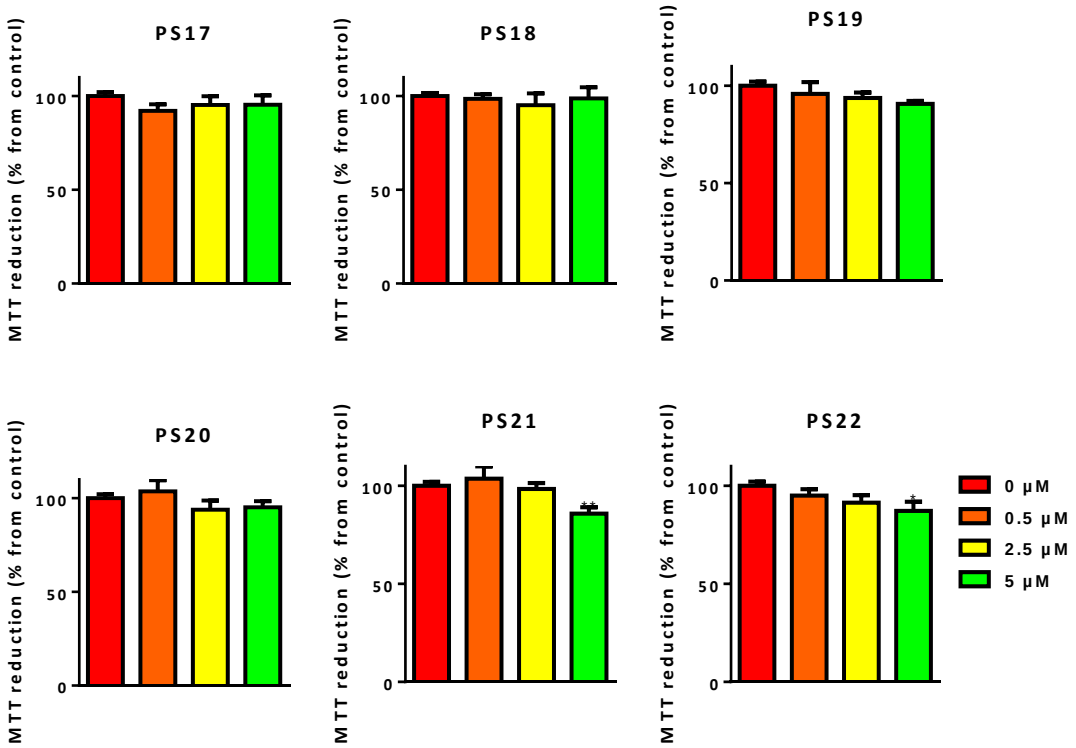

Figure 100 – Dark toxicity evaluated 24h after incubation with **PS17-22** for 2h using the MTT assay. The percentage of toxicity was calculated relatively to control cells. Data are the mean value ± S.E.M. of at least three independent experiments performed in triplicates. *(p≤0.05), **(p≤0.01), ***(p≤0.001), **** (p≤0.0001) significantly different from control cells.

Table 30 – Dark toxicity evaluated 24h after incubation with **PS17-22** for 2h using the MTT assay. The percentage of toxicity was calculated relatively to control cells. Data are the mean value ± S.E.M. of at least three independent experiments performed in triplicates.

C (µM)	PS17	PS18	PS19	PS20	PS21	PS22
0	100 ± 3	100 ± 2	100 ± 3	100 ± 2	100 ± 2	100 ± 2
0.5	76 ± 4	74 ± 4	90 ± 5	57 ± 5	58 ± 4	61 ± 3
2.5	46 ± 3	36 ± 2	66 ± 2	14 ± 1	14.0 ± 0.7	16 ± 1
5	23 ± 1	20 ± 1	40 ± 4	10 ± 1	13 ± 1	10 ± 1

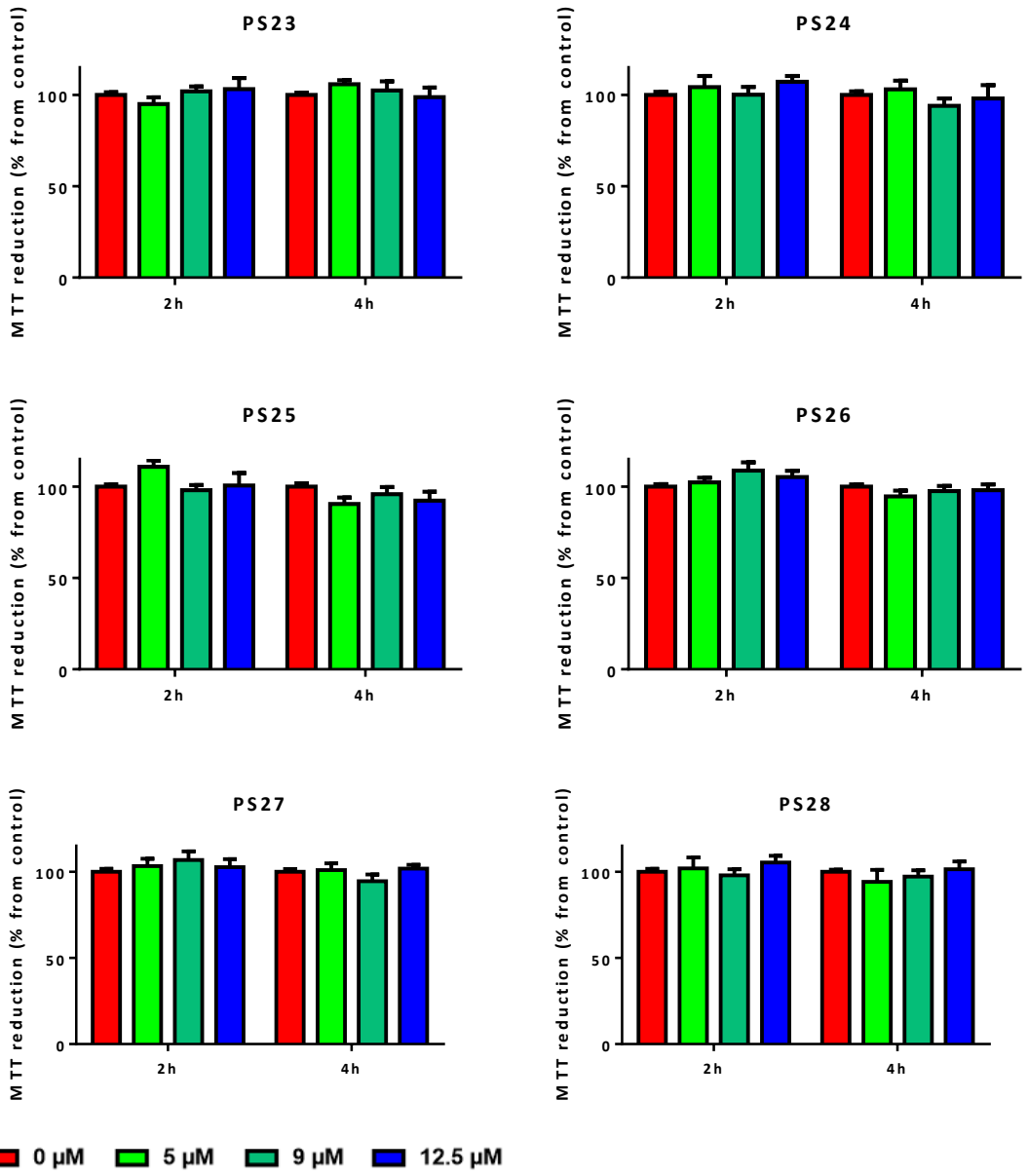

Figure 101 – Dark toxicity evaluated 24h after incubation with **PS23-28** for 2h and 4h using the MTT assay. The percentage of toxicity was calculated relatively to control cells. Data are the mean value ± S.E.M. of at least three independent experiments performed in triplicates. *(p≤0.05), **(p≤0.01), ***(p≤0.001), ****(p≤0.0001) significantly different from control cells.

Table 31 – Dark toxicity evaluated 24h after incubation with **PS23-28** for 2h and 4h using the MTT assay. The percentage of toxicity was calculated relatively to control cells. Data are the mean value ± S.E.M. of at least three independent experiments performed in triplicates.

	C (μM)	PS23	PS24	PS25	PS26	PS27	PS28
2h	0	100 ± 1	100 ± 2	100 ± 1	100 ± 1	100 ± 2	100 ± 2
	5	95 ± 4	104 ± 6	111 ± 4	102 ± 3	103 ± 4	102 ± 6
	9	102 ± 3	100 ± 4	98 ± 3	109 ± 4	107 ± 5	98 ± 4
	12.5	103 ± 6	107 ± 3	101 ± 7	105 ± 3	103 ± 5	105 ± 4
4h	0	100 ± 1	100 ± 2	100 ± 2	100 ± 1	100 ± 2	100 ± 1
	5	106 ± 2	103 ± 5	90 ± 3	95 ± 3	101 ± 4	94 ± 7
	9	102 ± 5	94 ± 4	96 ± 4	98 ± 3	94 ± 4	97 ± 4
	12.5	99 ± 5	98 ± 7	92 ± 5	98 ± 3	102 ± 2	101 ± 4

PS17-22 were incubated for 2h hours and then irradiated for 40 min with light of 20 mW/cm^2. The MTT assay performed 24h after treatment revealed the highest phototoxic effect for compounds bearing tertiary amino units (**PS20-22**), leading to a decrease in cell viability up to 14.0 ± 0.7 % from control, for the highest non-toxic concentration tested. Among these three compounds, no significant differences were observed with respect to the different carbohydrates attached to the macrocycles. In the case of RuPcs with alcohol functions (**PS17-19**), the lowest photodynamic effect was verified for **PS19**, bearing a mannose unit as axial ligand (reduction of cell metabolic activity to 40 ± 4 % from control).

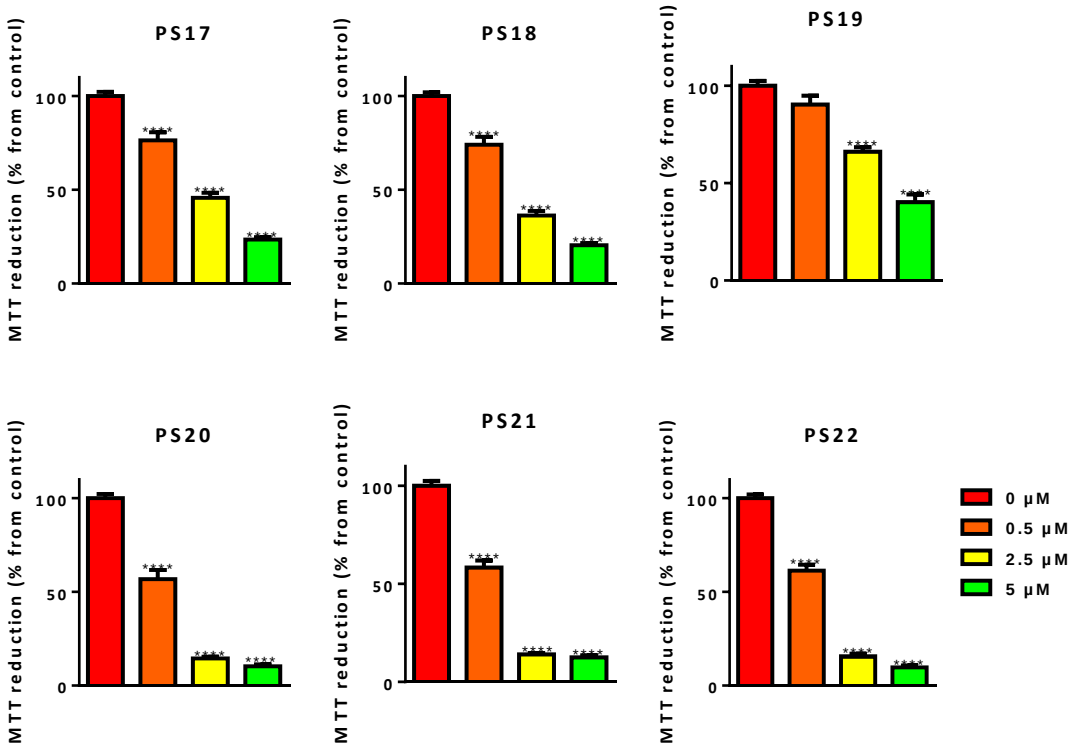

Figure 102 – Phototoxicity evaluated 24h after incubation with **PS17-22** for 2h and irradiation for 40 min at a fluence rate of 20 mW/cm^2. The percentage of toxicity was calculated relatively to control cells. Data are the mean value ± S.E.M. of at least three independent experiments performed in triplicates. *(p≤0.05), **(p≤0.01), ***(p≤0.001), **** (p≤0.0001) significantly different from control cells.

Table 32 – Phototoxicity evaluated 24h after incubation with **PS17-22** for 2h and irradiation for 40 min at a fluence rate of 20 mW/cm^2. The percentage of toxicity was calculated relatively to control cells. Data are the mean value ± S.E.M. of at least three independent experiments performed in triplicates.

C (µM)	PS17	PS18	PS19	PS20	PS21	PS22
0	100 ± 2	100 ± 2	100 ± 3	100 ± 2	100 ± 2	100 ± 2
0.5	76 ± 4	74 ± 4	90 ± 5	57 ± 5	58 ± 4	61 ± 3
2.5	46 ± 3	36 ± 2	66 ± 2	14 ± 1	14 ± 0.7	16 ± 1
5	23 ± 1	20 ± 1	40 ± 4	10 ± 1	13 ± 1	10 ± 1

PSs with peripheral polyether chains (**PS23-28**) revealed a much less accentuated photodynamic effect (**Figure 103** and **Table 33**), comparing with the corresponding unsubstituted analogues (**PS17-22**). These results can be rationalized based on the lower uptake of **PS23-28**, as well as by their lower singlet oxygen generation quantum yields, which range from only 0.07 to 0.10 in DMSO. For **PS23-28**, the best results were obtained after incubation with PSs for 4h.

In general, RuPcs functionalized with amines at the axial positions (**PS26-28**) showed a higher photodynamic effect than those bearing alcohol units (**PS23-25**), as observed for the corresponding unsubstituted analogues (**PS20-22**).

PS23 and **PS26**, bearing glucose moieties, showed the lowest phototoxic effect, despite their higher cellular uptake. Hence, **PS23** only exhibit some reduction on cell metabolic activity (91 ± 2 % from control) after 40 min irradiation at a fluence rate of 40 mW/cm^2. The phototoxic effect of **PS26** was slightly higher, with no significant changes among the three different sets of experiments performed with 4h incubation time. This compound reached to a cell metabolic activity reduction to 84 ± 4 % from control. RuPcs bearing galactose units (**PS24** and **PS27**) exhibit a reduction of cell metabolic activity to 84 ± 5 and 78 ± 6 % from control, respectively. Curiously, the highest phototoxic effect shown by **PS24** does not correspond to the highest concentration of incubation. In fact, with the exception of the irradiation at 40 mw/cm^2, all set of experiments revealed an increase in cell viability from the 9 μM solution to the 12.5 solution μM.

Finally, the highest phototoxic effect was displayed by RuPcs functionalized with mannose moieties (**PS25** and **PS28**). **PS25** did not show significant differences among the different set of experiments carried out after 4h of incubation, displaying a maximum reduction of cell metabolic activity to 81 ± 2 % from control. On the other hand, besides being the PS that revealed the most efficient phototoxic activity, **PS28** was also the compound that improved the most upon the changes performed in the irradiation method, among all the mixed PSs with PEG chains at the periphery (**PS23-28**). This compound proved most efficient upon irradiation for 40 min at a fluence rate of 40 mW/cm^2, resulting in a reduction of cell metabolic activity to 59 ± 5 % from control.

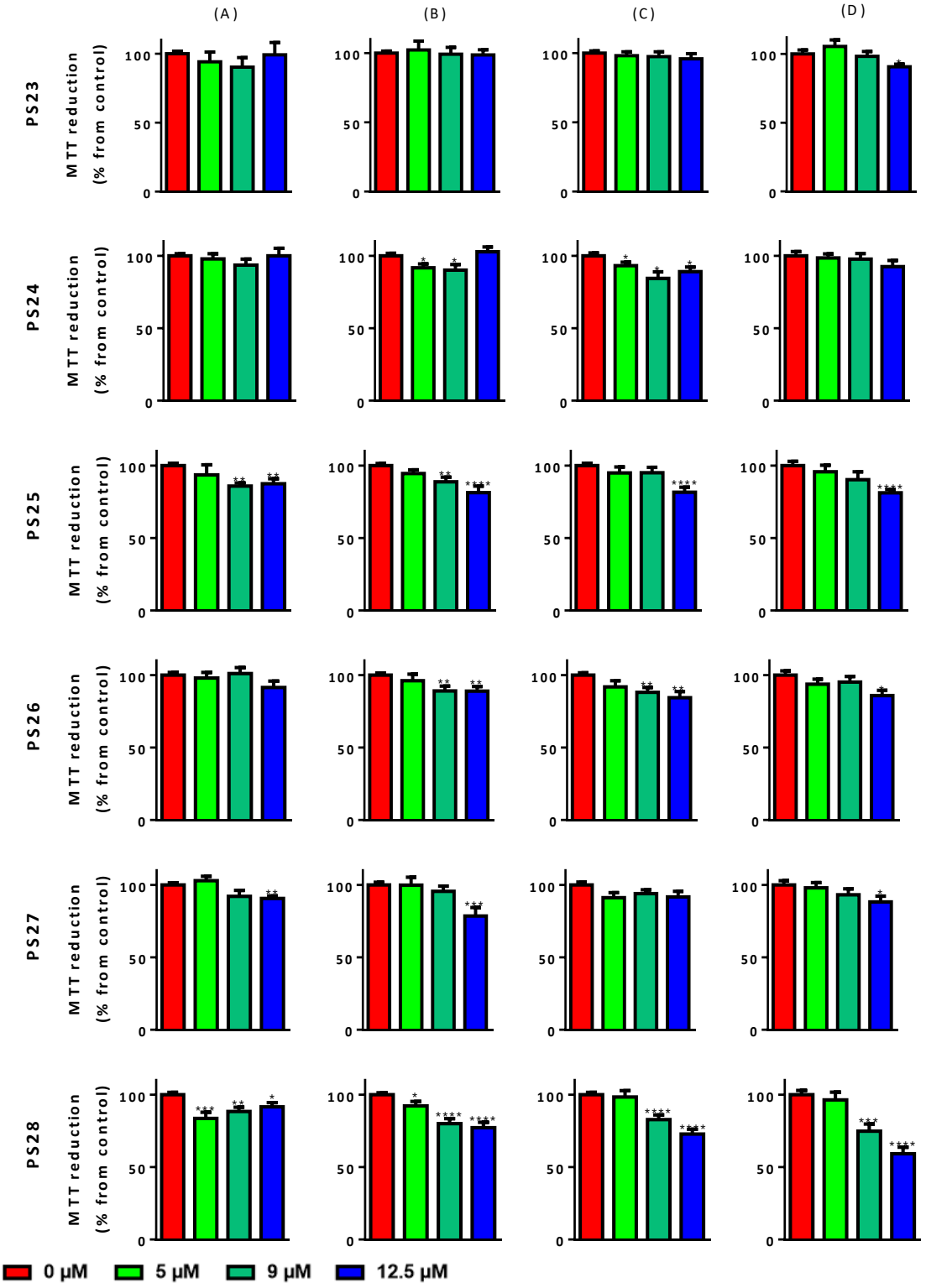

Figure 103 – Phototoxic effects of **PS23-28.** (A) incubation with PS for 2h and irradiation for 40 min at a fluence rate of 20 mW/cm^2; (B) incubation with PS for 4h and irradiation for 40 min at a fluence rate of 20 mW/cm^2; (C) incubation with PS for 4h and two irradiations for 40 min at a fluence rate of 20 mW/cm^2 with a time interval of 1.5 h; (D) incubation with PS for 4h and irradiation for 40 min at a fluence rate of 40 mW/cm^2. Data are the mean value ± S.E.M. of at least three independent experiments performed in triplicates. *(p≤0.05), **(p≤0.01), ***(p≤0.001), **** (p≤0.0001) significantly different from control cells.

Table 33 – Phototoxic effects of **PS23-28.** The percentage of toxicity was calculated relatively to control cells. Data are the mean value ± S.E.M. of at least three independent experiments performed in triplicates.

		C (μM)	PS 23	PS 24	PS 25	PS 26	PS 27	PS 28
2h	40min irradiation; 20mW/cm²	**0**	100 ± 2	100 ± 1	100 ± 2	100 ± 2	100 ± 1	100 ± 2
		5	94 ± 7	98 ± 4	94± 7	98 ± 4	103 ± 3	84 ± 4
		9	90 ± 7	94 ± 4	86 ± 2	101 ± 4	92 ± 4	88 ± 3
		12.5	99 ± 9	100 ± 5	87 ± 3	91 ± 4	91 ± 2	92 ± 3
4h	40min irradiation; 20mW/cm²	**0**	100 ± 1	100 2	100 ± 1	100 ± 1	100 ± 2	100 ± 1
		5	102 ± 6	92 ± 3	95 ± 3	96 ± 4	100 ± 5	92 ± 3
		9	99 ± 5	90 ± 4	89 ± 3	89 ± 3	96 ± 4	80 ± 3
		12.5	99 ± 5	103 ± 3	81 ± 4	89 ± 3	78 ± 6	77 ± 4
	2 irradiations for 40 min	**0**	100 ± 2	100 ± 2	100 ± 2	100 ± 2	100 ± 2	100 ± 2
		5	98 ± 3	93 ± 2	95 ± 4	92 ± 4	91 ± 3	98 ± 4
		9	97 ± 3	84 ± 5	95 ± 4	88 ± 3	94 ± 3	83 ± 3
		12.5	96 ± 4	89 ± 3	82 ± 3	84 ± 4	92 ± 4	73 ± 3
	40min irradiation; 40mW/cm²	**0**	100 ± 3	100 ± 3	100 ± 3	100 ± 3	100 ± 3	100 ± 3
		5	105 ± 5	99 ± 3	96 ± 4	94 ± 3	98 ± 4	96 ± 5
		9	98 ± 3	98 ± 4	90 ± 5	95 ± 4	93 ± 4	75 ± 5
		12.5	91 ± 2	92 ± 4	81 ± 2	86 ± 4	88 ± 4	59 ± 5

4.5. *In vitro* study of RuPcs bearing axial folic acid

PS29 functionalized with folic acid and DMSO as axial ligands, and with PEG chains as peripheral substituents (**Figure 104**). Was tested similarly to **PS14-16**, i.e., using concentrations of 5μM, 9μM and 12.5 μM and incubation times of 2h and 4h.

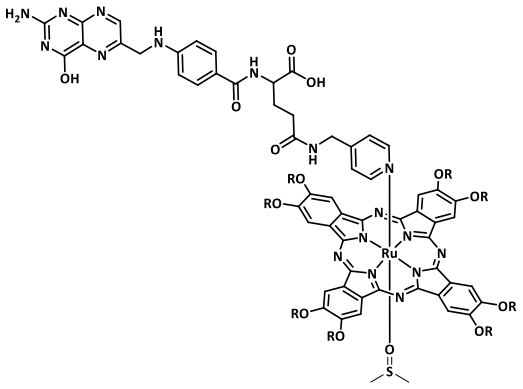

PS 29

Figure 104 – Structure of **PS29** containing axial folic acid and PEG chains as peripheral substituents, studied in this section.

4.5.1. Cellular uptake

The cellular uptake of **PS29** after incubation for 2h and 4h is described in **Figure 105** and **Table 34**. This compound exhibited a cellular uptake of 0.310 ± 0.007 nmol of PS/mg of protein after 2h of incubation and 0.35 ± 0.04 nmol of PS/mg of protein after incubation for 4h, thus, only a small increase in the cellular uptake upon prolonging the incubation time. Nonetheless, the cellular uptake of **PS29** was superior to that displayed by the corresponding analogues bearing deprotected carbohydrates (**PS14-16**), suggesting that folic acid plays an important role in the cellular internalization process.

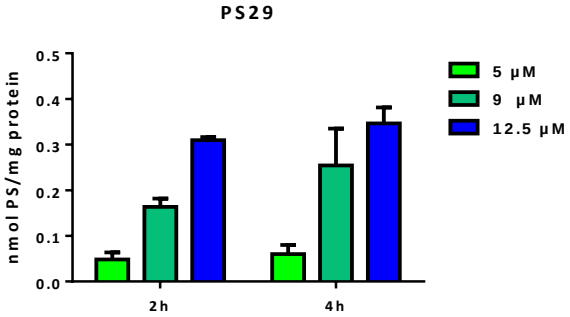

Figure 105 – Cellular uptake by HT-1376 cells of **PS29** after 2h and 4h incubation. Data are the mean value ± S.E.M. of at least two different experiments.

Table 34 – Cellular uptake by HT-1376 cells of **PS29** after 2h and 4h incubation. Data are represented as nmol of PS/mg of protein and are the mean value ± S.E.M. of at least two different experiments.

	C (µM)	PS 32
2h	**5**	0.05 ± 0.02
	9	0.16 ± 0.02
	12.5	0.310 ± 0.007
4h	**5**	0.06 ± 0.02
	9	0.19 ± 0.08
	12.5	0.35 ± 0.04

4.5.2. Phototoxic effect

PS29 did not cause any toxic effects upon incubation for 2h and 4h and in the absence of irradiation (**Figure 106** and **Table 35**).

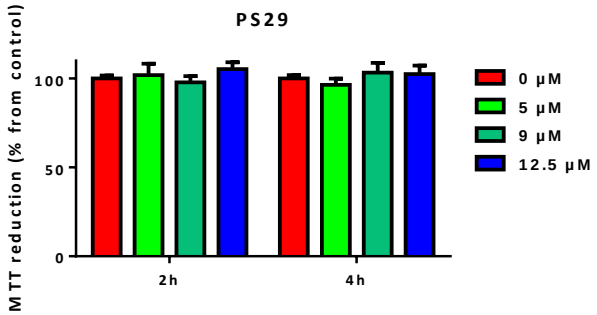

Figure 106 – Dark toxicity evaluated 24h after incubation with **PS29** for 2h and 4h using the MTT assay. Data are the mean value ± S.E.M. of at least three independent experiments performed in triplicates. *(p≤0.05), **(p≤0.01), ***(p≤0.001), ****(p≤0.0001) significantly different from control cells.

Table 35 – Dark toxicity evaluated 24h after incubation with **PS29** for 2h and 4h using the MTT assay. The percentage of toxicity was calculated relatively to control cells. Data are the mean value ± S.E.M. of at least three independent experiments performed in triplicates.

	C (μM)	PS29
2h	**0**	100 ± 2
	5	98 ± 6
	9	100 ± 5
	12.5	95 ± 7
4h	**0**	100 ± 2
	5	99 ± 4
	9	97 ± 3
	12.5	95 ± 6

In line with all the other RuPcs bearing PEG chains as peripheral substituents, four different sets of experiments were used to study the phototoxic effects of **PS29** (**Figure 107, Table 36**): *i)* incubation with PS for 2h and irradiation for 40 min at a fluence rate of 20 mW/cm^2; *ii)* incubation with PS for 4h and irradiation for 40 min at a fluence rate of 20 mW/cm^2; *iii)* incubation with PS for 4h and two irradiations for 40 min at a fluence rate of 20 mW/cm2 with a time interval of 1.5 h; and *iv*) incubation with PS for 4h and irradiation for 40 min at a fluence rate of 40 mW/cm^2.

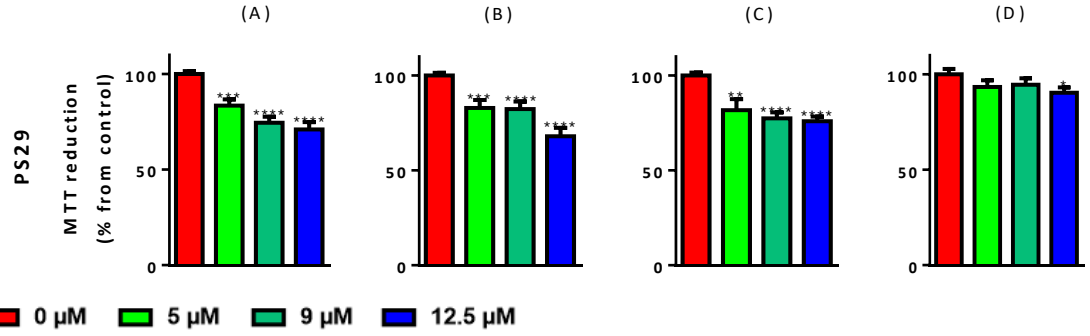

Figure 107 – Phototoxic effects of **PS29.** (A) incubation with PS for 2h and irradiation for 40 min at a fluence rate of 20 mW/cm^2; (B) incubation with PS for 4h and irradiation for 40 min at a fluence rate of 20 mW/cm^2; (C) incubation with PS for 4h and two irradiations for 40 min at a fluence rate of 20 mW/cm^2 with a time interval of 1.5 h; (D) incubation with PS for 4h and irradiation for 40 min at a fluence rate of 40 mW/cm^2. The percentage of toxicity was calculated relatively to control cells. Data are the mean value ± S.E.M. of at least three independent experiments performed in triplicates. *(p≤0.05), **(p≤0.01), ***(p≤0.001), **** (p≤0.0001) significantly different from control cells.

The incubation for 2h and posterior irradiation for 40 min at 20 mW/cm^2 resulted in a reduction in cell metabolic activity to 71 ± 4 % from control. No significant improvements were observed for the same irradiation conditions after 4h of incubation, which led to a decrease in cell metabolic activity to 68 ± 4 % from control. Irradiating twice for 40 min at 20 mW/cm^2 or irradiating

at 40 mW/cm^2 for 40 min, did not improve the phototoxic effect, reducing the cell metabolic activity to 76 ± 2 and 90 ± 3 % from control, respectively. The lack of improvement in the phototoxic effect with the increase in incubation period can be a consequence of the very small difference in the cellular uptake between the two incubation times.

Table 36 – Phototoxic effects of **PS29.** The percentage of toxicity was calculated relatively to control cells. Data are the mean value ± S.E.M. of at least three independent experiments performed in triplicates.

		C (μM)	**PS29**
2h	40min irradiation; 20mW/cm^2	**0**	100 ± 2
		5	84 ± 3
		9	75 ± 3
		12.5	71 ± 4
4h	40min irradiation; 20mW/cm^2	**0**	100 ± 1
		5	83 ± 4
		9	82 ± 4
		12.5	68 ± 4
	2 irradiations for 40 min with 1.5 h interval; 20mW/cm^2	**0**	100 ± 2
		5	82 ± 6
		9	77 ± 3
		12.5	76 ± 2
	40min irradiation; 40mW/cm^2	**0**	100 ± 3
		5	93 ± 4
		9	95 ± 3
		12.5	90 ± 3

4.6. Summary and conclusions

In this chapter, the *in vitro* efficacy of **PS1-4** and **PS11-29** was evaluated regarding their potential application as photosensitizers for cancer PDT.

- Overall, PSs without peripheral substituents exhibited higher phototoxic effect, which may be a consequence of their higher cellular uptake, as well as their higher singlet oxygen quantum yields.
- PSs bearing PEG chains at the peripheral positions exhibited a low internalization into the cells, accompanied by a low phototoxic effect, which may also be related to their low efficiency in producing singlet oxygen.
- PSs bearing PEG chains with terminal tertiary amine functions at the axial positions exhibited improved phototoxicity when compared to the corresponding PSs bearing alcohol groups.
- Functionalization with different carbohydrates introduced little differences in the cellular uptake and phototoxic effect; however, in general, these were higher for compounds bearing mannose units at axial positions.
- Among PSs bearing PEG chains at the axial positions (**PS1-4**), cationic **PS2a** exhibited the highest cellular uptake, probably due to the facilitated crossing of the negatively charged cellular membrane by endocytosis, as well as the highest phototoxic effect.
- Despite its lower cellular internalization, **PS4**, with twelve PEG chains at axial positions, revealed a remarkable photodynamic effect, which may be related to its high singlet oxygen quantum yield, together with its high solubility in aqueous environment.
- Carbohydrate functions at axial positions did not improve significantly the cellular uptake of PSs. However, in the case of PSs without peripheral substituents (**PS11-13** and **PS17-22**), it increased their photodynamic efficiency. From these, **PS11-13**, axially substituted with one deprotected monosaccharide and one DMSO molecule, exhibited a very efficient photodynamic effect even when lower doses where applied. Conversely, in spite of the high efficiency to generate singlet oxygen, **PS14-16**, with one deprotected monosaccharide and one DMSO molecule at axial positions and PEG chains at the periphery, showed low phototoxic effect, probably related to their poor uptake by cancer cells.
- Mixed **PS23-28**, with PEG chains at the periphery, displayed a low cellular uptake and a neglectable phototoxic effect.

- **PS29**, functionalized with a folic acid moiety and a DMSO molecule, revealed a higher cellular uptake than the corresponding **PS14-16**, with monosaccharides, although its phototoxic efficiency was lower.

Further studies are necessary to evaluate the selectivity of these photosensitizers towards tumor cells, namely experiments with non-cancerous cell lines as well as studies regarding the interaction of carbohydrate-bearing PSs with specific proteins, such as galectins and GLUT-1. Furthermore, tests with cell lines overexpressing the folate receptor are needed to evaluate the role of folic acid in **PS29** in the cellular uptake.

4.7. Experimental

4.7.1. General remarks

The centrifuge used was a SIGMA 2-16, the microcentrifuge was a VWR MiniFuge Galaxy MiniStar C1413 and the vortex was from VWR. The UV-visible absorbance measurements were performed on a microplate reader Synergy™ HT (Biotek Instruments) controlled by BioTek's Gen5™ Data Analysis Software. Near Infra-Red (NIR) spectra were recorded using a monochromator (JASCO CT-25CP) and a photomultiplier (Hamamatsu Photonics R5509-42), which was cooled at 193 K by a cold nitrogen gas flow system (Hamamatsu Photonics R6544-20). Irradiation was performed with a LC-122 LumaCare system, equipped with a halogen/quartz 250 W lamp coupled with the optic fiber probe. The fluence rates were determined with the energy meter Coherent FieldMaxII-Top with a Coherent PowerSens PS19Q energy sensor.

Canted neck cell culture flasks 75 cm2 with 0.2 µM vent cap were purchased from Corning. Culture plates were purchased from Orange Scientific, Brainel'Alleud, Belgium. The Neubauer chamber was from VWR.

Human bladder cancer cells HT-1376 derived from high-grade transitional cell carcinoma (from the American Type Culture Collection, ATCC, Manassas, VA, USA) were cultured in Roswell Park Memorial Institute (RPMI)-1640 medium, purchased from Sigma Aldrich, supplemented with 2 $g.L^{-1}$ of sodium bicarbonate (Sigma), 2 $mM.L^{-1}$ of glutamine (Sigma), 10% (v/v) of heat-inactivated fetal bovine serum (FBS; Life Technologies, Carlsbad, CA), and antibiotic-antimicotic containing 100 $units.mL^{-1}$ of penicillin, 100 $\mu g.mL^{-1}$ of streptomycin and 0.25 $\mu g.mL^{-1}$ amphotericin B (Sigma). SDS and 3-[4,5-dimethylthiazol-2-yl]-2,5-diphenyl-tetrazolium bromide (MTT) reagent were purchased from Sigma Aldrich, Trypsin-EDTA 0.25% (w/v) was purchased from Gibco and the trypan blue stain 0.4% was from BioWhittaker Reagents, Lonza.

The Pierce BCA Protein Assay Kit-Reducing Agent Compatible (containing the BCA Protein Assay Reagent and BSA standards at 2 mg/mL) was purchased from Thermo Scientific.

GraphPad Prism (v.5.00, GraphPad Software) was used for most of the displayed graphs, as well as for the statistical analysis.

4.7.2. Subculturing protocol

After removal of the culture medium and washing with 5 mL of warm sterile PBS, 2.5 mL of trypsin-EDTA 0.033 mL/cm^2 were added and the flasks were kept at 37 ºC until the cell layer begun to disperse from the bottom of the flask, a process that was monitored under an inverted microscope. Cell culture medium was added to inhibit the action of trypsin and the cell suspension was centrifuged at 1500 rpm at 20 ºC for 5 min. The supernatant was discarded and cells were suspended in new culture medium, from which appropriate aliquots were added to 25 or 75 cm^2 culture flasks, which were kept at 37 ºC in a humidified incubator gassed with 5% carbon dioxide (CO2) and 95% air. Cellular growth was monitored every day by inverted microscope and the culture medium was changed every two or three days.

4.7.3. Freezing and defrosting cells

For cell freezing, the same protocol was used as for the subculturing of cells. After suspension in new culture medium, at a concentration of about 3 x 10^6 cells/mL, 900 µL of cellular suspension were placed in sterile vials of 1 mL, already containing 100 µL of DMSO. The vials were quickly stored at -80 °C and, for storage for longer periods of time, were kept in liquid nitrogen.

Defrosting was carried out by heating the vials in a 37 °C bath and quickly adding the cell suspension to 5 mL of warm culture medium. After centrifuging at 1500 rpm at 20 °C for 5 min, culture medium was removed and cells were suspended in new culture medium from which appropriate aliquots were added to 25 or 75 cm^2 culture flasks.

4.7.4. PSs stock and work solutions

Sock solutions of 3mM in sterile DMSO were made for each PS and stored at −4 °C in the dark. Work solutions were prepared from stock solutions by dilution with sterile PBS, keeping the percentage (v/v) of DMSO under 0.45%.

4.7.5. Cellular uptake protocol

HT-1376 cells were seeded at a density of 9.5×10^4 cells per well in 48 well culture plates for 24 h. Cells were then incubated with the desired concentrations of each PS in the dark. After 2 or 4 hours of incubation, PS solution was removed, cells were washed twice with 500 µL of PBS and lysed with 190 µL of a 1% m/v SDS solution in PBS buffer at pH 7.0. PS intracellular emission in the samples was measured by NIR spectrofluorimetry and PS concentration was directly obtained by plotting the average of the emission for each PS standard in function of its concentration (µM).

The results were normalized by protein concentration, determined by bicinchoninic acid assay (BCA). For this, in a 96 well plate were placed aliquots (25µL) of each sample, to which were added 25µL of mQ water and 150µL of BCA reagent. After incubating at 37 °C for 30 min, absorption was measured at 570 nm. The amount of protein was calculated using a bovine serum albumin (BSA) calibration curve, which as prepared by adding to a 96 well plate 25 µL of lyse solution, 25 µL of standard solutions of BSA, prepared by successive dilutions of a stock solution of BSA with distilled water, and 150 µL of BCA reagent.

This procedure involves two steps. The first one consists on the biuret reaction, involving the reduction of cupric ion (Cu^{2+}) to cuprous ion (Cu^{+}) by peptide bonds in protein, in an alkaline environment. Hence, the concentration of Cu^{+} formed is proportional to the concentration of protein present in the solution. The second step comprises the chelation of two molecules of BCA with one Cu^{+} ion, originating a product that strongly absorbs light at the wavelength of 562 nm. Therefore, monitoring the absorption at 550-570 nm allows the determination of the amount of protein present in the sample.

4.7.6. MTT assay

HT-1376 cells were seeded at a density of 3.0×10^4 cells per well in 96 well culture plates for 24 h in a humidified incubator gassed with 5% CO_2 and 95% air, at 37 °C. Cells were then incubated with the desired concentrations of each PS in the dark. After 2 or 4 hours of incubation, PS solution was removed, cells were washed with PBS and 100 µL of culture medium RPMI-1640 was added. Cells were irradiated with light of $\lambda > 500$ nm delivered by a LC-122 LumaCare system either *i)* for 40 min at 20 mW/cm^2, *ii)* twice for 40 min at 20 mW/cm^2 with a time interval of 105h, or *iii)* for 40 min at 20 mW/cm^2. After incubation for 24h in a humidified incubator gassed with 5% CO_2 and 95% air, at 37 °C, 50 µL of culture medium were removed, 10 µL of MTT reagent were added to each

well and cells were incubated for 2h. Cell metabolic activity was determined by measuring the ability of cells to reduce (MTT) to (*E,Z*)-5-(4,5-dimethyltiazol-2-yl)-1,3-diphenylformazan. The formation of(*E,Z*)-5-(4,5-dimethyltiazol-2-yl)-1,3-diphenylformazan was quantified by absorption spectroscopy and the data were expressed in percentage of control (i.e. optical density of formazan from cells not exposed PSs). The same procedure was used for the dark toxicity experiments, in which cells were kept in the dark for the 40 min corresponding to the irradiation time.

Final Summary and Conclusions

In this thesis, RuPcs were designed and prepared to be used as photosensitizers for Photodynamic Therapy.

The axial functionalization of RuPcs was addressed with two different types of ligands:

- Pyridyl-based ligands, which were donated with:
  - PEG chains and/or charged functions, to produce PSs with improved solubility in water;
  - Carbohydrates or folic acid, to confer selectivity towards tumor cells.
- Phosphine ligands:
  - That were functionalized with cationic and anionic functions. These proved to be rather unstable ligands when compared to pyridyl-based ligands; all the attempted to prepare RuPcs bearing charged phosphine ligands were unsuccessful.

PS1-29, obtained from the coordination of different pyridyl ligands to the axial positions of RuPcs, were studied regarding their photophysical properties and their *in vitro* efficacy:

- PSs bearing four ammonium functions (**PS2a**) or with eight or more PEG chains, either as axial ligands (**PS4**) or at their periphery (**PS3**, **PS14-16** and **PS23-29**), exhibited good solubility in aqueous solutions.
- All compounds were able to produce singlet oxygen upon light activation.
  - The differences in the singlet oxygen quantum yields (Φ_Δ) provided by the axial ligands in the different PSs seem to be related to the electronic features of the pyridyl ligand, with π-electron donor groups decreasing Φ_Δ values, and π-electron withdrawing groups increasing Φ_Δ values.
  - The influence of axial functionalization in the ability to generate singlet oxygen seems to have an additive nature.
- *In vitro* studies in HT-1376 cancer cells revealed that RuPcs with different functionalizations at the axial positions are suitable compounds to be used as photosensitizers for PDT. The influence of the specific functionalization in the efficiency of the PS is summarized as follows:
  - PSs without peripheral substituents exhibited higher singlet oxygen quantum yields, higher cellular uptake and higher *in vitro* phototoxic effect.
  - RuPcs peripherally functionalized with polyether chains displayed a pronounced decrease in singlet oxygen quantum yields, cellular uptake and *in vitro* phototoxic effect.

- The presence of one carbohydrate unit seems to have little influence in the cellular uptake by HT-1376 cancer cells
- **PS2a**, with four terminal ammonium functions, **PS4**, with twelve axial PEG chains, and **PS11-12,** with one deprotected carbohydrate unit and one DMSO as axial ligands**,** exhibited the highest photodynamic efficiency, followed by **PS1-2** and **PS17-21**, bearing axial PEG chains and protected monosaccharides.